Comparative Analysis of Brick-to-Brick Modeling Techniques for Evaluating Compressive Behavior of Masonry

By

Swarnangshu Ghosh

In the partial fulfillment of the requirements for the degree of

Master of Science

in Structural Engineering

at the Delft University of Technology,

to be defended publicly on Wednesday, October 25th, 2023, at 14:00

Student number: 5531810

Graduation Thesis Committee: Dr. Rita Esposito (Chair)   (TU Delft)

Dr. Francesco Messali   (TU Delft)

Prof. Dr. Mauro Overend   (TU Delft)

TUDelft

ACKNOWLEDGEMENT

ABSTRACT

The preservation of historical heritage buildings frequently requires the assessment of brick masonry structures. These structures exhibit complex behaviour due to the arrangement of units and the interaction between bricks and mortar. This study aims to compare two modelling techniques for simulating masonry's compressive response and understanding which technique performs better.

This study employs two block-based modelling techniques: a simplified brick-to-brick model and a detailed brick-to-brick model. The block-based modelling technique was selected to capture the intricate structural details and crack patterns of masonry specimens. Wallet specimens were evaluated to understand the compressive behaviour of masonry.

Two experimental benchmarks were chosen to validate the selected modelling approach. First, experimental results by Thamboo (2020), also modelled with a simplified brick-to-brick model by Zahra et al. (2021), were considered. However, to obtain numerical results comparable to the experimental ones, unrealistic input parameters had to be assumed (i.e., very low value of elastic modulus for the bricks); consequently, this benchmark was ultimately deemed unreliable. Hence, a second benchmark from Jafari (2021) was chosen which did not present such issues.

Considering the effect of confinement was crucial to obtain results in agreement with experiments. The detailed brick-to-brick model, explicitly modelling each brick-and-mortar joint with solid elements and accounting for mortar confinement, proved to be the only modelling approach able to simulate the second experimental benchmark. The simplified modelling technique, considering mortar joints as zero-thickness interfaces between solid elements representing the bricks, consistently underestimated the peak loads as mortar confinement was not included. This may explain why unrealistic input parameters were used by Zahra et al. (2021) to simulate the first benchmark. In general, the post-peak behaviour was difficult to simulate.

A sensitivity study was performed by varying the boundary conditions, Poisson's ratio of mortar and integration scheme. The study on boundary conditions was performed on both the simplified and detailed models whereas the study on Poisson's ratio and integration scheme was performed on the detailed model. The boundary conditions did not have a significant influence on the global behaviour of the specimen in the detailed or simplified models. Small variation in compressive strength and crack pattern were observed, but the effect on post-peak behaviour could not be evaluated due to numerical instability. The Poisson's ratio of mortar was found to have a significant influence on the peak compressive strength of the masonry specimen. A higher Poisson's ratio resulted in a greater value in the peak compressive strength of masonry. A higher value of Poisson's ratio increases the amount of confinement in mortar layers resulting in higher values of compressive strength of masonry. A high integration scheme (3×3×3) and a regular integration scheme (2×2×2) effectively captured crack propagation. On the contrary, a reduced integration scheme (1×1×1) could not do so effectively. The reason can be attributed to the higher number of integration points in the former cases which allows for better propagation of cracks.

These investigations provide precious insight into the choice of modelling techniques for simulating the compressive behaviour of brick masonry. The detailed modelling technique can be implemented to study the compressive behaviour of masonry specimens if mortar confinement is accounted for. However, further effort is necessary to reduce numerical instability to simulate the post-peak response. This can be adopted further to study the influence of, for example, bond pattern, specimen thickness (e.g., multi- vs single-wythe masonry) and specimen shape (e.g. wallets, prism, core) on the compressive behaviour of masonry.

Table of Contents

1. INTRODUCTION

The chapter provides a brief overview of the background of the thesis, along with the research gap and the methodology to answer the formulated research questions.

1.1 Background

To preserve historical heritage buildings, very often engineers need to deal with the assessment of multi-wythe brick masonry structures, for example, churches, bridges, and quay walls. To assess these structures often nonlinear finite element analyses with different modelling techniques are used.

The 3D brick-to-brick modelling technique can be used to simulate local failure modes. This technique was used by Lourenco (1996), Sarhosis and Lemos (2018), D'Altri et al. (2020), and Zahra et al. (2021) when local failure modes and stress states are of main interest. Pina and Lourenco (2006) proposed a novel particle model to model double-wythe masonry.

1.2 Research question

What are the most relevant factors to consider in the modelling of the compressive behaviour of masonry?

Sub-research questions

- Which brick-to-brick modelling technique, simplified or detailed simulates the compressive behaviour of masonry better?
- How do the boundary conditions influence the global behaviour of a masonry wallet?
- How does Poisson's ratio of mortar affect the global behaviour of the masonry wallet in compression?
- What is the influence of the choice of integration scheme in simulating failure mechanisms?

1.3 Research Methodology

This thesis investigates different brick-to-brick modelling techniques to simulate the compressive behaviour of masonry specimens. The aim of this thesis is to understand which modelling technique gives a more accurate representation of the compressive behaviour of masonry. The work has been restricted to compressive tests on single-wythe wallets made of clay brick masonry with a strong-brick weak-mortar combination. A strong brick-weak mortar combination is generally adopted for brick masonry structures in Western countries (Gumaste et al. 2007).

In this study, two types of brick-to-brick models called the simplified-brick-to-brick model and detailed brick-to-brick model will be employed to model the wallets. By using this technique, a direct description of the actual masonry texture and the structural details can be interpreted. An explicit

illustration of the crack pattern can also be obtained. However, this technique requires great computational effort.

There are numerous other techniques to model masonry, namely continuum models and macro element models and geometry-based models A continuum model, in which there is no differentiation between blocks and mortar layers, requires much lesser computational effort. But since there is no distinction between the mortar and blocks, it is difficult to study the evolution of the cracks which will be performed in this study. Macro element models are generally preferred to model masonry panels, thus not preferred for this study. (D' Altri et al. 2019)
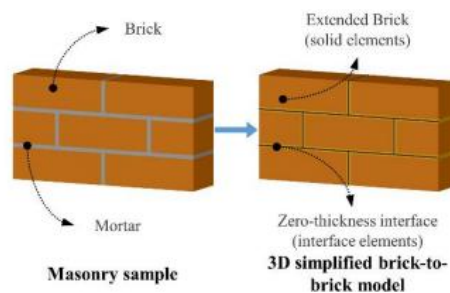
Figure 1.1: A figure depicting the 3D-brick-to-brick model (Chang 2019)

The compressive behaviour of wallet specimens will be evaluated in this study. The compressive behaviour of masonry is usually determined experimentally via prism and wallet tests. Prisms are small assemblages of masonry units having thicknesses of one to three units whereas masonry wallets are short wall specimens of several courses having a width of three or more units (Thaickavil and Thomas (2017)). American standards incorporate testing of prisms (ASTM C1314-18). On the other hand, European standards incorporate the testing of wallets (EN 1052-1:1998).

Up to now, there are limited studies available in literature regarding the modelling of the compressive behaviour of brick masonry. Zahra et al. (2021) used a simplified Finite element based micro modelling technique to analyse the compressive behaviour of bonded brickwork specimens. Drougkas et al. (2015) used detailed micro-modelling techniques for the numerical prediction of the compressive response of masonry. Zucchini and Lourenco (2002) proposed a novel micro-mechanical homogenisation model for masonry.

Now, the selected brick-to-brick model should be validated for being used to model masonry specimen. The 3D brick-to-brick model utilized by Zahra et al. (2021) proved to be reliable to simulate the cracking in multi-wythe prisms and wallets. This was the first benchmark selected for our thesis. The numerical models created in this thesis initially looked to simulate FE analysis of Zahra's study. The modelling was done in Abaqus using the concrete damage plasticity (CDP) constitutive model. However, in this study, the modelling will be performed in DIANA.

In the first set of models, a 3D-simplified brick-to-brick model (shown in **Fig. 1.1**) will be implemented. In this case, the masonry units are modelled as 3D solid elements with non-linear material behaviour and assembled through surface-to-surface contact interfaces to replicate the masonry interface behaviour without explicitly modelling the mortar layers. A suitable non-linear constitutive model is chosen for the solid elements and interface elements. A detailed brick-to-brick modelling technique was selected as the second modelling technique. In this technique, the bricks and mortar were explicitly modelled according to their real dimensions. A rotating smeared crack model was implemented for the bricks and mortar. Under tensile loading, an exponential softening curve is assumed for the bricks and mortar, after attaining the peak load.

A second benchmark was eventually chosen as the results obtained by Zahra's analysis proved to be unreliable. The experimental program of Jafari (2021) was selected as the second benchmark. The experimental results obtained by subjecting the MAT-3 type of wallet under compression was sought to be replicated.

A sensitivity study is also conducted. The Poisson's ratio and integration scheme are varied, and the results are compared with the initial analysis.

1.4 Outline of the Thesis

Chapter 1 provides the background and context for the research. The methodology for the study is also outlined, mentioning about different techniques to model masonry specimens. The research questions are also defined in this chapter.

Chapter 2 provides a background to the response of masonry under compressive loading. The methods of testing compressive behaviour and the various modelling strategies are discussed.

Chapter 3 presents the experimental benchmarks chosen for this thesis. The different modelling techniques adopted in this study have been discussed in detail. Also mentioned are the geometrical, shape and material properties along with the boundary conditions adopted for the numerical models.

Chapter 4 describes the various models developed by using the simplified brick-to-brick and detailed brick-to-brick modelling techniques. The results obtained by simulating these models are analyzed. The sensitivity study is also performed.

Chapter 5 presents the conclusions of this study.

Chapter 6 presents recommendations for future research.

2. LITERATURE REVIEW

2.1 Response of masonry under compressive load

The mechanics of masonry is intricate and exhibits non-linear behaviour. Masonry consists of blocks held together by mortar. Therefore, it is a heterogeneous material.

The mechanical properties of block, mortar, and the bond between them govern the global behaviour of the masonry structure/specimen. Masonry is stronger when subjected to compression as evident from higher values of strength and compressive fracture energy. The bond between mortar and blocks is weak resulting in masonry being fragile under tension. Hence, a combination of bricks and mortar under compression loading gives complex stress and strain distribution between the brick units and mortar joints. The relative stiffness of brick and mortar determines the internal state of stress which in turn determines the mode of failure. (D' Altri et al. 2019)

The onset of cracking in masonry under compression depends on the relative difference in stiffness of bricks and mortar. The failure of masonry is initiated by the tensile splitting of brick when the bricks are stiffer and stronger than the mortar. In this scenario, the mortar will be subjected to triaxial compression whereas the brick will be subjected to bilateral tension coupled with axial compression. On the contrary, tensile splitting failure of mortar will be the governing failure mechanism if the brick's stiffness is lower than the mortar's stiffness. In this scenario, the brick will be subjected to triaxial compression whereas the mortar will be subjected to uniaxial compression coupled with bilateral tension. (Kaushik et al., 2007; Shetty et al., 2020)

The scenarios mentioned in the previous paragraph are mentioned in **Fig. 2.1**

(a)

(b)
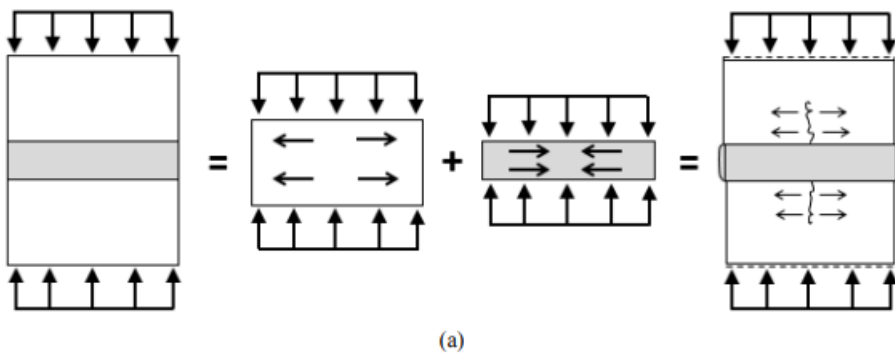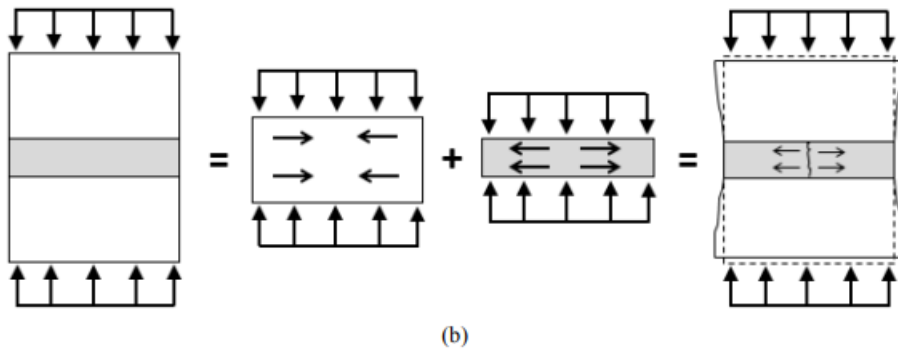
Figure 2.1: Representation of state of stress and crack initiation in (a) stiff brick coupled with soft mortar ($E_b > E_m$) (b) soft brick coupled with stiff mortar ($E_b < E_m$) (Shetty et al., 2020)

2.2 Compressive test of masonry

The compressive behaviour of masonry is usually studied by testing prisms and wallets. A detailed overview of prisms and wallets along with their failure mechanisms is presented below. Standards generally prescribe these tests for the determination of elastic modulus and compressive strength, but by applying a displacement control procedure the entire softening response can be obtained.

Prisms are small assemblages of masonry units having a thickness of one to three units (Thaickavil and Thomas 2018). Prisms are typically constructed in a stack bond with a full mortar joint. A masonry prism subjected to compression loading is depicted in **Fig. 2.2**. ASTM C1314 (2016) incorporates the procedure for the testing of prisms. Prism testing should be undertaken before construction begins to verify that the compressive strength of the assembled materials is not less than the specified compressive strength used in the design.

Masonry

Figure 2.2: Masonry prism subjected to compressive load.

An experimental study was conducted on masonry prisms using different types of brick and mortar by Singh and Munjal (2017). A direct correlation was fo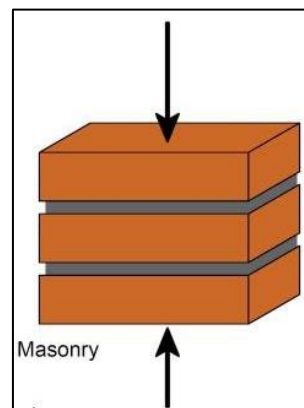und between compressive strength of masonry and the compressive strength of the constituent elements. Kaushik et al. (2007) attempted to obtain a generalized masonry stress-strain curve which would require compressive strength of brick and mortar as the input parameters. For this purpose, uniaxial compression testing of 84 prisms were conducted.

Wallettes are short wall specimens of several courses having a width of three or more units (Thaickavil and Thomas 2019). The wallet (shown in **Fig. 2.3**) is an element that better represents a real masonry wall because it contains all its parts, i.e.: bed and head joints and individual units lay in and bound together by mortar (Azevedo et al. 2018). Hence wallets have been chosen for this study.
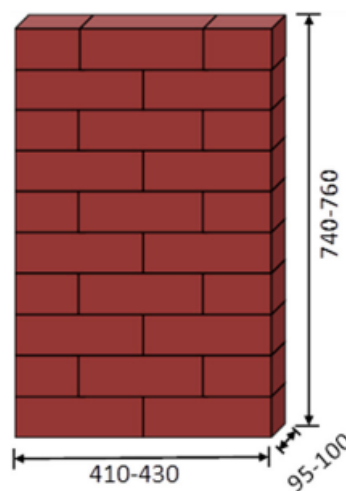
Figure 2.3. A masonry wallet.

Medine and Alper (2013) studied the compressive behaviour of historical masonry wallets through experimental investigation. It was observed that the existing codes present an unconservative prediction of the compressive strength of masonry thus emphasizing the need for a significant safety margin for structural assessment. Several empirical equations were also deduced for the strength and stress-strain relationships of these wallets.

Thamboo and Dhanasekhar (2020) subjected numerous lime-mortared masonry wallets to monotonic and cyclic compression. The failure mechanisms of wallets were mostly governed by parallel vertical cracks originating at the brick-mortar interface. These cracks later propagated through the middle of the bricks. The double and triple-thick brick wallets mainly showed single splitting cracks on the short sides in addition to tensile parallel cracks on the long sides. These failure mechanisms are shown in **Fig. 2.4**.

Figure 2.4: Failure modes of wallettes under compression (a) Single (b) Double (c) Triple (d) Double wythe wallette splitting cracks (e) Triple wythe wallette splitting crack. (Thamboo and Dhanasekhar 2020)

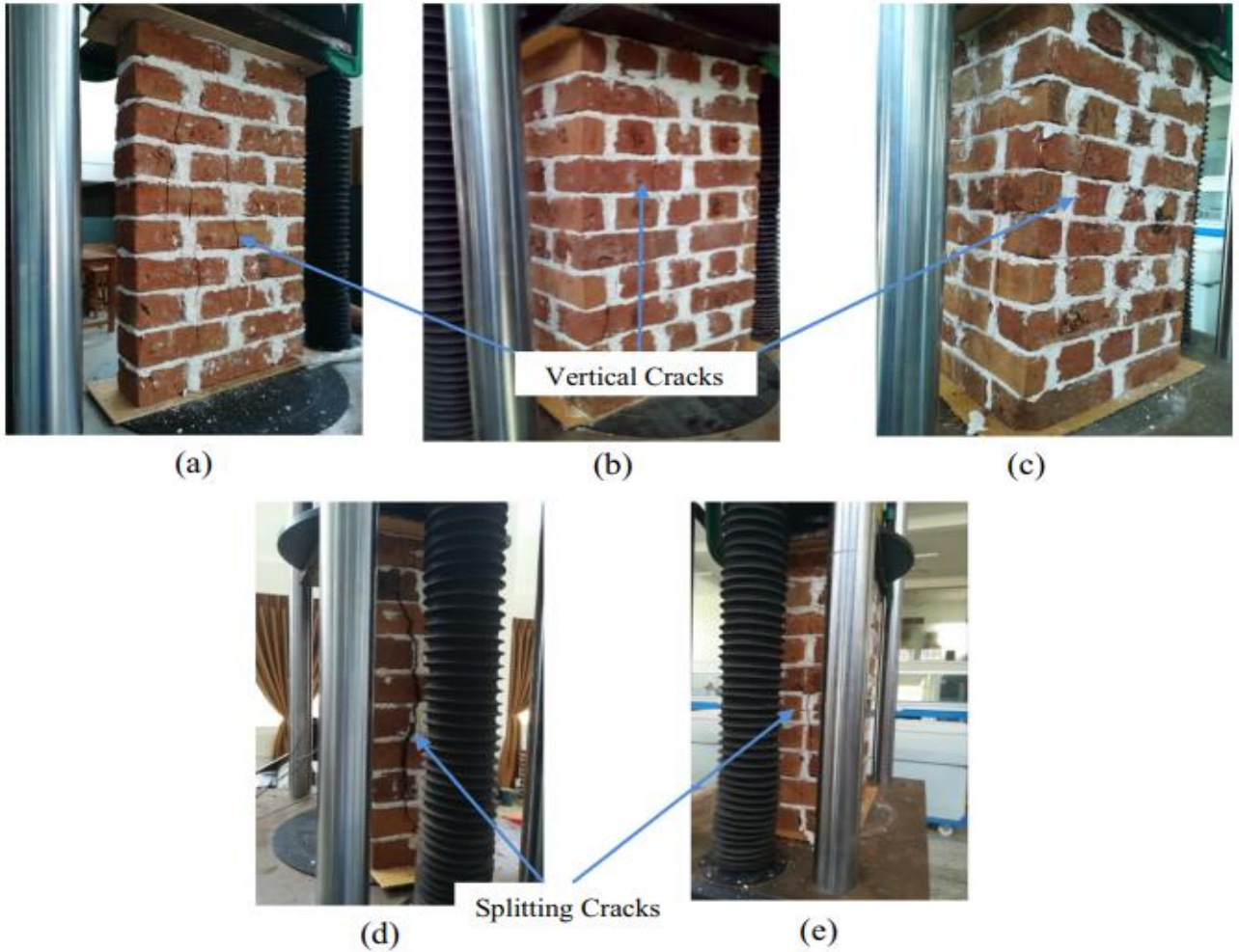Raghu Prasad et al. (2014) attempted to understand the influence of the size of masonry wallet on it's compressive strength. A reduction in strength with an increase in size is observed for strong brick-weak joint type wallets.

Jafari (2021) subjected single and double-wythe clay masonry wallets under vertical and horizontal compression. In the case of vertical compression for the single-wythe specimen, the cracks mainly occurred in the central part of the specimens. In the post-peak phase, in the case of vertical loading, splitting cracks along the thickness of the wallets. In the case of the double-wythe specimens, vertical splitting cracks started in the bricks in the top and bottom parts of the specimens. In the post-peak phase, splitting cracks in the bricks and interface debonding in subsequent layers resulted in the formation of a diagonal shearing crack. Jafari et al. (2021) correlated the stress-strain relationships.

However numerical/experimental studies of the behaviour of wallets with more than three bricks in thickness, under compression loading have not been explored in the past. Hence, the failure

mechanisms of these specimens remain largely unexplored. This thesis aims to shed light on these questions.

There are various factors that can affect masonry's compressive strength. Jafari (2021) conducted tests on five different masonry types to investigate the influence of mortar compressive strength, unit compressive strength, masonry size, and joint thickness on the compressive strength of masonry wallets. A small variation was observed while comparing the compressive strength of masonry wallets made of solid clay brick and perforated clay brick, despite a considerable difference in the compressive strength of mortar in both cases. The compressive strength and Young's modulus of solid clay brick and perforated clay brick were very similar. But in the case of CS brick masonry and perforated clay brick masonry, the latter showed a significantly higher compressive strength due to stronger bricks. Mortars with similar values of compressive strength were used for CS brick masonry and perforated clay brick masonry specimens. Hence it was concluded that the influence of mortar compressive strength on the compressive strength of masonry was not as significant as the brick compressive strength.

Thamboo and Dhanasekhar (2020) subjected single, double, and triple wythe wallets consisting of lime mortar bonded brickwork to monotonic and cyclic loading. Two types of clay bricks were used. A slight increase in the compressive strength of double-wythe wallets was found in comparison with single-wythe wallets. Monotonically loaded wallets also showed higher compressive strength than cyclically loaded wallets.

The influence of unit and mortar properties on Young's modulus of masonry was studied by Jafari (2021). Five types of masonry were considered and subjected to compression loading. Perforated clay masonry with stiffer mortar than solid clay masonry resulted in a higher value of Young's Modulus, even though perforated clay brick and solid clay brick have similar values of compressive strength and Young's Modulus. It was concluded that masonry with stiffer mortar resulted in stiffer masonry. It was also found that increasing the stiffness of masonry constituents did not necessarily increase the stiffness of masonry. The conclusion was reached that mortar contributes little to the stiffness of masonry with large elements and a thin layer of joints.

Gumaste et al. (2007) found out that elastic modulus of stack bonded, and English bonded prisms made of table moulded bricks were in close range. But in the case of wire-cut brick prisms, a large scatter was observed in the elastic modulus value. But in case of wallets, table moulded brickwork showed higher scatter in the elastic modulus value than wire cut brickwork. This may be attributed to the high coefficient of variation of strength for table moulded bricks.

2.3 Techniques to model masonry

In this study, brick-to-brick based modelling technique has been employed to model the masonry wallets. There are numerous techniques to model masonry, namely brick-to-brick based models, continuum models, macro element models and geometry-based models. (D' Altri et al. 2019)
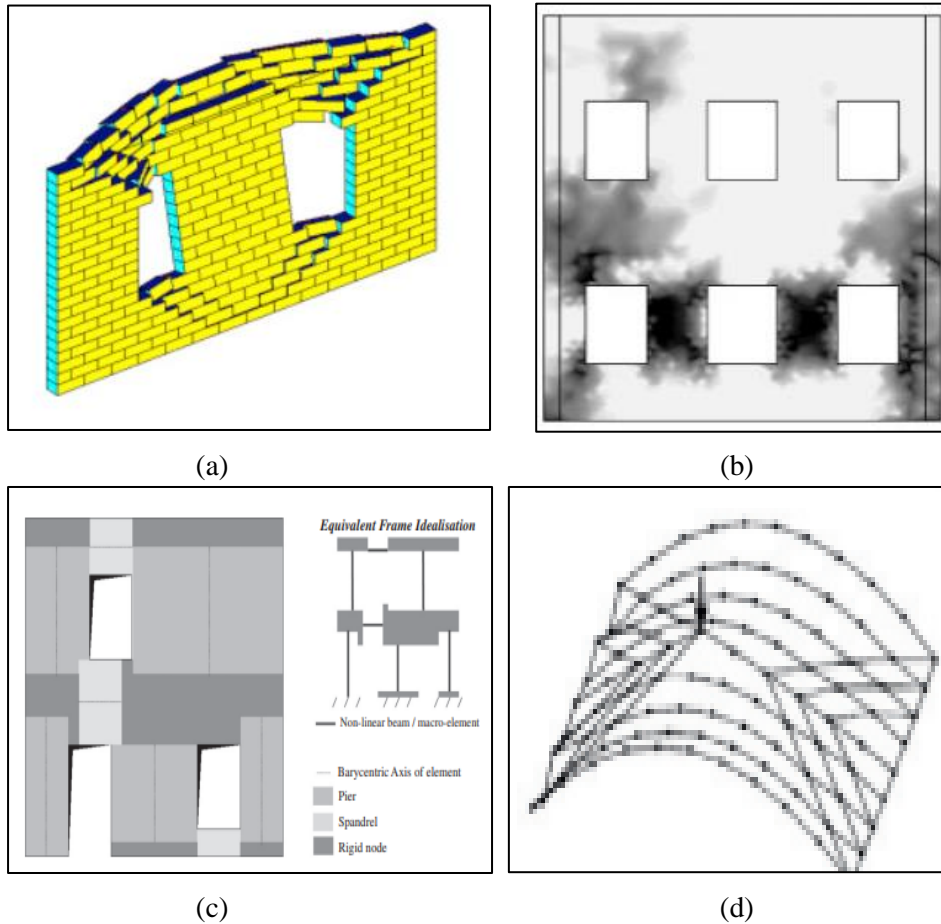

<div align="center">(a)</div>

<div align="center">(b)</div>

<div align="center">(c)</div>

<div align="center">(d)</div>

Figure 2.5. (a) Brick-to-brick model (Baraldi and Cecchi 2017) ; Continuum model (Berto et al. 2002); (c) Macro element model (Lagomarsino et al. 2013); Geometry based model (O'Dwyer 1999)

Continuum models (shown in **Fig. 2.5b**) perceive the masonry as a continuous body without differentiating between blocks and mortar layers. In one approach of this technique, homogenous constitutive laws for masonry required as input. But due to the heterogeneity of masonry, this is a challenging task. In the second approach, a representative volume element (RVE) is selected for the homogenization of masonry. The RVE can capture the heterogeneity of masonry. This modelling technique requires lesser computational effort. But since there is no distinction between the mortar and blocks, it is difficult to study the evolution of the cracks which will be performed in this study.

Macro element models (shown in **Fig. 2.5c**) interpret the structure in the form of panel-scale structural components with a mechanical based behaviour. Piers and Spandrels are the two structural components. The constitutive law of macro elements attempts to simulate the behaviour of panel elements. The local failure modes are generally not considered in this modelling technique. This

modelling technique is employed to understand the behaviour of masonry structures to seismic loading. In this study, the selected modelling technique should be able to accurately simulate the local failure modes. Hence this technique is not suitable for this study.

In a geometry-based model (shown in **Fig. 2.5d**), only the geometry of the structure is required as an input. These models are mainly aimed at the investigation of structural equilibrium or collapse through static or kinematic theorem. But in this study, we are interested in learning about the failure modes. Hence geometry-based models are not preferred for this study.

On the other hand, brick-to-brick models (shown in **Fig. 2.5a**) attempt to simulate the response of the material at the scale of principal heterogeneity of the structure, which is consists of blocks with mortar joints. By using this technique, a direct description of the actual masonry texture and the structural details can be interpreted. An explicit illustration of the crack pattern can also be obtained. This technique requires great computational effort.

Droughkas et al. (2015) used a detailed micro-modelling technique to predict the compressive response of masonry. The mortar, units and interfaces were defined separately. The modelling method could provide reliable results. Petracca et al. (2017) proposed a continuous micro-model which discretizes both units and mortar joints. A damage model in both compression and tension were utilized for this purpose. These damage models were then refined to simulate the non-linear response under shear and to control the dilatancy.

3. NUMERICAL MODELLING

In this chapter, first, the experimental benchmarks are presented and subsequentially the numerical modelling techniques adopted are described. The work has been restricted to compressive tests on single-wythe wallets made of clay brick masonry with a strong-brick weak-mortar combination. Two brick-to-brick modelling techniques were used; a simplified model in which the mortar and the interface were modelled with zero-thickness interface elements due to which the bricks were extended in thickness and a detailed model in which the bricks and mortar were modelled explicitly according to the real dimensions.

3.1 Experimental benchmarks

In this section, the chosen experimental benchmarks are described.

3.1.1 Benchmark 1: Thamboo et al. (2020)

The experimental program of Thamboo et al. (2020) was selected as the first benchmark. In this experimental program, eighteen specimens comprising single, double, and triple wythe wallets were tested under axial compression. For our study, the single-wythe wallet constructed using the B1 type of brick was considered. A new benchmark was eventually selected after some discrepancies were found with Benchmark 1. This discrepancy has been discussed in the next chapter.
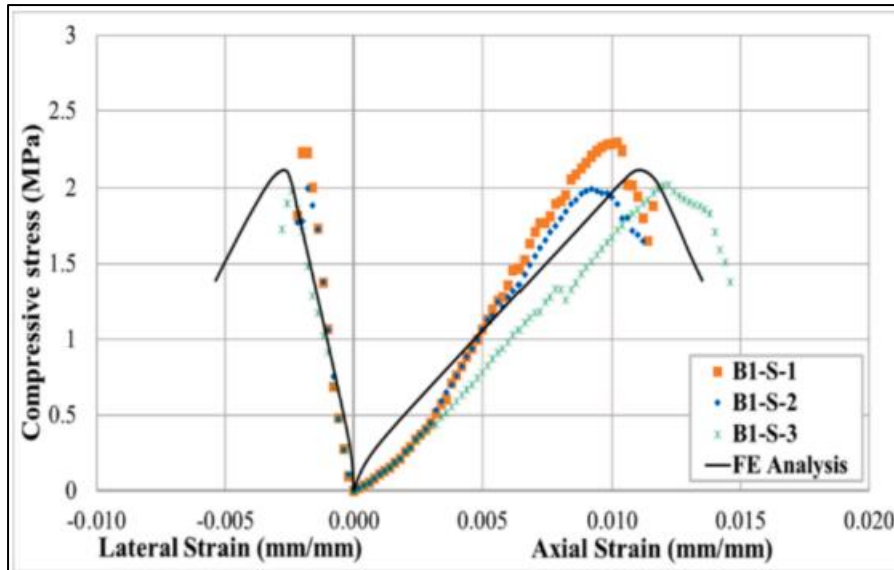
The experimental setup for the single wythe wallet along with the dimensions is shown in **Fig. 3.1a.** The thickness of the mortar bed and head joints was 10mm.
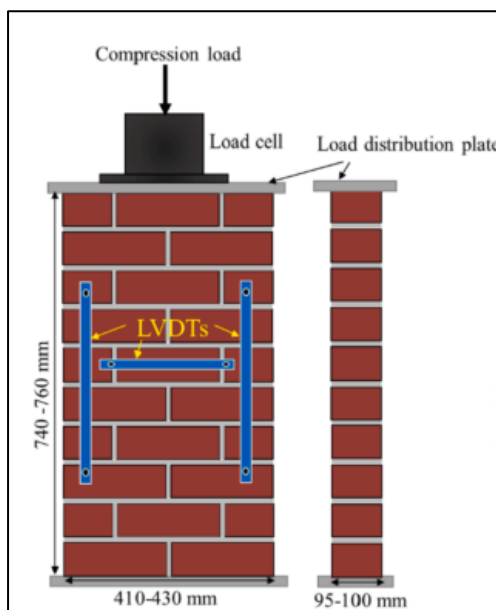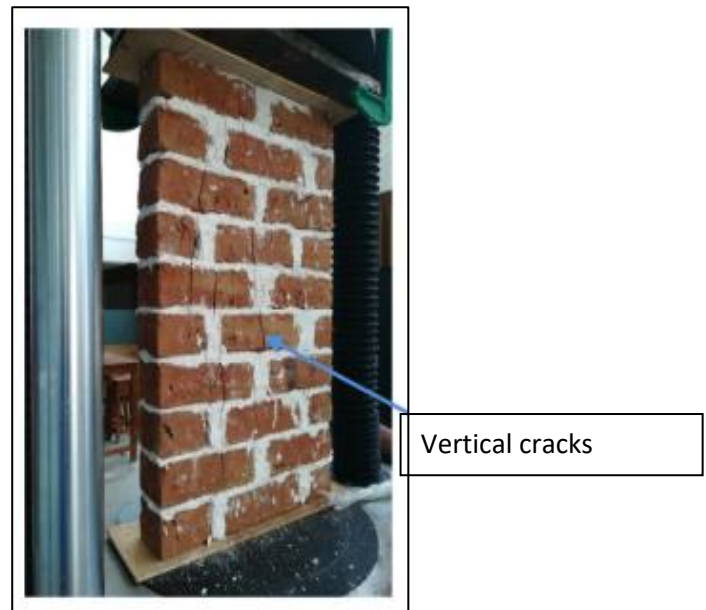
(a)   (b)

(c)

Figure 3.1: (a) Compression test setup for single wythe specimen; (b) Failure mode of single wythe wallet; (c) Stress-Strain plots of single-wythe wallets along with curve obtained from the Finite Element analysis. (Zahra et al. 2021)

The compressive strength of the brick and mortar are mentioned in **Table 3.1.**

Table 3.1: Material properties of the B1 brick.

Material	Compressive Strength	Tensile Strength
B1 Brick	5.1 (9.5) MPa	0.52 (8.3) MPa

It was observed that the primary cause of failure was the development of parallel vertical cracks in the brick-mortar interface which later propagated to the middle of the bricks as shown in **Fig. 3.1b**.

The wallets were modelled with a simplified brick-to-brick modelling technique by Zahra et al. (2021). The masonry units were modelled as 3D solid elements whereas interface elements were used to model the mortar and the brick-mortar interface. A concrete damage plasticity model was used to represent the non-linear behaviour of the bricks considering exponential softening in tension and parabolic softening in compression. A traction-separation constitutive law was used for the interface elements. A linear elastic response was considered initially for the interface of this model followed by the initiation and evolution of damage in the interface. The model was calibrated on the experimental results of the single-wythe masonry and then used to simulate the double and triple-wythe specimens. The stress-strain plot obtained from the numerical analysis is mentioned in **Fig. 3.1c**.

Through the numerical models created in this thesis, an attempt will be made to replicate the experimentally obtained compressive stress-axial strain plots and to simulate the failure modes.

3.1.2 Benchmark 2: Jafari (2021)

The experimental program of Jafari (2021) was selected as the second benchmark. Jafari (2021) tested five different types of wallets under axial compression. The MAT-3 type wallets were selected for this thesis. The material properties of the brick used to construct this wallet has been mentioned in **Table 3.2.**

Table 3.2. Material properties of the MAT 3 wallet.

Material	Compressive Strength	Tensile Strength
Solid clay Brick	28.31(0.10) MPa	4 (0.11) MPa

In this study, an attempt was made to emulate the experimental results of the MAT 3 type of wallet shown in **Fig 3.2a**.

(a)   (b)
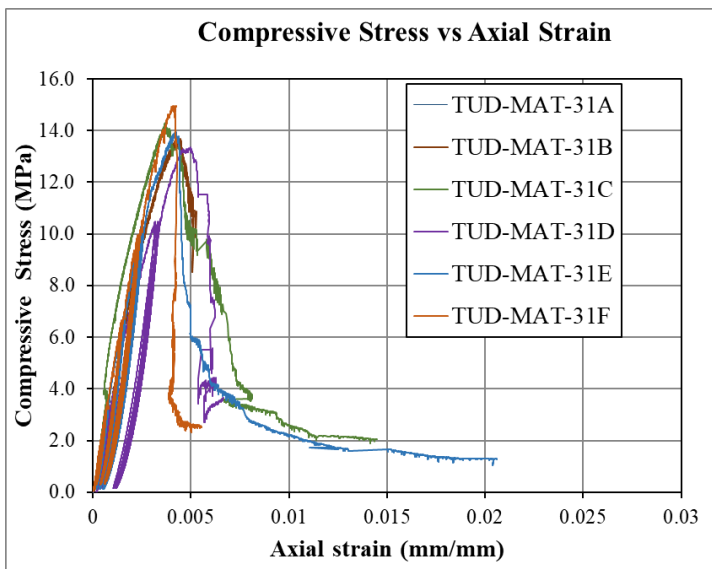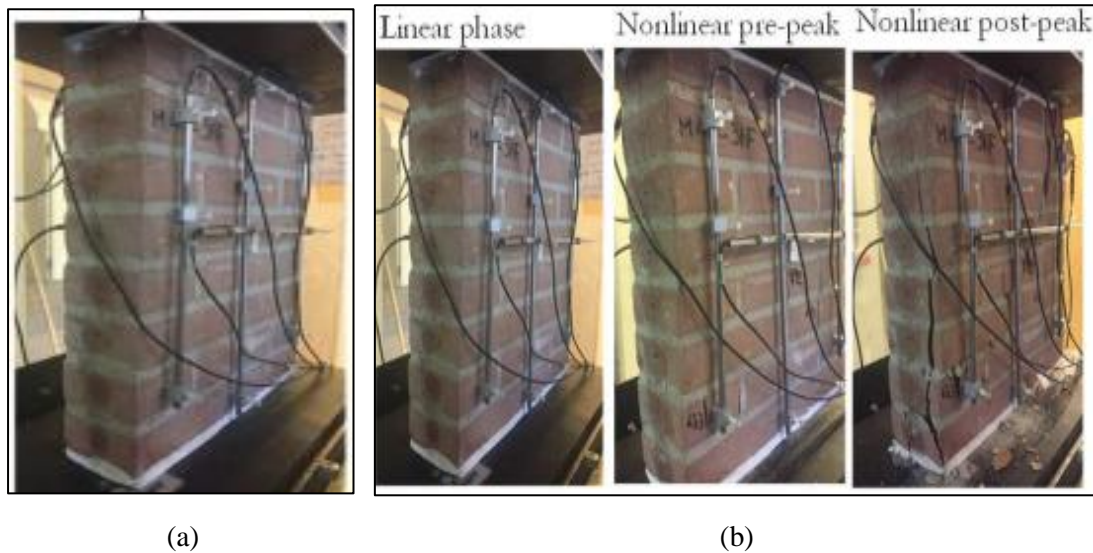
(c)

Figure 3.2: (a) Single wythe MAT 3 wallet; Failure modes of the single-wythe wallet; (c) Experimentally obtained stress-strain plots. (Jafari 2021)

Fig. 3.2b shows the failure modes of the specimen. It was observed that cracks mainly occurred in the central part of the specimen. During the post-peak phase, vertical splitting cracks developed along the thickness of the wallets. **Fig 3.2c.** shows the compressive stress-axial strain plots of tested MAT 3 wallets.

Through the numerical models created in this thesis, an attempt will be made to replicate the experimentally obtained compressive stress-axial strain plots and to simulate the failure modes.

19

3.2 Modelling techniques

In this study, two types of block-based models have been used to model the masonry specimens. They are here named in short as Simplified Model and Detailed Model. A brief description of the modelling techniques along with the constitutive laws adopted for each type of model has been provided below.

3.2.1 Simplified brick-to-brick Model

In this modelling strategy, the mortar joints and the brick-mortar interfaces were modelled with zero-thickness interface elements. The bricks were modelled with solid elements and they were extended in thickness to account for the thickness of the mortar. A full-Newton Raphson iterative scheme was selected for the analysis of these models. Energy and force convergence norms were selected. The simplified model for a single wythe wallet is shown in **Fig. 3.3(a)**
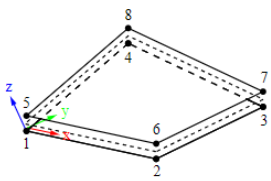

(a)   (b)
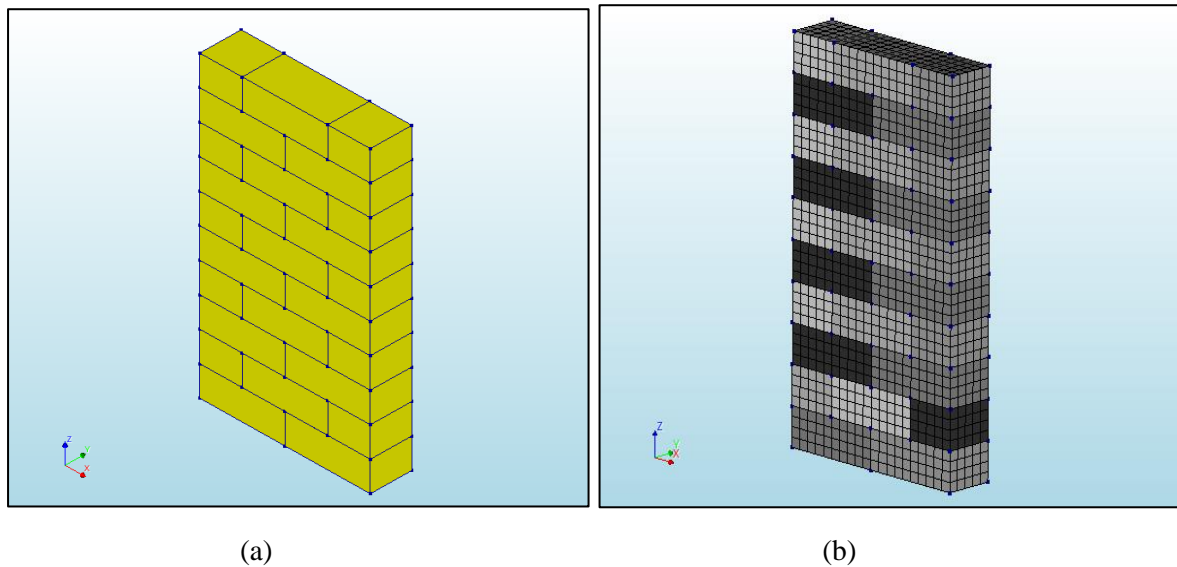
Figure 3.3. (a) Simplified brick-to-brick model; (b) Mesh of a simplified brick-to-brick model

The mesh generated for the simplified model is shown in **Fig. 3.3(b)** The mesh size selected for this modelling technique was 20 mm.

The element types and properties of the element in the simplified model are mentioned in **Table 3.3**.

Table 3.3: Element types and properties used in the simplified model.
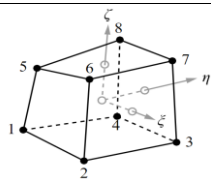
Element type	Illustration	Description	Interpolation scheme	Integration scheme	Application
HX24L		8 node solid brick element	Linear	Regular (2×2×2)	Brick
Q24IF		Plane quadrilateral, 4+4 nodes, 3D	Linear	Regular (2×2)	Mortar interface

A rotating smeared crack model was implemented for the bricks. Under tensile loading, an exponential softening curve is assumed for the bricks, after attaining the peak load. It is shown below in **Fig. 3.4a.**
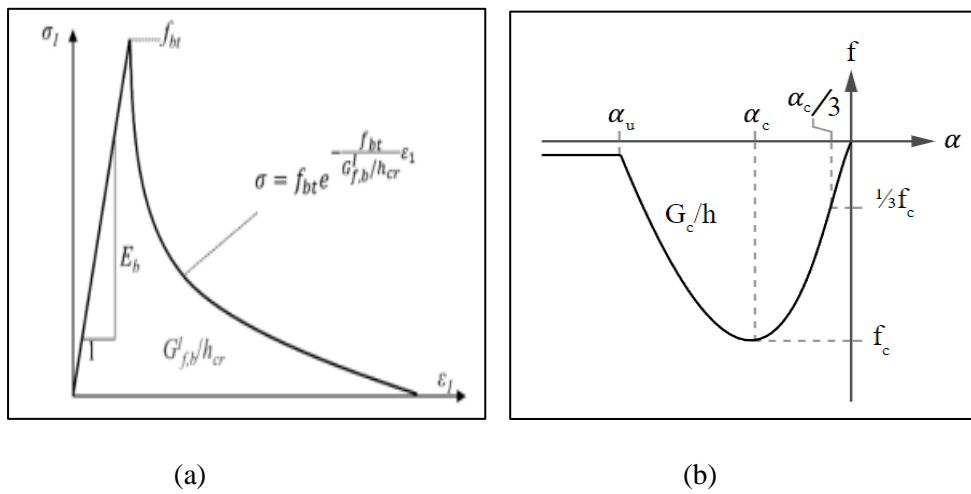

(a)   (b)

Figure 3.4. (a) Tensile softening in rotating smeared crack model for the bricks (b) Uniaxial compression curve for the brick.

Under compression loading, a parabolic compression curve based on fracture energy was implemented for the bricks. It is shown below in **Fig 3.4b**. The procedure to compute α_c and α_u can be found in DIANA manual.

The mortar and the brick-mortar interface were modelled using zero-thickness interface elements. Both bed and head joints were present in the specimens. A combined cracking crushing shear model was used to model the brick-mortar interface. It was first developed by Lourenco and Rots (1997) for 2D line interface elements. This model considers both the tensile and shear deformation acting on the joint. It is based on multi-surface plasticity comprising a Coulomb friction model combined with tension cut-off and an elliptical compression cap. The applicability of this model was further extended to 3D interface elements by van Zijl (2000).

Within the elastic range, the constitutive relations normal stress σ - normal displacement u and shear stress τ_s (τ_t) – shear displacement v_s (v_t) is given by

$$\begin{Bmatrix} \sigma \\ \tau_s \\ \tau_t \end{Bmatrix} = \begin{bmatrix} k_{nn} & 0 & 0 \\ 0 & k_{ss} & 0 \\ 0 & 0 & k_{tt} \end{bmatrix}$$

(3.1)

k_{nn} is the normal stiffness of the interface element. $k_{ss}(k_{tt})$ is the shear stiffness of the interface element. The 3D version of the combined cracking crushing shear model along with variables are mentioned in **Fig. 3.5.**
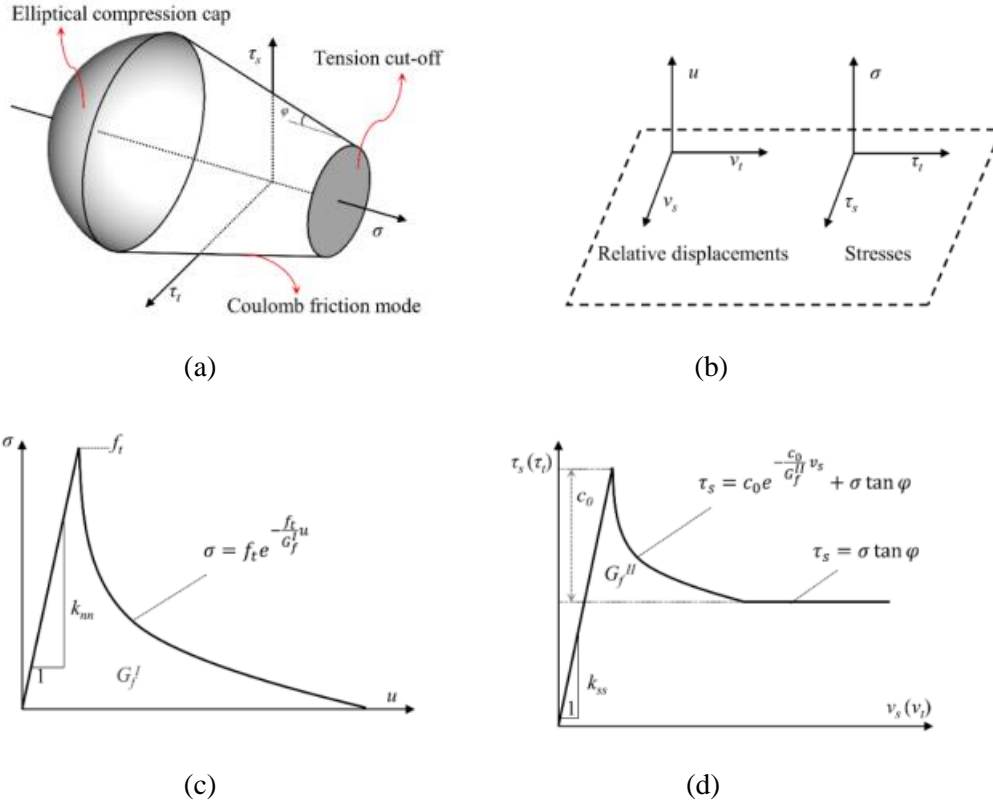
Figure 3.5. (a) Multi-surface plasticity model; (b) Relative displacements and stresses of the 3D interface elements; (c) Behaviour of the interface under tension; (d) Behaviour of the interface under shear. (Chang 2019)

The behaviour of the interface under tension is assumed to be linearly elastic till the peak stress followed by exponential softening as mentioned in the equation below.

$$\sigma = f_t\, e^{-\frac{f_t}{G_f^I}u} \tag{3.2}$$

Where G_f^I is the Mode I fracture energy, f_t is the maximum tensile stress of the interface element.

The Coulomb friction mode is given by

$$\tau = \sigma\, tan\emptyset + c \tag{3.3}$$

Where c is the cohesion of the brick-mortar interface and $\emptyset$ is the friction angle.

The cohesion softening is given by

$$c = c_o e^{-\frac{c_o}{G_f^{II}}v}$$

Where c_o is the initial cohesion of the brick-mortar interface and G_f^{II} is the Mode II fracture energy.

3.2.2 Detailed Brick-to-brick Model

In this modelling strategy, the bricks and the mortar were modelled explicitly according to their real dimensions. A full-Newton Raphson iterative scheme was selected for the analysis of these models. Energy and force convergence norms were selected. A detailed brick-to brick model of a single wythe wallet has been shown in **Fig. 3.6(a)**

(a)   (b)
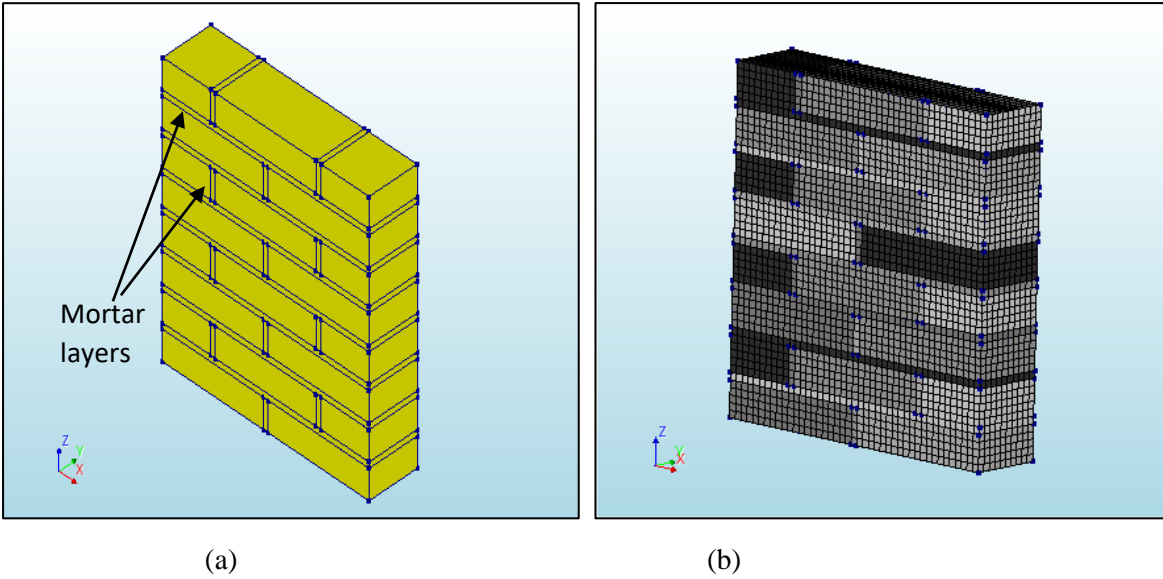
Figure 3.6. (a) A detailed brick-to-brick model; (b) Mesh of a detailed brick-to-brick model.

The mesh generated for the detailed model is shown in **Fig. 3.6b**. The explicitly modelled mortar layers are also shown in the Fig. A mesh size of 10mm was selected for this modelling technique.

Table 3.4: Element types and properties used in the detailed model.

Element type	Illustration	Description	Interpolation scheme	Integration scheme	Application
HX24L		8 node solid brick element	Linear	Regular (2×2×2)	Brick, mortar

A rotating smeared crack model was implemented for the bricks and mortar. Under tensile loading, an exponential softening curve is assumed for the bricks and mortar, after attaining the peak load. The tensile softening curve for the bricks is shown below in **Fig. 3.7a.** An analogous curve was used to describe the behaviour for mortar under tensile loading.

(a)   (b)
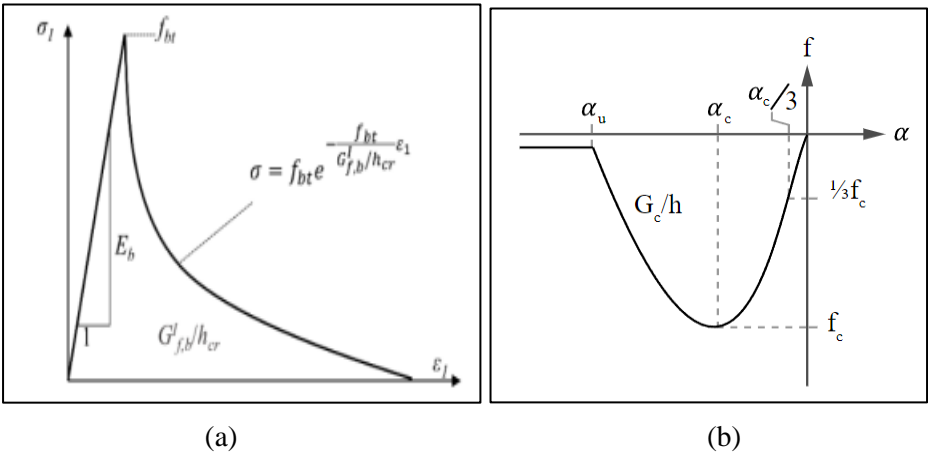
Figure 3.7. (a) Tensile softening in rotating smeared crack model for the bricks; (b) Uniaxial compression curve for the brick and mortar

Under compression loading, a parabolic compression curve based on fracture energy was implemented for both the bricks and mortar. It is shown in **Fig. 3.7b**.

In the last model created using this technique, mortar confinement was also included. It was considered by using the Selby and Vecchio (1993) confinement effect provided by DIANA. **Fig. 3.8** shows the difference in the behaviour of a material under uniaxial compressive stress with and without the influence of compression loading.
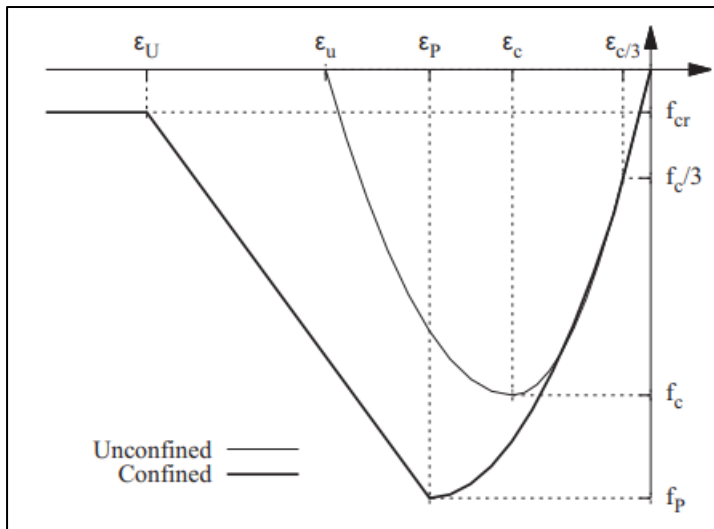
Figure. 3.8 (a) Uniaxial Compression Curve; (b) Compression curve under lateral compression loading. (Drougkas et al. 2015)

3.3 Boundary Conditions

In this study, two types of boundary conditions were utilized, namely boundary conditions with and without lateral restraints. They are described below.

In the boundary condition with lateral restraints, the translation of a node is constrained in the x, y and z directions. In this case, the translational degrees of freedom were constrained at all the nodes of the top and bottom faces. It is shown in **Fig 3.9a**.

The following condition was applied: - u_x, u_y, $u_z = 0$
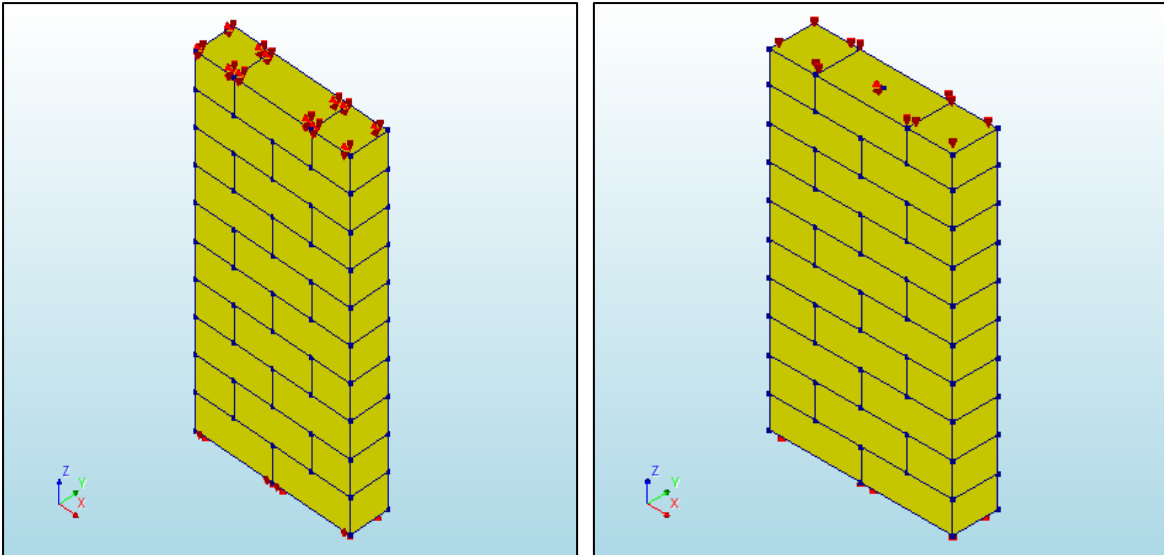
Figure 3.9. (a) Boundary condition with lateral restraints; (b) Boundary condition without lateral restraints.

Fig. 3.9b shows the boundary condition without lateral restraints. In case of boundary condition without lateral restraints, the translation in the z-direction was constrained at all the nodes. ($u_z = 0$)

At the node in the middle of the top and bottom faces, translations in x and y directions, u_x and u_y respectively, were also made zero.

3.4 Application of loads

A uniform monotonic displacement of 10 mm was applied at the top face of the specimen. This applied load was the same for all the created models discussed in the next chapter.
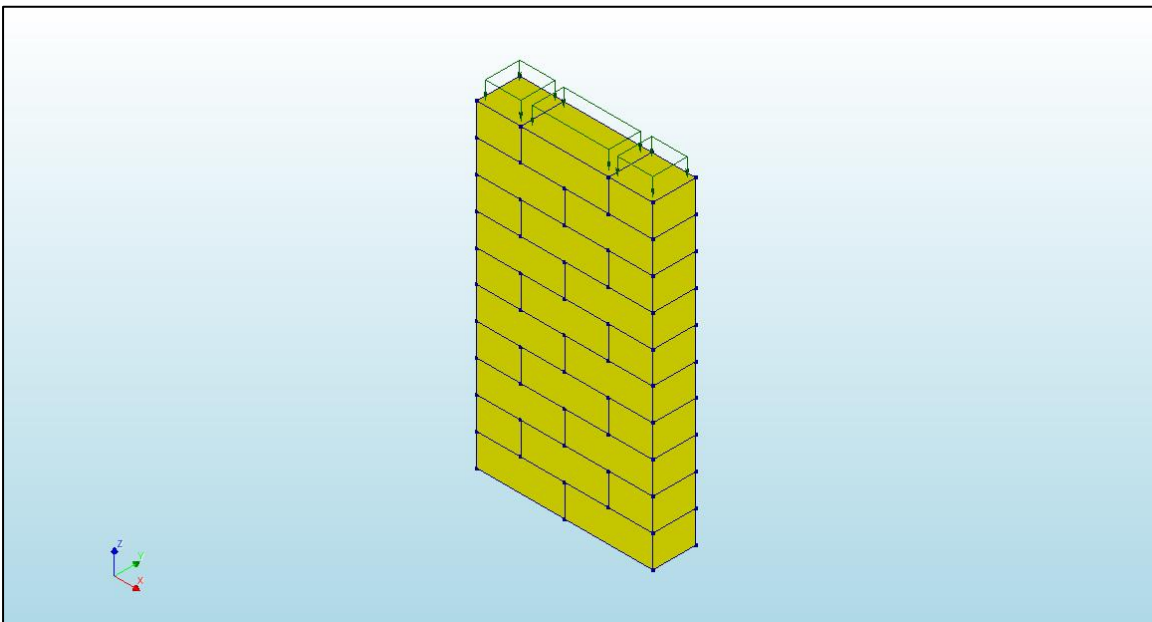
Figure 3.10. Applied load on the single-wythe wallet.

Fig. 3.10 shows the applied load on the specimen.

4. RESULTS AND DISCUSSION

In this chapter, the created numerical models have been described. Later, the results obtained after the analysis of these models were discussed and compared with the selected benchmarks.

The input parameters were varied from model to model. These variations are mentioned in **Table 4.1 and Table 4.2**.

Table 4.1: List of variations of the simplified brick-to-brick models

	Models	Model 1	Model 2	Model 3	Model 4	Model 5	Model 6
Brick	Young's Modulus of brick, (MPa)	4123	200	4123	200	6902	6902
	Compressive Strength of brick (MPa)	5.1	5.1	5.1	5.1	28.31	28.31
	Tensile Strength of brick (MPa)	0.52	0.52	0.52	0.52	4	4
	Crack	Smeared	Smeared	Smeared	Discrete	Smeared	Smeared
Mortar	Tensile Strength of Mortar (MPa)	0.2	0.2	0.2	0.2	0.57	0.57
	Compressive Strength of Mortar (MPa)	2.4	2.4	2.4	2.4	3.81	38
	Mortar confinement	NA	NA	NA	NA	NA	NA
	Boundary Conditions	With lateral constraints	No lateral constraints	With lateral constraints	With lateral constraints	With lateral constraints	With lateral constraints

Table 4.2: List of variations of the detailed brick-to-brick models.

Models	Model 7	Model 8	Model 9
Young's Modulus of brick, (MPa)	6902	6902	6902
Compressive Strength of brick (MPa)	28.31	28.31	28.31
Tensile Strength of brick (MPa)	4	4	4
Crack	Smeared	Smeared	Smeared
Tensile Strength of Mortar (MPa)	0.57	0.57	0.57
Compressive Strength of Mortar (MPa)	3.81	3.81	3.81
Poisson's ratio of mortar	0.18	0.18	0.18
Mortar confinement	No	Yes	Yes
Boundary Conditions	With lateral constraints	With lateral constraints	No lateral constraints

4.1 Simplified brick-to-brick models

In this section, all the models created using the simplified brick-to-brick modelling technique are described and compared against the necessary benchmark.

4.1.1. Model 1: Simulation of Benchmark 1

In this model, the numerical values of Young's modulus of brick, compressive strength of brick and compressive strength of mortar were extracted from the experiments of Thamboo (2020).
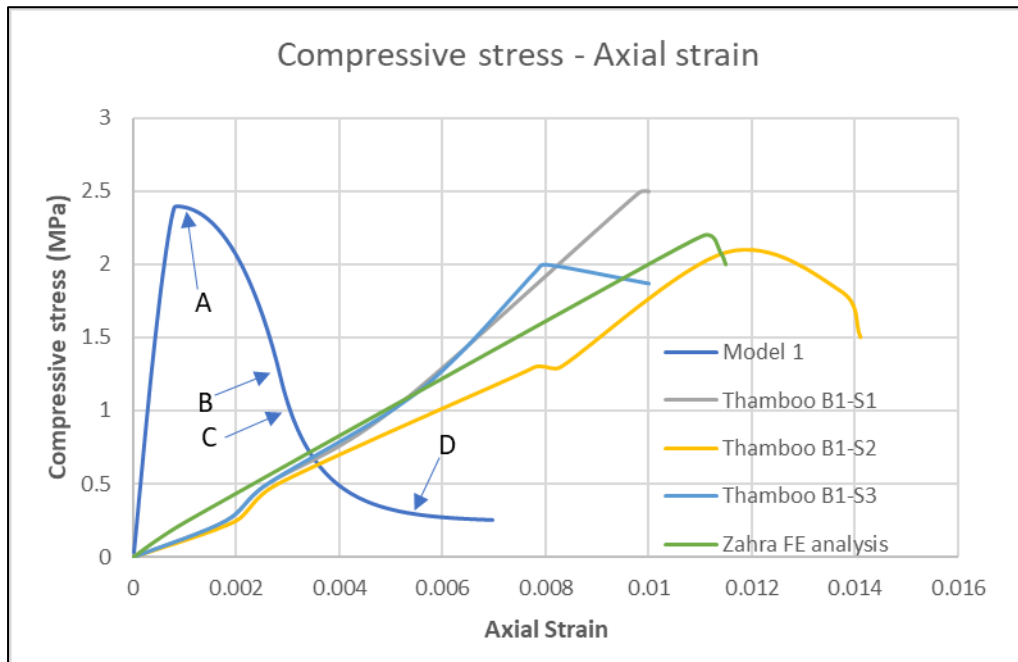

Figure 4.1. Stress -Strain plots of Model 1, experiments of Thamboo and FE analysis of Zahra.

Fig 4.1. shows the stress-strain plots obtained from Model 1, experiments of Thamboo and FE analysis of Zahra. Points A, B, C correspond to onset of mortar crushing, onset of cracking in brick and onset of cracking in mortar respectively. Point D refers to an arbitrarily chosen load step towards the end of the analysis to show the progression of potential failure mechanisms. S1, S2 and S3 represent the three single wythe wallets tested in the experimental program of Thamboo (2020).

It can be observed that the slopes of the experimentally obtained plots and Zahra's FE analysis are similar. The slope of model 1 is extremely stiff compared to that of the experimentally obtained plots and the FE analysis of Zahra. A complete post-peak behaviour could also be simulated for Model 1 in comparison with the FE analysis Zahra.
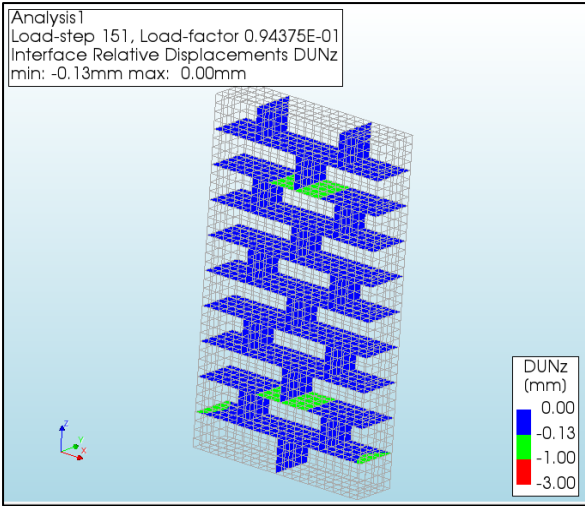
(a)
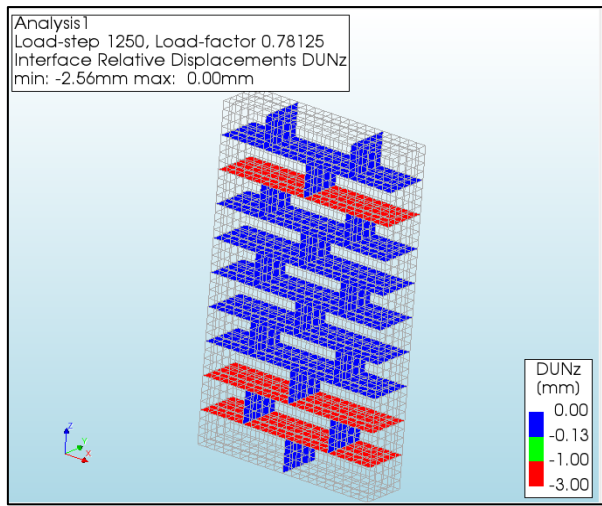
(b)
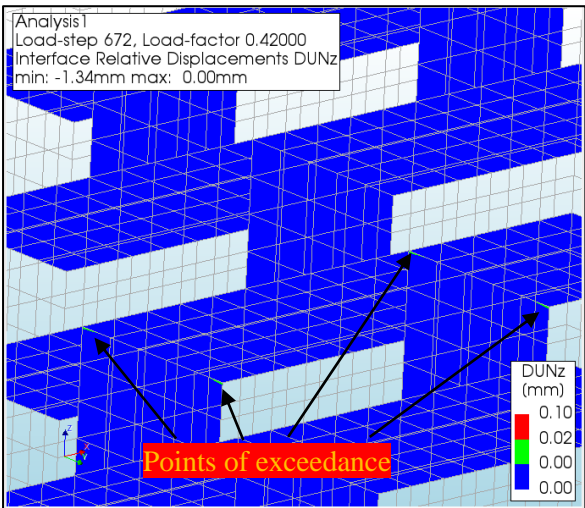
(c)
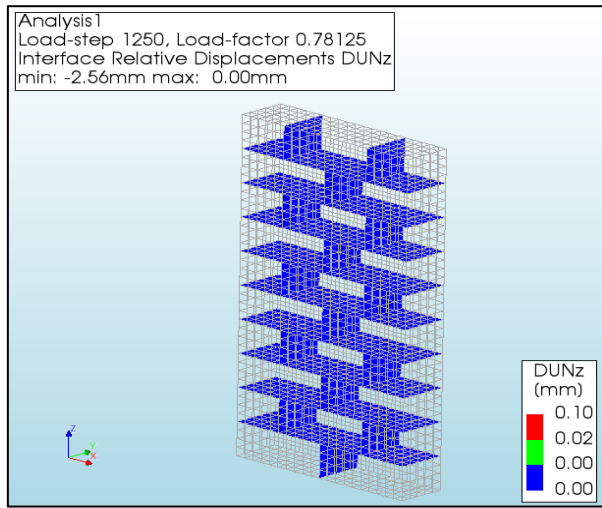
(d)
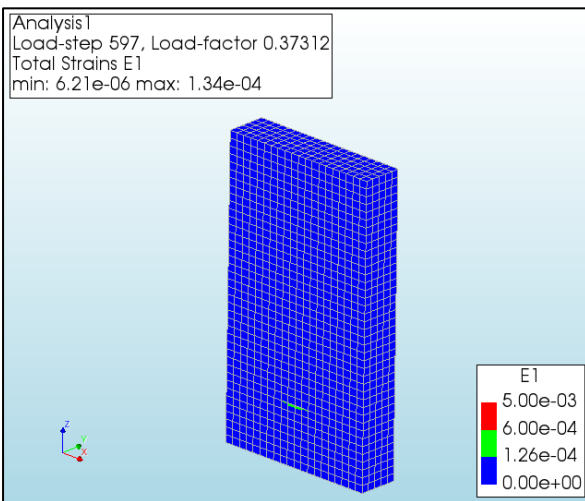
(e)
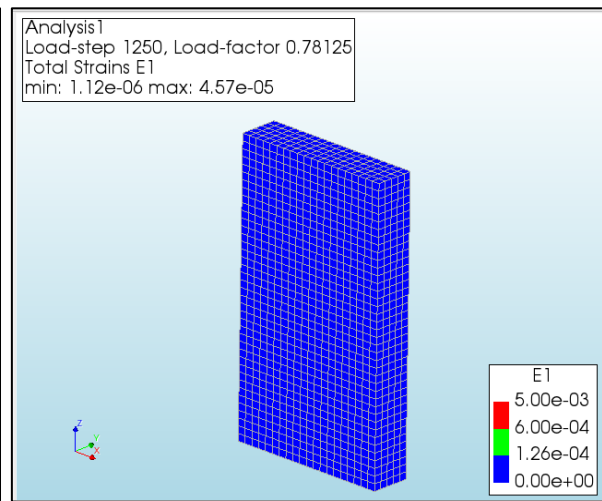
(f)
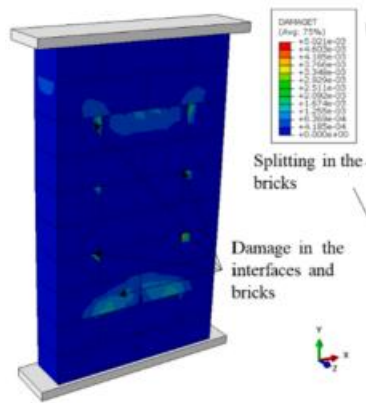
(g)

Figure 4.2. (a) onset of mortar crushing; (b) Relative normal displacement DUNz (-) at load step D; (c) onset of cracking in mortar; (d) Relative normal displacement DUNz (+ve) at load step D; (e) Onset of cracking in brick; (f) Principal Strain E1 at load step D; (g) numerical failure modes of Zahra's FE analysis.

Fig. 4.2a and **Fig. 4.2b** shows the progression of mortar crushing in the specimen. Mortar crushing failure occurred only in the bed joints. The location of these bed joints is identical to the location of damage of interfaces as shown in **Fig**.**4.3 g**. However, there is no mention of mortar crushing failure in the experimental program of Thamboo et al. (2020).

Fig. 4.2c , **Fig. 4.2d** and **Fig. 4.2e** , **Fig. 4.2f** correspond to the progression of cracking in mortar and brick respectively. Mortar cracking was observed only in the head joints. The location of the cracking in the brick and mortar coincides with the damage in the interface and bricks in the bottom portion of the specimen as shown in **Fig. 4.2g**. The observation of vertical cracks in the experimental program is in line with the failure mechanisms obtained numerically. However, in the experimental program, vertical cracks were observed in the brick and mortar at several locations. Model 1 could only simulate these occurrences at the bottom portion of the specimen. A detailed analysis of this model is mentioned in **Appendix – A.**

In conclusion, this model was able to simulate the numerical failure modes from Zahra's analysis and the vertical cracking as observed in the experimental program of Thamboo et al. (2020) at specific locations. However, the model is extremely stiff compared to the experiments and FE analysis of Zahra et al. (2021).

Therefore, to mitigate this issue, in the next model, the Young's modulus of the brick was extracted directly from Zahra's FE analysis.

4.1.2. Model 2: Simulation of benchmark 1, change in Young's Modulus of brick

In this model, the Young's modulus of brick is input directly from FE analysis of Zahra et al. (2021).
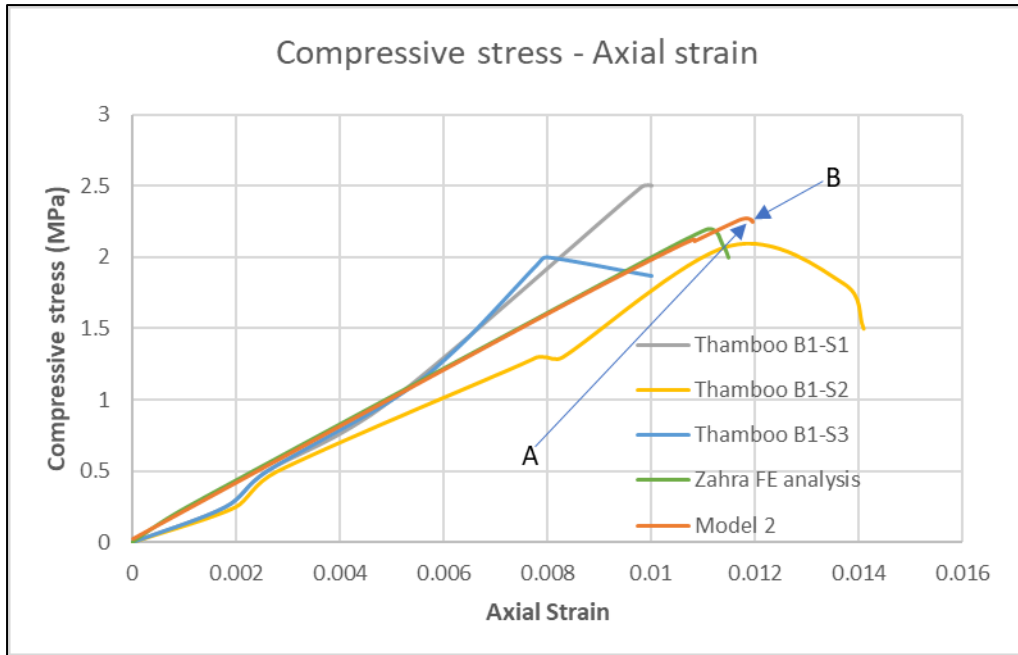
Figure 4.3: Stress-Strain plots obtained from Model 2, experiments of Thamboo et al. (2020), and FE analysis of Zahra et al. (2021)

Fig. 4.3. shows the stress-strain plots obtained from Model 2, experiments of Thamboo and FE analysis of Zahra. Point A corresponds to onset of mortar crushing. Point B refers to an arbitrarily chosen load step towards the end of the analysis to show the progression of potential failure mechanisms.

It can be observed that the slopes of the stress-strain plots of Model 2, FE analysis of Zahra and the experiments are very similar. However, a post-peak region could not be simulated as the analysis diverged shortly after attaining peak load.

(a)   (b)
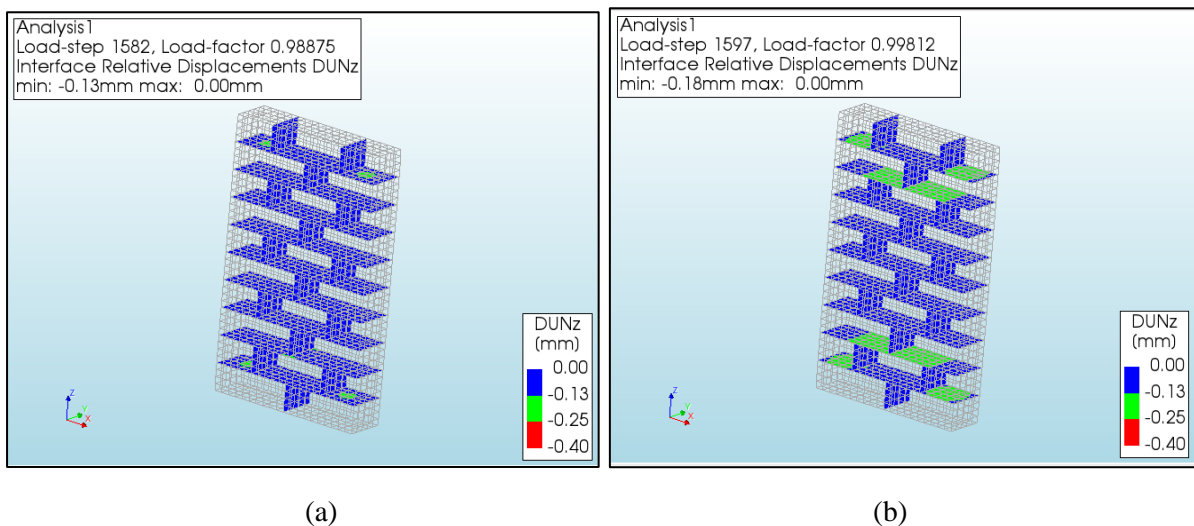
Figure 4.4. (a) Onset of mortar crushing; (b) Relative normal displacement DUNz (-ve) at load step B.

Fig. 4.4a and Fig. 4.4b shows the progression of mortar crushing in the specimen. Mortar crushing failure only occurred in the bed joints. Similar to model 1, the location of these bed joints coincides with the location of damage in interfaces of Zahra's FE model. No other failure mechanism was observed. Hence the damage in the bricks and interface related to cracking of brick and mortar, as

30

seen in Zahra's FE analysis could not be simulated using Model 2. Similarly, the vertical crack which were observed in the wallets during the experimental program also could not be simulated.

A detailed analysis of this model is mentioned in **Appendix – B.**

In the next model, the boundary conditions are altered and its influence on the failure mechanisms and the global behaviour of the model is studied.

4.1.3. Model 3: Simulation of Benchmark 1, change in boundary conditions

In this model, the boundary conditions are changed to one with no lateral constraints. It has been done to study the influence of boundary conditions on failure mechanisms and the global behaviour of the structure. The results of this model has been discussed in Section 4.3. A detailed analysis of this model is mentioned in **Appendix – C.**

4.1.4. Model 4: Simulation of Benchmark 1, choice of discrete crack for bricks

In this model, discrete cracks were modelled to simulate cracking in brick. Apart from mortar crushing, none of the other failure mechanisms could be simulated using this model. A detailed analysis of this model has been shown in **Appendix – D**.

4.1.5. Discrepancy

From the analysis of all the models mentioned above, it was observed that only model 1 could simulate mortar crushing failure, mortar cracking failure and cracking failure of brick. The value of Young's modulus of brick for this model is 4123 MPa. This value was obtained from the experimental results of Thamboo (2020) which were used to calibrate FE modelling technique of Zahra.

In this thesis, an attempt was made to simulate the results from the FE analysis of Zahra (2021). In the analysis done by Zahra (2021), Young's modulus of the brick was chosen as 200 MPa. Further, it is claimed in this study that numerical models were created to simulate the experiments of Thamboo (2020) where the Youngs's modulus of the brick was 4123 MPa.

Therefore, even though Model 1 simulated the failure mechanisms as depicted by the experiments of Thamboo (2020), we cannot conclude that this model is the most suitable as the stress-strain plot of this model deviates from that of Zahra's analysis. The models created to simulate Zahra's FE analysis also cannot be relied upon. This is because the chosen value of Young's Modulus of brick in Zahra's analysis (200 MPa) largely deviates from the realistic range of values for elastic modulus of a brick.

Hence a new benchmark was selected, and the subsequent models aimed at simulating the results obtained from the newly chosen benchmark.
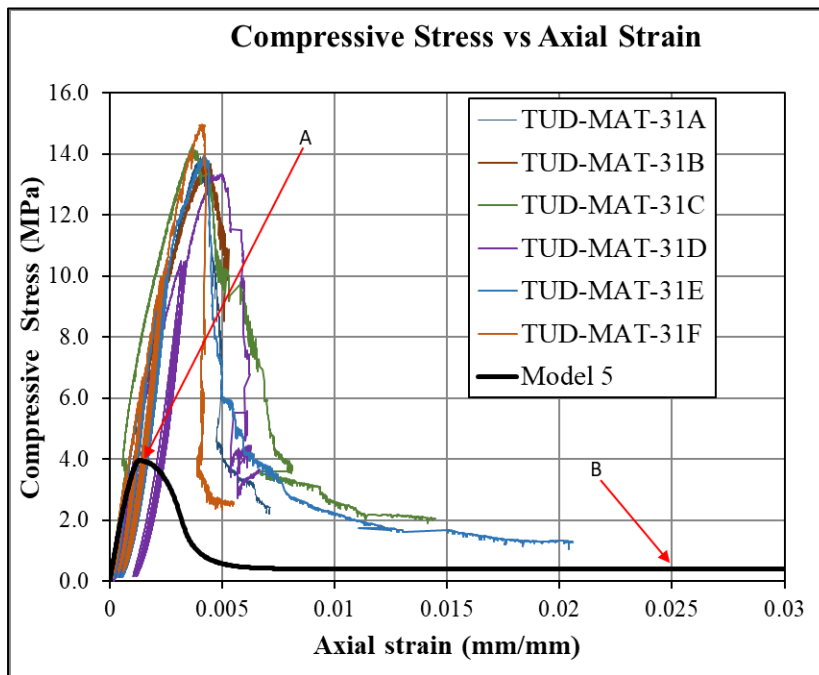
4.1.6. Model 5: Simulation of Benchmark 2

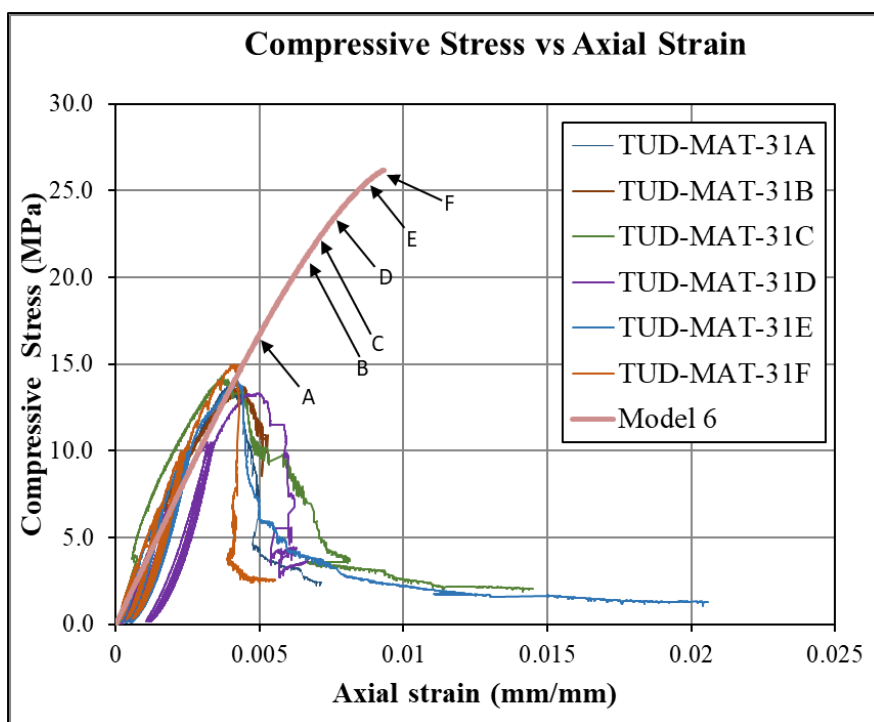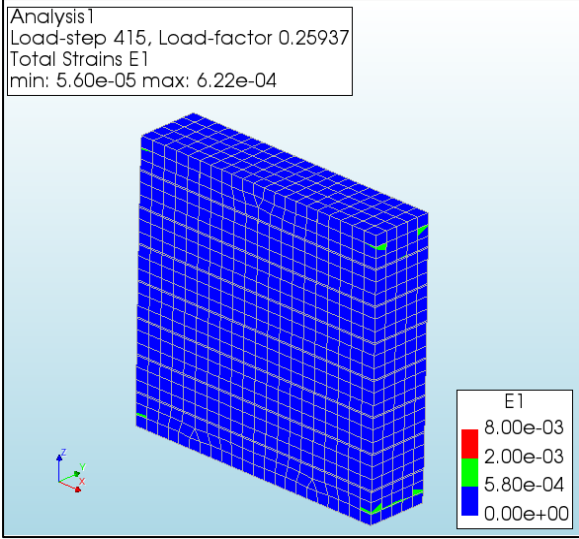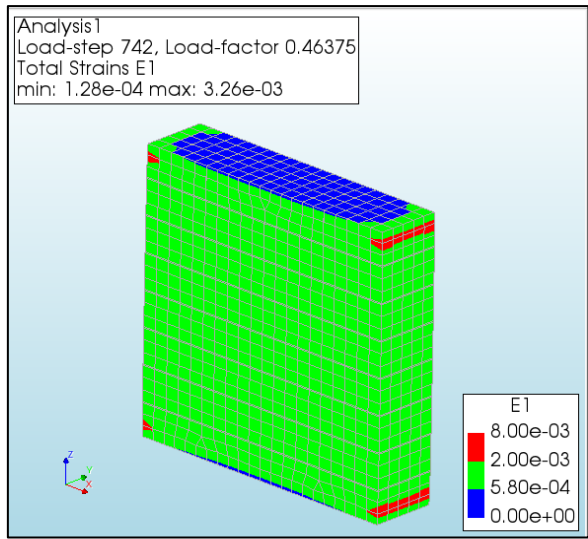**Figure 4.5.** Stress-strain plots obtained from Model 5 and experiments of Jafari (2021).

Fig. 4.5. shows the stress-strain plots of Model 5, and the experiments of Jafari (2021). Point A refers to the onset of mortar crushing. Point B refers to an arbitrarily chosen load step towards the end of the analysis to show the progression of potential failure mechanisms.
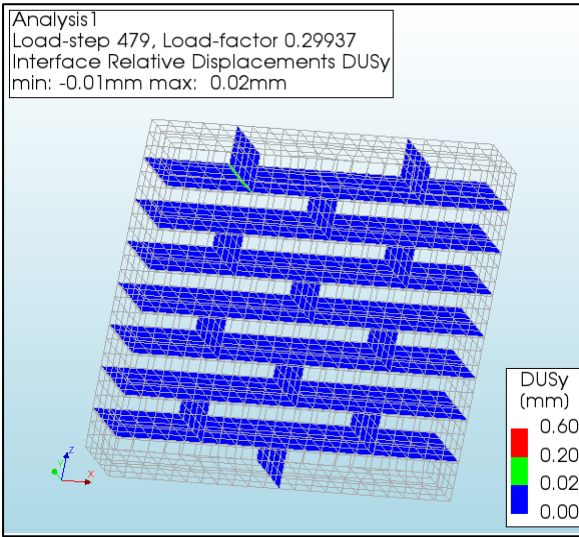
It can be observed that the peak compressive stress of the numerical curve is much lower than that of the experimental curves. A larger post-peak region is also observed in the numerical curve than the experiments.
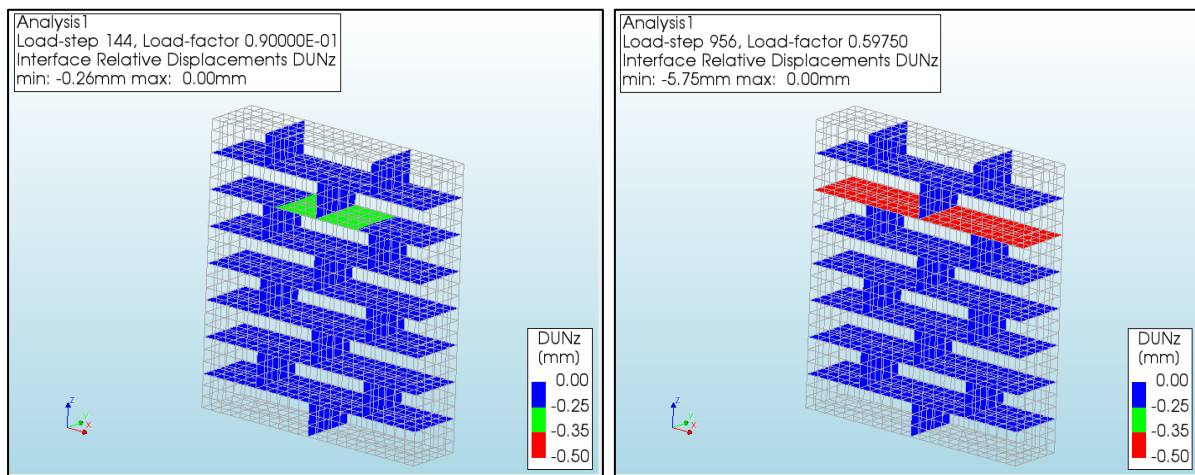
Figure 4.6: (a) Onset of mortar crushing; (b) Relative normal displacement DUNz (-ve) at load step B.

Fig 4.6. shows the progression of mortar crushing in the specimen. Mortar crushing failure occurred in a bed joint at the top of the specimen. Similar to the previous models, the cracking of the brick and mortar interface could not be simulated. A detailed analysis of this model is mentioned in **Appendix − E.**

The peak compressive stress obtained from the numerical model (3.91 MPa) is very close to the compressive strength of mortar (3.81 MPa). Hence, it could be possible that the compressive stress–axial strain plot is simulating the local failure of mortar. The critical stress values in the compression cap of the combined cracking crushing shear model are reached before the onset of other failure mechanisms. The development of other failure mechanisms might have been hindered due to the critical stress values attained in the compression cap. Hence a new model has been developed to mitigate this problem.

Hence a new model has been developed to mitigate this problem.

4.1.7. Model 6: Simulation of Benchmark 2, High mortar compressive strength

In this model, the compressive strength of mortar is chosen 10 times that of the previous model. This change has been implemented to potentially accommodate the remaining failure mechanisms before the onset of mortar crushing.

Figure 4.7. Stress-strain plots obtained from Model 6 and experiments of Jafari (2021).

Fig 4.7. shows the stress-strain plots obtained from Model 1, and experiments of Jafari (2021) Points A, B, C, D, E correspond to onset of cracking in brick, onset of shear failure, onset of crushing in brick, onset of mortar crushing and onset of mortar cracking respectively. Point F refers to an arbitrarily chosen load step towards the end of the analysis to show the progression of potential failure mechanisms.

It can be observed that the peak compressive stress of the Model 6 is higher than the plots obtained experimentally. This was caused due to the high value of compressive strength of mortar (38 MPa) when compared with the experiments (3.81 MPa). The peak compressive stress is almost double that of the experiments. Till a compressive stress of 10 MPa, the DIANA curve is linear. But for the experimental specimens, there is a gradual change in slope till a compressive stress of 5 MPa.

Analysis 1
Load-step 415, Load-factor 0.25937
Total Strains E1
min: 5.60e-05 max: 6.22e-04

E1
8.00e-03
2.00e-03
5.80e-04
0.00e+00

(a)

Analysis 1
Load-step 742, Load-factor 0.46375
Total Strains E1
min: 1.28e-04 max: 3.26e-03

E1
8.00e-03
2.00e-03
5.80e-04
0.00e+00

(b)

Analysis 1
Load-step 479, Load-factor 0.29937
Interface Relative Displacements DUSy
min: -0.01mm max: 0.02mm

DUSy
(mm)
0.60
0.20
0.02
0.00

(c)

Analysis 1
Load-step 742, Load-factor 0.46375
Interface Relative Displacements DUSy
min: -0.02mm max: 0.02mm

DUSy
(mm)
0.60
0.20
0.02
0.00

(d)

Analysis 1
Load-step 589, Load-factor 0.36812
Total Strains E3
min: -7.00e-03 max: -3.56e-03

E3
0.00e+00
-6.83e-03
-2.00e-02
-7.00e-02

(e)

Analysis 1
Load-step 742, Load-factor 0.46375
Total Strains E3
min: -1.47e-02 max: -4.47e-03

E3
0.00e+00
-6.83e-03
-2.00e-02
-7.00e-02

(f)

34

(g)

(h)

(i)

(j)

Figure 4.8: (a) Onset of cracking in brick; (b) Principal strain E1 at load step F; (c) Onset of shear failure of mortar interface; (d) Relative shear displacement DUSy at load step F; (e) onset of crushing in brick; (f) Principal strain E3 at load step F; (g) onset of mortar crushing; (h) Relative normal displacement DUNz (-ve) at load step F; (i) onset of mortar cracking; (j) Relative normal displacement (+ve) at load step F.

Five different failure mechanisms were identified during the analysis. It commenced with cracking failure of brick, which then extended to almost the entire specimen. It significantly overestimates the number of vertical cracks observed in the experiments of Jafari (2021). Shear failure was observed at a bed and head joint at the top of the specimen. This was followed by the onset of crushing failure of brick. It occurred mainly and the top and bottom faces of the specimen. Crushing failure of mortar occurred in all the bed joints. The last failure mechanism observed was cracking of mortar, which occurred in the central part of the specimen. The analysis diverged shortly after attaining peak load, due to which vertical splitting cracks in the thickness of the wallets could not be simulated.

A detailed analysis of this Model has been shown in **Appendix – F**.

Model 6 was successful in simulating all the possible failure mechanisms. However, the value of compressive strength assumed for this model is not in line with the experiments. Hence, this model still cannot be utilized to simulate experimental results due to unrealistic values of the compressive strength of mortar.

Therefore, we proceed with the detailed brick-to-brick modelling technique as the simplified modelling technique was unsuccessful in simulating the experimental results.

4.2. Detailed brick-to-brick models

In this section, the detailed brick-to-brick models have been discussed.

4.2.1. Model 7: Simulation of Benchmark 2, no mortar confinement

In this model, the input parameters have been extracted directly from the MAT-3 experiemnts of Jafari (2021).
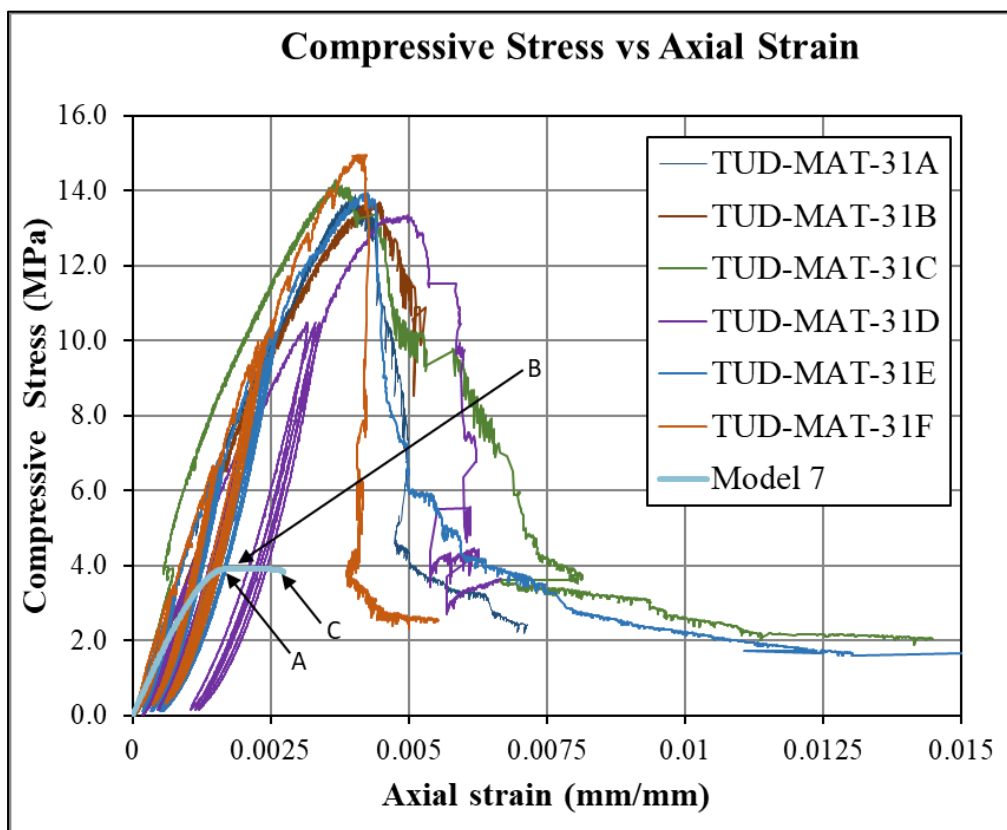
Figure 4.9. Stress-Strain plots of Model 7 and experiments of Jafari (2021).

Fig. 4.9. shows the stress-strain plot obtained from Model 7 and from experiments of Jafari. Points A and B correspond to the onset of cracking of mortar and onset of mortar crushing respectively. Point C refers to an arbitrarily chosen load step to show the progression of failure mechanisms.

Once again, it can be observed that the peak compressive stress of the numerical curve is much lower than that of the experimental curves. A small post-peak region is also observed.

(a)   (b)
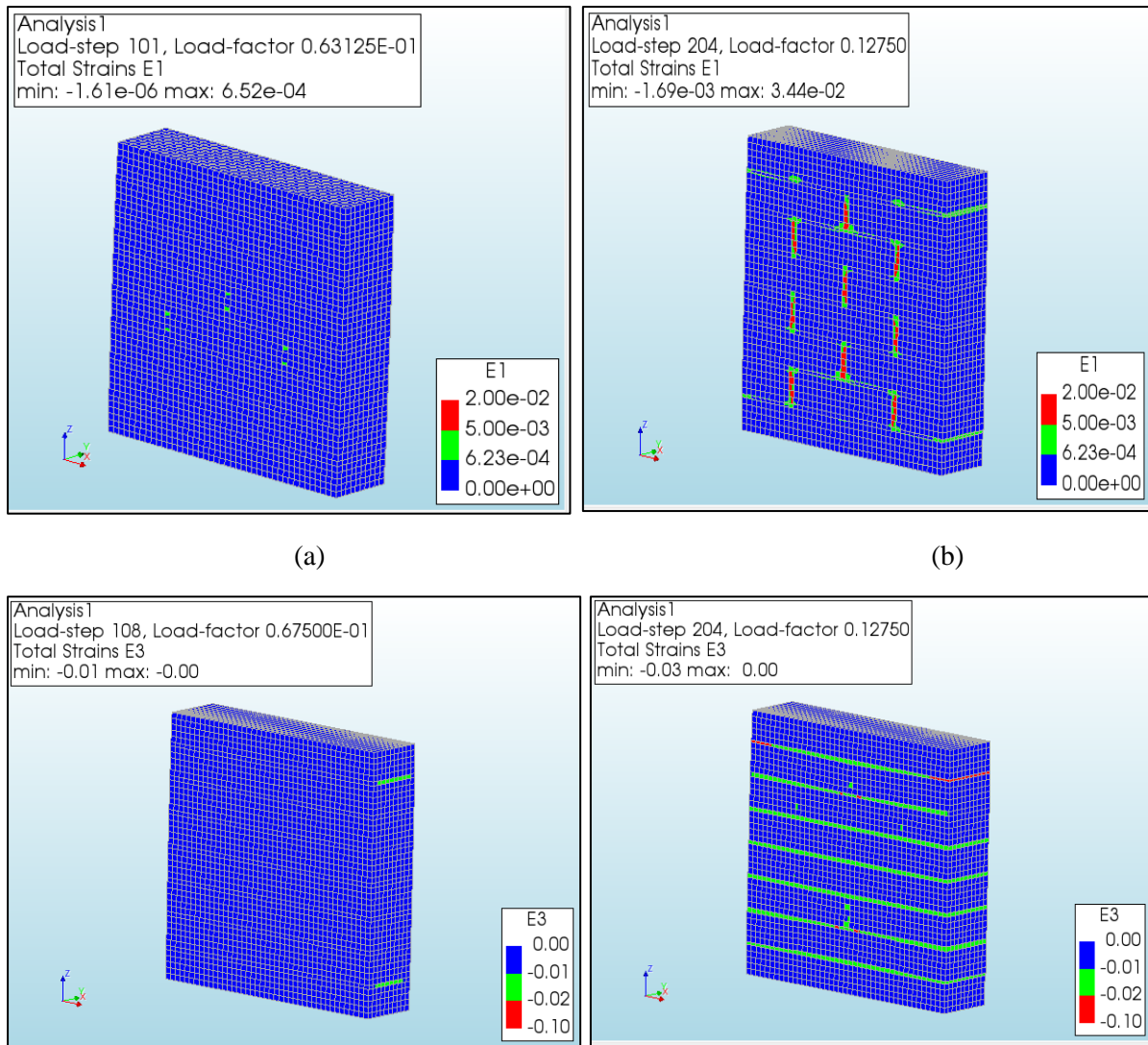
Figure 4.10: (a) Onset of cracking in mortar; (b) Principal strain E1 at load step C; (c) Onset of crushing in mortar; (d) Principal Strain E3 at load step C.

Fig 4.10a. and Fig. 4.10b. shows the progression of mortar cracking in the specimen. Mortar cracking failure occurred in most of the head joints. Towards the end of the analysis, mortar cracking could also be observed in bed joints. **Fig 4.10c** and **Fig. 4.10d.** shows the progression of mortar crushing in the specimen. It can be observed that all the bed joints underwent crushing. In the next model, mortar confinement effect is included. Towards the end of the analysis, mortar crushing could also be observe in head joints. A detailed analysis of this model is mentioned in **Appendix – G.**

In the next model, mortar confinement effect is also included.

4.2.2. Model 8: Simulation of benchmark 2, mortar confinement included

In this model, the confinement effect of mortar was considered. Selby and Vecchio (1993) stress confinement was selected for mortar. The remaining parameters were the same as that of the previous model.
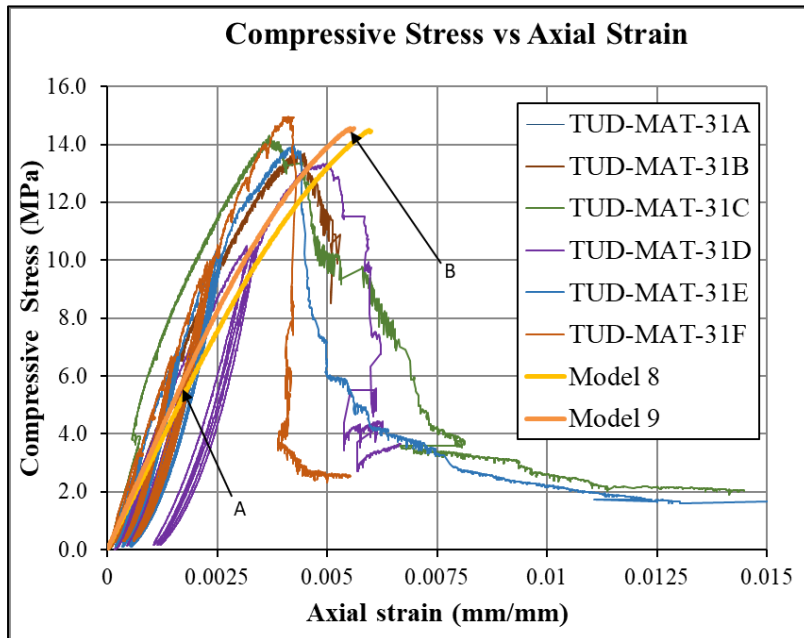
37
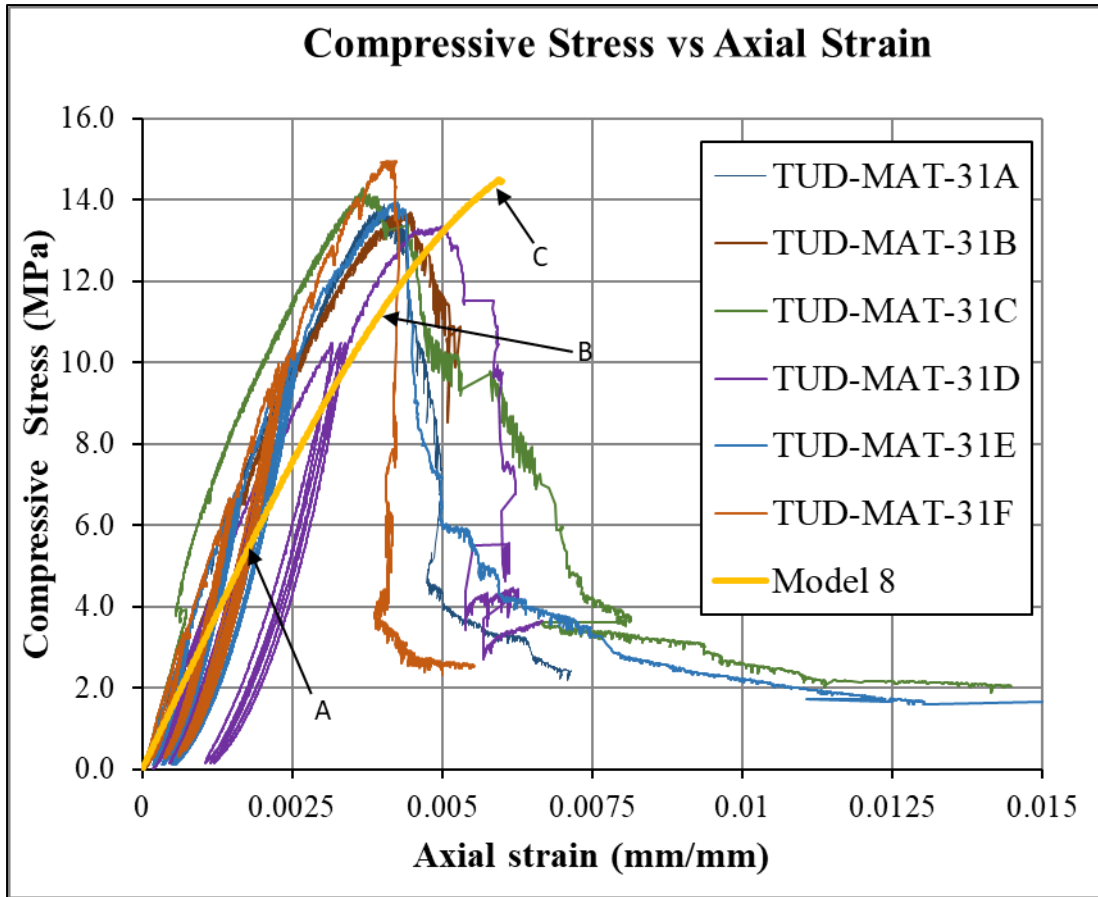
Figure 4.11. Stress-Strain plots of Model 8 and experiments of Jafari (2021).

Fig. 4.11. shows the stress-strain plot obtained from Model 8 and from experiments of Jafari (2021). Points A and B correspond to the onset of cracking of mortar and the onset of cracking in brick respectively.

It can be observed that there is a small difference in the peak compressive stress of model 8 and plots obtained experimentally. The slope of the experimental curves is slightly higher than that of Model 8. Out of all the models analysed so far, Model 8 is closest in terms of simulating the global behaviour of the masonry wallet.

(a)   (b)

<center>(c)</center> <center>(d)</center>
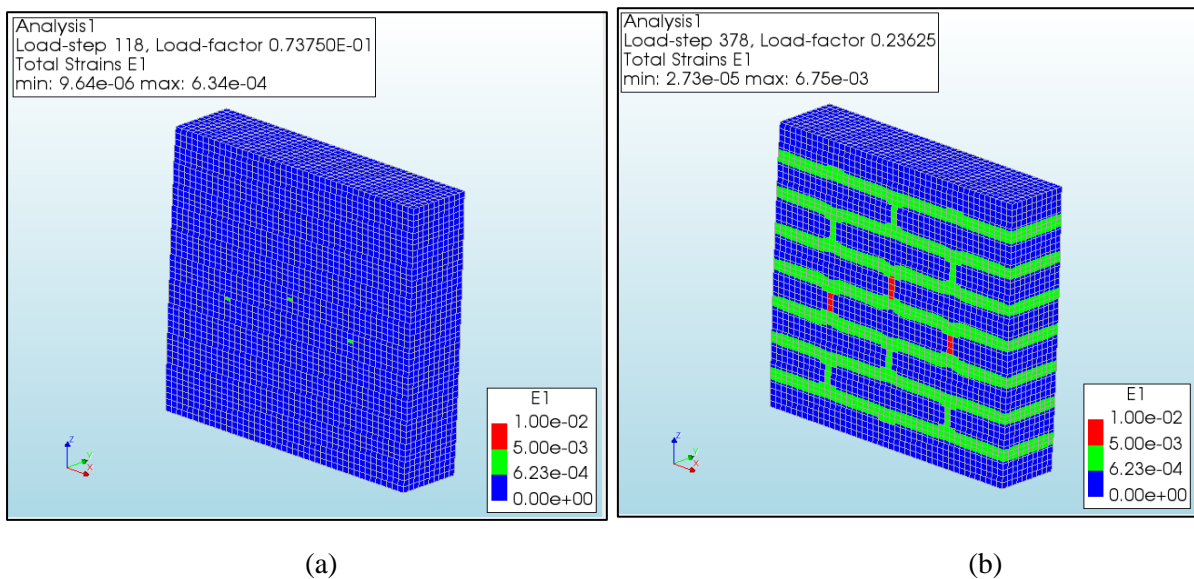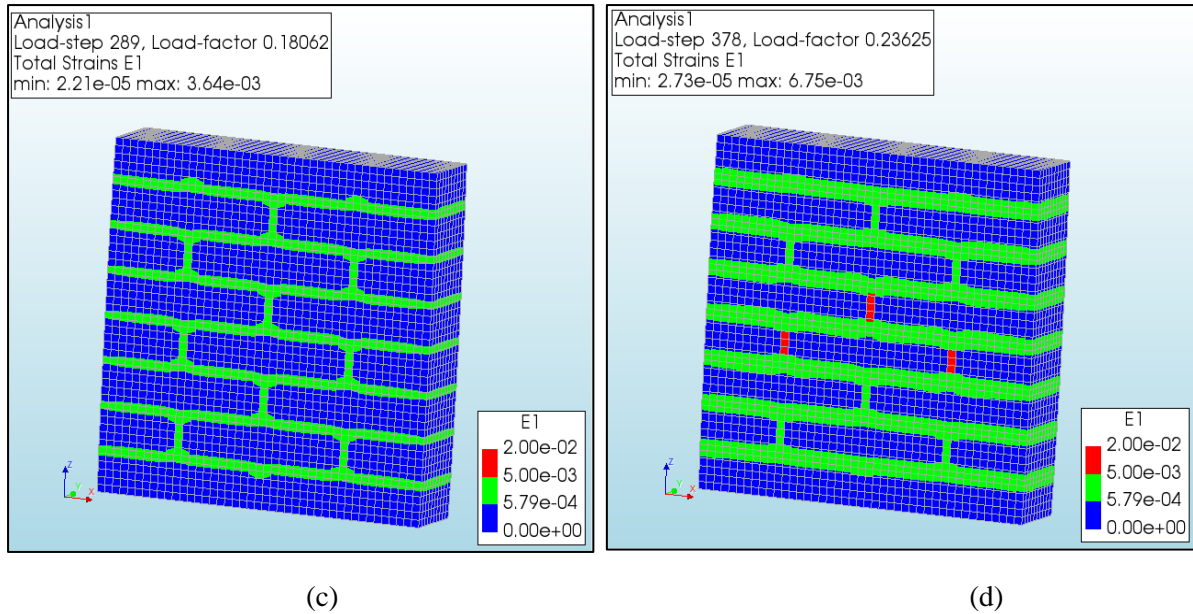
Figure 4.12: (a) Onset of cracking in mortar; (b) Principal strain E1 at penultimate load step; (c) Onset of cracking in brick; (d) Principal Strain E1 at penultimate load step.

Fig 4.12a. and Fig. 4.12b. shows the progression of mortar cracking in the specimen. Mortar cracking failure occurred in almost all the head and bed joints. In the central portion of the specimen, head joints approached the fully cracked stage. **Fig 4.12c** and **Fig. 4.12d.** shows the progression of cracking in the brick. All of the cracks in the bricks are propagating from the bed joints. Potential cracks along the thickness of the wallet specimen as observed during experiments of Jafari (2021) could be simulated. A detailed analysis of this model is mentioned in **Appendix – H.**

4.2.3. Model 9: Simulation of Benchmark 2, Change in boundary conditions

In this model, the boundary conditions were changed to one without lateral constraints. Mortar confinement was included. The results of this model are discussed in Section 4.3.A detailed analysis of this model is mentioned in **Appendix – I.**

4.3 Sensitivity study

In this section, the influence of change in boundary conditions, Poisson's ratio of mortar and integration scheme on Model 8 is investigated.

4.3.1. Boundary Conditions

New models were created to study the influence of change in boundary conditions on the failure modes and the global behaviour of the specimen. A boundary condition without lateral restraints was implemented for these models. Model 3 and Model 9 were created for this purpose to understand the impact of change in boundary conditions for the simplified and etailed modelling techniques respectively.

<center>39</center>
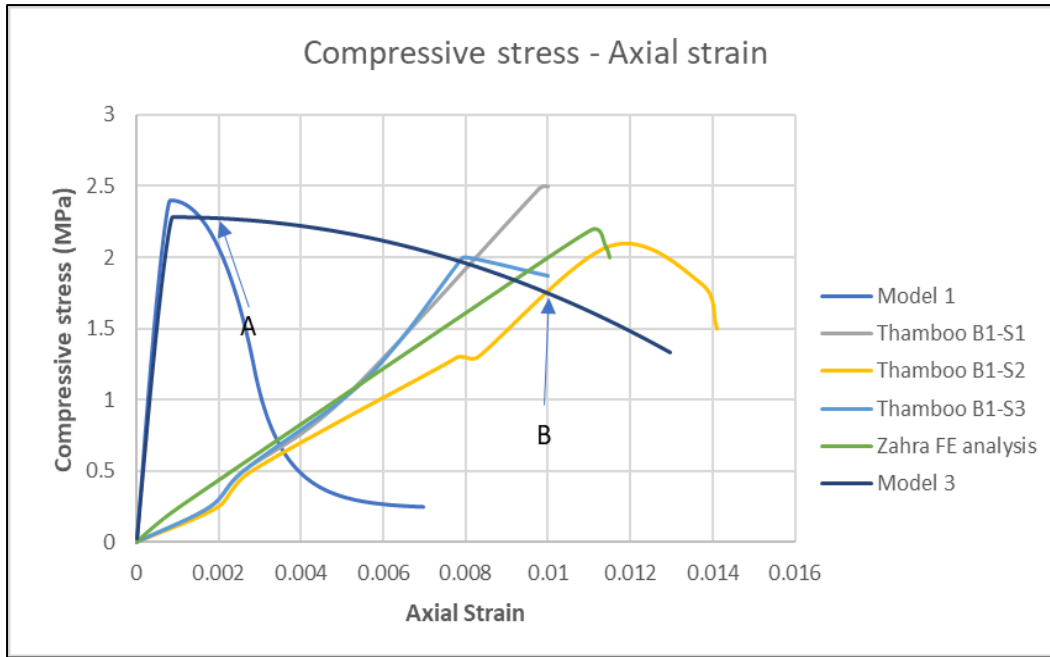
Figure 4.13. Stress-Strain plots obtained from Model 3, Model 1, FE analysis of Zahra et al. (2021) and experiments of Thamboo et al. (2020).

Fig. 4.13. shows the stress-strain plots of Model 3, Model 1, FE analysis of Zahra and the experiments of Thamboo. Point A refers to the onset of mortar crushing. Point B refers to an arbitrarily chosen load step towards the end of the analysis to show the progression of potential failure mechanisms.
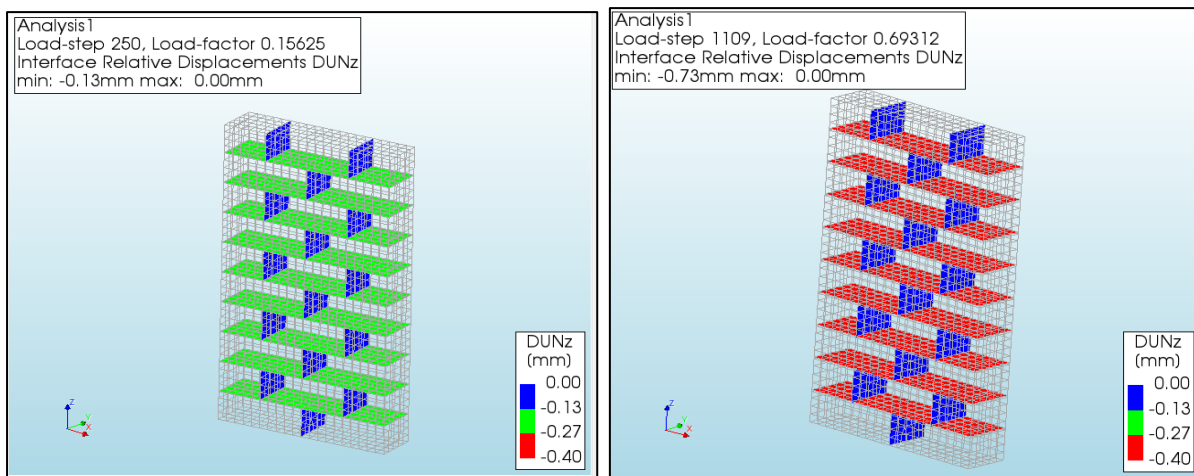
Figure 4.14: (a) Onset of mortar crushing; (b) Relative normal displacement DUNz (-ve) at load step B.

Fig 4.14. shows the progression of mortar crushing in the specimen. Mortar crushing failure occurred in all the bed joints. However, the FE analysis of Zahra only simulated damage at a top and bottom interface. Similar to Model 2, the cracking of the brick and interface could not be simulated. A detailed analysis of this model is mentioned in **Appendix – C.**

As expected, the slope of the stress-strain curve of Model 3 is very stiff compared to that of the experiments and Zahra's FE analysis. A significant post-peak region could be simulated in this case. Instead of an abrupt softening behaviour after peak load as in the case of Model 1, a gradual softening behaviour was observed this case.

40

Model 1 could simulate 3 failure mechanisms namely mortar crushing, cracking of mortar and cracking of brick. But Model 3 could only simulate mortar crushing.

A sensitivity study regarding boundary conditions was also performed on the detailed brick-to-brick models. A new model (Model 9) without lateral constraints was created.

Figure 4.15. Stress-Strain plots of Model 9 and experiments of Jafari (2021).

Fig. 4.15. shows the stress-strain plot obtained from Model 9 and from experiments of Jafari (2021). Points A and corresponds to the onset of cracking of mortar. Point B corresponds to the penultimate load step in the analysis.

It can be observed that the initial slopes of Model 8 and Model 9 are very similar. The peak loads attained by the two models also have a close resemblance.

(a)   (b)

41
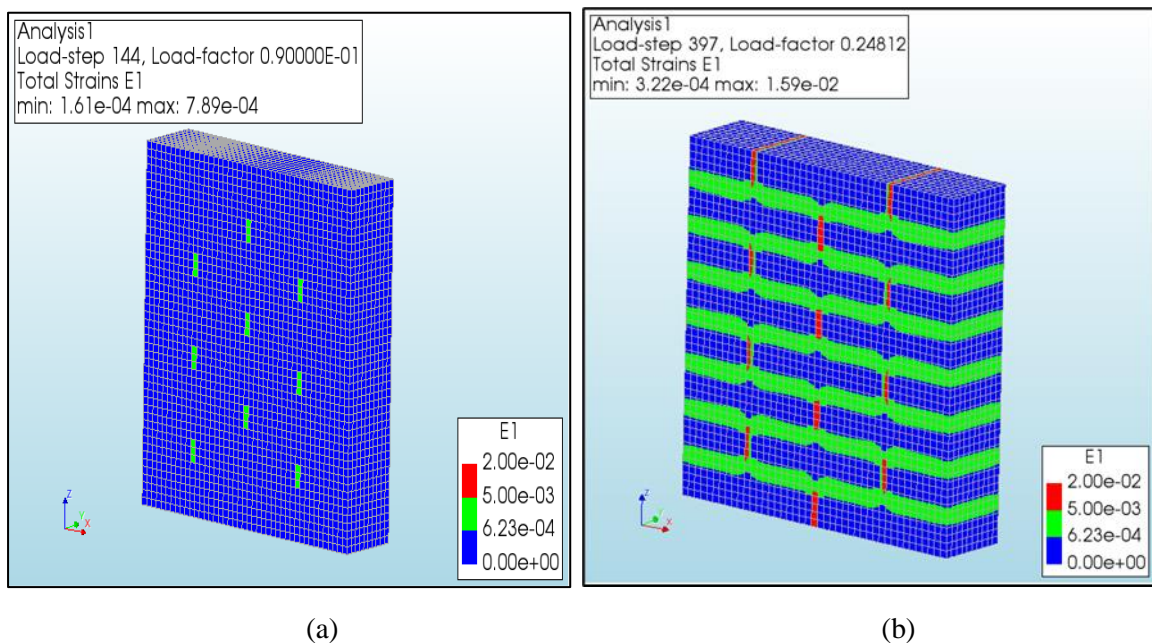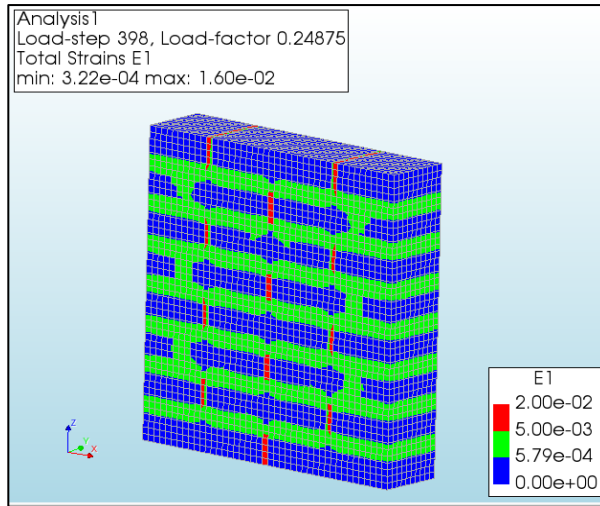
(c)

Figure 4.16: (a) Onset of cracking in mortar; (b) Principal strain E1 at penultimate load step; (c) Principal Strain E1 at penultimate load step.

Fig 4.16a. and Fig. 4.16b. shows the progression of mortar cracking in the specimen. Mortar cracking failure occurred in all the head and bed joints. All the head joints approached the fully cracked stage. **Fig 4.16c** shows the Principal strain E1 at the penultimate load step. A larger number of cracks in the brick developed in this case when compared with Model 8. The cracks in the brick were not restricted to the vicinity of the bed joints as in the earlier model. Potential cracks along the thickness of the wallet specimen as observed during experiments of Jafari (2021) could be simulated. A detailed analysis of this model is mentioned in **Appendix – I.**

4.3.2. Poisson's Ratio of mortar
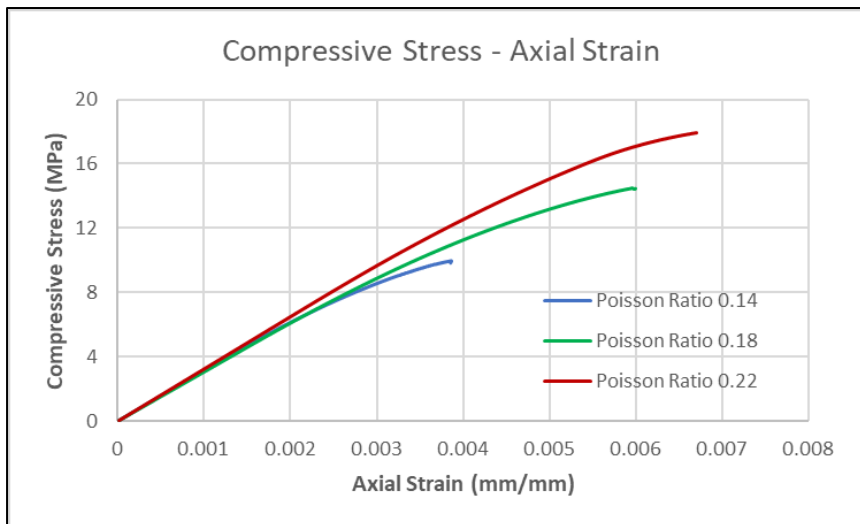
Figure 4.17. Stress-strain plots for 3 different values of Poisson's ratio of mortar.

Fig. 4.17 shows the stress-strain plots for three different values of Poisson's ratio of mortar. The Poisson's ratio of brick was kept the same for all the three scenarios. It can be observed that with the increase in the Poisson's ratio of mortar, the peak compressive stresses attained by the model also increases. The initial slope of the three stress-strain curves is the same.

The observation from this analysis is in line with the observations of Drougkas et al. (2015). Drougkas et al. (2015) observed an overestimation of the compressive strength of masonry upon using higher values of Poisson's ratio of mortar. A higher value of Poisson's ratio increases the amount of confinement in mortar layers resulting in higher values of compressive strength of masonry. The sequence of failure mechanisms remained the same for the specimens with different values of Poisson's ratio.

4.3.3. Integration scheme

In this section, the influence of implementing a reduced and higher integration scheme on the cracking of mortar is discussed. A reduced integration scheme implies a $1 \times 1 \times 1$ integration scheme. A high integration scheme implies a $3 \times 3 \times 3$ integration scheme.

(a)   (b)
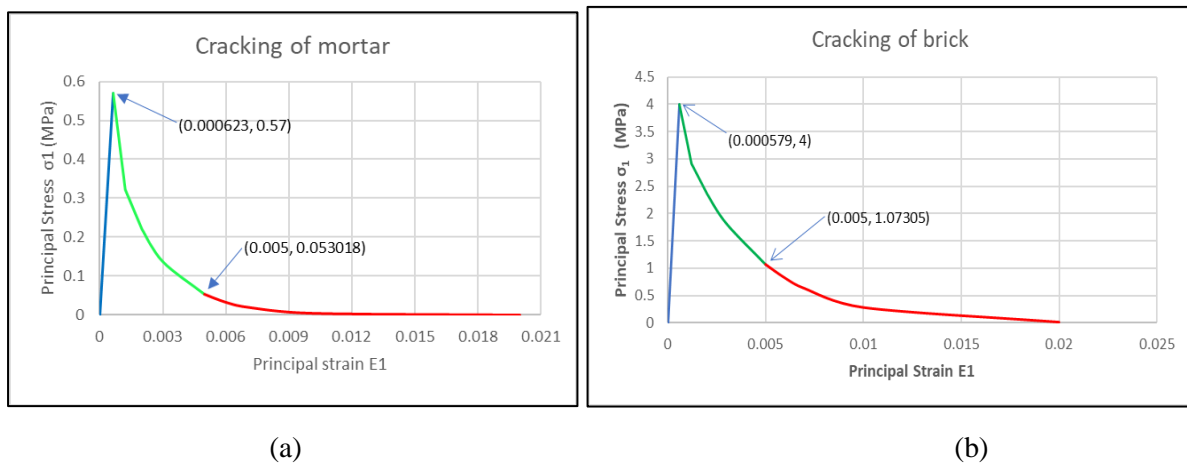
Figure 4.18. Constitutive law for (a) Cracking of mortar ; (b) Cracking of brick of Model 8

The constitutive laws for cracking of mortar and brick of Model 8 are mentioned in **Fig. 4.21.**

(a)   (b)
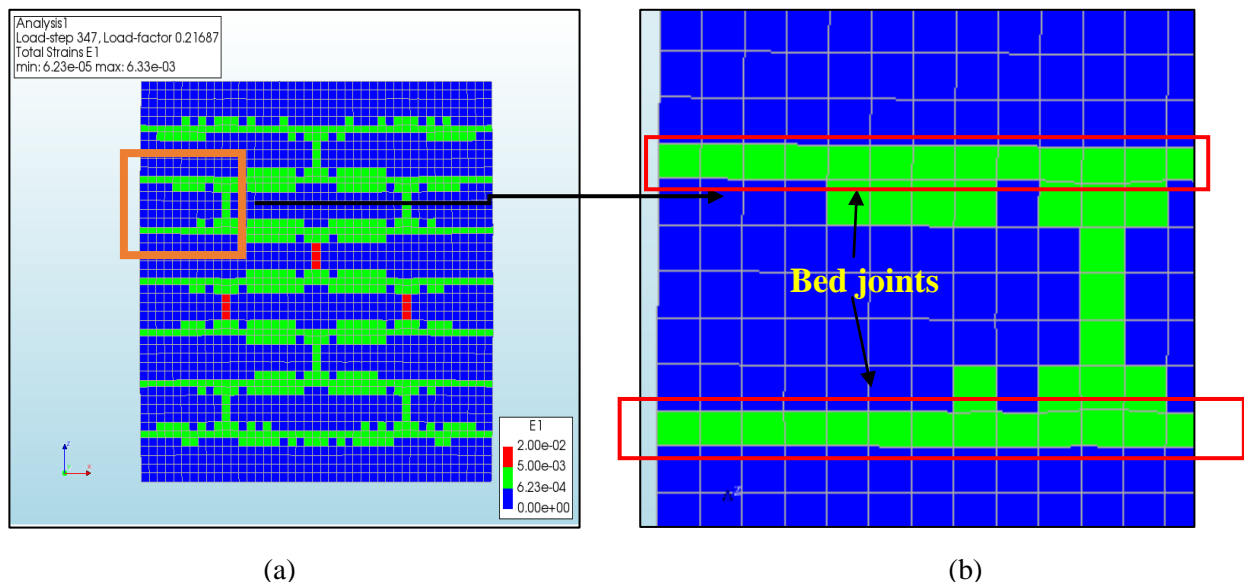
Figure 4.19. (a) Progression of Principal Strain E1; (b) enlarged view of a chosen portion of the model in case of reduced integration scheme

43

	(a)		(b)
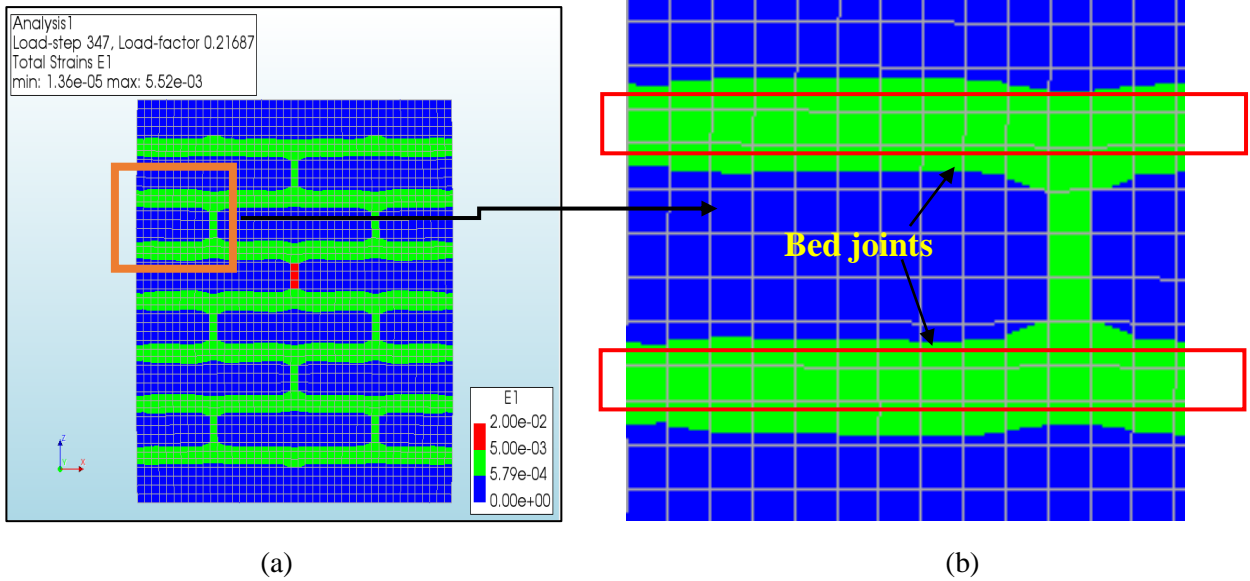
Figure 4.20. (a) Progression of Principal Strain E1; (b) enlarged view of a chosen portion of the model in case of higher integration scheme.

Fig 4.19a shows the development of principal strain E1 at a particular load step. A reduced integration scheme has been utilized to obtain the principal strains in this case. **Fig 4.19b** shows an enlarged view of a selected portion of the model.

Fig 4.20a shows the development of principal strain E1 at a particular load step. A higher integration scheme has been utilized to obtain the principal strains in this case. Similar to **Fig 4.19b**, **Fig 4.20b** shows an enlarged view of a selected portion of the model.

From both **Figs. 4.19b** and **4.20b**, it can be observed that cracking of mortar has taken place. All the finite elements of the bed joints have experienced mortar cracking.

However, in the reduced integration scheme, not all the brick elements in the vicinity of the bed joints are activated in cracking. But in case of the high integration scheme, all the brick elements are activated in cracking. The reason can be attributed to the higher number of integration points in the latter case which allows for better propagation of cracks.
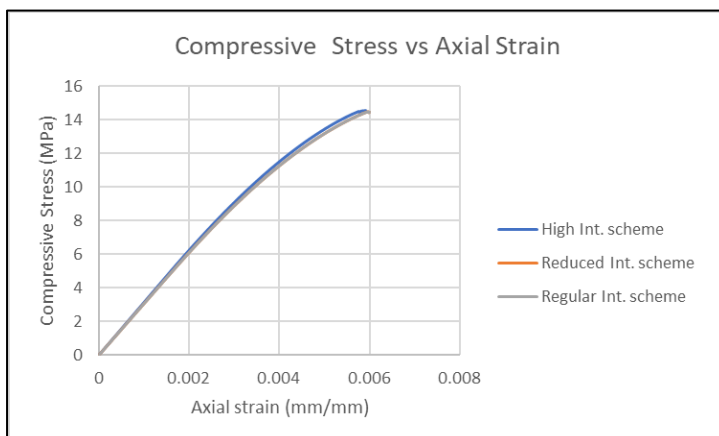
Figure 4.21 Plot of Compressive Stress vs Axial Strain for reduced and high integration scheme.

Fig. 4.21 shows the plot of compressive stress vs Axial Strain for reduced, regular and higher integration schemes. It can be observed that the initial slope of the three curves is same till a

compressive stress of 4 MPa. The peak loads attained by the either integration scheme is almost the same.

4.4. Discussion

In this section, an overview of all the results of the models is provided. Initially, numerical models were created to simulate the results of Benchmark 1. The numerical modelling commenced with Model 1. This model was found to be very stiff compared to the experiments of Thamboo et al. (2020) and FE analysis of Zahra et al. (2021). This can be directly attributed to the very high value of Young's Modulus of brick (4123 MPa vs 200 MPa). The slope of stress-strain plot of masonry is directly correlated to the Young's modulus of the constituent elements (brick and mortar). To alleviate this issue, Model 2 was created in which the input parameters were directly extracted from the numerical analysis of Zahra et al. (2021). Hence the Young's modulus of the brick was chosen as 200 MPa. The slope of the stress-strain plot obtained was in close accordance with the experiments of Thamboo et al. (2020) and the FE analysis of Zahra et al. (2021). However, only mortar crushing could be simulated. Even though Model 1 could simulate the necessary failure mechanisms, the stress-strain plot deviated largely from the experiments of Zahra et al. (2021). This was due to a huge variation in Young's Modulus of brick. However, the value of Young's modulus of brick (200 MPa) chosen by Zahra is unrealistic. Hence a new benchmark was selected.

Models 1-4 implemented the simplified brick-to-brick modeling technique to simulate the experiments of Thamboo et al. (2020) and subsequent FE analysis by Zahra et al. (2021). Model 5, on the other hand, attempted to simulate the experiment of Jafari (2021). However, none of these models could accurately predict the global behaviour of the masonry specimen. A large difference in the peak loads was observed. This is because, in a simplified modelling technique, the confinement effect of mortar is not considered. In a confined state, the compressive strength of mortar is increased.

In Model 5, the compressive strength of mortar was increased tenfold. In this case, all the possible failure mechanisms could be simulated namely cracking of brick, cracking of mortar, shear failure of mortar interface, crushing of mortar, and crushing of brick. The critical values of the compression cap were increased in the combined cracking crushing shear state to accommodate the other failure mechanisms before the onset of mortar crushing. The results of this model reinforced the argument to include the confinement effect of mortar.

Models 7-9 attempted to simulate the experiments of Jafari (2021) using the detailed brick-to-brick modelling technique. The confinement effect was not included in Model 7. Hence, the peak loads were underestimated again. Mortar crushing and mortar cracking were the only failure modes that could be simulated. In Models 8-9, the confinement effect of mortar was included. The confinement curve mentioned in Selby and Vecchio (1993) was chosen. These models provided the most accurate representation of the global behaviour of masonry. The peak loads obtained were very close to that of the experiments of Jafari (2021).

In both the simplified and detailed brick-to-brick models, a sensitivity study was performed based on change in boundary conditions, namely considering or not lateral restraints at the connection with loading plates. For the simplified model, model 1 considered fully restrained surfaces at top and bottom, while model 3 accounts for possible lateral movements. The peak loads attained by either model were very similar but the post-peak behaviour of the two models is different. A steep declining curve was observed in case of Model 1 (with lateral restraints) while a gradual softening curve was observed in case of Model 3. In case of the detailed brick-to-brick modelling technique, model 8 considered fully restrained surfaces at top and bottom, while model 9 accounts for possible lateral movements. There was little impact on the global behaviour of the specimen but only the pre-peak behaviour could be modelled. However, more brick elements were subjected to cracking in Model 9 (without lateral constrains) with respect to Model 8 (with lateral constraints). The topmost and

bottommost head joints were fully cracked for the entire height in Model 9, since lateral expansion was possible at the top and bottom surface. On the contrary, due to the presence of lateral constraints, these cracks were not formed in the case of Model 8.

Another such sensitivity study was performed with regards to change in Poisson's ratio of mortar. Three different values of Poisson's ratio of mortar were chosen and global behaviour of the masonry specimen was analysed. The Poisson's ratio of the brick was kept the same in all the three scenarios. It was found that the higher Poisson's ratio of mortar was responsible for a higher peak load attained by the specimen. This is because a higher Poisson's ratio of mortar implies more lateral confinement afforded by the neighbouring bricks.

The integration scheme also plays a pivotal role in understanding the failure mechanisms. For Model 8, the effect of a high (3×3×3) integration and a reduced (1×1×1) integration scheme was studied. The higher integration scheme implies a higher number of integration points. The propagation of cracks to the bricks in the vicinity of mortar bed joint was much more in the case of higher integration scheme. Almost all the neighbouring brick elements were activated in cracking when a higher integration scheme was used. The regular integration scheme proved equally effective as the higher integration scheme to study propagation of cracks in the vicinity of the mortar bed joints. Only a few brick elements in the vicinity of the mortar bed joint were activated in cracking in case of reduced integration scheme.

5. CONCLUSIONS

In this study, two modelling techniques namely the simplified brick-to-brick and detailed brick-to-brick methods were compared with regards to their accuracy in simulating compressive behaviour of masonry. Two experimental benchmarks, namely experimental results of Thamboo et al. (2020) and Jafari (2021) were selected for this purpose. Numerous models were created using both techniques to simulate the results of the benchmarks. The most relevant factors to consider while simulating compressive behaviour of masonry were also investigated. The key conclusions drawn from this thesis are listed below.

1) The results of the first experimental benchmark chosen, i.e., experiments of Thamboo et al. (2020) and the subsequent FE analysis by Zahra et al. (2021) proved to be unreliable. Zahra et al. (2021) selected a value of 200 MPa for the Young's Modulus of the brick. The value largely deviates from the realistic value of Young's Modulus of brick.

2) The simplified brick-to-brick modelling technique is unsuccessful in simulating the global compressive behaviour of a masonry wallet under compression loading. The peak loads obtained by using this modelling technique are severely underestimated when compared with the experiments. This is because mortar confinement is not considered while using this modelling technique.

3) A simplified brick-to-brick model is successful in simulating the failure modes observed from the experiments if a very high value of compressive strength of mortar was selected. This allowed observing both tensile failure in mortar and bricks before mortar crushing failure started. This once more suggests that the confinement effect is relevant to be modelled.

4) A detailed brick-to-brick modelling technique is successful in simulating the global compressive behaviour of a masonry wallet only if mortar confinement is taken into consideration. The peak loads attained by using this modelling is comparable to that of the experiments. All the experimentally observed failure mechanisms could also be simulated by using this modelling technique. In case confinement effects are excluded, similar results to the simplified brick-to-brick model are obtained. However, this statement concerns only pre-peak behaviour and more effort should be put in resolving numerical instability to simulate also post-peak behaviour.

5) A change in boundary conditions does not significantly affect the pre-peak response with both modelling approaches. However, in the case of the detailed brick-to-brick model accounting for mortar confinement, more brick elements were prone to cracking. There was also increased cracking in the mortar head joints.

6) The Poisson's ratio of mortar plays a key role in determining the peak compressive strength of the masonry structure. A higher value of Poisson's ratio implies a higher peak compressive strength.

7) Care should be taken in selecting the integration scheme. A high (3×3×3) and reduced (1×1×1) integration scheme can successfully simulate the cracking in bricks propagating from bed joints. If a reduced integration scheme (1×1×1) is used, the entire propagation of cracks cannot be captured successfully due to a lesser number of integration points. Both the regular and higher integration schemes perform equally well in capturing the entire propagation of cracks from the bed joints.

6. RECOMMENDATIONS

The present study provides precious insight into the choice of modelling techniques for simulating the compressive behaviour of brick masonry. An attempt has been made to shed some light on some key factors to consider in the modelling of the compressive behaviour of masonry. However, there are still possibilities for future research as stated below.

- This study was restricted to simulating the compressive behaviour of single-wythe wallets. In the future, this can be extended to multi-wythe wallets.

- The bond pattern was not altered in this study. The influence of bond patterns on the choice of modelling technique can prove to be an exciting endeavour.

- In this study, the factor C_s, which controls the shear traction contribution to compressive failure, was kept constant. By varying this factor, its influence on the subsequent failure modes can be investigated.

- The findings of this study can be used to simulate the effect of specimen geometry (e.g., wallets, prisms, cores) on the compressive behaviour of masonry.

- In this study, the post-peak behaviour could not be simulated accurately. Simulation of the post peak behaviour accurately can be undertaken in future studies.

References

Thamboo, J. A., and Dhanasekhar, M., (2020). "Assessment of the characteristics of lime mortar bonded brickwork wallettes under monotonic and cyclic compression". *Construction and Building Materials*. 261 120003. https://doi.org/10.1016/j.conbuildmat.2011.04.049

Jafari, S., (2021). "Material characterisation of existing masonry: A strategy to determine strength, stiffness, and toughness properties for structural analysis" (Doctoral thesis, Delft University of Technology, Delft, The Netherlands). https://doi.org/10.4233/uuid:3bcbbc72-0212-44e9-ac86-2fdc54ec5987

Thaickavil, N.N., and Thomas, J., (2018). "Behaviour and strength assessment of masonry prisms". *Case Studies in Construction Materials*. 8: 23-38. https://doi.org/10.1016/j.cscm.2017.12.007

Thamboo, J.A., and Dhanasekhar, M., (2019). "Correlation between the performance of solid masonry prisms and wallettes under compression". *Journal of Building engineering*. 22(2019): 429-438. https://doi.org/10.1016/j.jobe.2019.01.007

Zahra, T., Asad, M., Thamboo, J., (2021). "Effect of geometry on the compression characteristics of bonded brickwork". *Structures*. 32: 1408-1419. https://doi.org/10.1016/j.istruc.2021.03.040

Sarangapani G., Venkatrama Reddy, B. V., Jagadish, K. S., (2005). "Brick-Mortar Bond and Masonry Compressive Strength". *Journal of Materials in Civil Engineering*. 17(2): 229-237. https://doi.org/10.1061/(ASCE)0899-1561(2005)17:2(229)

Azevedo, A., Delgado, J. Q., Guimaraes, A., Silva, F. A., Oliviera, R., (2019). "Compression behaviour of clay bricks prisms, wallets and walls - Coating influence". *Revista de la Construccion*., 18(1): 123-133. http://dx.doi.org/10.7764/rdlc.18.1.123.

Shetty, N., Livitsanos, G., Verstrynge, E., Aggelis, D.G., Van Hemelrijck, D., Van Balen, K. and Wevers, M. (xxxx) 'Observation of crack initiation zone in brick masonry couplets under compression using X-ray microfocus computed tomography and digital image correlation', *Int. J. Masonry Research and Innovation*, Vol. X, No. Y, pp.xxx–xxx.

Gumaste, K.S., Nanjuda Rao, K. S., Venkatrama Reddy, Jagadish, K.S. (2007). Strength and elasticity of brick masonry prisms and wallets under compression. *Materials and Structures*, 40, 241-253. DOI 10.1617/s11527-006-9141-9

Chang, L. (2022). Parametric numerical study on two-way bending capacity of unreinforced masonry walls: Evaluation of the influence of geometric parameters to improve analytical formulations. https://doi.org/10.4233/uuid:1a99cc80-3fea-4ed3-894f-bf3afeca6745

D'Altri, A.; Sarhosis, V.; Milani, G.; Rots, J.; Cattari, S.; Lagomarsino, S.; Sacco, E.; Tralli, A.; Castellazzi, G.; De Miranda, S (2019). A Review of Numerical Models for Masonry Structures; *Numerical Modeling of Masonry and Historical Structures*, 3–53. https://doi.org/10.1016/B978-0-08-102439-3.00001-4

D'Altri, A.; Sarhosis, V.; Milani, G.; Rots, J.; Cattari, S.; Lagomarsino, S.; Sacco, E.; Tralli, A.; Castellazzi, G.; De Miranda, S (2020). Modeling Strategies for the Computational Analysis of Unreinforced Masonry Structures: Review and Classification. *Archives of Computational Methods in Engineering*, 1153–1185. https://doi.org/10.1007/s11831-019-09351-x

Van Zijl, G., (2004). Modeling masonry shear-compression: Role of dilatancy highlighted. *Journal of Engineering Mechanics*, 130(11), 1289-1296. https://doi.org/10.1061/(ASCE)0733-9399(2004)130:11(1289)

Van Zijl, G., (2000). "Computational Modelling of Masonry Creep and Shrinkage" (Doctoral thesis, Delft University of Technology, Delft, The Netherlands).

Pina-Henriques, J., and Lourenco, P., B., (2006). "Masonry compression: a numerical investigation at the meso-level". Engineering Computations, 23 (4), 382-407. https://doi.org/10.1108/02644400610661163

Petracca, M.; Pela, Luca, P.; Rossi, R.; Oller, S.; Camata, G.; Spacone, E (2017). Multiscale computational first order homogenization of thick shells for the analysis of out-of-plane loaded masonry walls. *Computer Methods in Applied Mechanics and Engineering*, 315, 273-301. https://doi.org/10.1016/j.cma.2016.10.046

Milani, G., & Lourenço, P. B. (2013a). Simple Homogenized Model for the Nonlinear Analysis of FRP-Strengthened Masonry Structures. I: Theory. *Journal of Engineering Mechanics, 139*(1), 59-76. https://doi.org/10.1061/(ASCE)EM.1943-7889.0000457

Kaushik, H.B., Rai, D.C., and Jain, S.K. (2007) 'Stress-strain characteristics of clay brick masonry under uniaxial compression', *Journal of Materials in Civil Engineering*, 19(9), 728–739. 10.1061/(ASCE)0899-1561(2007)19:9(728)

De Villiers, W. I., (2019). Computational and Experimental Modelling of Masonry Walling towards Performance-Based Standardisation of Alternative Masonry Units for Low-Income Housing. https://core.ac.uk/download/pdf/268883067.pdf

Lourenco, P., B., and Rots, J. G., (1997). "Multisurface Interface Model for Analysis of Masonry Structures". *Journal of Engineering Mechanics*. 123(7). https://doi.org/10.1061/(ASCE)0733-9399(1997)123:7(660)

Mohammed, A., Hughes, T. G., Danraka, M. N., (2015). "Fracture energy of full scale and half scale masonry bricks". *International journal of Modern Engineering Research*. 5(9) ISSN: 2249-6645. https://www.researchgate.net/profile/AbbaganaMohammed/publication/282643061_Fracture_energy_of_full_scale_and_half_scale_masonry_bricks/links/5614e9e008ae983c1b4166a3/Fracture-energy-of-full-scale-and-half-scale-masonry-bricks.pdf

Standard Test Method for Compressive Strength of Masonry Prisms, ASTM C1314-16. ASTM International, Inc., 2016.

Methods of test for masonry - Part 1: determination of compressive strength, NEN-EN 1052-1:1998, European Committee for Standardization, 1998.

Drougkhas, A., Roca, P., and Molins, C., (2015). "Numerical prediction of the behaviour, strength and elasticity of masonry in compression". *Engineering Structures*. 90, 15-28. http://dx.doi.org/10.1016/j.engstruct.2015.02.011

Baraldi, D.; and Cecchi, A., (2016). Discrete approaches for the non-linear analysis of in plane loaded masonry walls: molecular dynamic and static algorithm solutions. *Eur. J. Mech. -A/Solids* 57, 165-177. https://doi.org/10.1016/j.euromechsol.2017.01.012

Berto, L., Saetta, A., Scotta, R., Vitaliani, R., (2002). An orthotropic damage model for masonry structures. *Int. J. Numer. Methods Eng*. 55(2), 127-157. https://doi.org/10.1002/nme.495

Lagomarsino, S., Penna, A., Galasco, A., Cattari, S., (2013). Tremuri program: an equivalent frame model for the nonlinear seismic analysis of masonry buildings. *Eng. Struct.* 56, 1787-1799. https://doi.org/10.1016/j.engstruct.2013.08.002

O'Dwyer, D., (1999). Funicular analysis of masonry vaults. *Comput. Struct.* 73(1-5), 187-197. https://doi.org/10.1016/S0045-7949(98)00279-XGet rights and content

Singh, S., B., and Munjal, P., (2017). "Bond strength and compressive stress-strain characteristics of brick masonry*". Journal of Building Engineering*. 9, 10-16. https://doi.org/10.1016/j.jobe.2016.11.006

Ispir, M., and Ilki, A., (2013). "Behaviour of Historical Unreinforced Brick Masonry Walls under Monotonic and Cyclic Compression". *Arabian Journal for Science and Engineering*. 38, 1993-2007. https://doi.org/10.1007/s13369-013-0567-4

Kaushik, H., B., Rai, D., C., Jain, S., K., (2007). "Stress-strain characteristics of clay brick masonry under uniaxial compression". *J. Mater. Civil Eng.*, 19(9), 728-739.

Prasad, B., K., R., Nasir., O., B., Amarnath., K, (2014). "Size effect in brick masonry wallets". *International Journal of Research in Engineering and Technology*., 3, 15-18.

Sarhosis, V., and Lemos, J., V., (2018). "A detailed micro-modelling approach for the structural analysis of masonry assemblages". *Computers & Structures*, 206, 66-81.

List of Figures

List of Tables

APPENDIX – A

In this section, the results of Model 1 are discussed in detail.

Table A.1: - List of input parameters in DIANA, corresponding values and references used for Model 1.

Parameter	Value	Reference
BRICK		
Young's Modulus	4123 MPa	Thamboo (2020), obtained by evaluating one-third of peak stress and corresponding strain on the stress-strain curve.
Poisson's ratio	0.18	Zahra (2021)
Crack orientation	Rotating	
Tensile curve	Exponential	Chang (2021)
Tensile strength	0.52 N/mm^2	Thamboo (2020), $f_{tb} = 0.67 \times$ Modulus of rupture
Mode 1 Tensile fracture energy	0.009 N/mm	Chang (2021),
Compression curve	Parabolic	Petracca et al. (2017)
Compressive strength	5.1 N/mm^2	Thamboo (2020), obtained from compression test of clay brick
Compressive fracture energy	0.0474 N/mm	Mohammed et al. (2015)
MORTAR INTERFACE		
Normal stiffness modulus	212 N/mm^3	Petracca et al. (2017)
Shear stiffness modulus-x	90 N/mm^3	Chang (2021)
Shear stiffness modulus-y	90 N/mm^3	Chang (2021)
Tensile strength	0.2 N/mm^2	Thamboo (2020); $f_t = 0.67 \times$ Flexural strength
Fracture energy	0.01 N/mm	Chang (2021), Rots et al. (1997): $G_{fIm} = 0.05 \times f_{tm}$
Cohesion	0.2 N/mm^2	Chang (2021), Milani and Lourenco (2013); $c_0 = f_{tm}$
Friction angle	0.64 rad	Jafari (2021)
Dilatancy angle	0.54 rad	Zahra (2021)
Residual friction angle	0.64 rad	Zahra (2021)
Confining normal stress	-1.57 N/mm^2	Van Zijl (2004)
Exponential degradation coefficient	5.6	Van Zijl (2004)
Parameter a	-0.09 mm	De Villiers (2019), Van Zijl (2004)
Parameter b	0.006 N/mm	De Villiers (2019), Van Zijl (2004)
Compressive strength	2.4 N/mm^2	Thamboo (2020), obtained from compression test of mortar prism as per EN 1015-11
Factor Cs	0.8	Assumption
Compressive fracture energy	2.5 N/mm	Jafari (2021); $250 \times G_{fIm}$
Equivalent plastic relative displacement	0.0125 mm	De Villiers (2019)
CONVERGENCE METHOD		
Load steps	1600	
Step size	0.000625	
Maximum number of iterations	1000	
Method	Newton Raphson	

Type	Regular	
Energy Convergence tolerance	0.001	
Displacement Convergence tolerance	0.01	
Force convergence tolerance	0.01	
Satisfied simultaneously?	No	

A.1 Checking Convergence norms
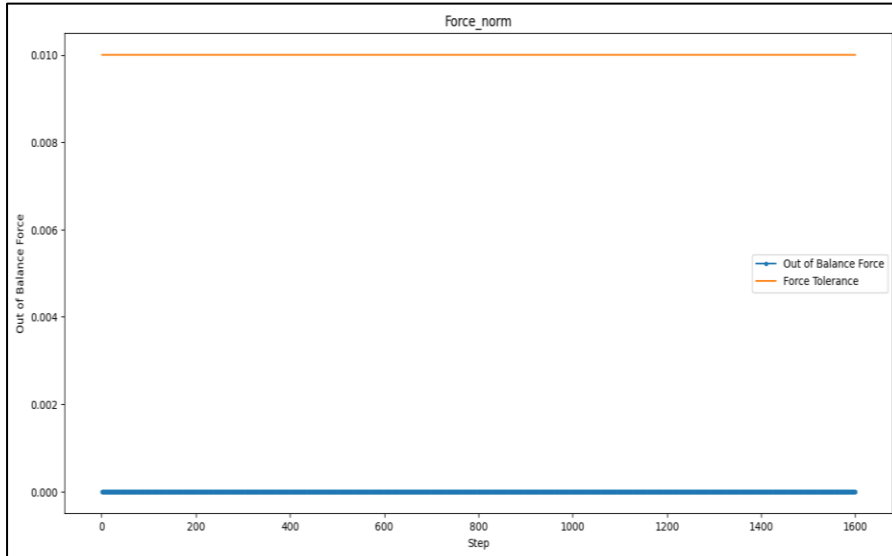
(a)
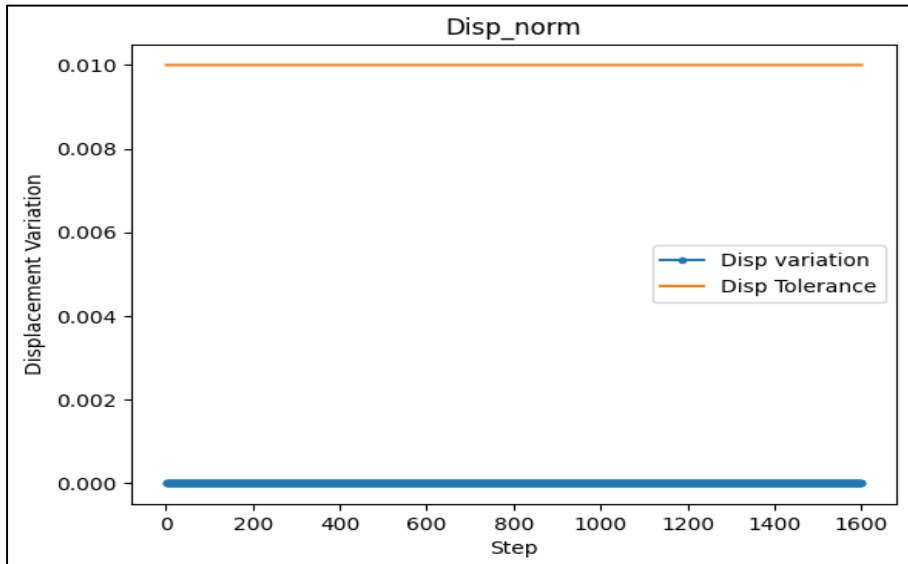
(b)
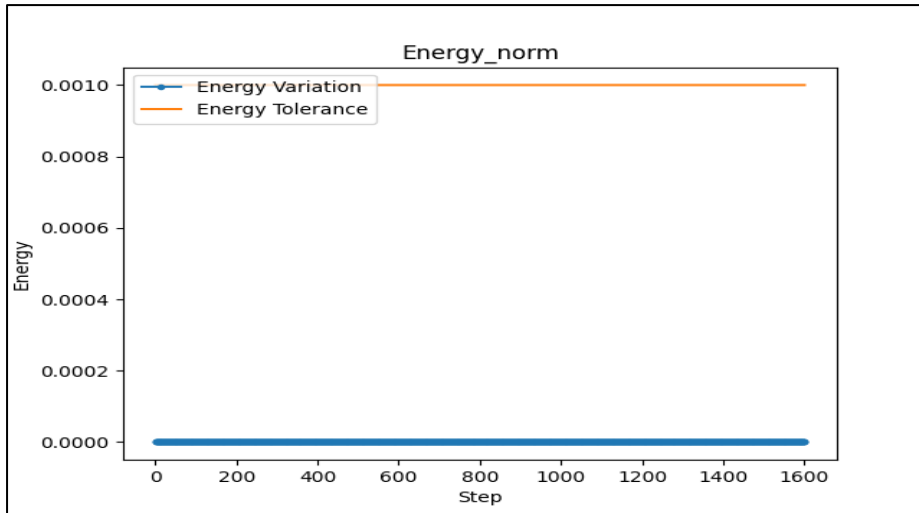
(c)

Figure A.1: Figure showing variation in (a) force; (b) displacement; (c) energy during analysis.

Fig. A.1 shows the variation in force, displacement, and energy during analysis. By observing the variations in force, displacement, and energy after the analysis, it can be said that the results of this analysis are trustworthy. All the variations are within the convergence norms. The variations are in the order of 10^{-14}.

A.2 Stress-Strain graph of the model

Figure. shows the plot of compressive stress-axial strain for Model 1. The load levels shown in the figure have been used to study the progression of potential failure mechanisms.
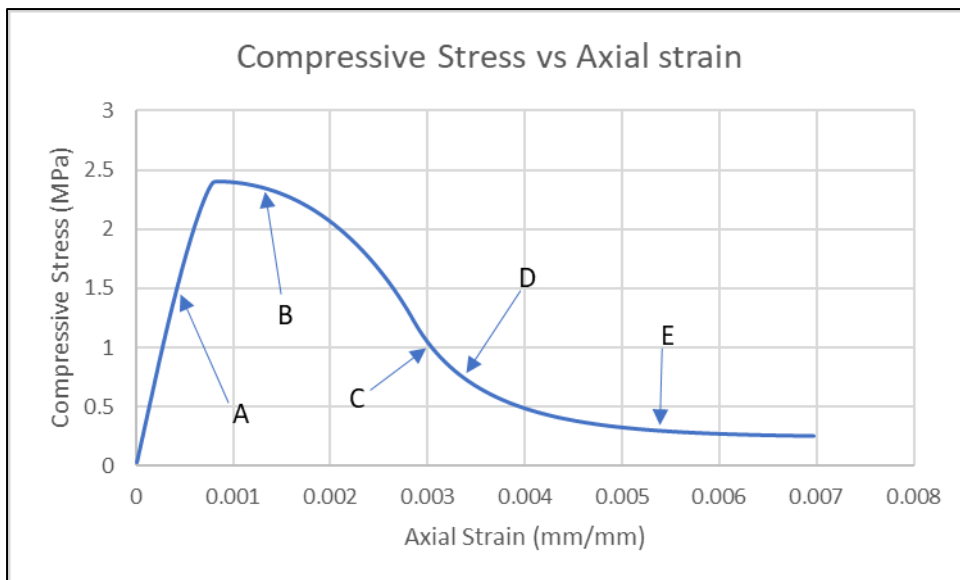
Figure A.2: Plot of compressive Stress – Axial Strain along with specified load levels for Model 1**.**

A.3 Analysis for cracking failure of brick

In this section, the cracking failure of brick is discussed. The constitutive law for the behaviour of a brick element under tensile stress is shown in **Figure A.3**.
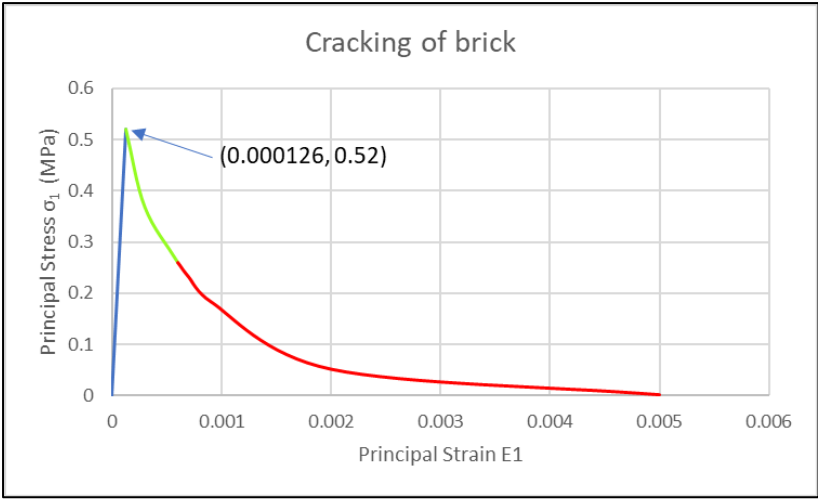
Figure A.3: Constitutive law for cracking of a brick element of Model 1

The point (0.000126, 0.52) indicates the value of principal strain at the tensile strength of the brick. The value of principal strain was calculated by dividing the tensile strength of the brick by Young's Modulus.
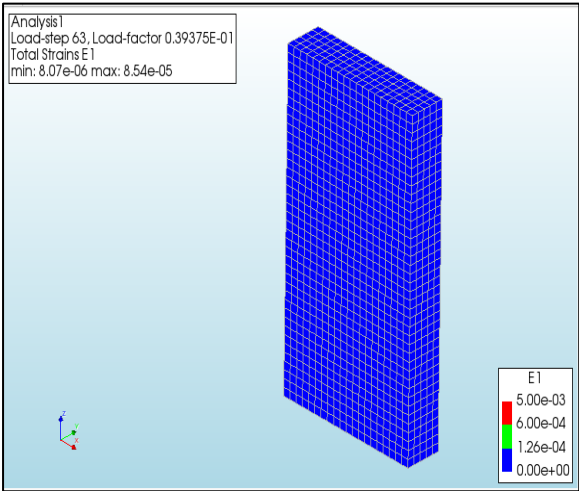
(a)
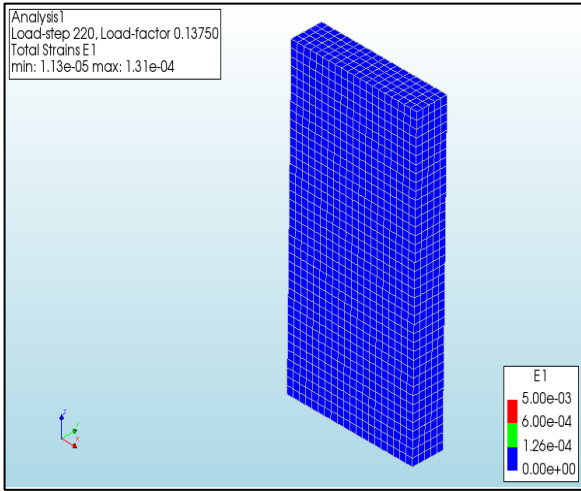
(b)
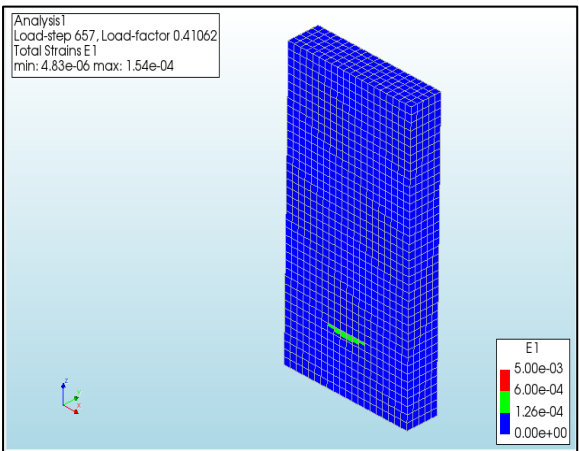
(c)
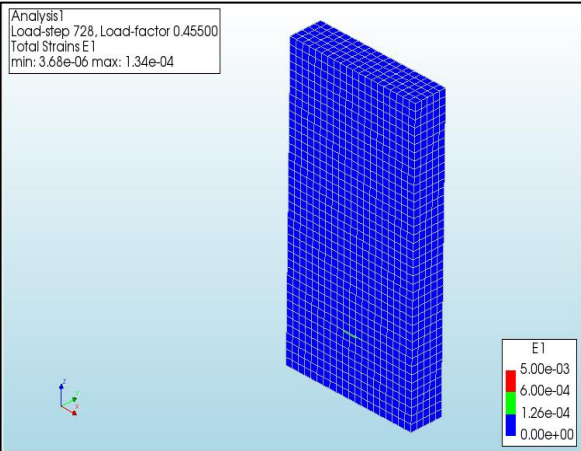
(d)
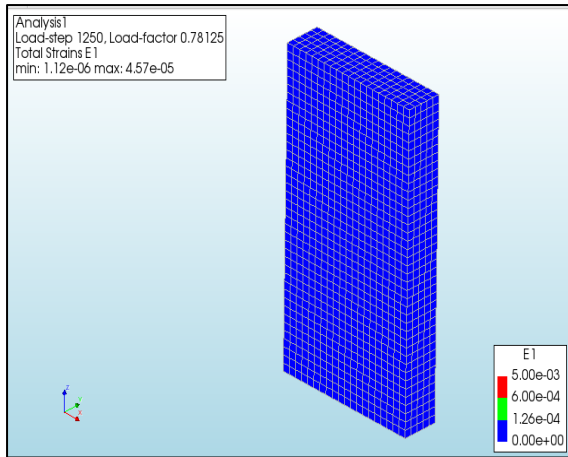
(e)

Figure A.4: Progression of Principal Strain E1 in the specimen.

The evolution of principal strain E1 in the specimen during the analysis is shown in **Figs. A.4 (a – e)**. From **Fig. A.3**, it can be said that there is an onset of cracking in the brick if the principal strain value exceeds 0.000126. This value was exceeded during the analysis as seen in **Figure A.4c**. Hence it can be said that cracking failure of brick did occur in the specimen.

A.4 Analysis for cracking of mortar interface

In this section, the cracking of the mortar interface is discussed. The constitutive law for a mortar element under tensile stress is shown in **Figure A.5**.
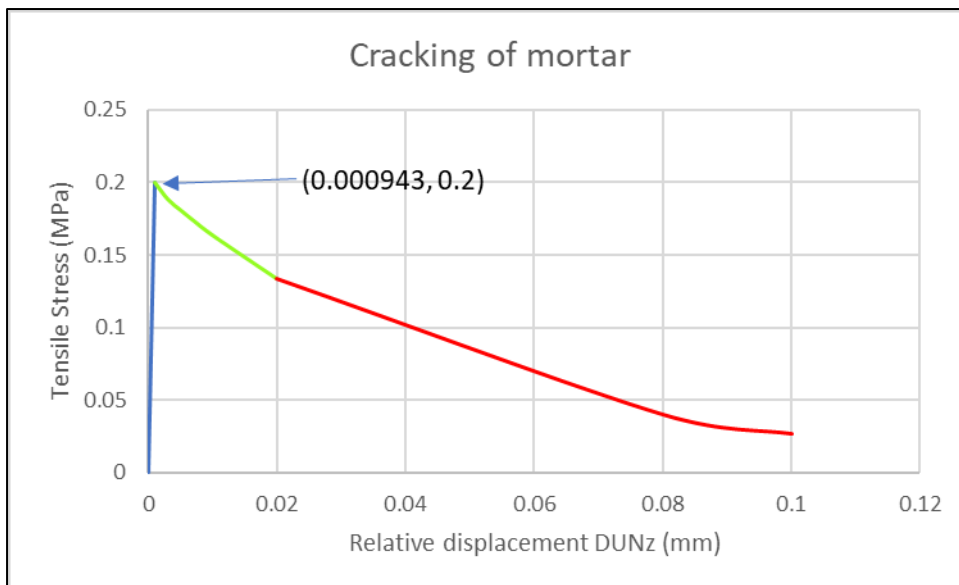
Figure A.5. Constitutive law for cracking of mortar for Model 1.

The point (0.000943, 0.2) indicates the value of relative displacement at the tensile strength of mortar. The value of relative displacement was calculated by dividing the tensile strength of the mortar by the normal stiffness modulus. The positive value of relative displacement was utilized to analyse the potential cracking of mortar interface.

(a)   (b)
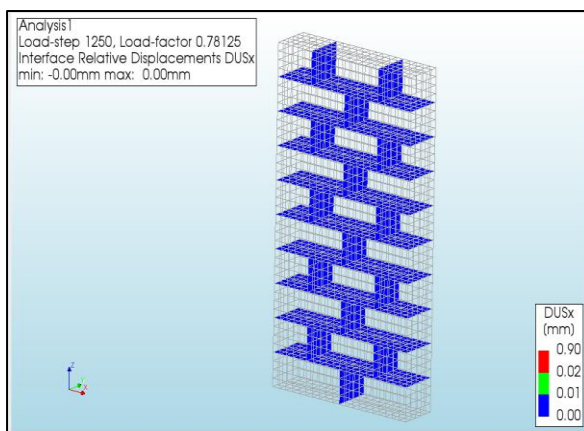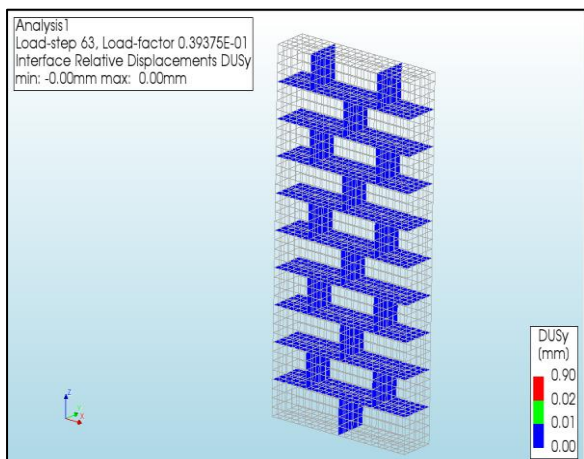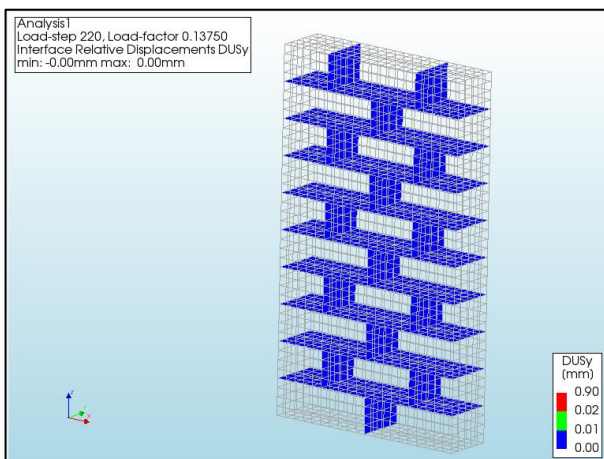
(c)   (d)

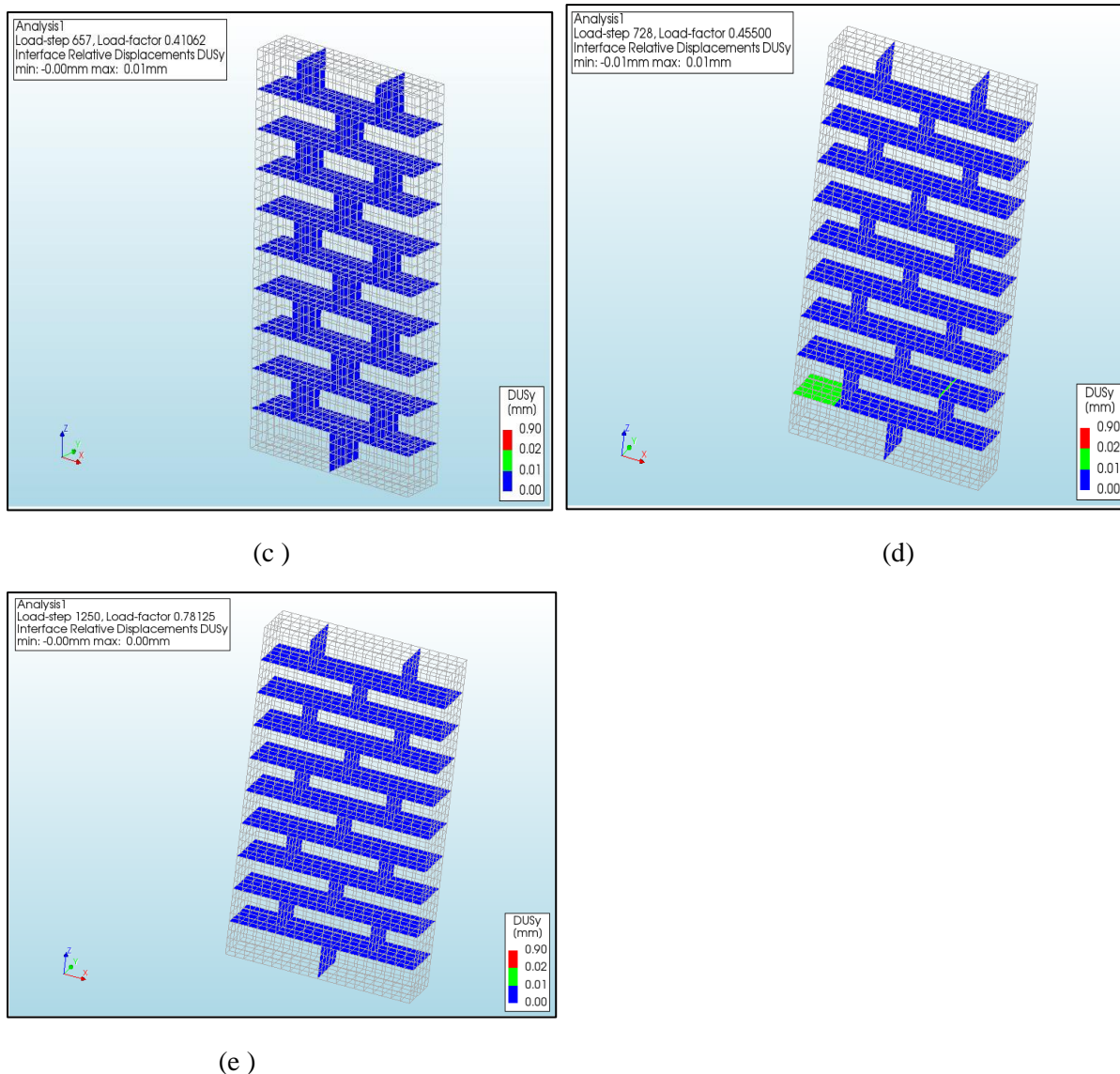(e)
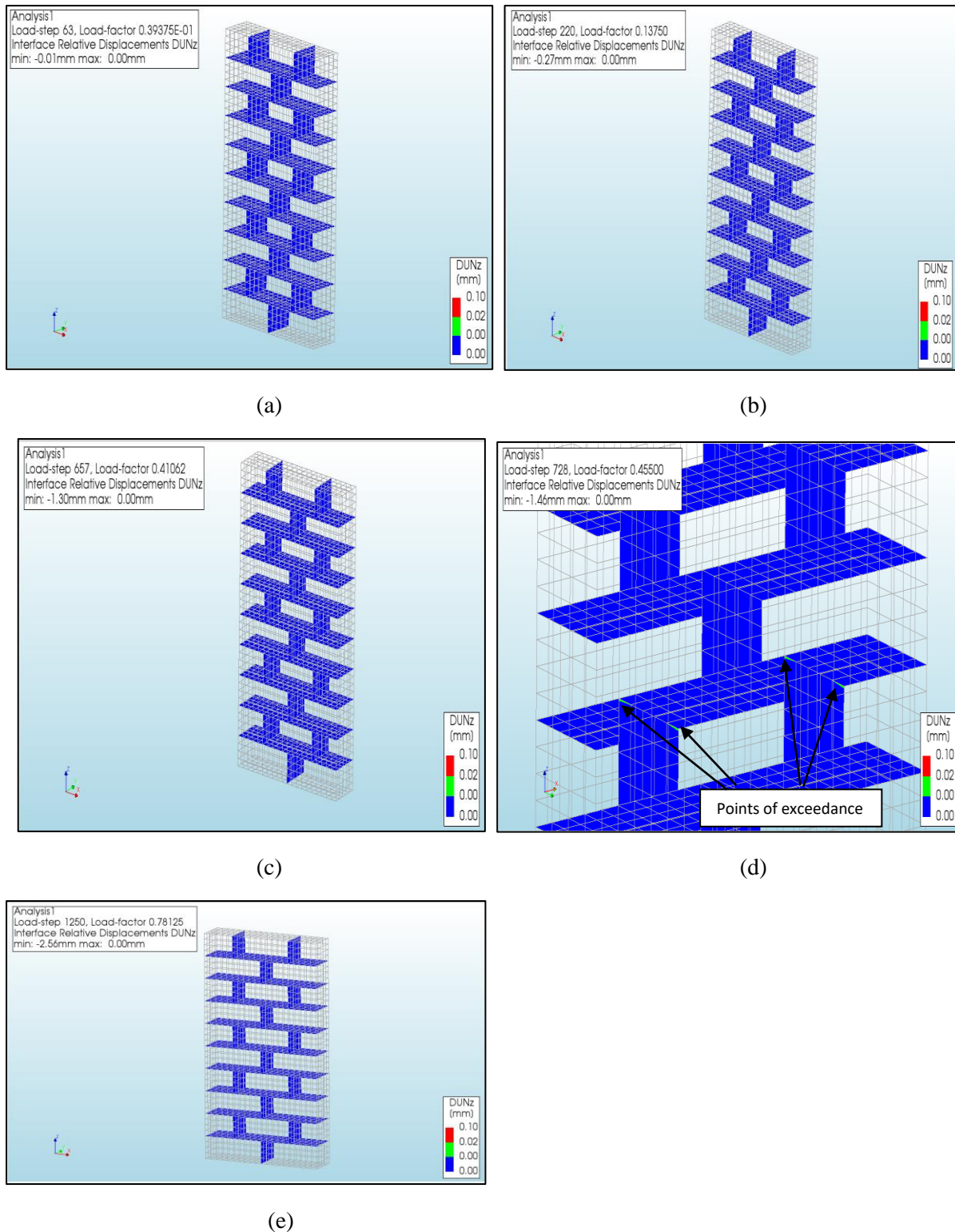
Figure A.6. Progression of Relative displacement DUNz (+ ve) in the specimen.

The evolution of relative normal displacement DUNz (+ve) in the specimen during the analysis is shown in **Figs. 27(a – e)**. From **Fig. A.3**, it can be said that there is an onset of cracking in the mortar interface if the relative displacement value exceeds 0.000943. This value was exceeded during the analysis as can be seen from **Figure A.6**. It can also be observed that the cracking of mortar only occurred in head joints.

A.5 Analysis for crushing of mortar interface

In this section, the crushing of the mortar interface is discussed. The negative value of relative displacement was utilized to analyse the potential crushing of the mortar interface.
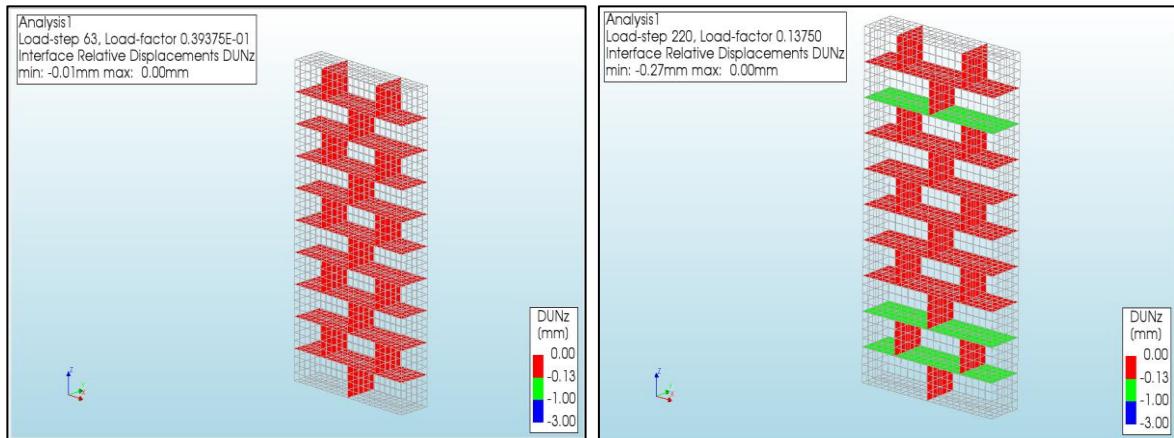
(a)   (b)
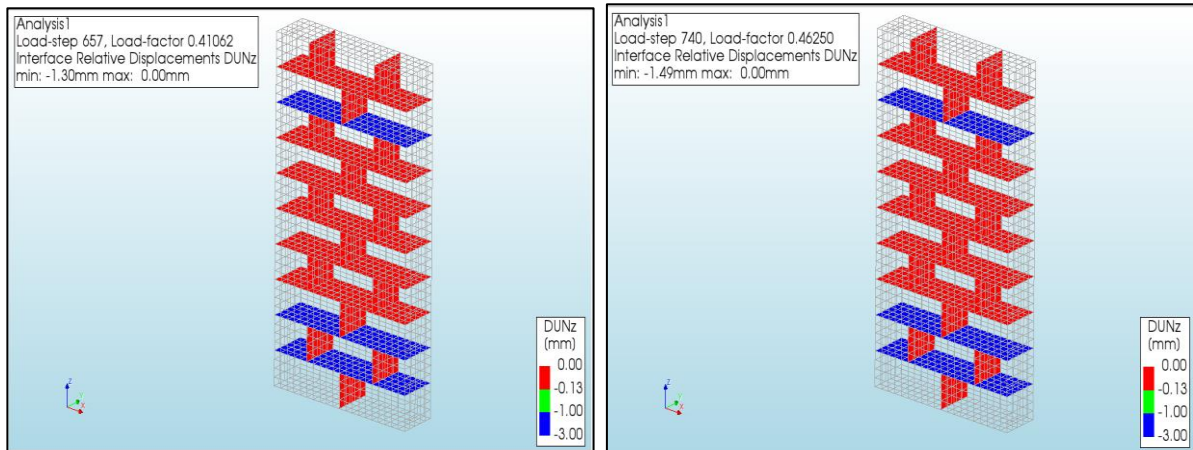
(c)   (d)
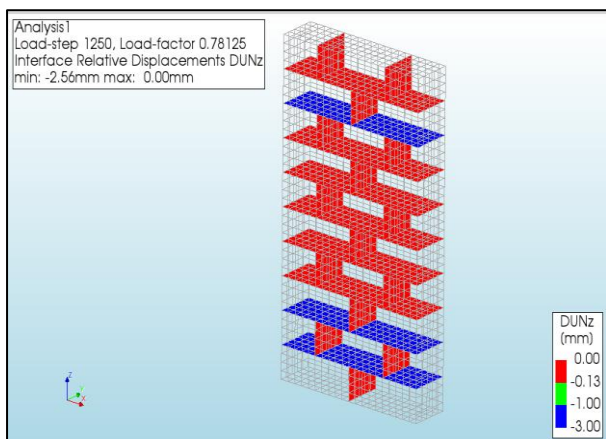
(e)

Figure A.7. Progression of DUNz (- ve) in the specimen.

The evolution of relative displacement DUNz (-ve) in the specimen during the analysis is shown in **Figs. A.7(a – d)**. From **Table A.1**, it can be observed that the value of equivalent plastic relative displacement is 0.0125. This can be interpreted as the strain at peak compressive stress of mortar. To obtain the relative displacement, the strain is multiplied by the thickness of the mortar interface. The value of 0.125 is exceeded during the analysis. It can also be observed that crushing failure of mortar occurred only in the bed joints.

A.6 Analysis for shear failure of mortar interface

In this section, the shear failure of mortar interface is discussed. The constitutive law for the behaviour of a mortar element under shear stress is shown in **Figure 28**.
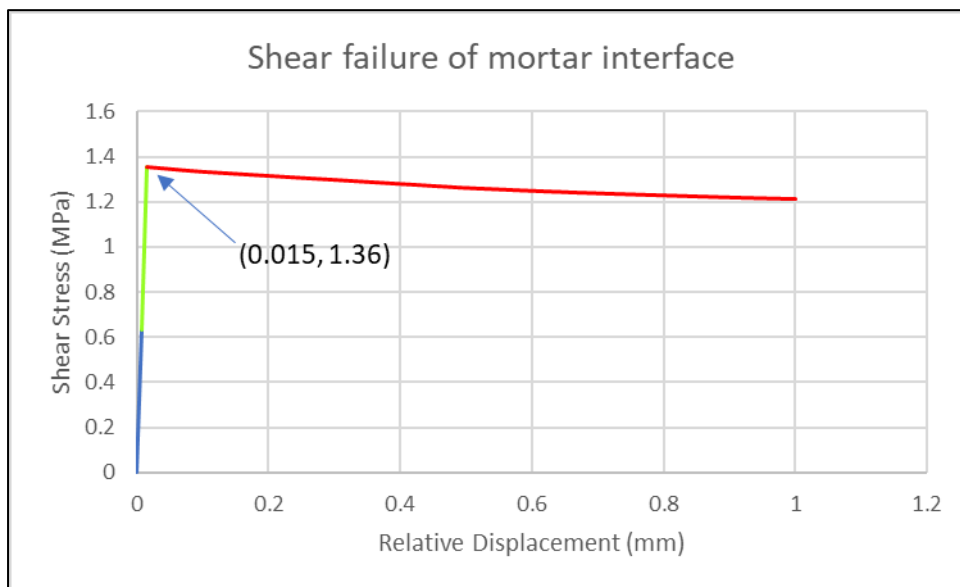
Figure A.8. Behaviour of mortar element under shear stress.

The point (0.015, 1.36) indicates the value of relative displacement at peak mortar shear strength. The value of relative displacement was calculated by dividing the shear strength of the mortar by the shear stiffness modulus.

(a)   (b)
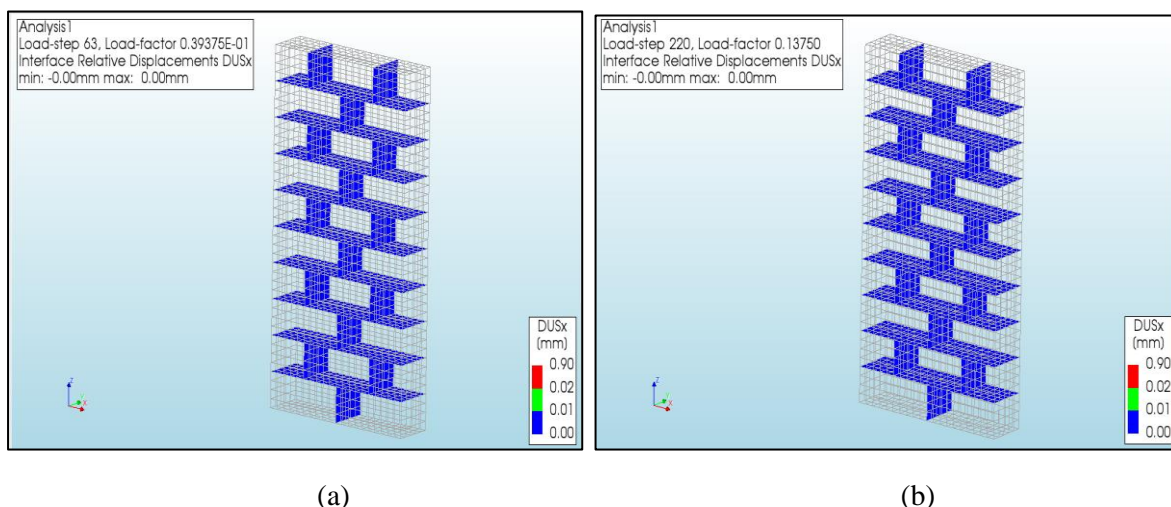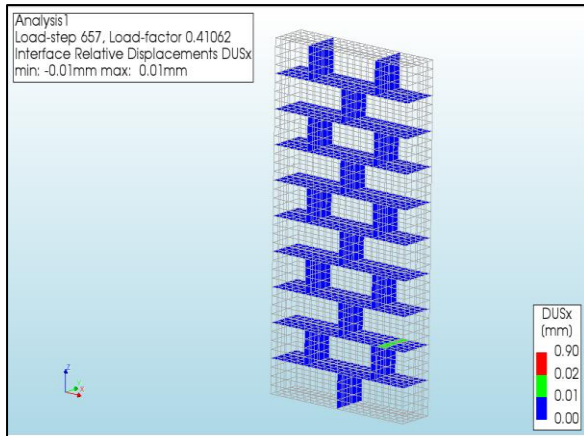
(c)
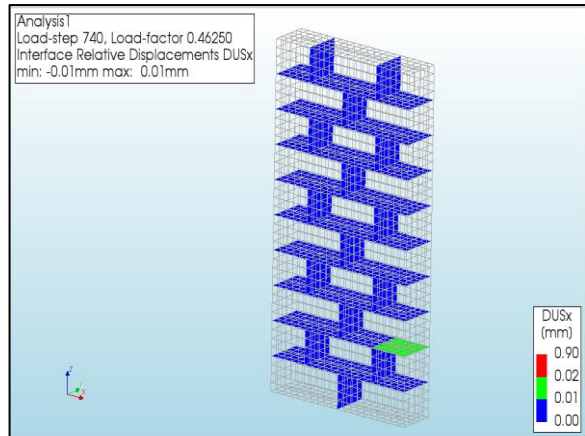
(d)

(e)

Figure A.9. Progression of Relative displacement DUSx in the specimen

(a)

(b)

(c)

(d)

(e)

Figure A.10. Progression of Relative Displacement DUSy

The evolution of relative sliding displacement DUSx in the specimen during the analysis is shown in **Figs. A.9 (a – d)** while the evolution of relative sliding displacement DUSy is shown in **Figs. A.10(a – d)**. From both **Figs. A.9 (a – d)** and **Figs. A.10 (a – d)**, it can be noted that the critical value 0.015, which indicates the onset of shear failure, was not exceeded. Hence it can be concluded that the shear failure of the specimen did not take place.

A.7 Analysis for crushing of brick

This section discusses the crushing failure of a brick. As per **Table 1**, The peak compressive strength of the brick is 5.1 MPa. If principal stress S3 exceeds 5.1 MPa, it can be inferred that the brick has undergone crushing failure. The principal strain E3 was not utilized for this analysis as it was observed that the maximum principal stress S3 attained by the brick was much lower than the compressive strength of the brick.
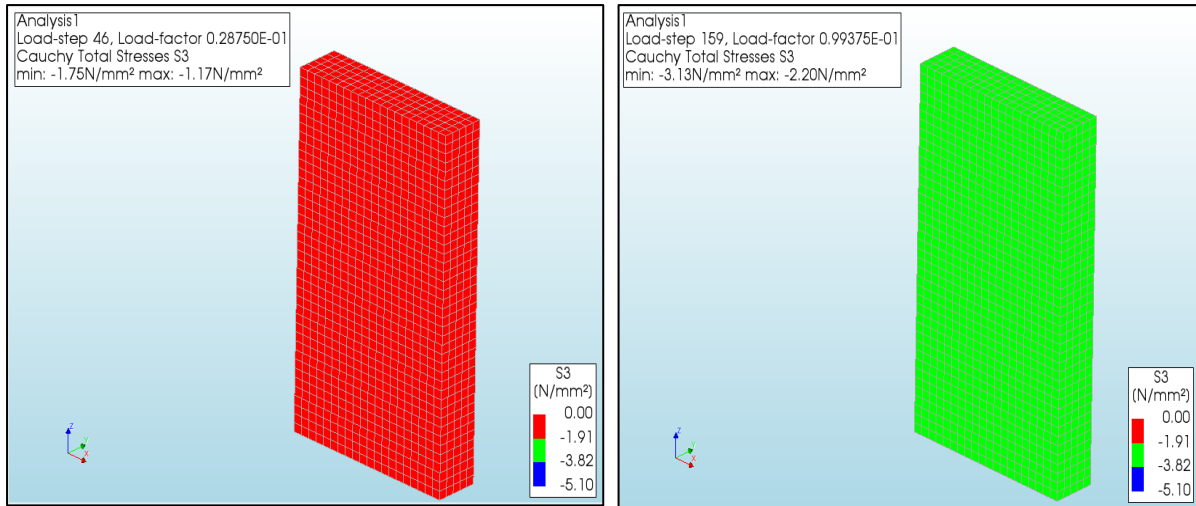
(a)

(b)
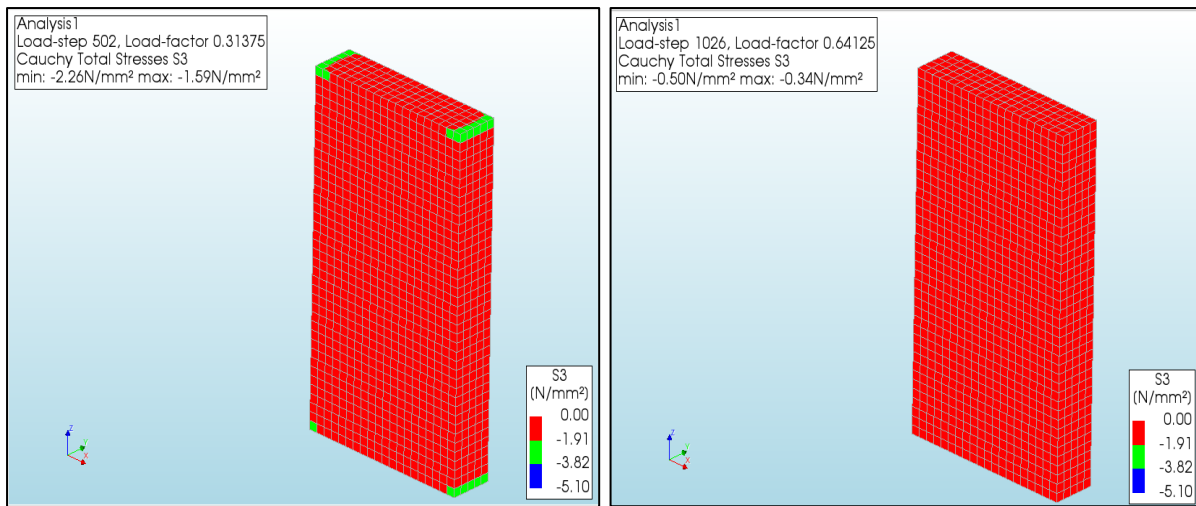
(c)

(d)

Figure A.11. Progression of Principal Stress S3 in the specimen.

From **Figs. A.11(a-d)**, it can be observed that the principal stress S3 doesn't exceed the compressive strength of a brick. Hence crushing failure of brick did not occur.

APPENDIX – B

In this section, the results of Model 2 are discussed in detail.

Table B.1. List of input parameters in DIANA, corresponding values and references used for Model 2.

| Parameter	Value	Reference
BRICK		
Young's Modulus	200 MPa	Zahra (2021)
Poisson's ratio	0.18	Zahra (2021)
Crack orientation	Rotating	
Tensile curve	Exponential	Chang (2021)
Tensile strength	0.52 N/mm^2	Thamboo (2020), Jafari (2021); $f_{tb} = 0.67 \times$ Modulus of rupture
Mode 1 Tensile fracture energy	0.009 N/mm	Chang (2021), Jafari (2021): $G_{fIb} = 0.018 \times f_{tb}$
Compression curve	Parabolic	Petracca et al. (2017)
Compressive strength	5.1 N/mm^2	Thamboo (2020), obtained from compression test of clay brick
Compressive fracture energy	0.0474 N/mm	Mohammed et al. (2015)
MORTAR INTERFACE		
Normal stiffness modulus	28 N/mm^3	Zahra (2021)
Shear stiffness modulus-x	32 N/mm^3	Zahra (2021)
Shear stiffness modulus-y	32 N/mm^3	Zahra (2021)
Tensile strength	0.2 N/mm^2	Thamboo (2020); $f_t = 0.67 \times$ Flexural strength
Fracture energy	0.02 N/mm	Chang (2021), Rots et al. (1997): $G_{fIm} = 0.05 \times f_{tm}$
Cohesion	0.2 N/mm^2	Chang (2021), Milani and Lourenco (2013); $c_0 = f_{tm}$
Friction angle	0.64 rad	Jafari (2021)
Dilatancy angle	0.54 rad	Zahra (2021)
Residual friction angle	0.64 rad	Zahra (2021)
Confining normal stress	-1.57 N/mm^2	Van Zijl (2004)
Exponential degradation coefficient	5.6	Van Zijl (2004)
Parameter a	-0.09 mm	De Villiers (2019), Van Zijl (2004)
Parameter b	0.006 N/mm	De Villiers (2019), Van Zijl (2004)
Compressive strength	2.4 N/mm^2	Thamboo (2020), obtained from compression test of mortar prism as per EN 1015-11
Factor Cs	0.8	Assumption
Compressive fracture energy	2.5 N/mm	Jafari (2021); $250 \times G_{fIm}$
Equivalent plastic relative displacement	0.0125 mm	De Villiers (2019)
CONVERGENCE METHOD		
Load steps	1600	
Step size	0.000625	
Maximum number of iterations	1000	
Method	Newton Raphson	
Type	Regular	

Energy Convergence tolerance	NA	
Displacement Convergence tolerance	0.01	
Force convergence tolerance	0.01	
Satisfied simultaneously?	No	

B.1 Stress-Strain plot of the model
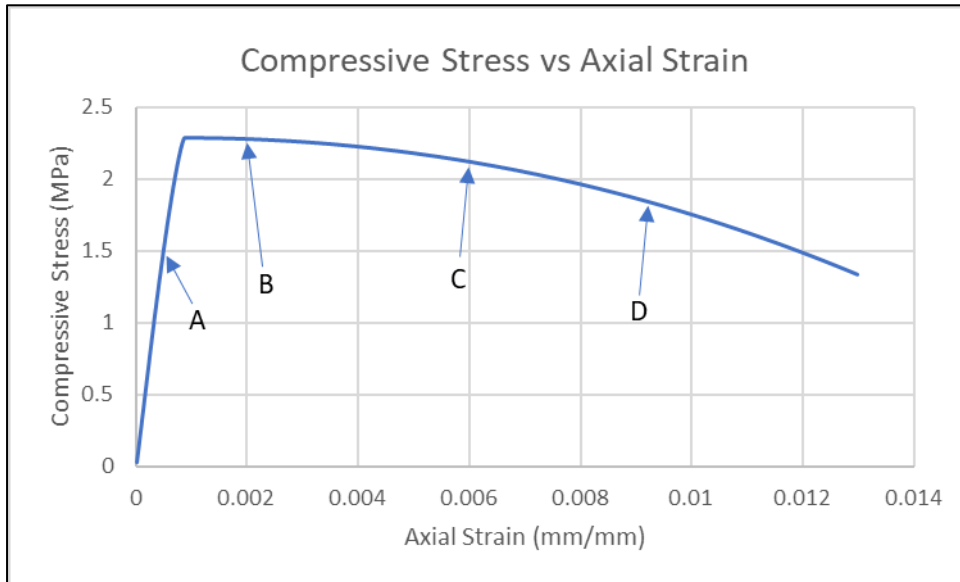
Figure B.1. Plot of compressive stress-axial strain along with specified load levels.

Figure B.1. shows the plot of compressive stress-axial strain for Model 2. The load levels shown in the figure have been used to study the progression of potential failure mechanisms.

B.2 Analysis for shear failure of mortar interface

In this section, the shear failure of mortar is discussed. The constitutive law for the behaviour of a mortar element under shear stress is shown in **Figure B.2.**
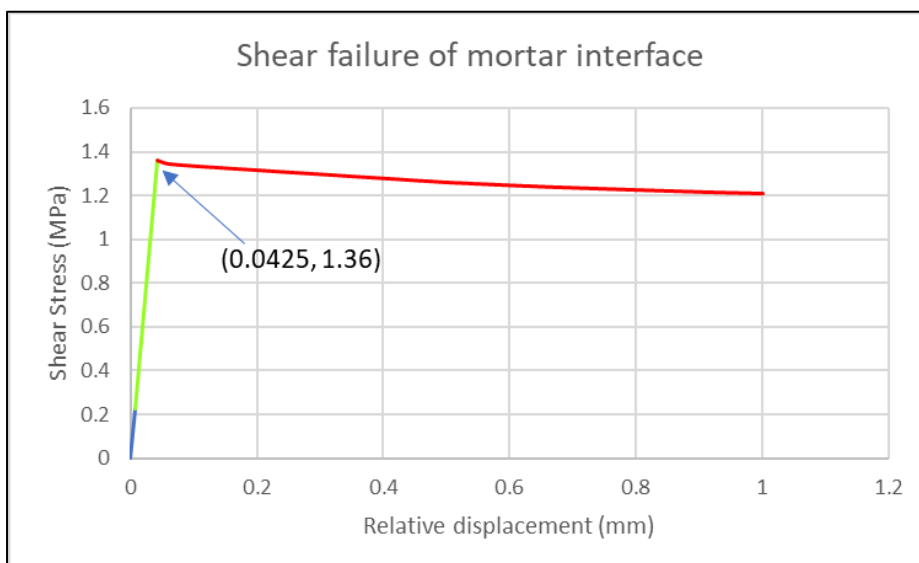
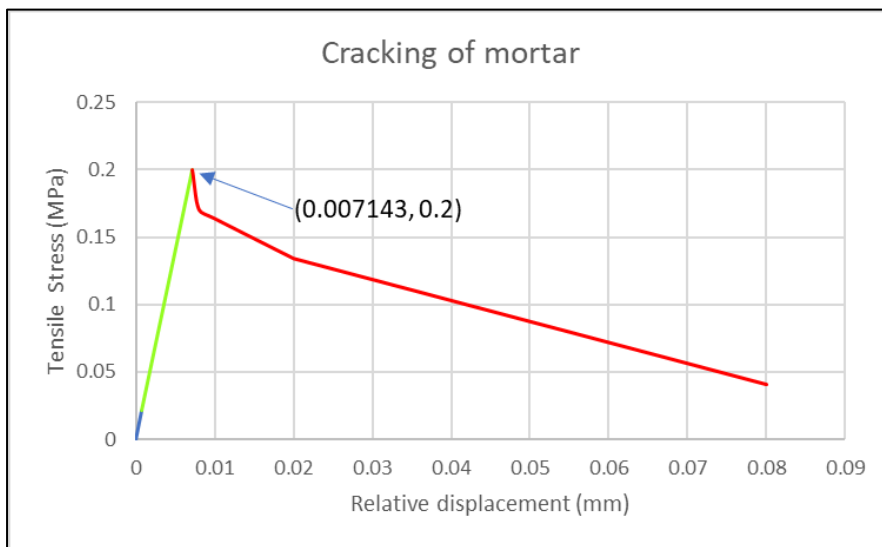**Figure B.2**. Behaviour of mortar element under shear stress.

The point (0.0425, 1.36) indicates the value of relative displacement at peak mortar shear strength. The value of relative displacement was calculated by dividing the shear strength of mortar by the shear stiffness modulus.
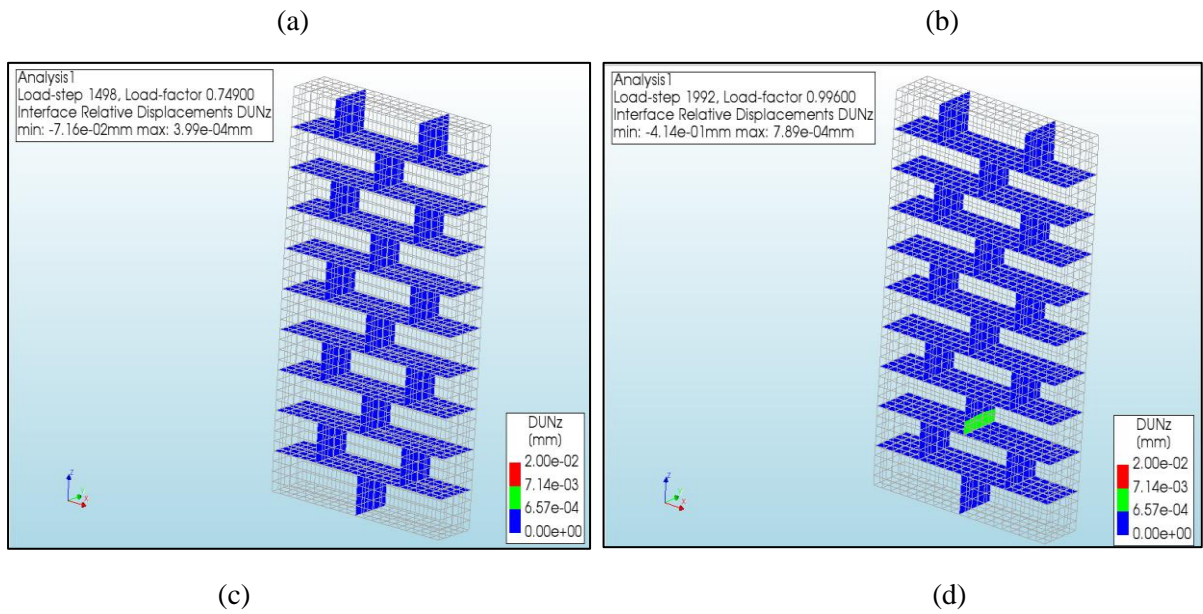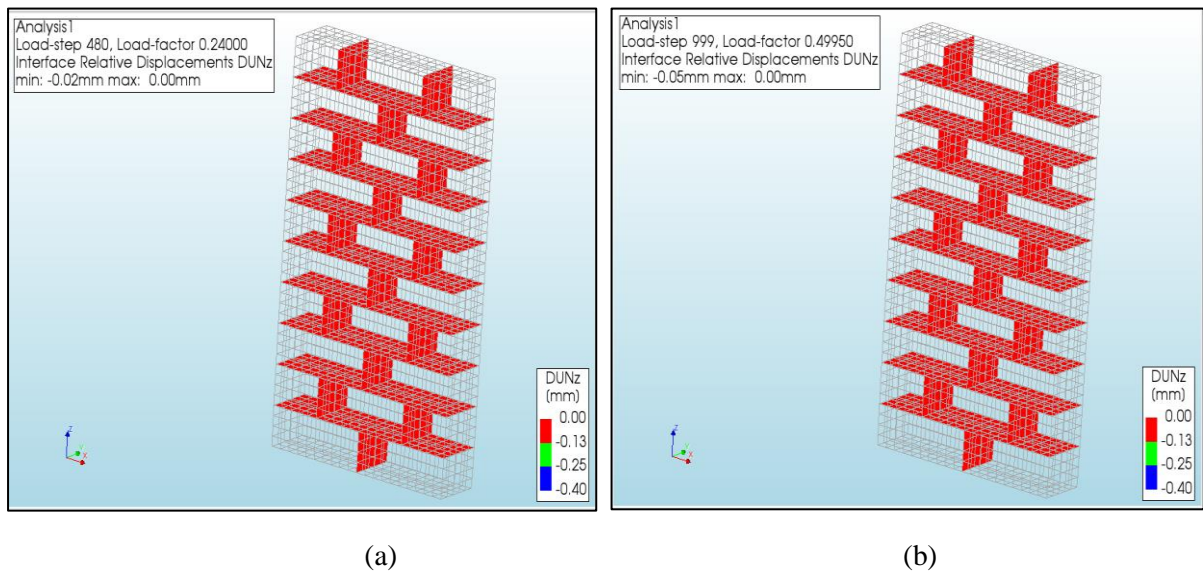

(a)

(b)

(c)

(d)
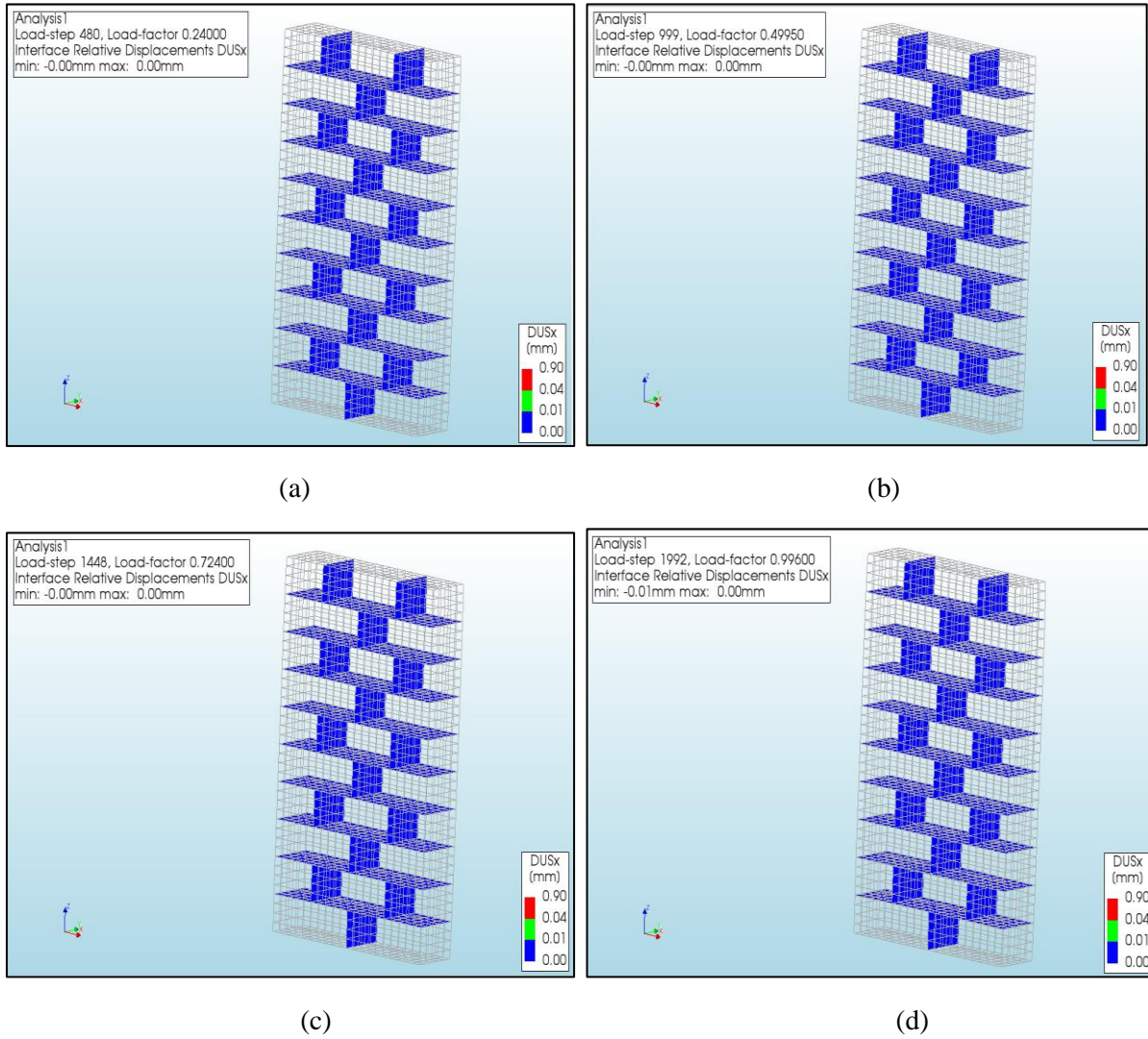
Figure B.3: Progression of DUSx

(a) (b)

(c) (d)
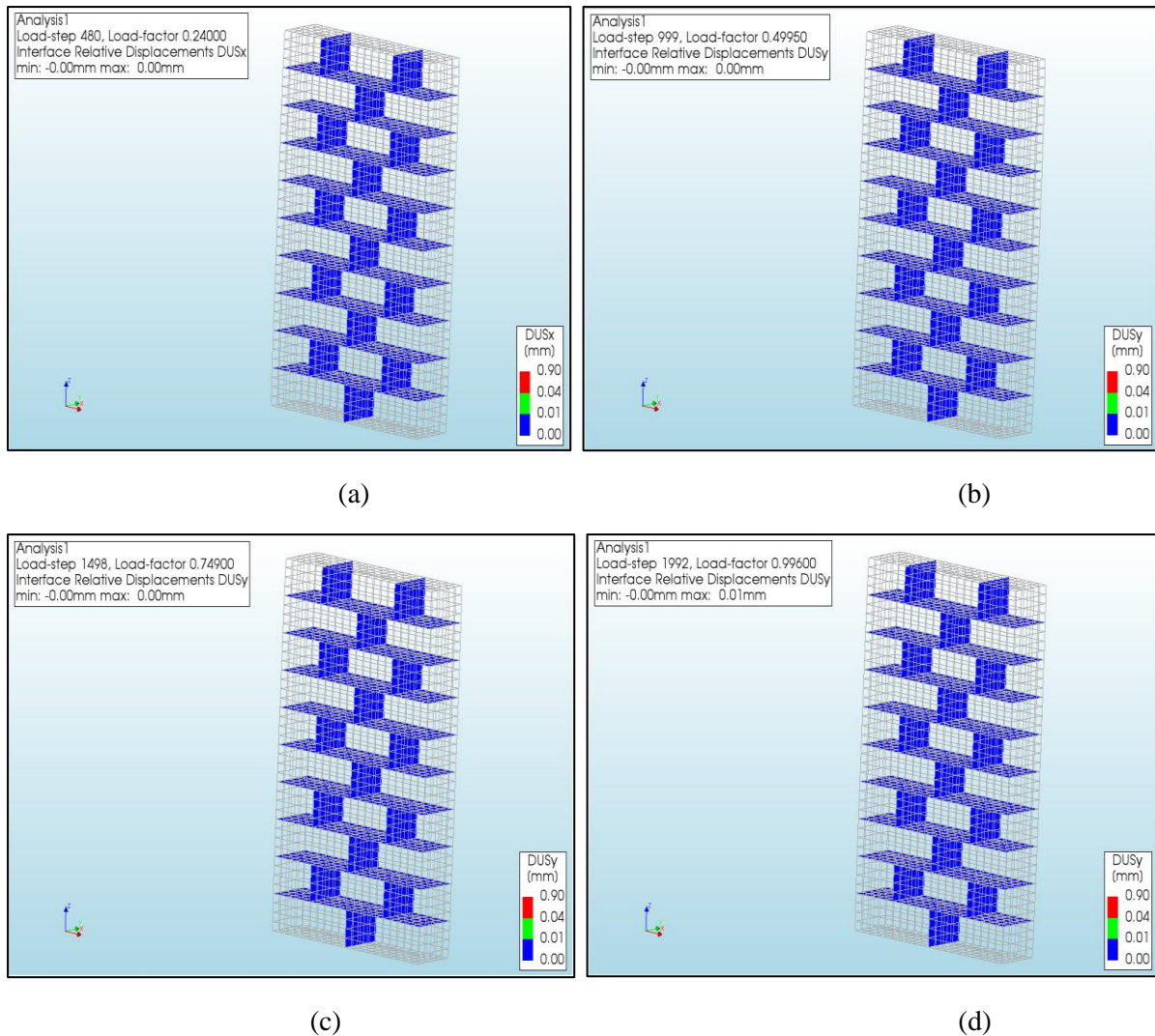
Figure B.4: Progression of DUSy

The evolution of relative displacement DUSx in the specimen during the analysis is shown in **Figs. B.3 (a – d)** while the evolution of relative displacement DUSy is shown in **Figs. B.4(a - d)**. From both **Figs. B.3 (a – d)** and **Figs. B.4 (a – d)**, it can be noted that the critical value 0.0425, which indicates the onset of shear failure, was not exceeded. Hence it can be concluded that the shear failure of the specimen did not take place.

B.3 Analysis for crushing of brick

This section discusses the crushing failure of a brick. The peak compressive strength of brick chosen for this study is 5.1 MPa. If this value of principal stress S3 is exceeded, it can be inferred that the brick has undergone crushing.

(a)

(b)

(c)

(d)
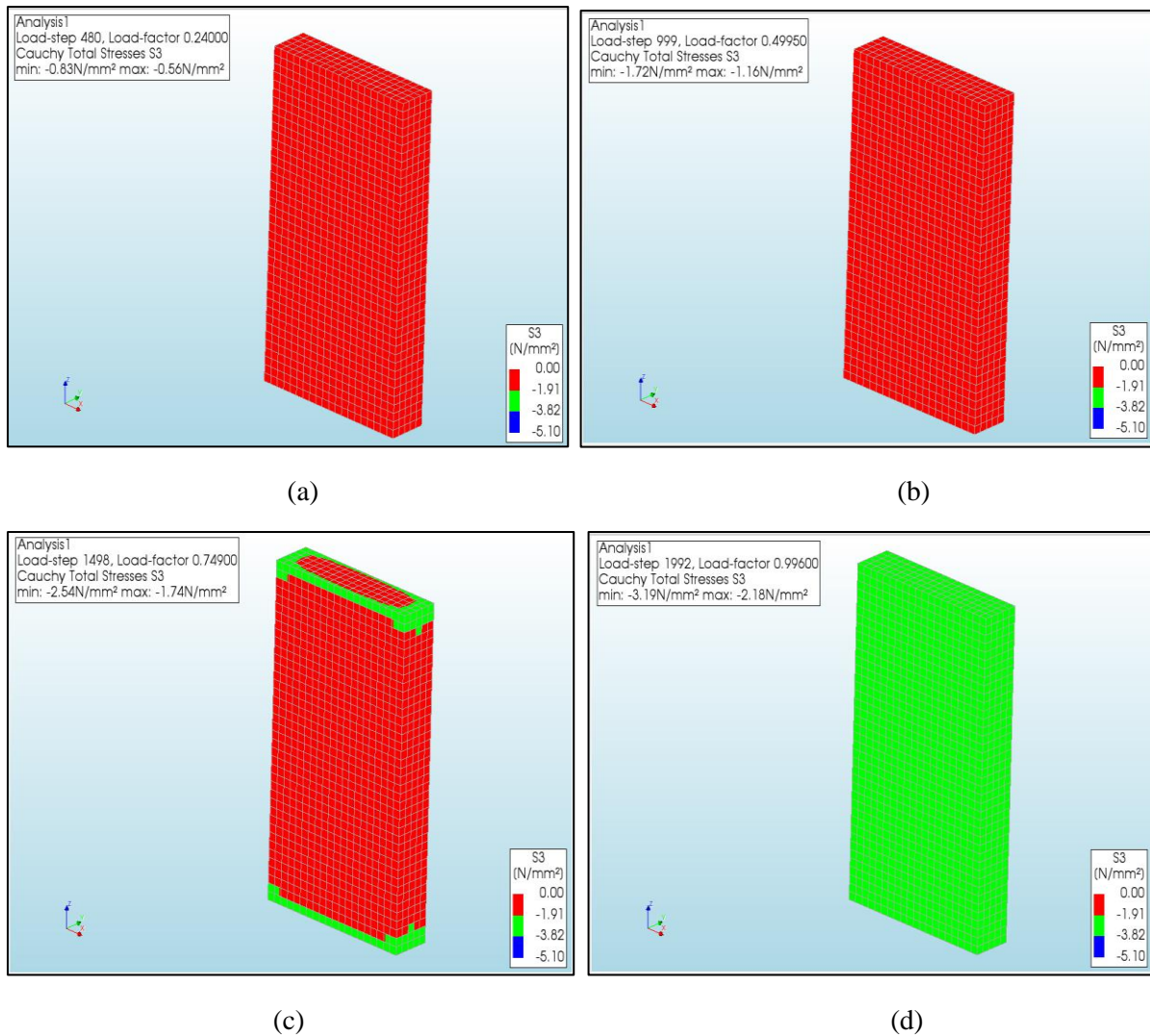
Figure B.5. Progression of Principal Stress S3 in the specimen.

From **Figs. B.5 (a-d)**, it can be observed that the principal stress S3 doesn't exceed the compressive strength of a brick. Hence crushing failure of brick did not occur.

B.4 Analysis for cracking failure of brick

In this section, the cracking failure of brick is discussed. The constitutive law for the behaviour of a brick element under tensile stress is shown in **Figure B.6**.
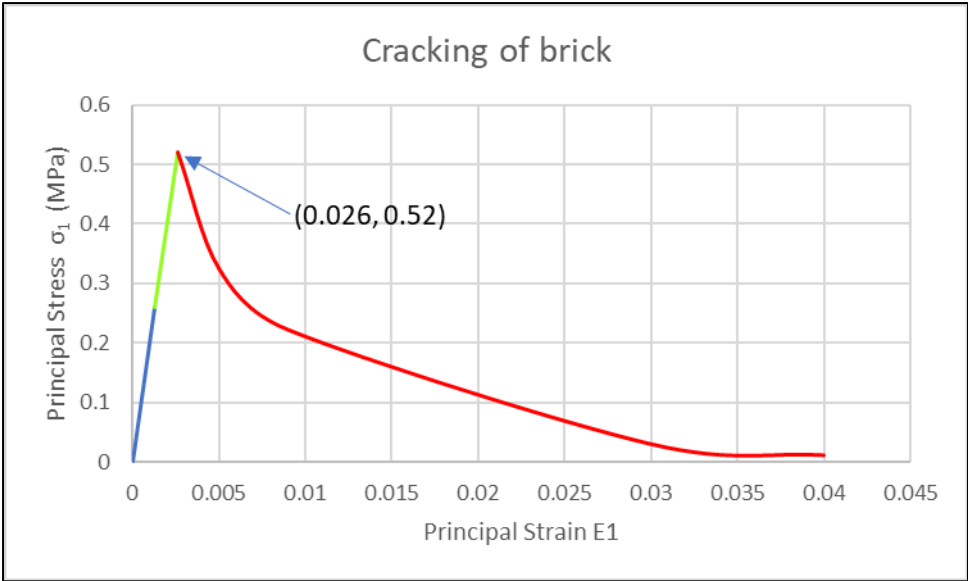
Figure B.6. Behaviour of brick element under tensile stress for Model 2.

The point (0.0026, 0.52) indicates the value of principal strain at peak brick tensile strength. The value of principal strain was calculated by dividing the tensile strength of brick by the Young's Modulus.

(a)

(b)
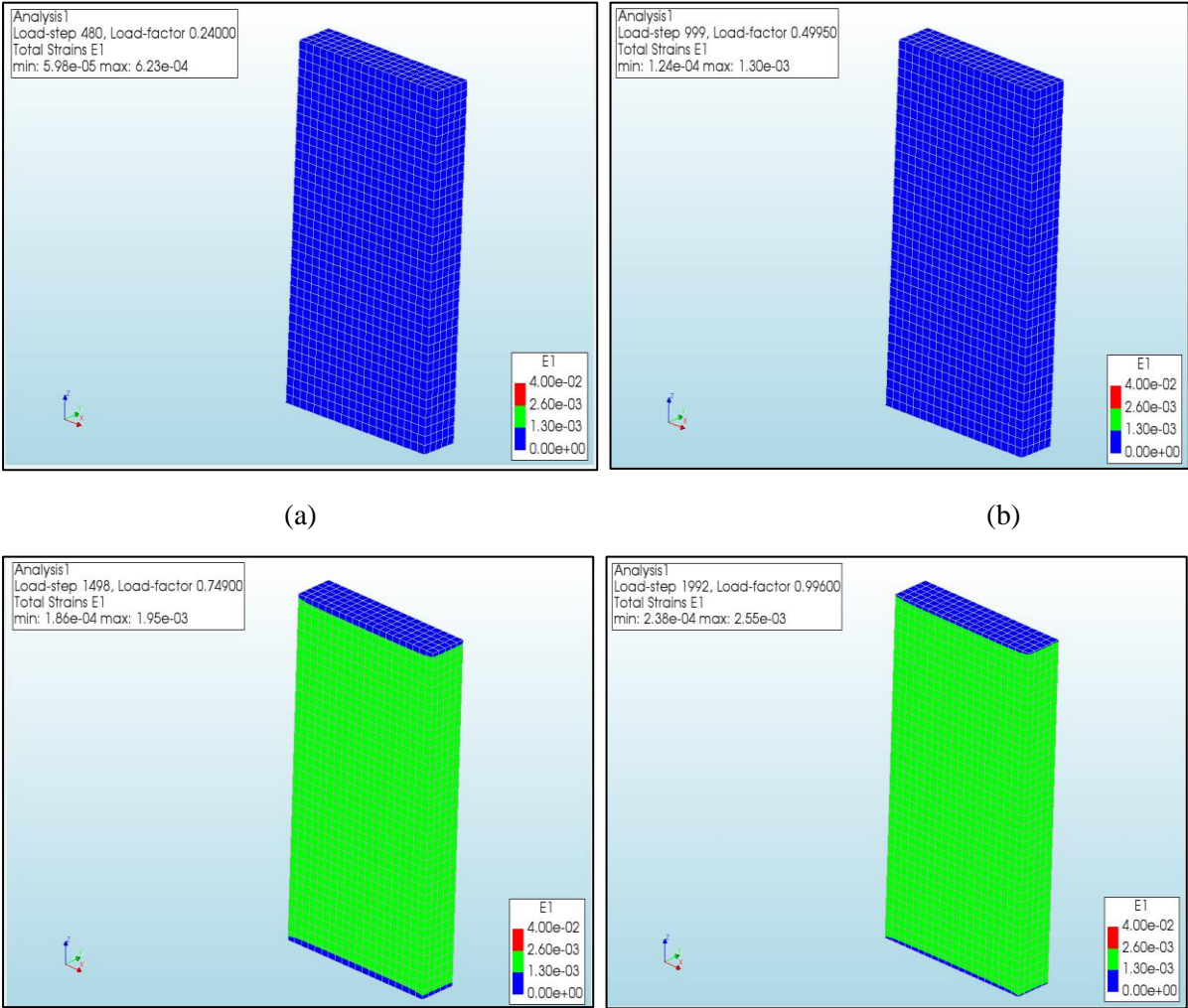
(c)   (d)

Figure B.7. Progression of Principal Strain E1 in the specimen.

The evolution of principal strain E1 in the specimen during the analysis is shown in **Figs. 37(a – d)**. From **Figure B.6**, it can be said that there is an onset of cracking in the brick if the principal strain value exceeds 0.0026. During the analysis, this value was not exceeded. Hence it can be concluded that the cracking failure of bricks did not occur.

B.5 Analysis for cracking of mortar interface

In this section, the cracking of the mortar interface is discussed. The constitutive law for the behaviour of a mortar element under tensile stress is shown in **Figure B.8**.



Figure B.8. Behaviour of mortar element under tensile stress for Model 2.

The point (0.007143,0.2) indicates the value of relative displacement at peak mortar tensile strength. The value of relative displacement was calculated by dividing the tensile strength of mortar by the normal stiffness modulus.
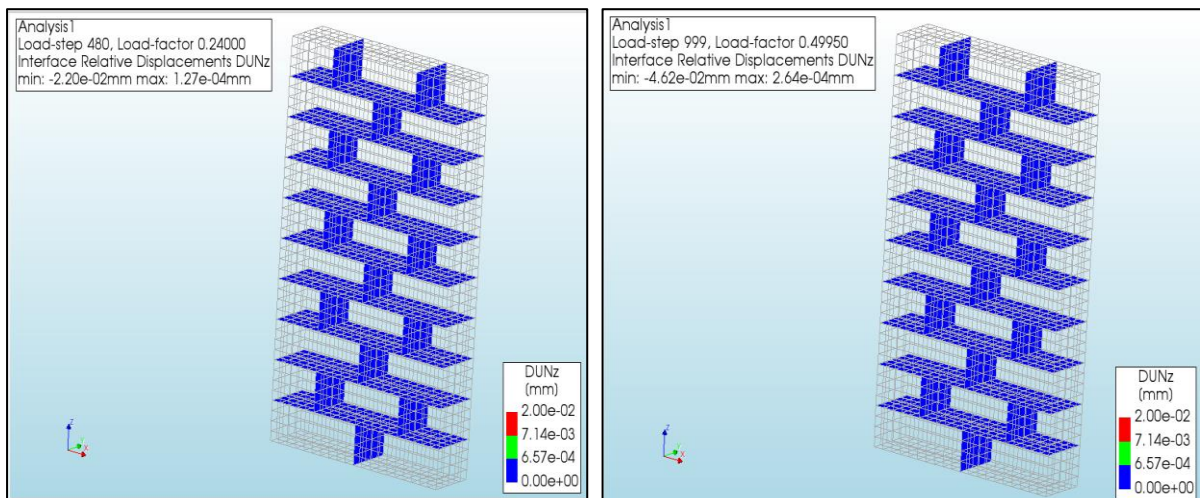
Figure B.9. Progression of relative displacement DUNz (+ve) in the specimen

The evolution of DUNz (+ve) in the specimen during the analysis is shown in **Figs. B.9(a – d)**. From **Fig. B.8**, it can be said that there is an onset of cracking in the brick if the principal strain value exceeds 0.007143. During the analysis, this value was not exceeded. Hence it can be concluded that the cracking failure of bricks did not occur.

B.6 Analysis for crushing of mortar interface

In this section, the crushing of the mortar interface is discussed. The negative value of relative displacement was utilized to analyse the potential crushing of the mortar interface.

(a)   (b)
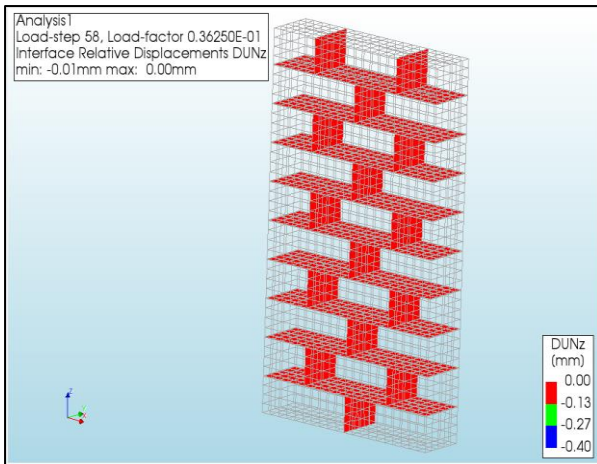
72

<center>(c)</center>

<center>(d)</center>
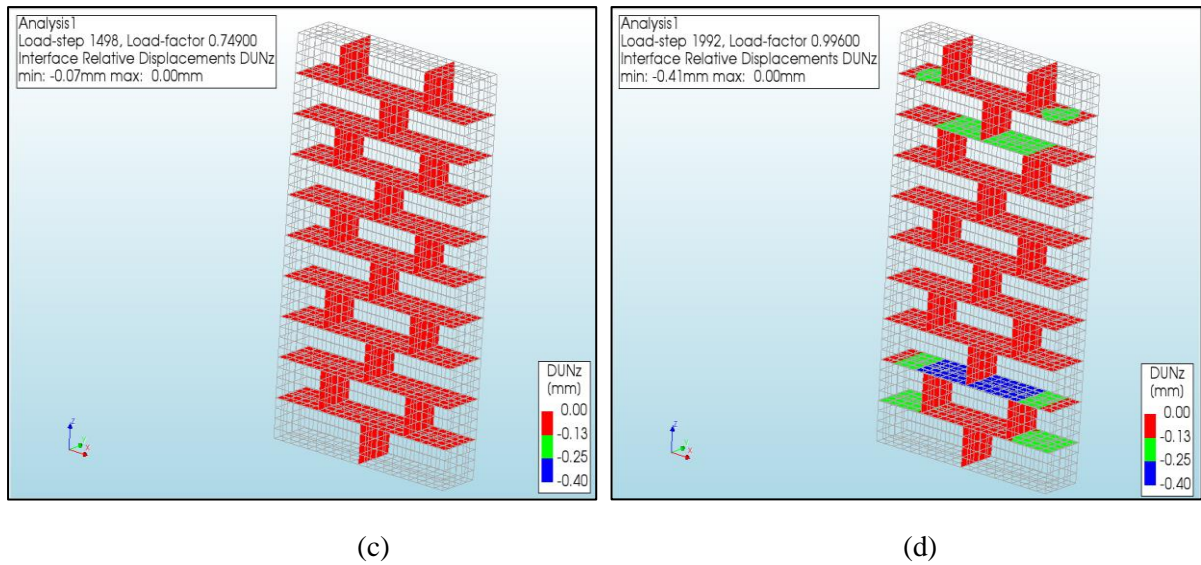
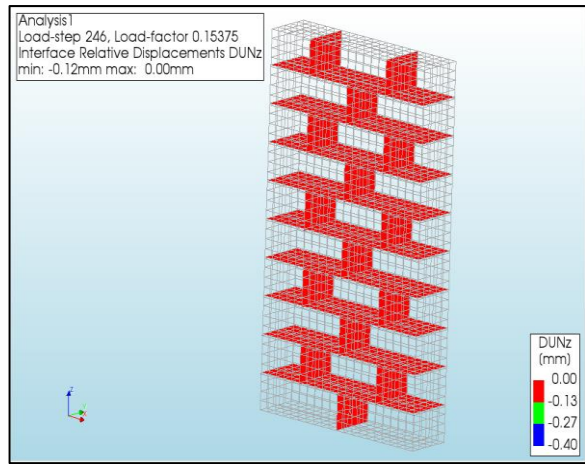**Figure B.10.** Progression of relative displacement DUNz (-ve)

The evolution of relative displacement DUNz (-ve) in the specimen during the analysis is shown in **Fig B.10(a − d)**. From **Table B.1**, it can be observed that the value of equivalent plastic relative displacement is 0.0125. This can be interpreted as the strain at peak load. To obtain the displacement, we multiply the strain by the thickness of the mortar interface. In the 1964th load step, the value of 0.125 is exceeded. Mortar crushing only occurred in bed joints, one at the top portion of the specimen and the other at the bottom portion of the specimen.

APPENDIX- C

In this section, the results of Model 3 have been discussed in detail.

C.1 Stress-Strain Plot of Model
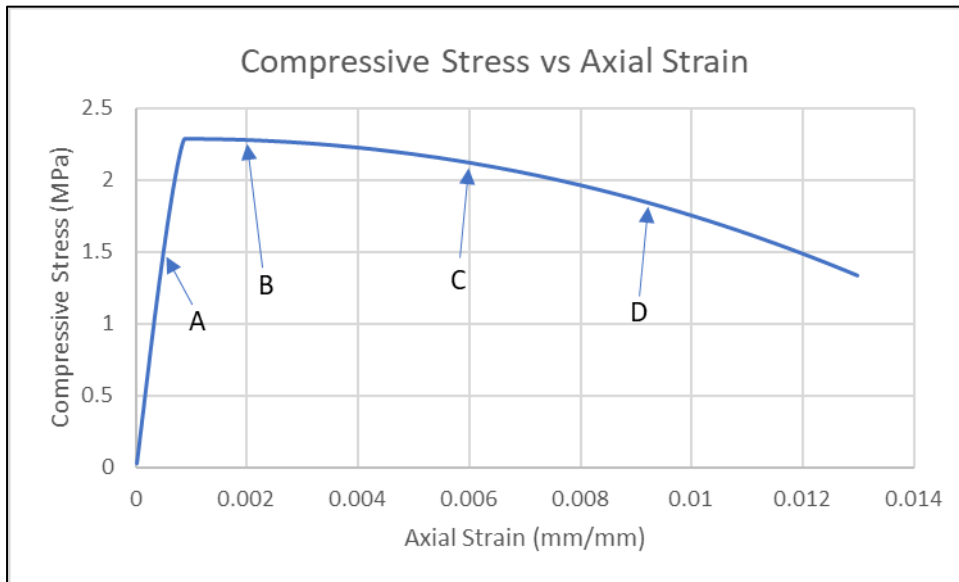
Figure C.1. Plot of compressive stress-axial strain along with specified load levels.

Fig. C.1. shows the plot of compressive stress-axial strain for Model 3. The load levels shown in the figure have been used to study the progression of potential failure mechanisms.

C.2 Analysis for cracking failure of brick

In this section, the cracking failure of a brick is discussed. The constitutive law for the behaviour of a brick element under tensile stress is shown in **Figure C.2**.
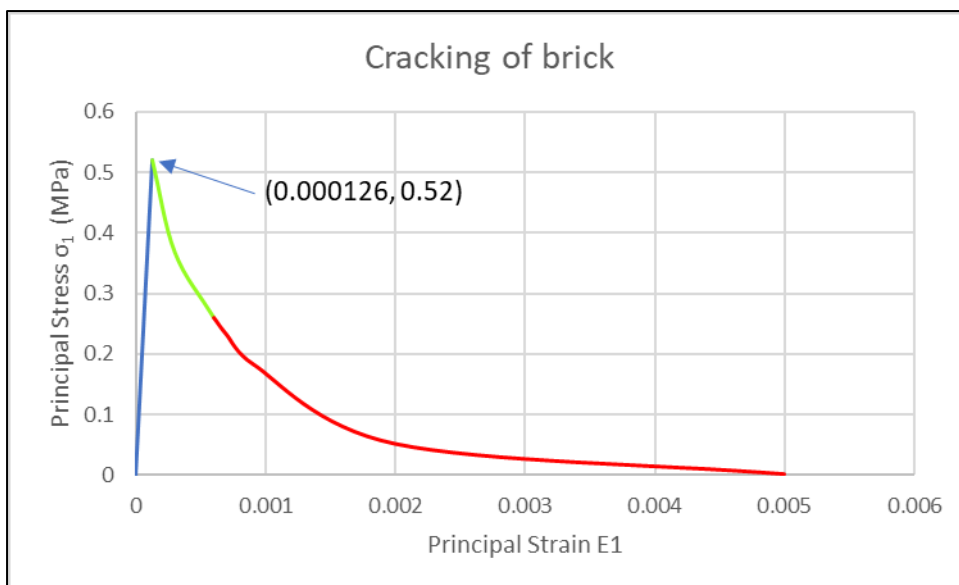
Figure C.2. Behaviour of a brick element of Model 5 under tensile stress.

The point (0.000126, 0.52) indicates the value of principal strain at peak brick tensile strength. The value of principal strain was calculated by dividing the tensile strength of brick by the Young's Modulus.

C.3 Analysis for cracking of mortar interface

In this section, the cracking of the mortar interface is discussed. The constitutive law for the behaviour of a mortar element under tensile stress is shown in **Fig. C.3**.
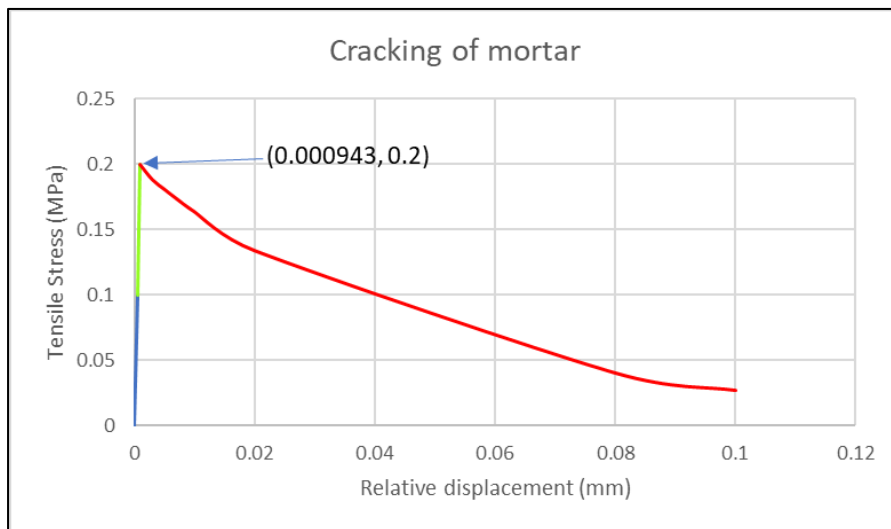
Figure C.3. Behaviour of mortar element under tensile stress.

The point (0.000943, 0.2) indicates the value of relative displacement at peak mortar tensile strength. The value of relative displacement was calculated by dividing the tensile strength of the mortar by the normal stiffness modulus. The positive value of relative displacement was utilized to analyse the potential cracking of the mortar interface.

(a)   (b)
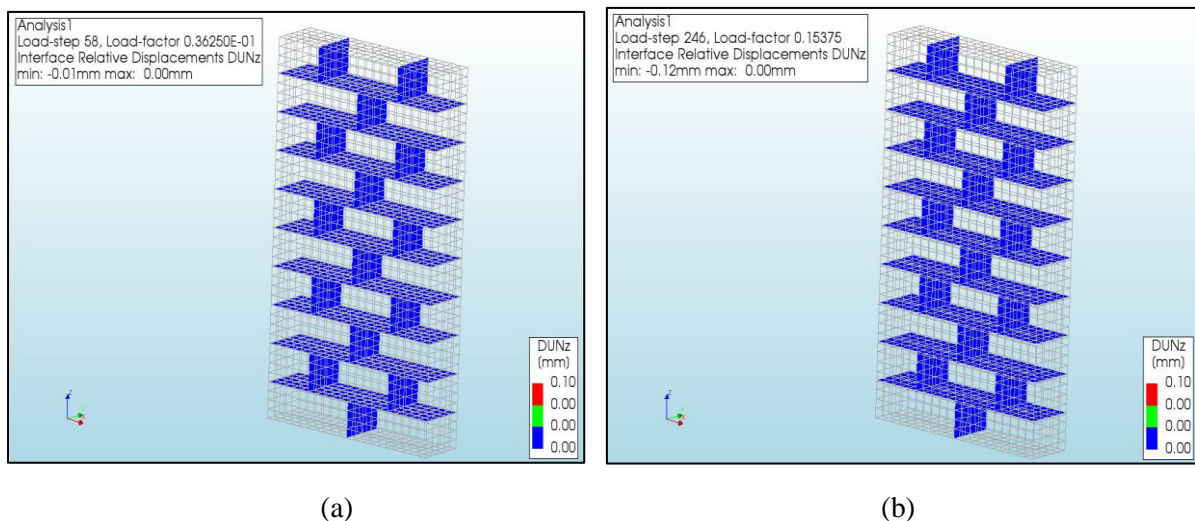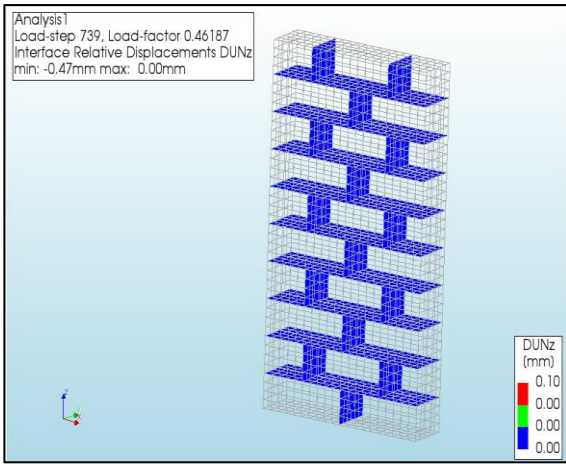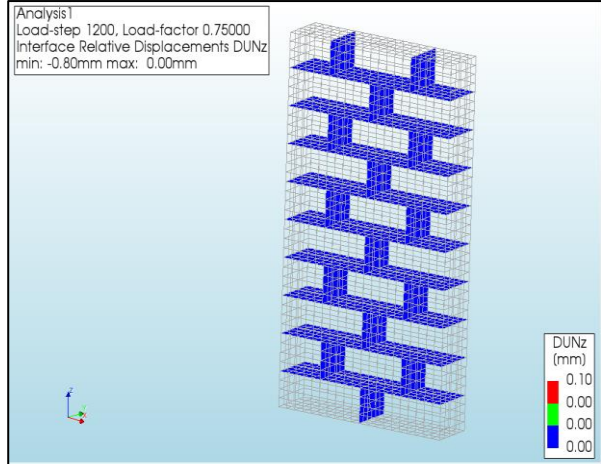
(c)   (d)

Figure C.4. Progression of relative displacement DUNz (+ ve)

The evolution of relative displacement DUNz (+ve) in the specimen during the analysis is shown in **Figs. C.4 (a – d)**. From **Fig. C.3,** it can be said that there is an onset of cracking in the mortar interface if the relative displacement value exceeds 0.000943. This value was not exceeded during the analysis. Hence it can be concluded that the cracking failure of mortar did not occur in the specimen.

C.4 Analysis for crushing of mortar interface

In this section, the crushing of the mortar interface is discussed. The negative value of relative displacement was utilized to analyse the potential crushing of the mortar interface.

(a)   (b)

<div align="center">(c)</div>

<div align="center">(d)</div>
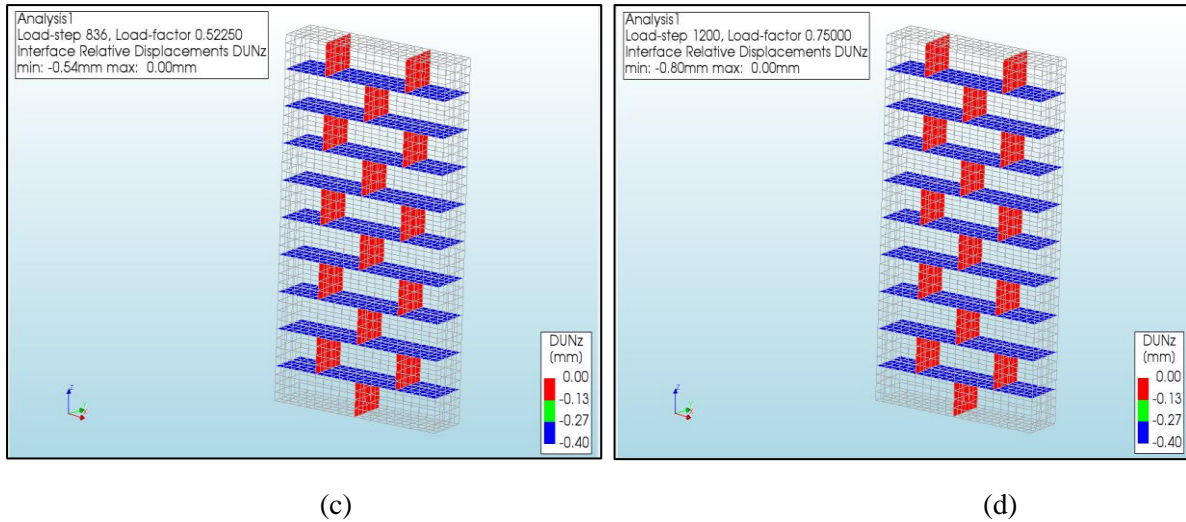
Figure C.5: Progression of DUNz (-ve)

The evolution of relative displacement DUNz (-ve) in the specimen during the analysis is shown in **Figs. C.5 (a – d)**. From **Table C.1**, it can be observed that the value of equivalent plastic relative displacement is 0.0125. This can be interpreted as the strain at peak compressive stress of mortar. To obtain the relative displacement, the strain is multiplied by the thickness of the mortar interface. In the 204th load step, the value of 0.125 is exceeded. It can also be observed from **Figs. C.5 (c and d)** that crushing failure of mortar occurred only in the bed joints.

C.5 Analysis for crushing of brick

This section discusses the crushing failure of a brick. The peak compressive strength of brick chosen for this study is 5.1 MPa. If this value of principal stress S3 is exceeded, it can be inferred that the brick has undergone crushing.

<div align="center">(a)</div>

<div align="center">(b)</div>

(c)   (d)
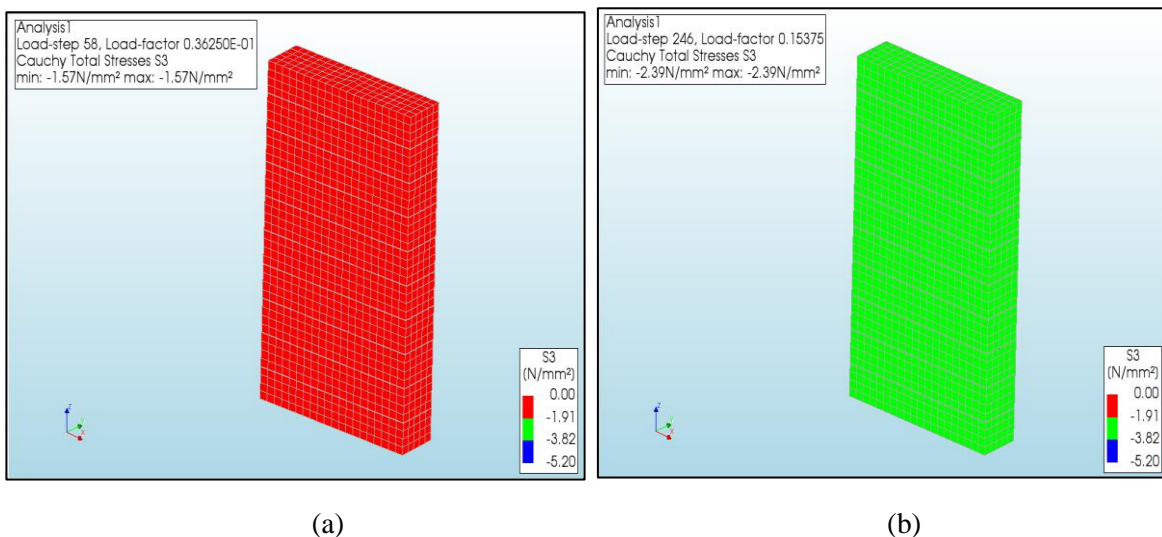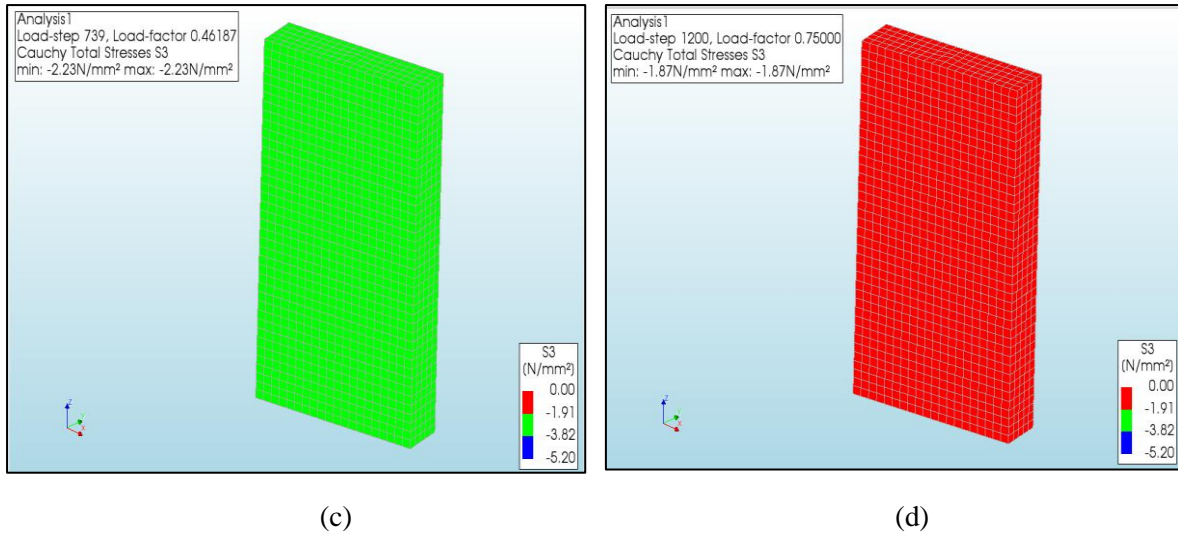
Figure C.6. Progression of Principal Stress S3

The evolution of principal stress S3 in the specimen during the analysis is shown in **Figs. C.6 (a – d)**. From **Figs. C.6 (a-d)**, it can be observed that the principal stress S3 doesn't exceed the compressive strength of a brick. Hence crushing failure of brick did not occur.

C.6 Analysis for shear failure of mortar interface

In this section, the shear failure of mortar is discussed. The constitutive law for the behaviour of a mortar element under shear stress is shown in **Figure C.7**.
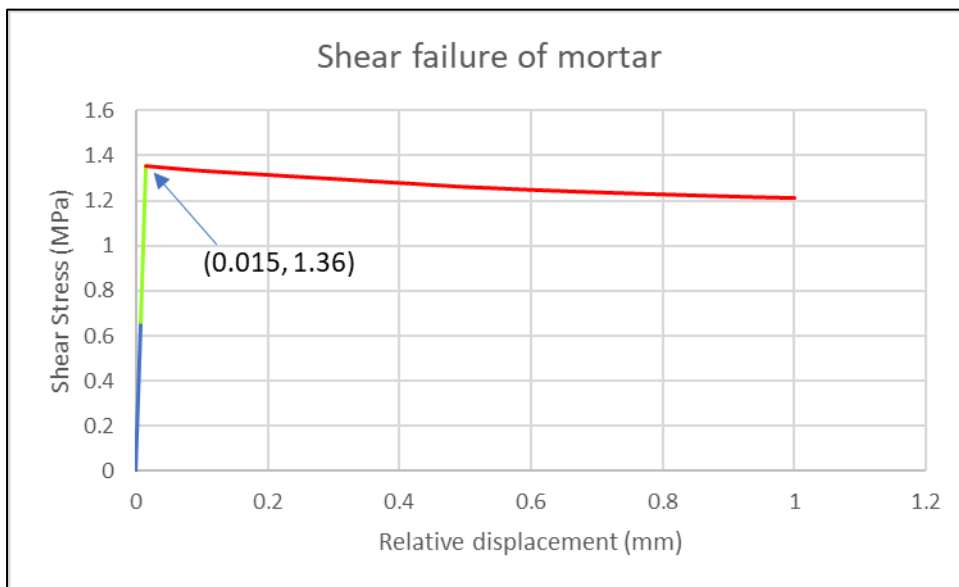
Figure C.7. Behaviour of mortar element under shear stress.

The point (0.015, 1.36) indicates the value of relative displacement at peak mortar shear strength. The value of relative displacement was calculated by dividing the shear strength of the mortar by the shear stiffness modulus.
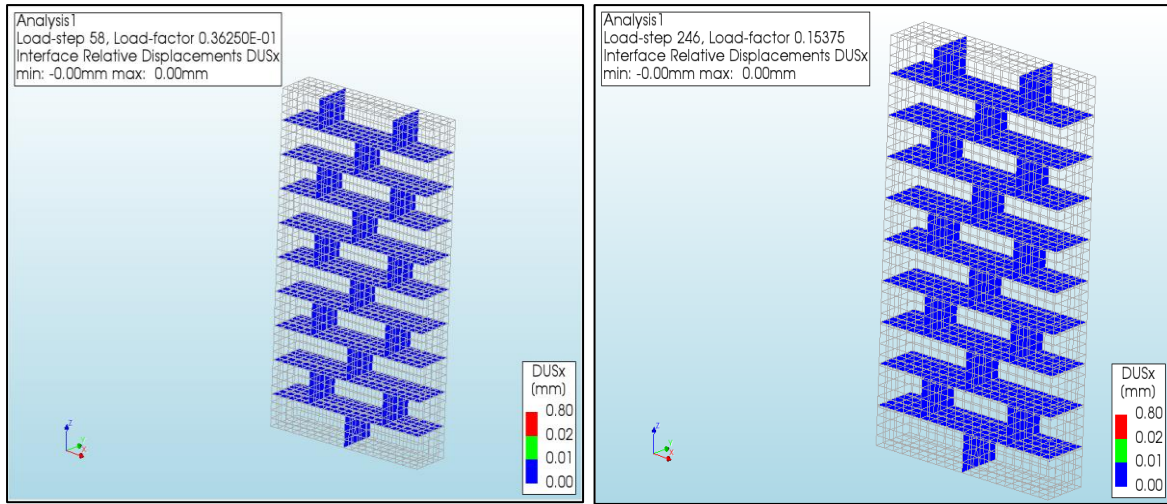
(a)   (b)
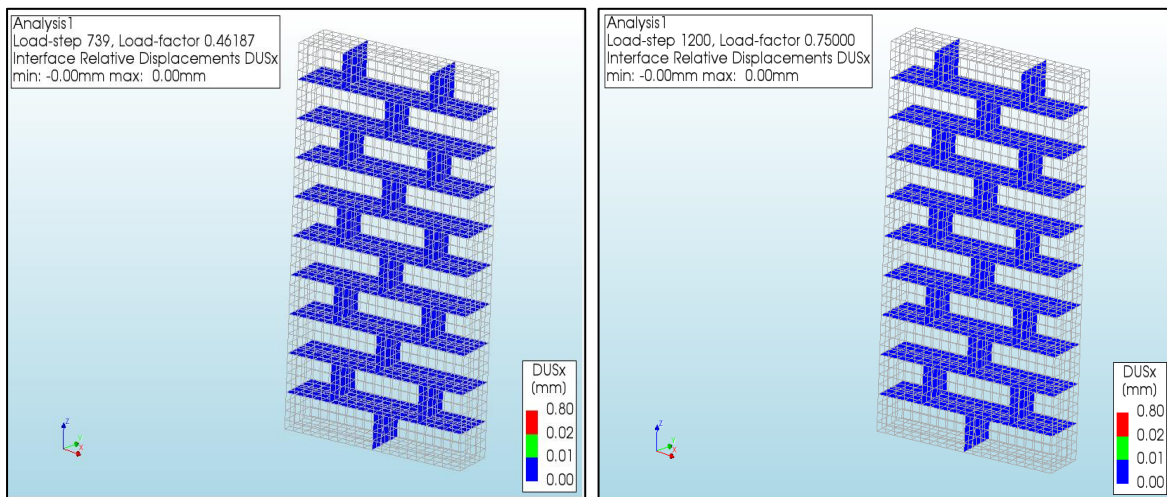
(c)   (d)

Figure C.8. Progression of relative displacement DUSx

(a)   (b)

(c)   (d)
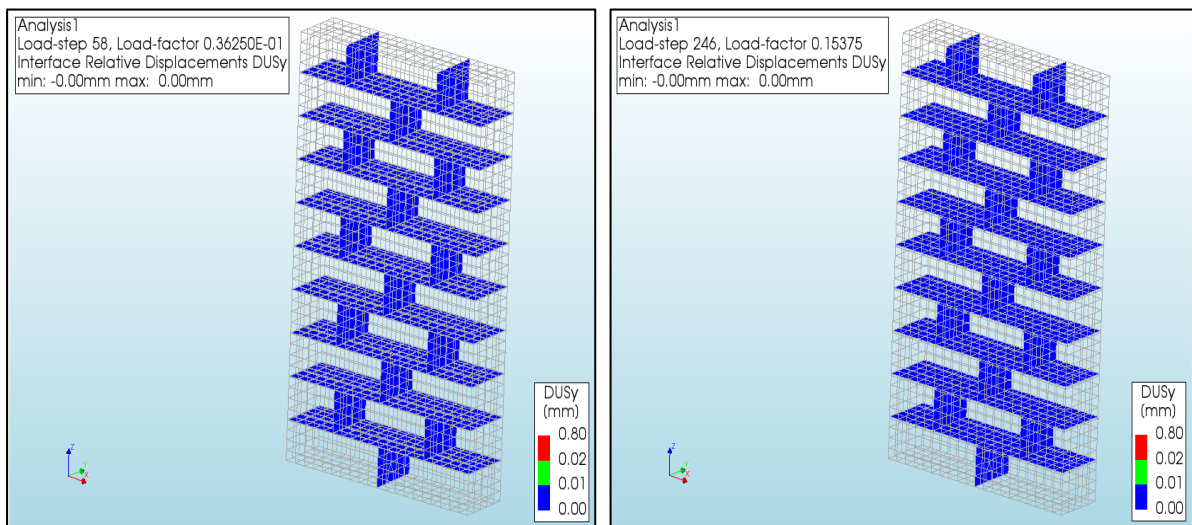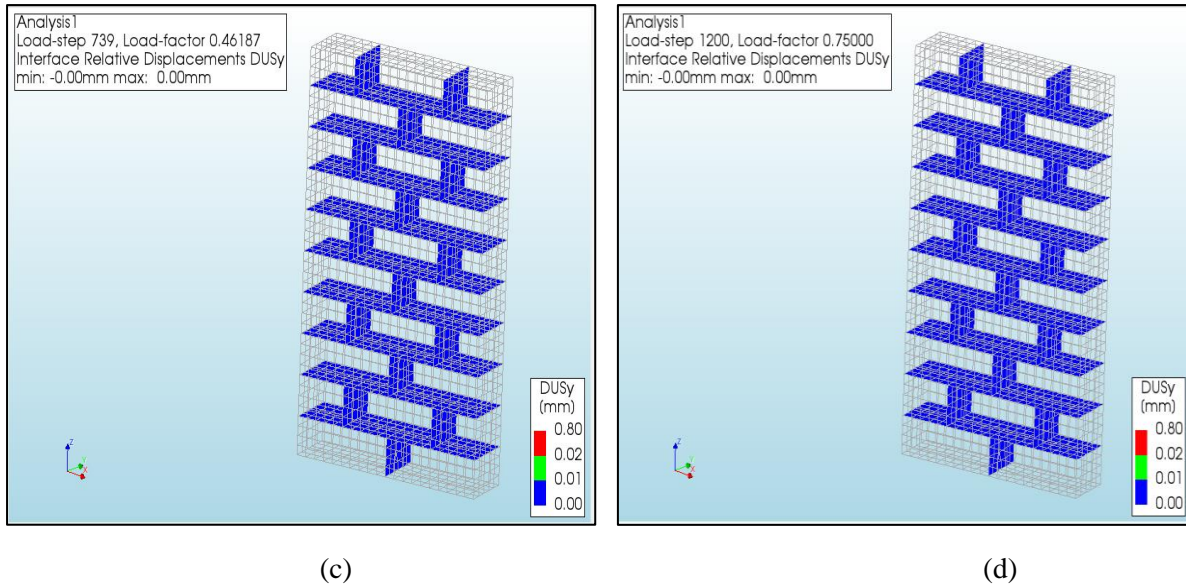
Figure C.9. Progression of relative displacement DUSy

The evolution of relative displacement DUSx in the specimen during the analysis is shown in **Figs. C.8 (a – d)** while the evolution of relative displacement DUSy is shown in **Figs. C.9 (a - d)**. From both **Figs. C.8 (a – d)** and **Figs. C.9 (a – d)**, it can be noted that the critical value 0.015, which indicates the onset of shear failure, was not exceeded. Hence it can be concluded that the shear failure of the mortar interface did not take place.

'

APPENDIX – D

In this section, the results of Model 4 are discussed in detail.

Table. List of input parameters in DIANA, corresponding values and references used for this model.

Parameter	Value	Reference
BRICK		
Young's Modulus	200 N/mm^2	Zahra (2021)
Poisson's ratio	0.18	Zahra (2021)
DISCRETE CRACK		
Normal Stiffness Modulus	10000 N/mm^3	$k_n = 1000 \dfrac{E}{l}$
Shear Stiffness Modulus - x	4237 N/mm^3	$k_t = 1000 \dfrac{G}{l}$
Shear Stiffness Modulus - y	4237 N/mm^3	$k_t = 1000 \dfrac{G}{l}$
Tensile Strength	0.52 MPa	
Mode 1 tension softening criterion	Linear	
Fracture energy	0.11 N/mm	
Mode 1 unloading/reloading model	Secant	
Mode 2 shear retention for crack development	Zero Shear Traction	
MORTAR INTERFACE		
Normal stiffness modulus	28 N/mm^3	Zahra (2021)
Shear stiffness modulus-x	32 N/mm^3	Zahra (2021)
Shear stiffness modulus-y	32 N/mm^3	Zahra (2021)
Tensile strength	0.2 N/mm^2	Thamboo (2020); $f_t = 0.67 \times$ Flexural strength
Fracture energy	0.01 N/mm	Chang (2021), Rots et al. (1997): $G_{fIm} = 0.05 \times f_{tm}$
Cohesion	0.2 N/mm^2	Chang (2021), Milani and Lourenco (2013); $c_0 = f_{tm}$
Friction angle	0.64 rad	Jafari (2021)
Dilatancy angle	0.54 rad	Zahra (2021)
Residual friction angle	0.64 rad	Zahra (2021)
Confining normal stress	-1.57 N/mm^2	Van Zijl (2004)
Exponential degradation coefficient	5.6	Van Zijl (2004)
Parameter a	-0.09 mm	De Villiers (2019), Van Zijl (2004)
Parameter b	0.006 N/mm	De Villiers (2019), Van Zijl (2004)
Compressive strength	2.4 N/mm^2	Thamboo (2020), obtained from compression test of mortar prism as per EN 1015-11
Factor Cs	0.8	Assumption
Compressive fracture energy	2.5 N/mm	Jafari (2021); $= 250 \times G_{fIm}$
Equivalent plastic relative displacement	0.0125 mm	De Villiers (2019)
CONVERGENCE METHOD		
Load steps	1600	

Maximum number of iterations	1000	
Method	Newton Raphson	
Type	Regular	
Energy Convergence tolerance	0.01	
Displacement Convergence tolerance	NA	
Force convergence tolerance	0.01	
Satisfied simultaneously?	No	

D.1 Stress-Strain plot of model
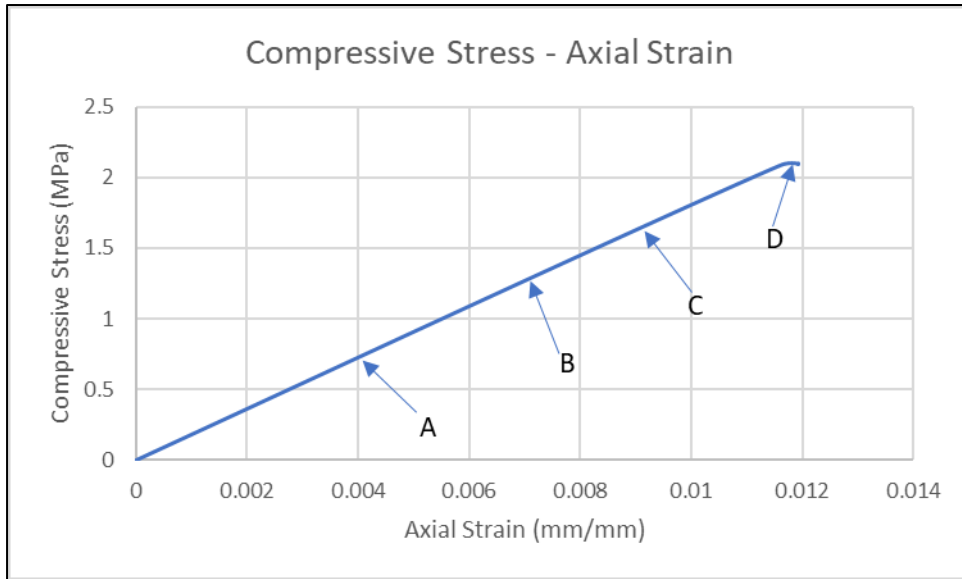
Figure D.1. Plot of compressive stress-axial strain along with specified load levels.

Figure. shows the plot of compressive stress-axial strain for Model 3. The load levels shown in the figure have been used to study the progression of potential failure mechanisms.

D.2 Analysis for shear failure of mortar interface

In this section, the shear failure of mortar is discussed. The constitutive law for the behaviour of a mortar element under shear stress is shown in **Figure D.2**.
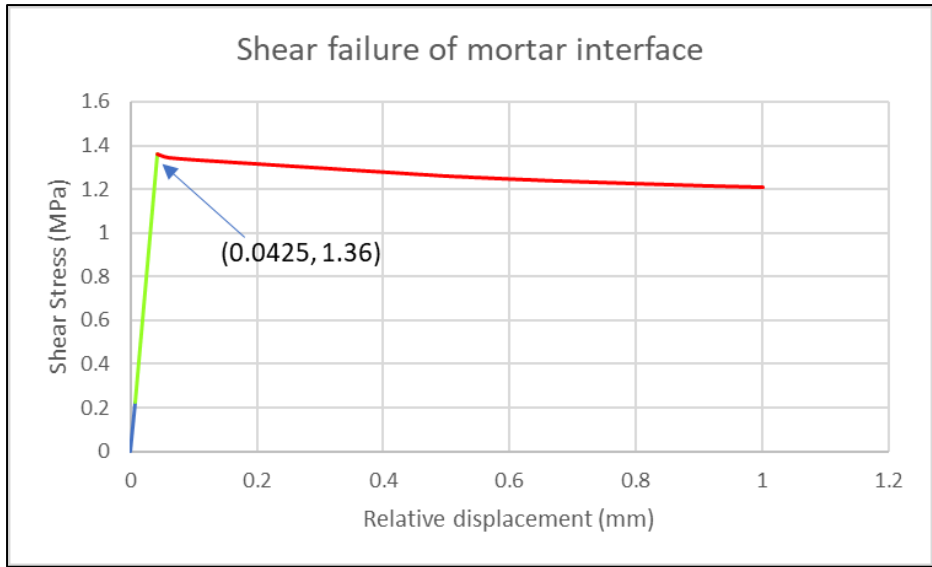
Figure D.2. Behaviour of mortar element under shear stress.

The point (0.0425, 1.36) indicates the value of relative displacement at peak mortar shear strength. The value of relative displacement was calculated by dividing the shear strength of the mortar by the shear stiffness modulus.
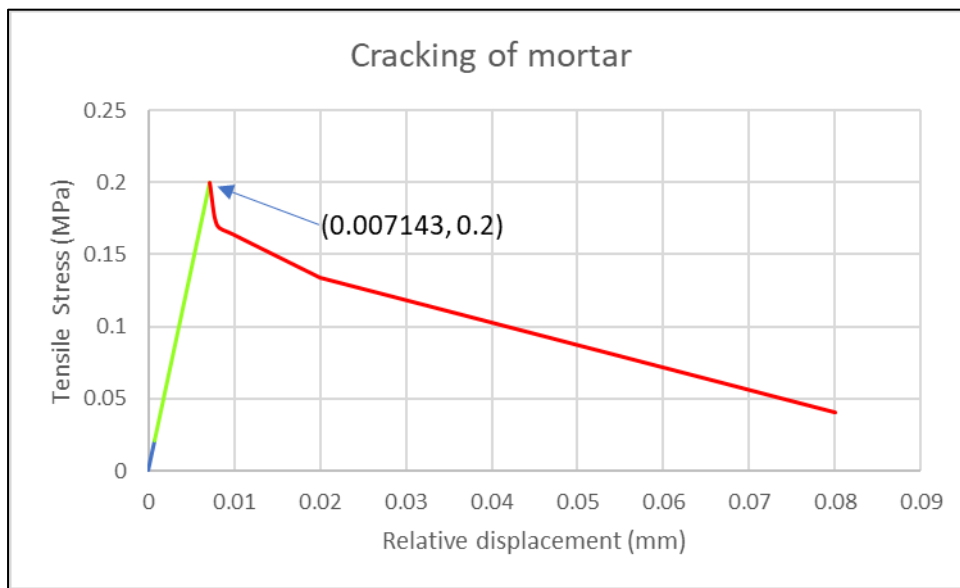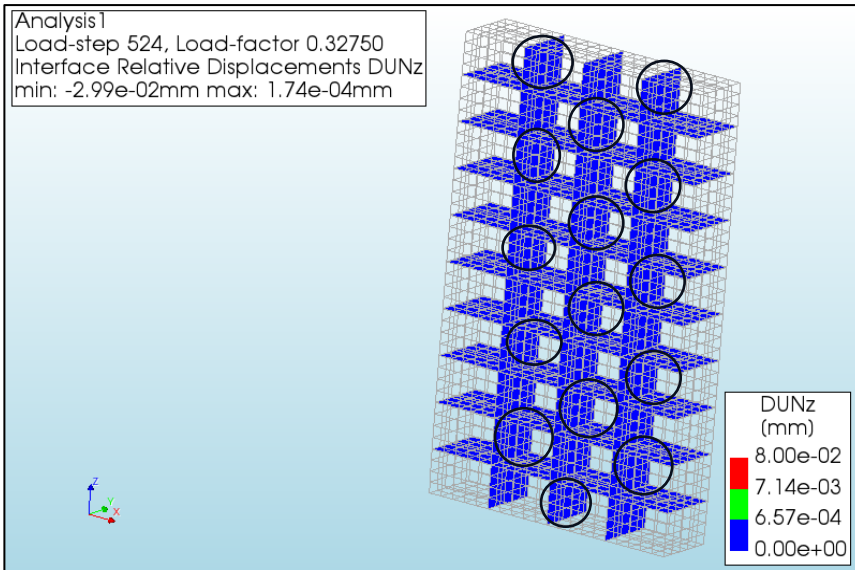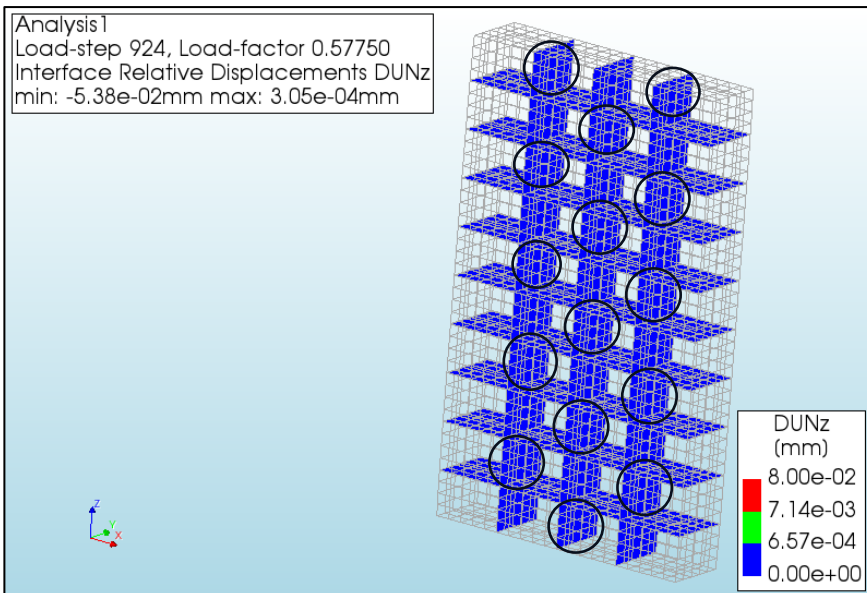

(a)

(b)

(c)

(d)
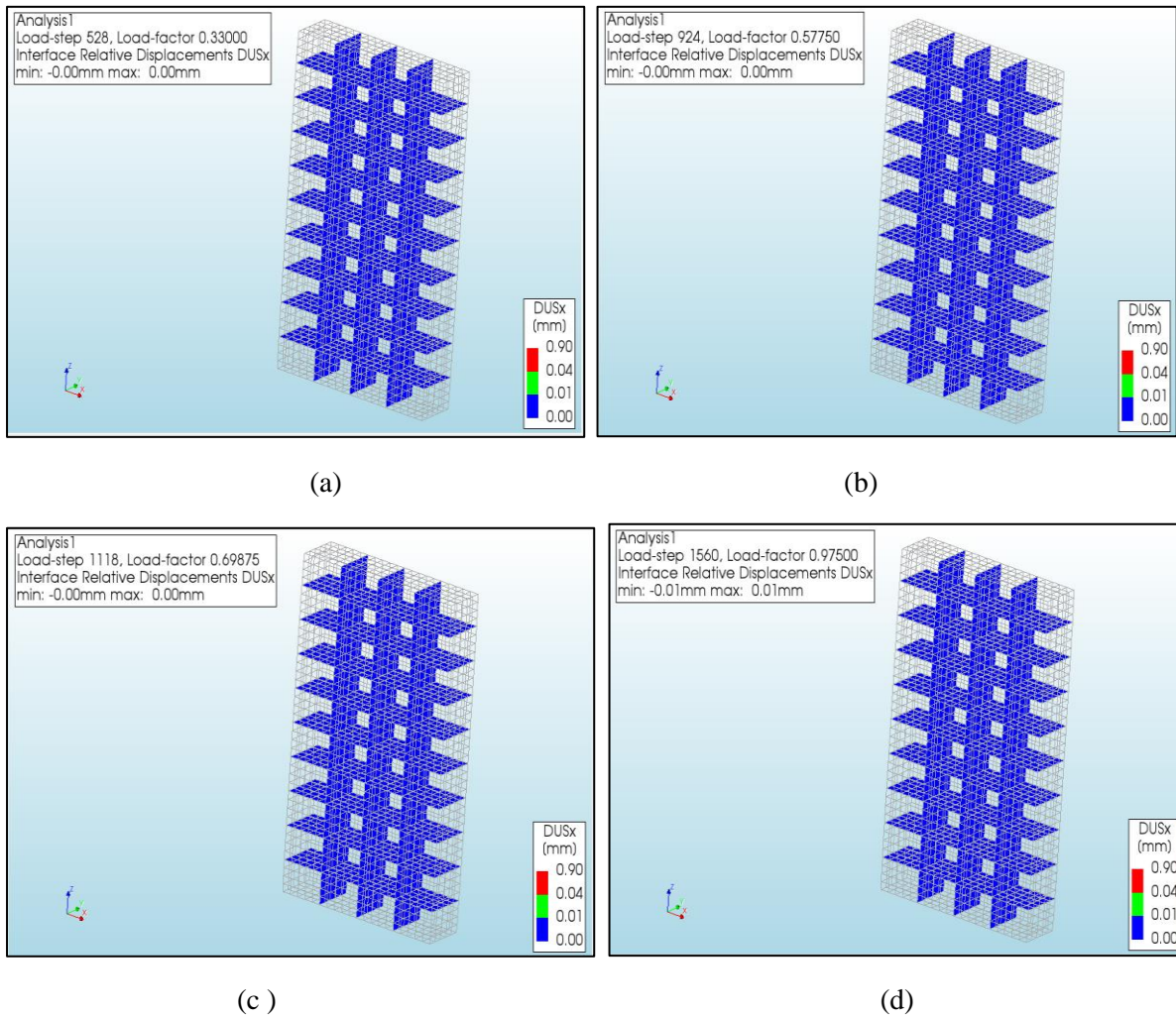
Figure D.3. Progression of Relative displacement DUSx

(a)

(b)

(c)

(d)
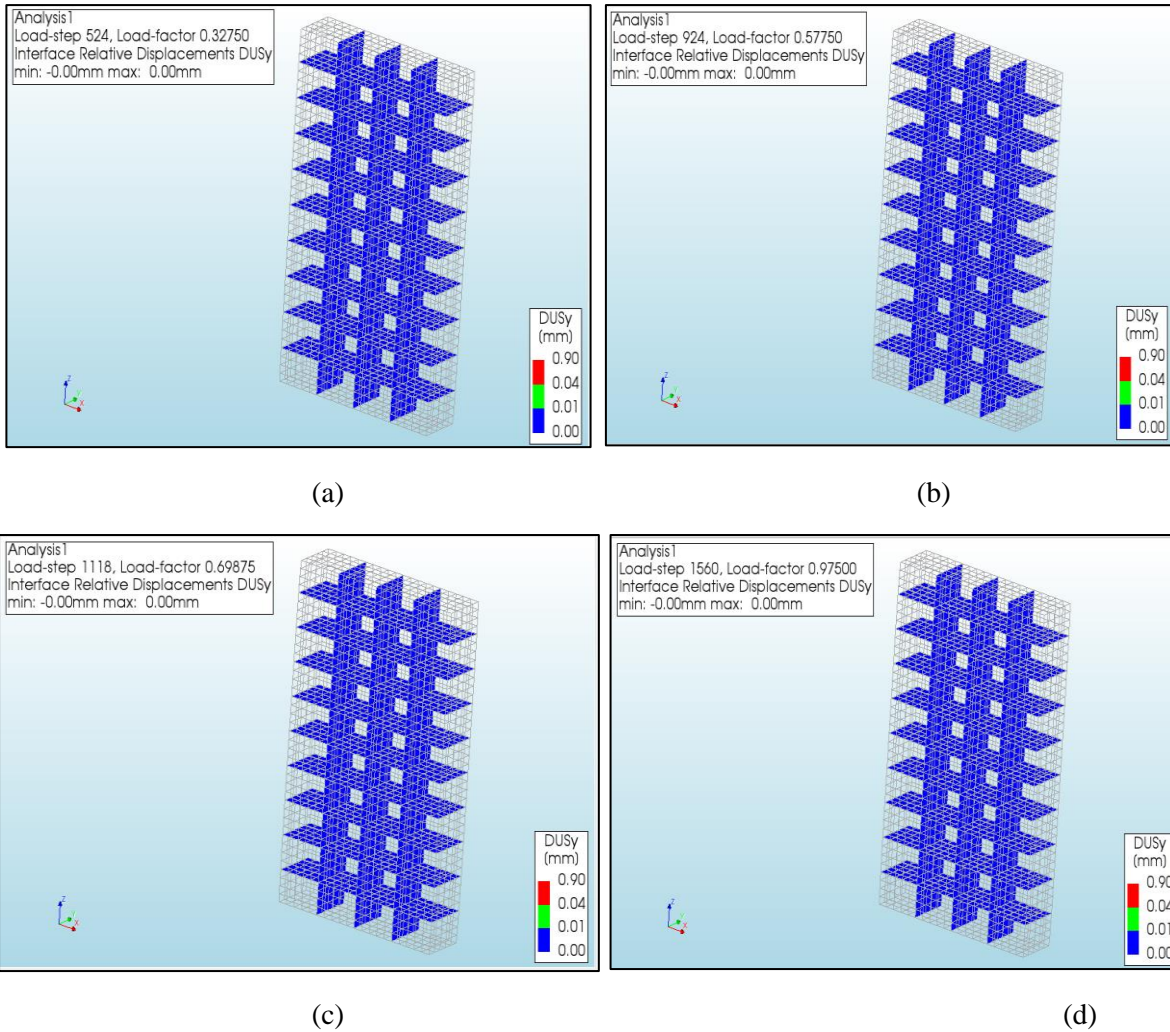
Figure D.4. Progression of relative displacement DUSy

The evolution of relative displacement DUSx in the specimen during the analysis is shown in **Figs. D.3 (a – d)** while the evolution of relative displacement DUSy is shown in **Figs. D.4 (a - d)**. From both **Figs. D.3 (a – d)** and **Figs. D.4 (a – d)**, it can be noted that the critical value 0.0425, which indicates the onset of shear failure, was not exceeded. Hence it can be concluded that the shear failure of the specimen did not take place.

D.3 Analysis for crushing of brick

This section discusses the crushing failure of a brick. As per **Table D.1** , The peak compressive strength of the brick is 5.1 MPa. If principal stress S3 exceeds 5.1 MPa, it can be inferred that the brick has undergone crushing failure.

(a)   (b)

(c)   (d)
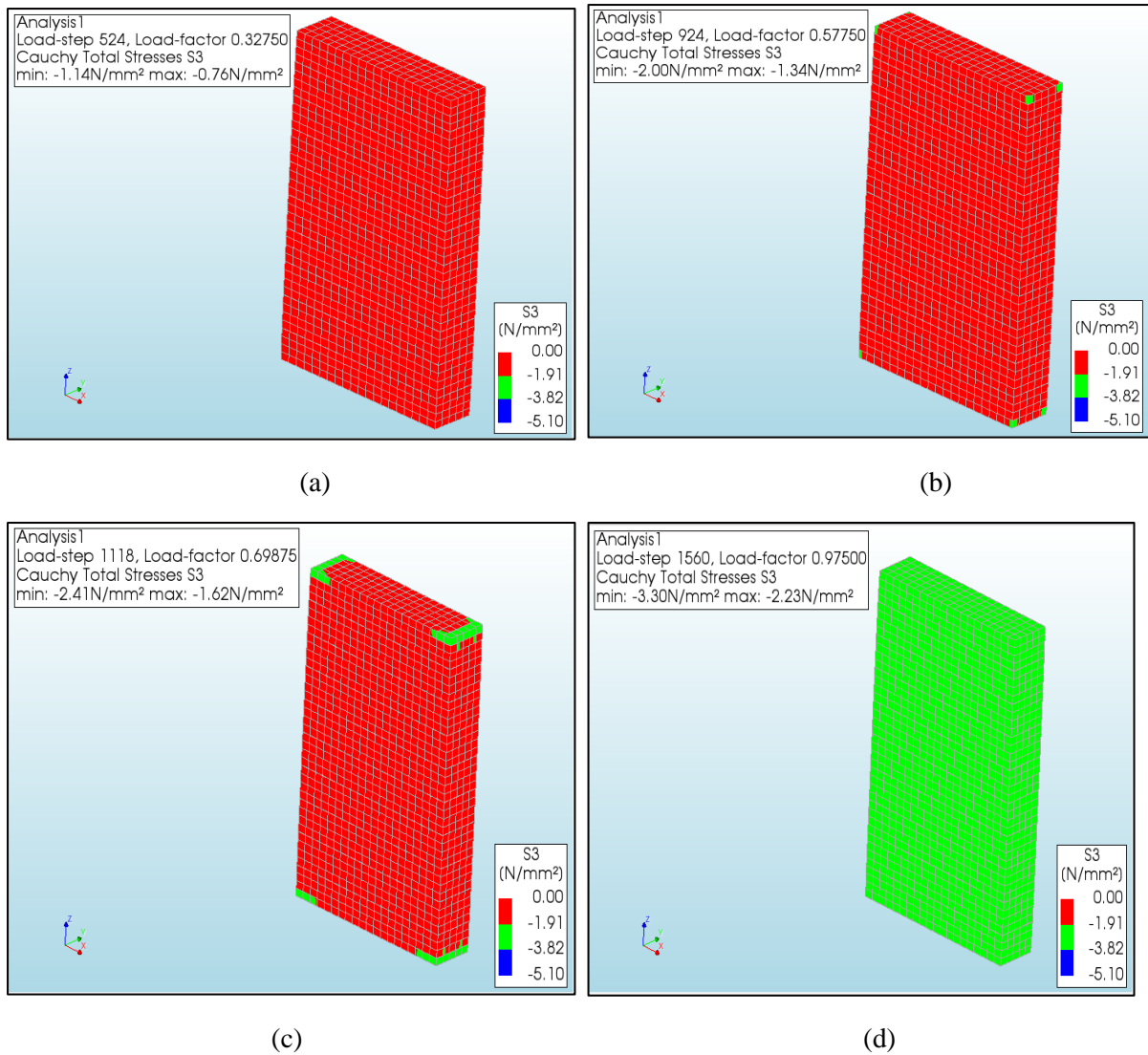
Figure D.5. Progression of Principal Stress S3 in the specimen.

From **Figs. D.5 (a-d)**, we can observe that peak compressive strength was not exceeded. Hence crushing failure of the brick did not take place.

D.4 Analysis for cracking failure of brick

In this section, the cracking failure of brick is discussed. The constitutive law for the behaviour of a brick element under tensile stress is shown in **Figure 82**.
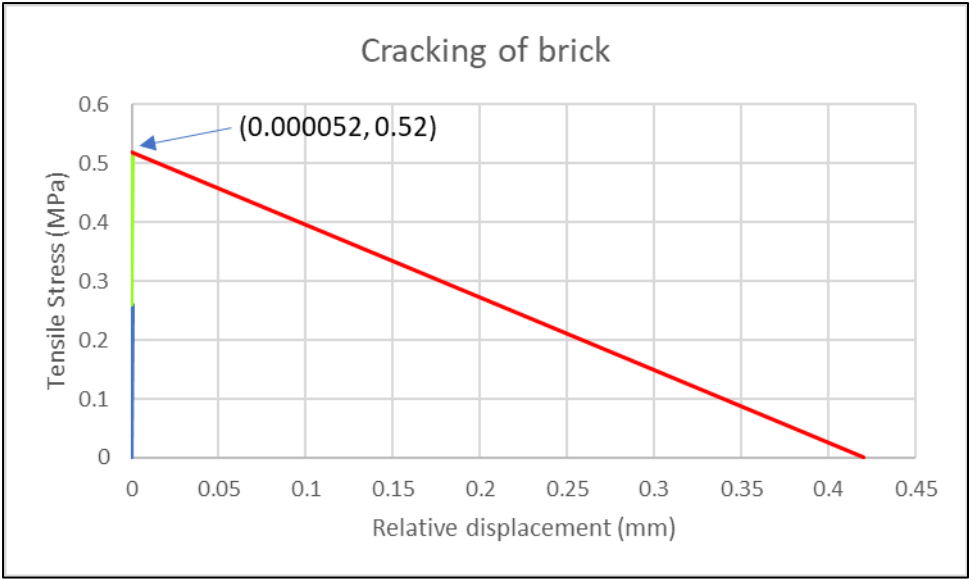
**Figure D.6.** Behaviour of discrete crack under tensile stress.

The point (0.000052, 0.52) indicates the value of relative displacement at the tensile strength of the brick. The value of relative displacement was calculated by dividing the tensile strength of the brick by the normal stiffness modulus of the crack.
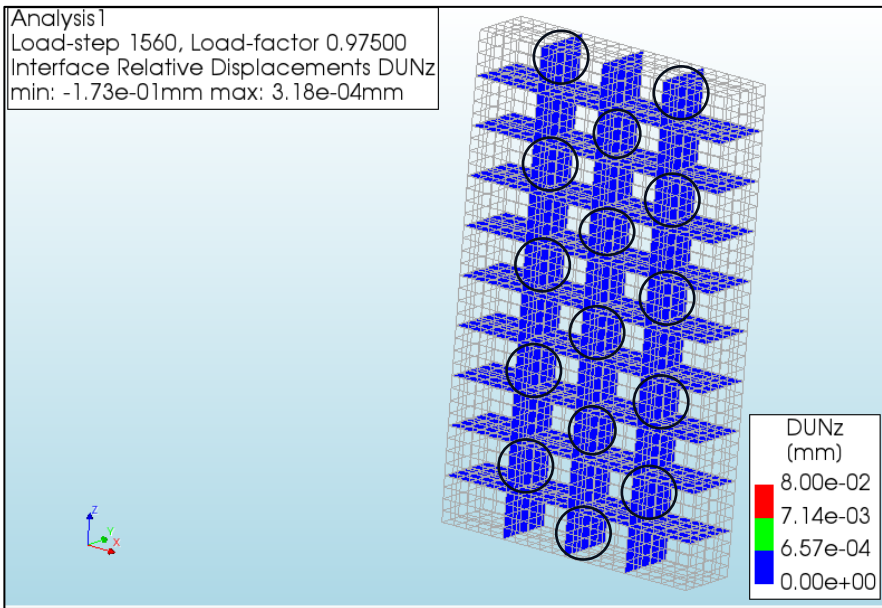

(a)

(b)

(c)

87
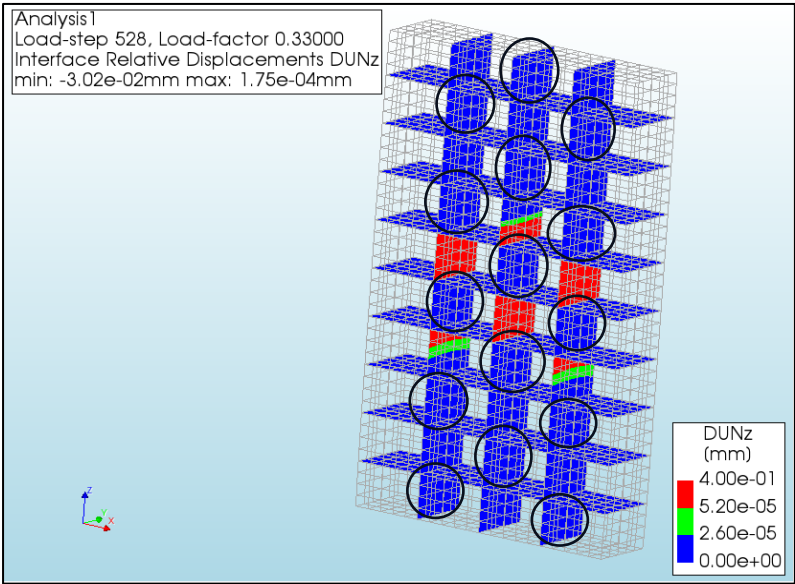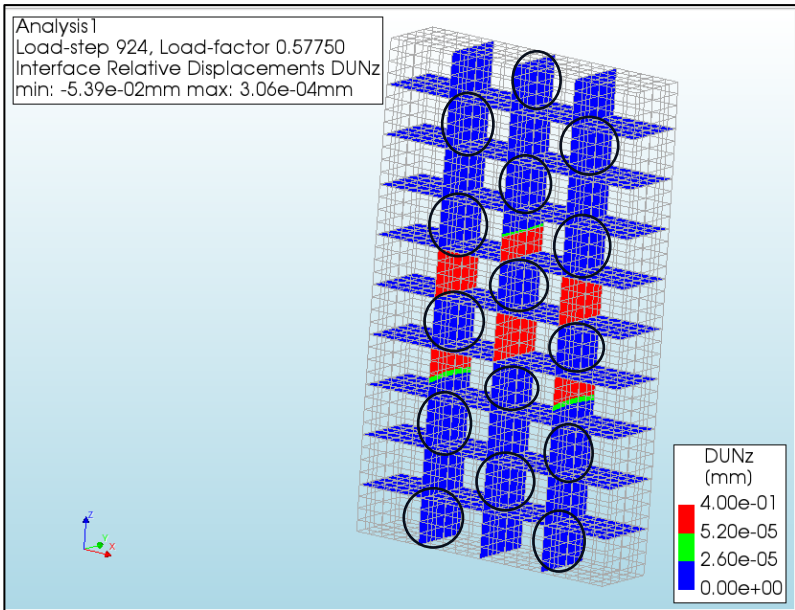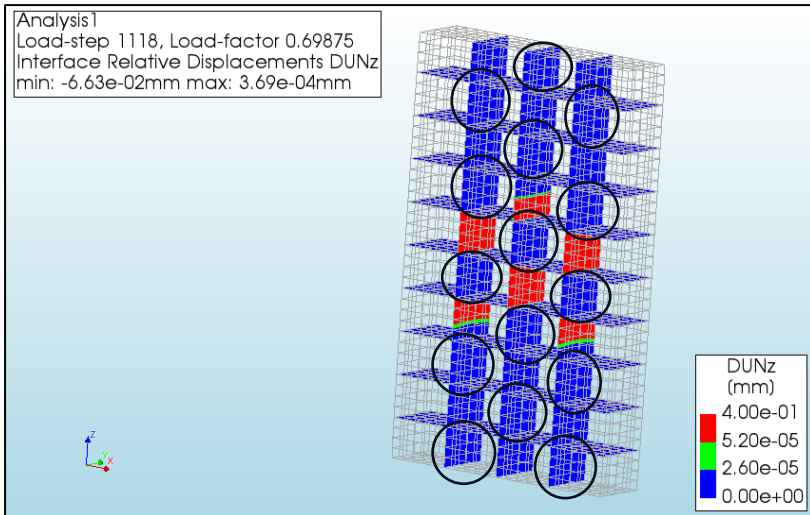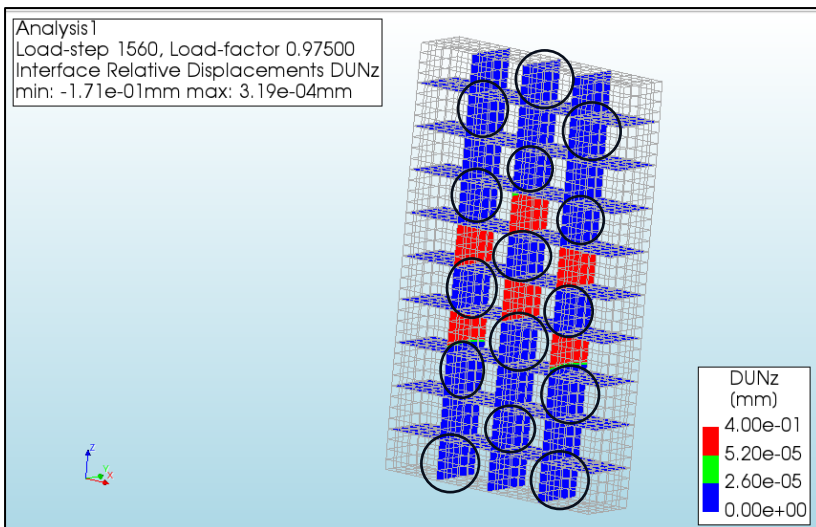
Figure D.7. Progression of relative displacement DUNz (+ ve) in the specimen. [black circles indicate the location of the potential discrete crack]

The evolution of relative displacement DUNz (+ve) in the specimen during the analysis is shown in **Figs. D.7 (a – d)**. From **Table D.6**, it can be said that there is an onset of cracking in the brick if the principal strain value exceeds 0.000052. During the analysis, this value was not exceeded in the location of the potential discrete cracks. Hence it can be concluded that the cracking failure of bricks did not occur.

D.5 Analysis of cracking of mortar interface

In this section, the cracking of mortar interfaces is discussed. The constitutive law for the behaviour of a mortar element under tensile stress is shown in **Figure D.8**.

Figure D.8. Behaviour of a mortar element under tensile stress.

The point (0.007143, 0.2) indicates the value of relative displacement at tensile strength of mortar. The value of relative displacement was calculated by dividing the tensile strength of the mortar by the normal stiffness modulus.

(a)

(b)
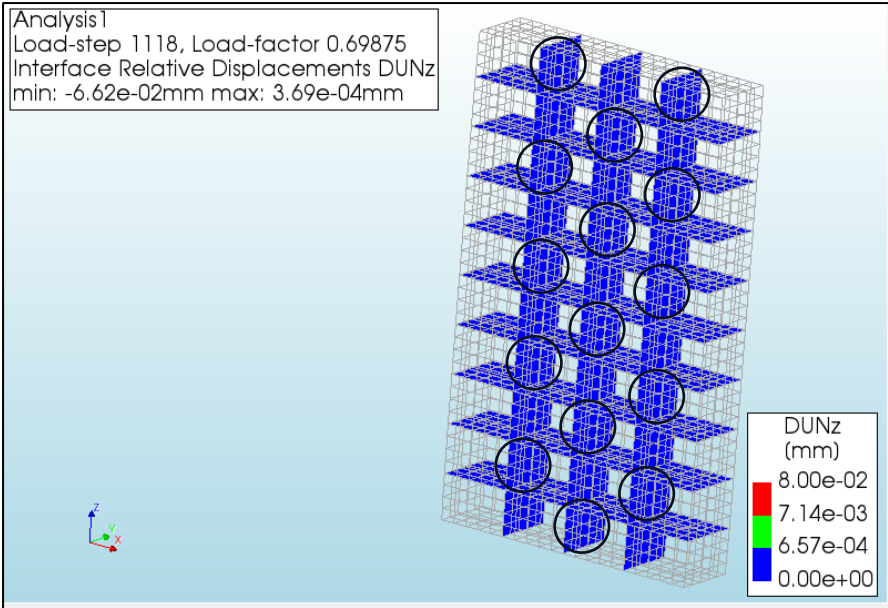
(c)

(d)

Figure D.9. Progression of relative displacement DUNz (+ve). [black circles indicate the location of mortar interface]

The evolution of DUNz in the specimen during the analysis is shown in **Figs. D.9 (a – d)**. From **Fig. D.8**, it can be said that there is an onset of cracking in the mortar interface if the principal strain value exceeds 0.007143. This value was not exceeded during the analysis. Hence it can be concluded that cracking failure of mortar did not take place.

D.6 Analysis of crushing of mortar interface

In this section, the crushing of the mortar interface is discussed. The negative value of relative displacement was utilized to analyse the potential crushing of the mortar interface.

(a)

(b)

(c)

(d)
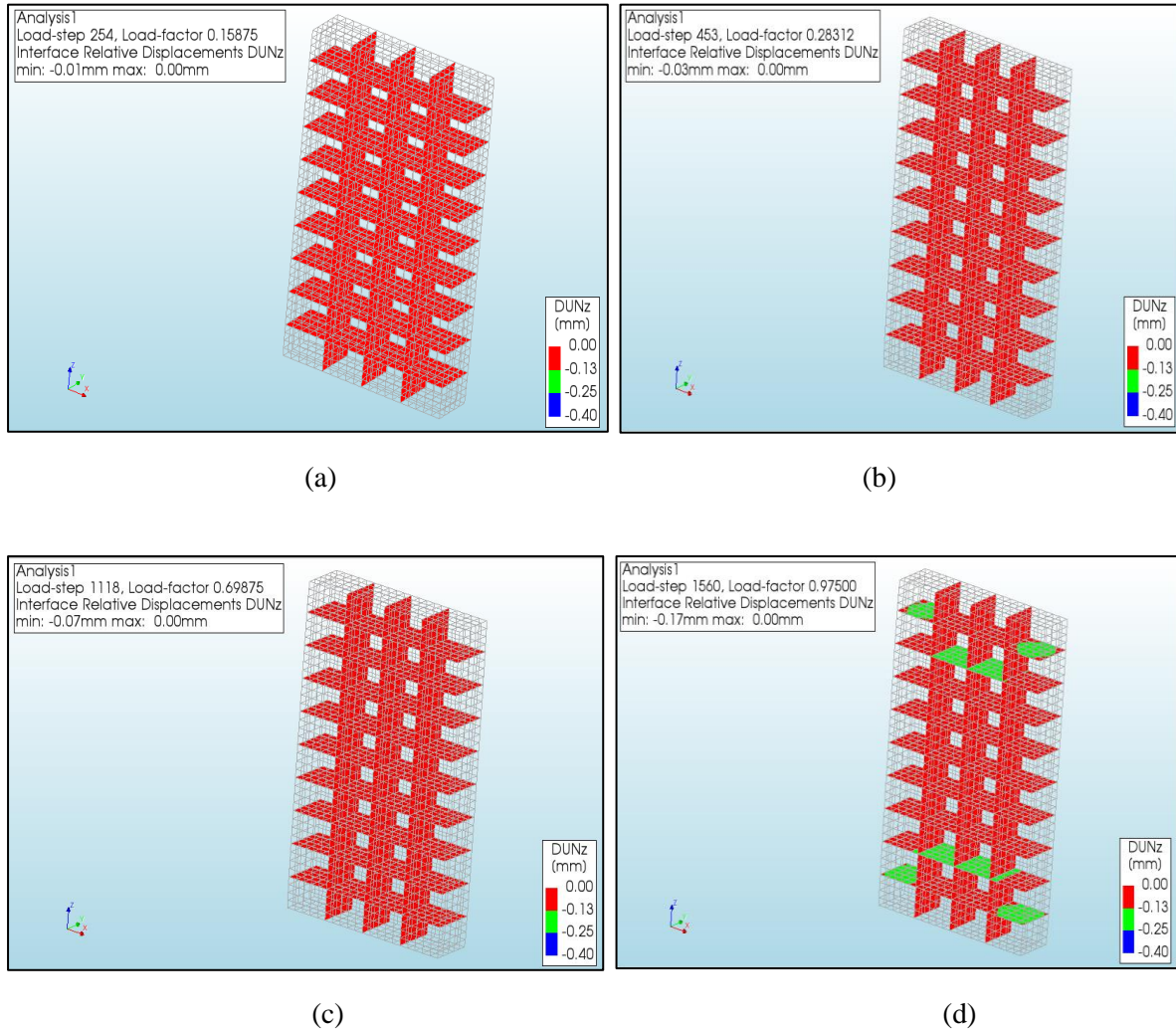
Figure D.10. Progression of DUNz (-ve) in the specimen.

The evolution of relative displacement DUNz (-ve) in the specimen during the analysis is shown in **Figs. D.10 (a – d)**. From **D.1,** it can be observed that the value of equivalent plastic relative displacement is 0.0125. This can be interpreted as the strain at peak load. To obtain the displacement, we multiply the strain by the thickness of the mortar interface. In the 1546th load step, the value of 0.125 is exceeded. It can also be observed from **Figs. D.10 (c and d)** that crushing failure of mortar occurred only in the bed joints.

APPENDIX – E

In this section, the results of Model 5 are discussed in detail.

Table E.1: - List of important input parameters in DIANA, corresponding values and references used for Model 5.

Parameter	Value	Reference
BRICK		
Young's Modulus	6902 N/mm^2	Jafari (2021)
Poisson's ratio	0.18	Zahra (2021)
Crack orientation	Rotating	
Tensile curve	Exponential	Chang (2021)
Tensile strength	4 N/mm^2	Samira (2021)
Mode 1 Tensile fracture energy	0.152 N/mm	Samira (2021), $G_{ftb} = 0.038 \times f_{tb}$
Compression curve	Parabolic	Petracca et al. (2017)
Compressive strength	28.31 N/mm^2	Thamboo (2020), obtained from compression test of clay brick
Compressive fracture energy	12.16 N/mm	Samira (2021), $80 \times G_{ftb}$
MORTAR INTERFACE		
Normal stiffness modulus	102.4N/mm^3	Adjusted using Petracca et al. (2017)
Shear stiffness modulus-x	43 N/mm^3	Adjusted using Chang (2021)
Shear stiffness modulus-y	43 N/mm^3	Adjusted using Chang (2021)
Tensile strength	0.57 N/mm^2	Samira (2021)
Fracture energy	0.0033 N/mm	Samira (2021), $G_{ftm} = 0.025 \times \sqrt[0.7]{\dfrac{f_m}{10}}$
Cohesion	0.57 N/mm^2	Chang (2021), Milani and Lourenco (2013); $c_0 = f_{tm}$
Friction angle	0.64 rad	Jafari (2021)
Dilatancy angle	0.54 rad	Zahra (2021)
Residual friction angle	0.64 rad	Zahra (2021)
Confining normal stress	-1 N/mm^2	De Villiers (2019)
Exponential degradation coefficient	5.6	Van Zijl (2004)
Parameter a	-0.09 mm	De Villiers (2019), Van Zijl (2004)
Parameter b	0.006 N/mm	De Villiers (2019), Van Zijl (2004)
Compressive strength	3.8 N/mm^2	Samira (2021)
Factor Cs	0.8	Assumption
Compressive fracture energy	2.5 N/mm	Samira (2021)
Equivalent plastic relative displacement	0.025 mm	De Villiers (2019)
CONVERGENCE METHOD		
Load steps	1600	
Step size	0.000625	
Maximum number of iterations	1000	
Method	Newton Raphson	
Type	Regular	

Energy Convergence tolerance	0.001	
Displacement Convergence tolerance	NA	
Force convergence tolerance	0.01	
Satisfied Simultaneously?	No	

E.1 Stress-Strain plot of Model
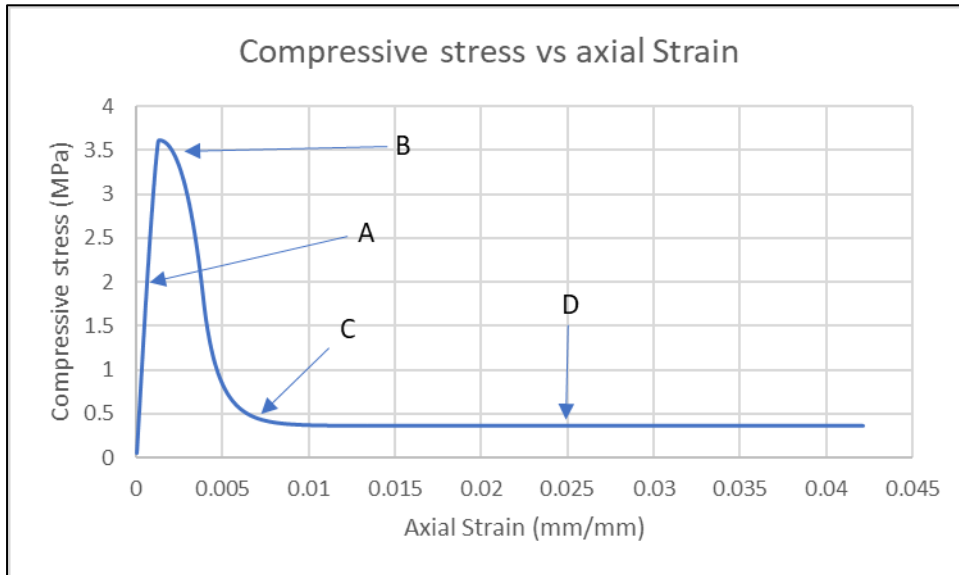
Figure E.1. Plot of compressive stress – axial strain along with specified load levels.

Fig. E.1 shows the plot of compressive stress-axial strain for Model 5. The load levels shown in the figure have been used to study the progression of potential failure mechanisms.

E.2 Analysis for cracking of mortar interface

In this section, the cracking failure of mortar interface is discussed. The constitutive law for the behaviour of a brick element under tensile stress is shown in **Figure 94**.
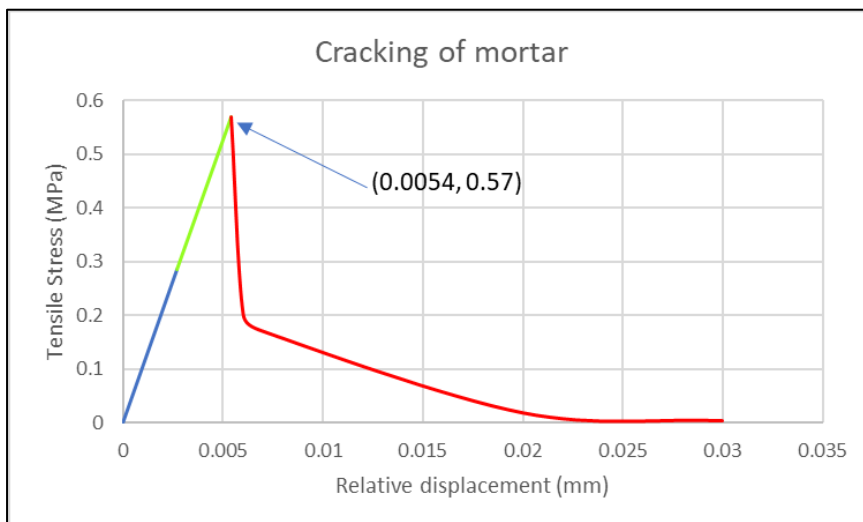
Figure E.2. Behaviour of mortar element of Model 5 under tensile stress.

The point (0.0054, 0.57) indicates the value of relative displacement at the tensile strength of mortar. The value of relative displacement was calculated by dividing the tensile strength of the mortar by the normal stiffness modulus. The positive value of relative displacement was utilized to analyse the potential cracking of mortar interface.
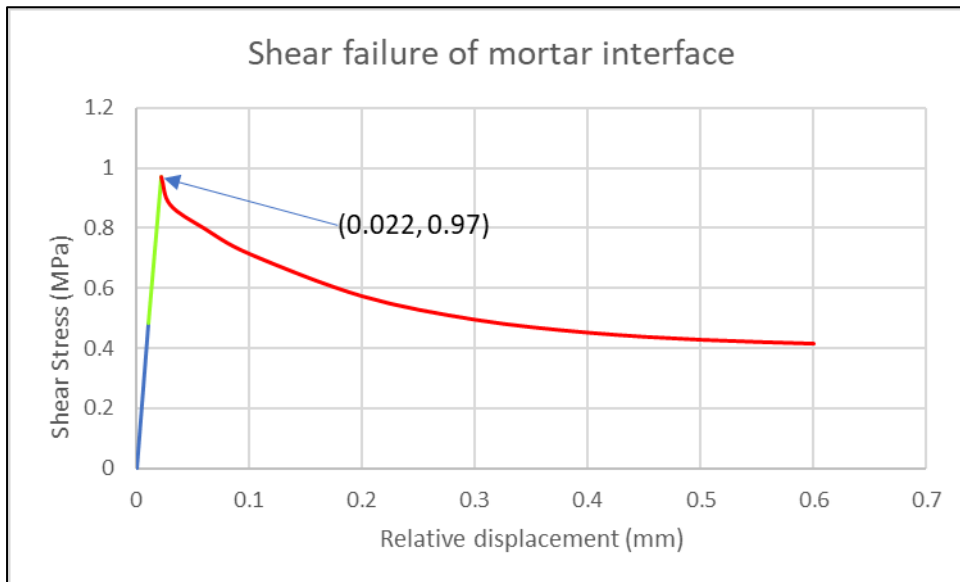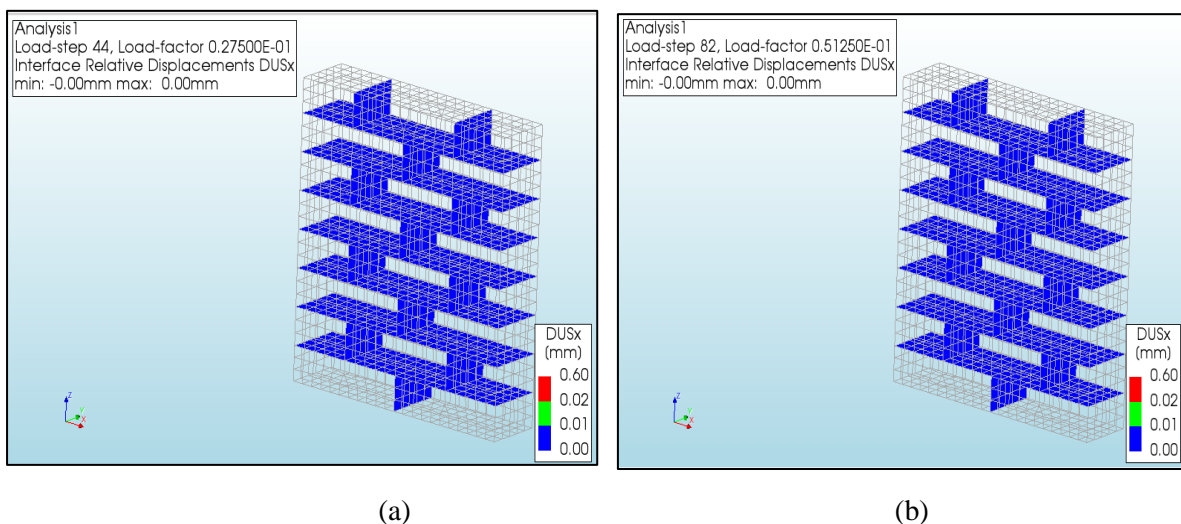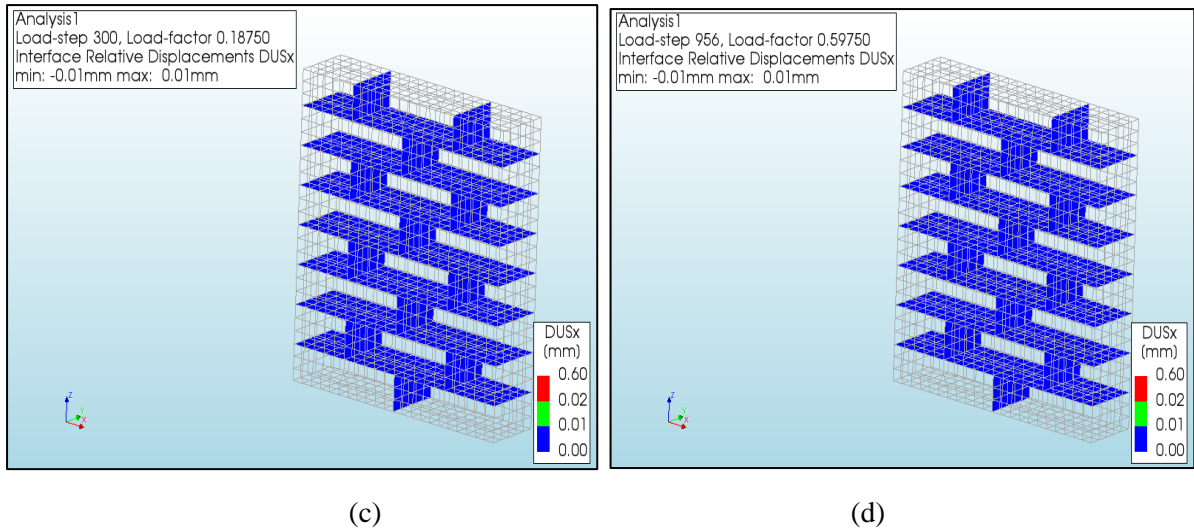

(a)

(b)

(c)

(d)
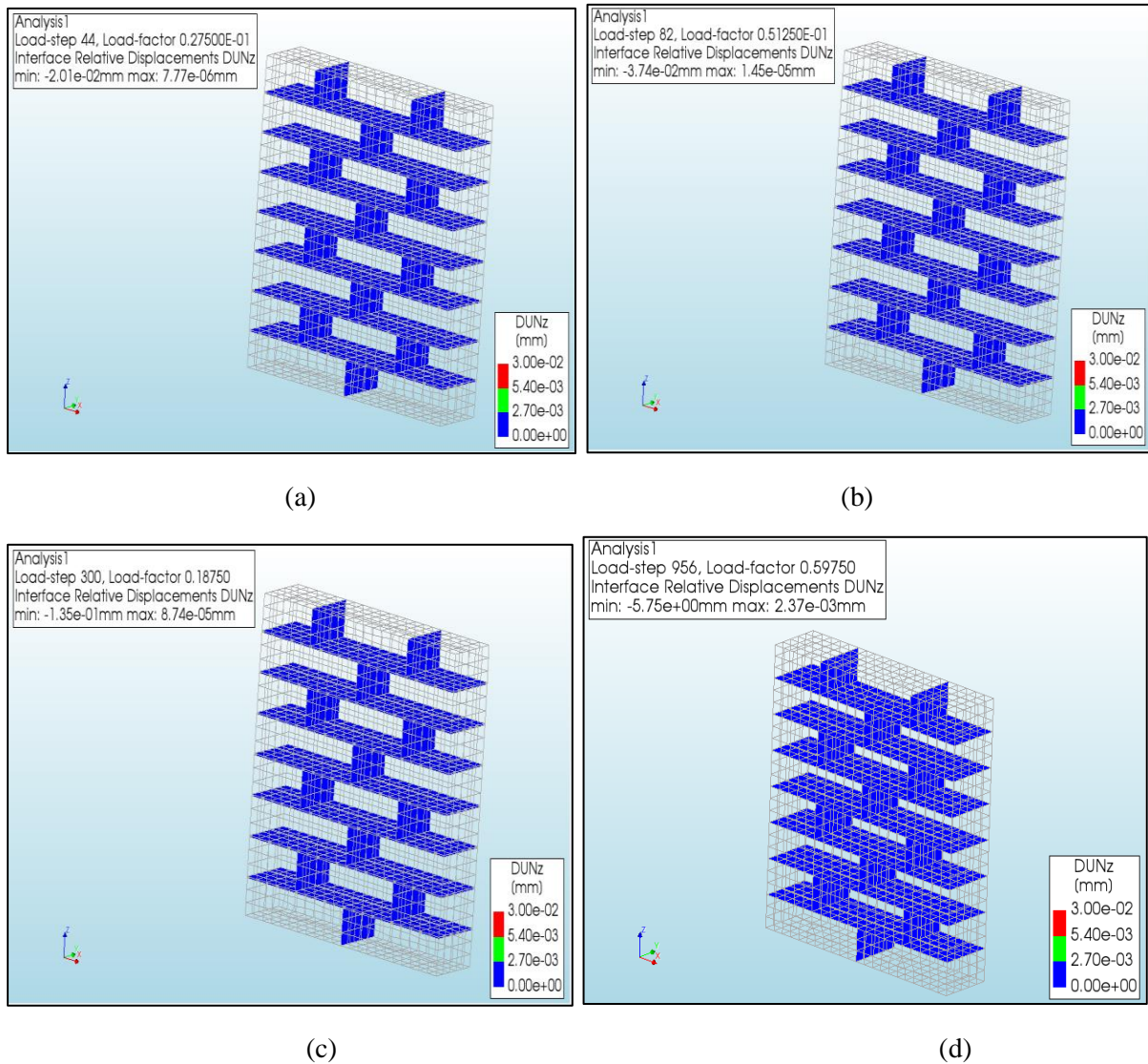
Figure E.3: Progression of relative displacement DUNz (+ve).

The evolution of relative displacement DUNz (+ve) in the specimen during the analysis is shown in **Figs. E.3 (a – d)**. From **Fig. E.2**, it can be said that there is an onset of cracking in the mortar interface if the relative displacement value exceeds 0.0054. This value was not exceeded during the analysis. Hence it can be concluded that the cracking of mortar did not occur.

E.3 Analysis for cracking failure of brick

In this section, the cracking failure of brick is discussed. The constitutive law for the behaviour of a brick element under tensile stress is shown in **Fig. E.4.**
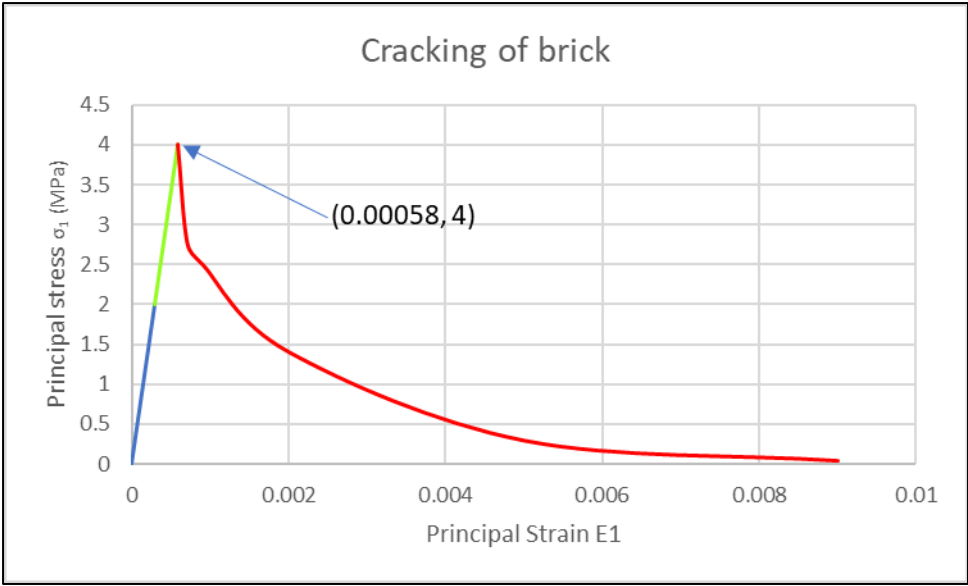
Figure E.4. Behaviour of a brick element under tensile stress.

The point (0.00058, 4) indicates the value of principal strain at the tensile strength of the brick. The value of principal strain was calculated by dividing the tensile strength of the brick by Young's Modulus.

(a)

(b)

95
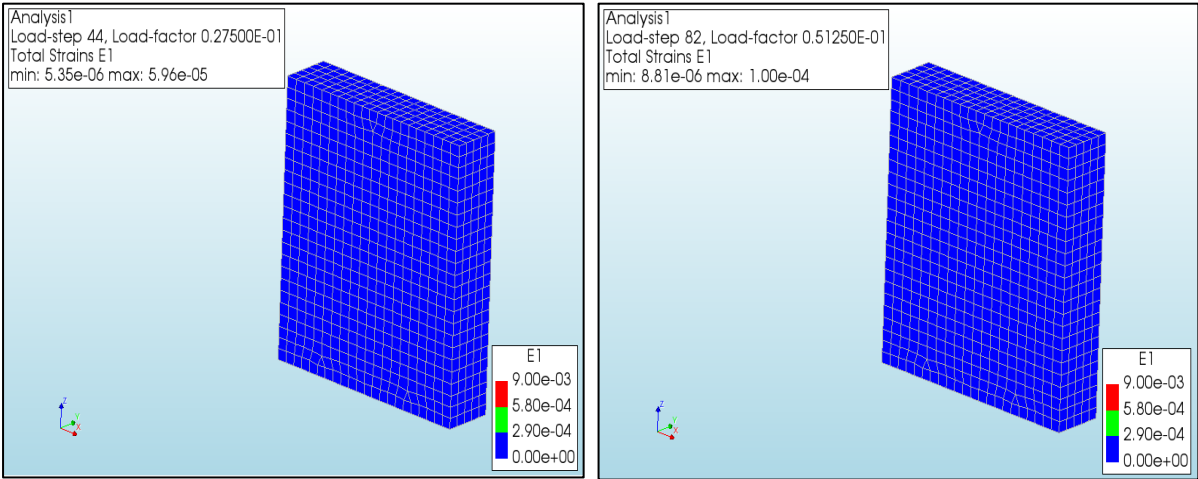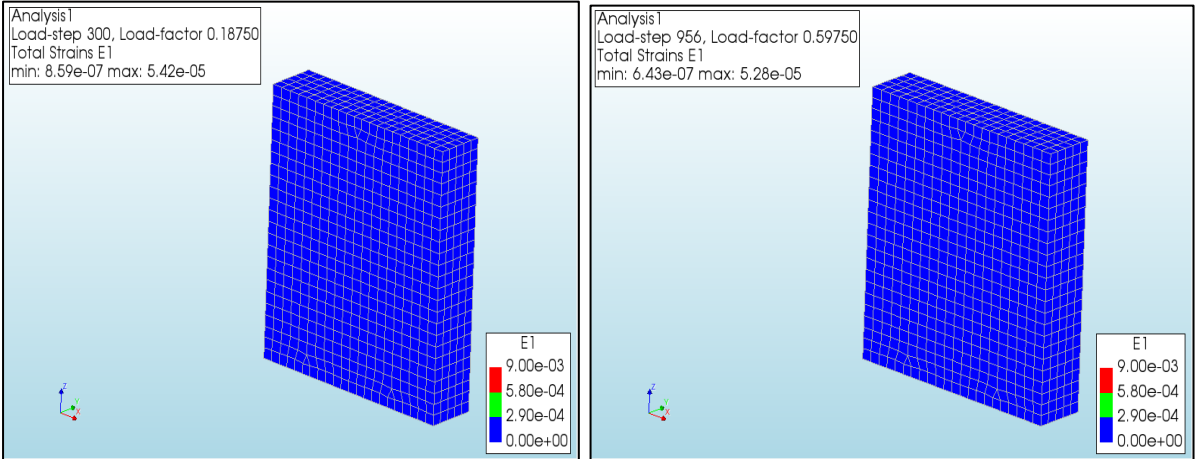
Figure E.5. Progression of Principal strain E1.

The evolution of principal strain E1 in the specimen during the analysis is shown in **Figs. E.5 (a – d)**. From **Fig. E.4**, it can be said that there is an onset of cracking in the brick if the relative displacement value exceeds 0.0058. This value was not exceeded during the analysis. Hence it can be concluded that the cracking of brick did not occur.

E.4 Analysis for crushing of mortar

In this section, the crushing of the mortar interface is discussed. The negative value of relative displacement was utilized to analyse the potential crushing of the mortar interface.

(a)   (b)

(c)   (d)
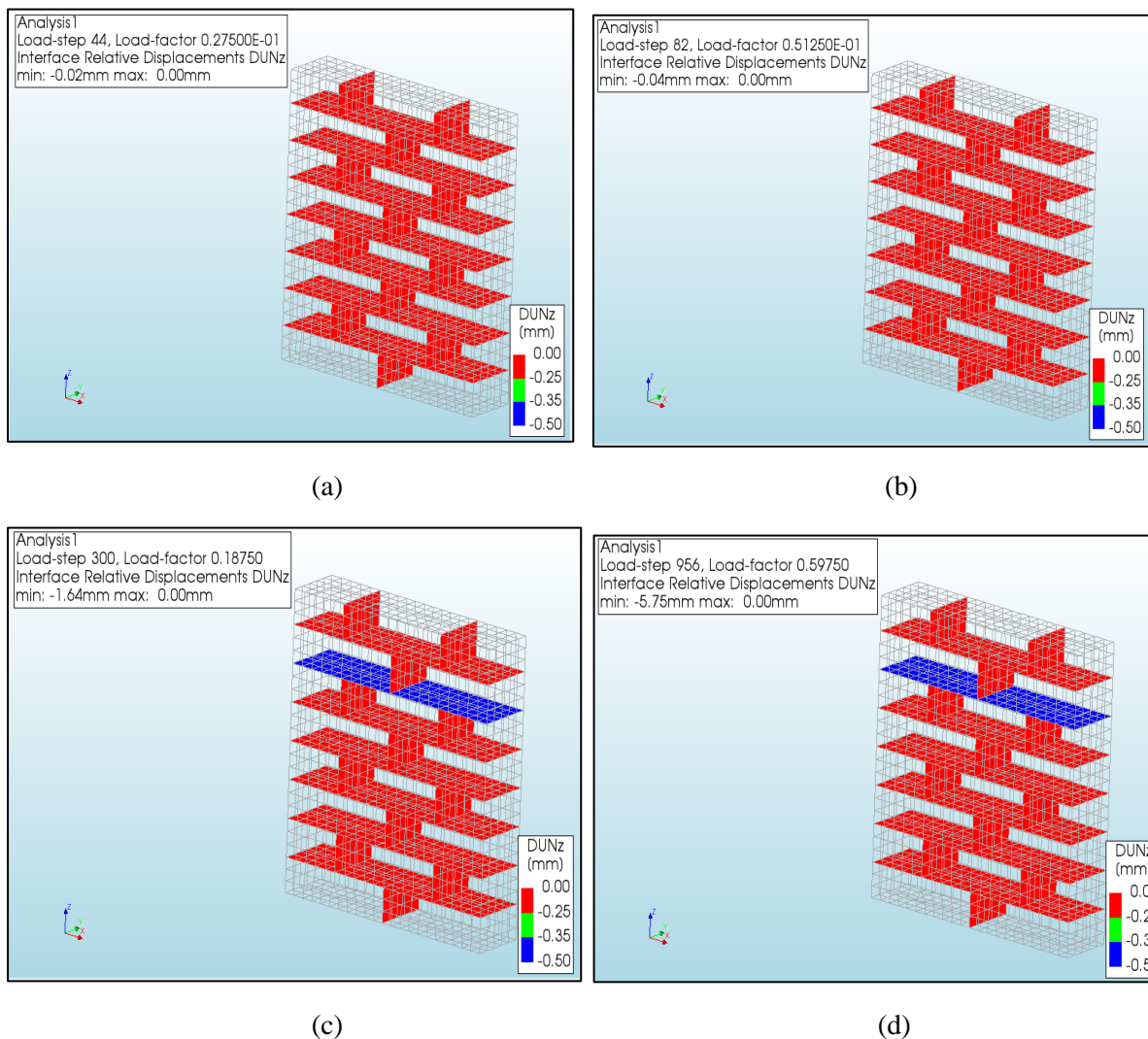
Figure E.6. Progression of DUNz (- ve) in the specimen.

The evolution of relative displacement DUNz (-ve) in the specimen during the analysis is shown in **Figs. E.6(a – d)**. From **Table E.1**, it can be observed that the value of equivalent plastic relative displacement is 0.25. This can be interpreted as the strain at peak compressive stress of mortar. To obtain the relative displacement, the strain is multiplied by the thickness of the mortar interface.

During analysis, it was observed that the value of 0.25 was exceeded. It can also be observed from Figs. 7(c and d) that crushing failure of mortar occurred only in the bed joints.

E.5 Analysis for shear failure of mortar interface

In this section, the shear failure of mortar interface is discussed. The constitutive law for the behaviour of a mortar element under shear stress is shown in **Figure 99**.

Figure E.7. Behaviour of mortar element of Model 5 under shear stress.

The point (0.022, 0.97) indicates the value of relative displacement at peak mortar shear strength. The value of relative displacement was calculated by dividing the shear strength of the mortar by the shear stiffness modulus.

(a)	(b)

$$\text{(c)} \qquad\qquad \text{(d)}$$

Figure E.8. Progression of relative displacement DUSx

$$\text{(a)} \qquad\qquad \text{(b)}$$

$$\text{(c)} \qquad\qquad \text{(d)}$$
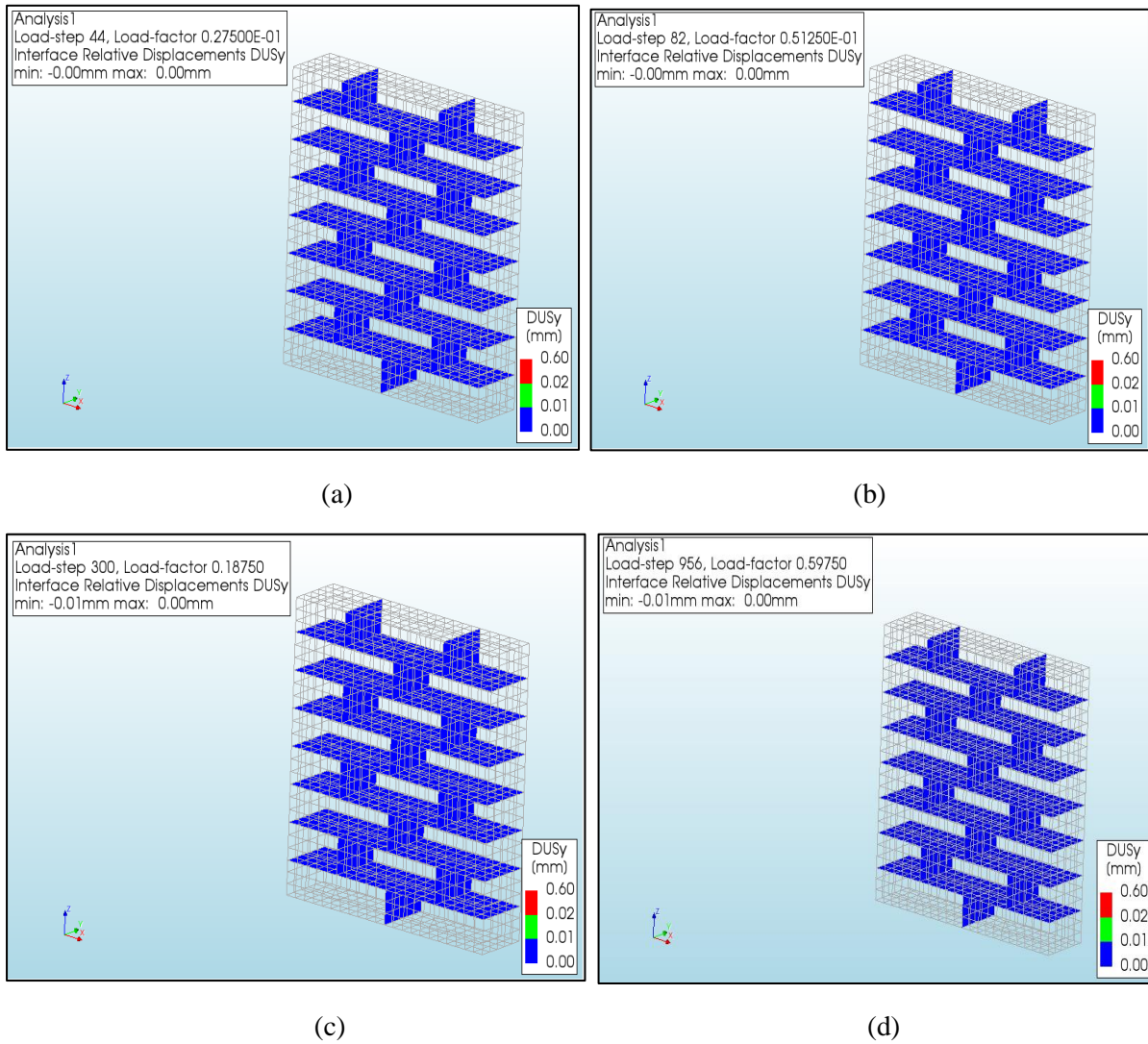
Figure E.9. Progression of DUSy

The evolution of relative displacement DUSx in the specimen during the analysis is shown in **Figs. E.8 (a − d)** while the evolution of relative displacement DUSy is shown in **Figs. E.9 (a - d)**. From

both **Figs. E.8 (a − d)** and **Figs. E.9 (a − d),** it can be noted that the critical value 0.021, which indicates the onset of shear failure, was not exceeded. Hence it can be concluded that the shear failure of the specimen did not take place.

E.6 Analysis for crushing of brick

This section discusses the crushing failure of a brick. As per Table 1, The peak compressive strength of the brick is 28.31 MPa. If principal stress S3 exceeds 28.31 MPa, it can be inferred that the brick has undergone crushing failure.

(a)

(b)

(c)

(d)
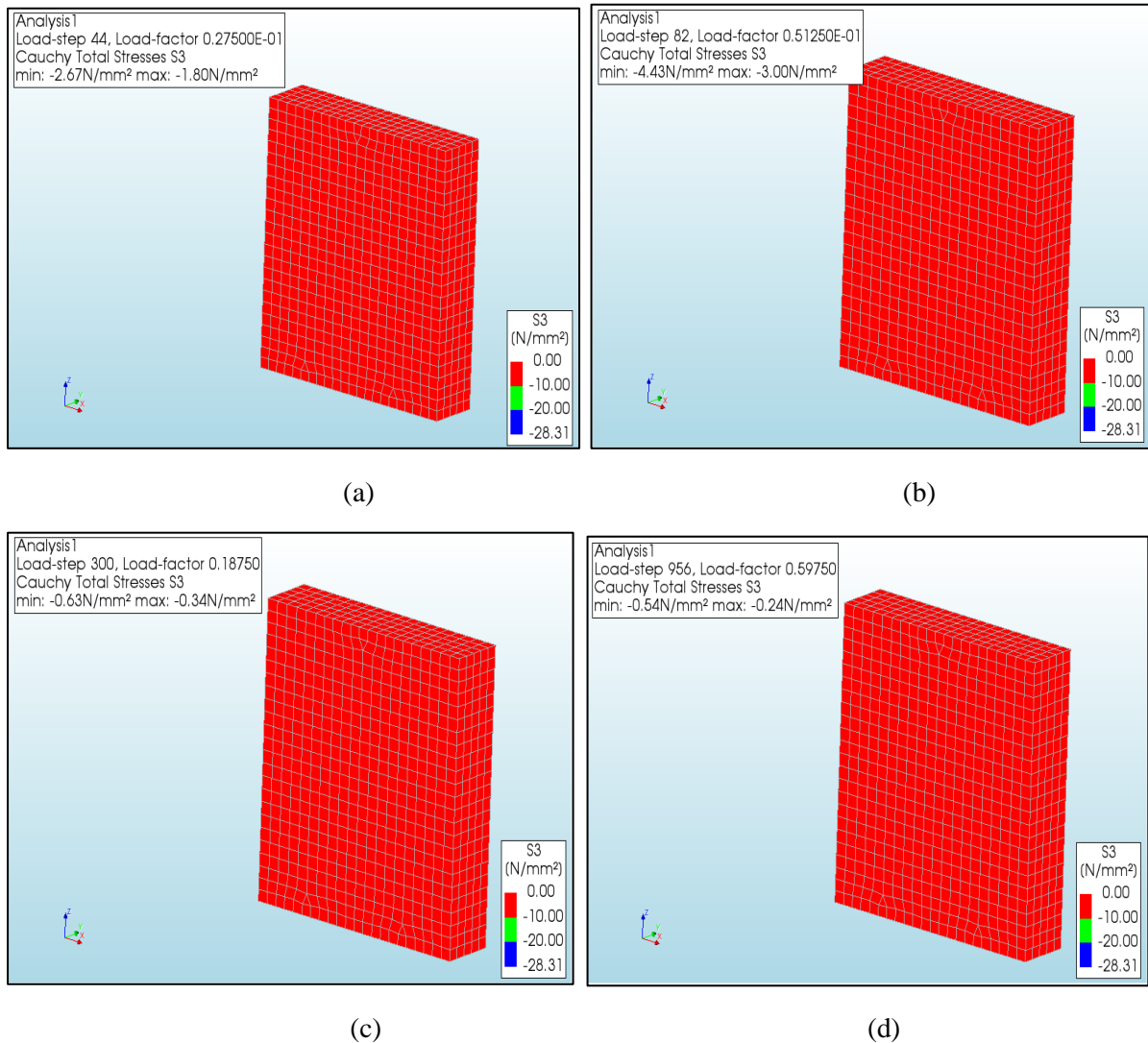
Figure E.10. Progression of principal stress S3.

From **Figs. E.10 (a-d)**, it can be observed that the principal stress S3 doesn't exceed the compressive strength of a brick. Hence crushing failure of brick did not occur.

APPENDIX – F

In this section, the results of Model 6 are discussed in detail.

Table F.1. List of input parameters in DIANA, corresponding values and references used for this model.

Parameter	Value	Reference
BRICK		
Young's Modulus	6902 N/mm^2	Samira (2021)
Poisson's ratio	0.18	Zahra (2021)
Crack orientation	Rotating	
Tensile curve	Exponential	Chang (2021)
Tensile strength	4 N/mm^2	Samira (2021)
Mode 1 Tensile fracture energy	0.152 N/mm	Samira (2021), $G_{ftb} = 0.038 \times f_{tb}$
Compression curve	Parabolic	Petracca et al. (2017)
Compressive strength	5.1 N/mm^2	Thamboo (2020), obtained from compression test of clay brick
Compressive fracture energy	12.16 N/mm	Samira (2021), $80 \times G_{ftb}$
MORTAR INTERFACE		
Normal stiffness modulus	104 N/mm^3	Adjusted using Petracca et al. (2017)
Shear stiffness modulus-x	45 N/mm^3	Adjusted using Chang (2021)
Shear stiffness modulus-y	45 N/mm^3	Adjusted using Chang (2021)
Tensile strength	0.25 N/mm^2	Thamboo (2020); $f_{tm} = 0.67 \times$ Flexural strength
Fracture energy	0.012 N/mm	Samira (2021), $G_{ftm} = 0.025 \times \sqrt[0.7]{\frac{f_m}{10}}$
Cohesion	0.57 N/mm^2	Chang (2021), Milani and Lourenco (2013); $c_0 = f_{tm}$
Friction angle	0.64 rad	Jafari (2021)
Dilatancy angle	0.54 rad	Zahra (2021)
Residual friction angle	0.64 rad	Zahra (2021)
Confining normal stress	-1 N/mm^2	De Villiers (2019)
Exponential degradation coefficient	5.6	Van Zijl (2004)
Parameter a	-0.09 mm	De Villiers (2019), Van Zijl (2004)
Parameter b	0.006 N/mm	De Villiers (2019), Van Zijl (2004)
Compressive strength	38 N/mm^2	Assumption
Factor Cs	0.8	Assumption
Compressive fracture energy	25 N/mm	Jafari (2021); $250 \times G_{fIm}$
Equivalent plastic relative displacement	0.025 mm	De Villiers (2019)
CONVERGENCE METHOD		
Load steps	1600	
Step size	0.000625	
Maximum number of iterations	1000	
Method	Newton Raphson	
Type	Regular	
Energy Convergence tolerance	0.001	

Displacement Convergence tolerance	NA	
Force convergence tolerance	0.01	
Satisfied Simultaneously?	No	

F.1 Stress-Strain plot of the model
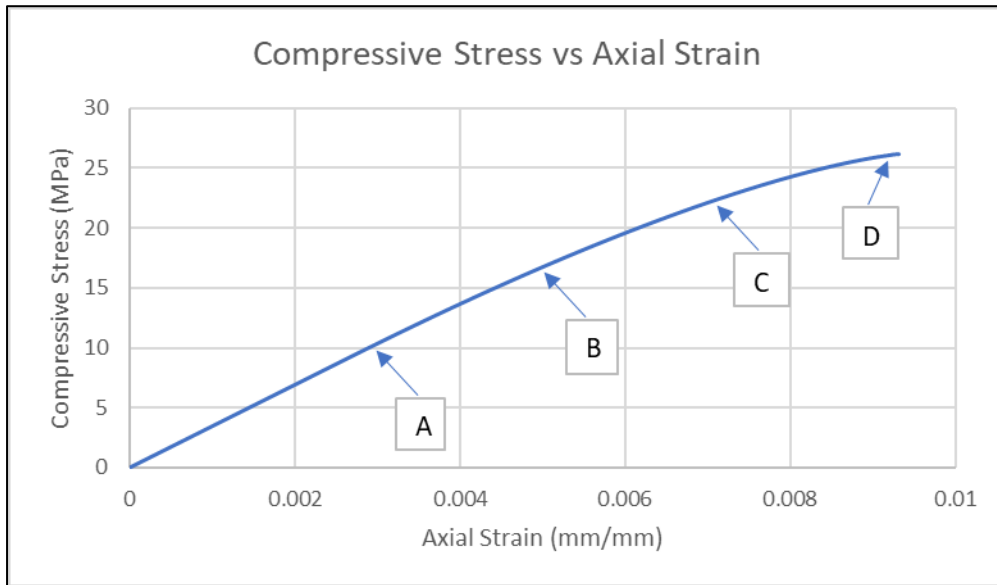
Figure F.1. Plot of compressive stress – axial strain along with specified load levels.

Fig. F.1. shows the plot of compressive stress-axial strain for Model 6. The load levels shown in the figure have been used to study the progression of potential failure mechanisms.

F.2 Analysis for cracking of mortar

This section encompasses the cracking of mortar interfaces. The constitutive law for the behaviour of a mortar element under tensile stress is shown in **Fig. F.2**.
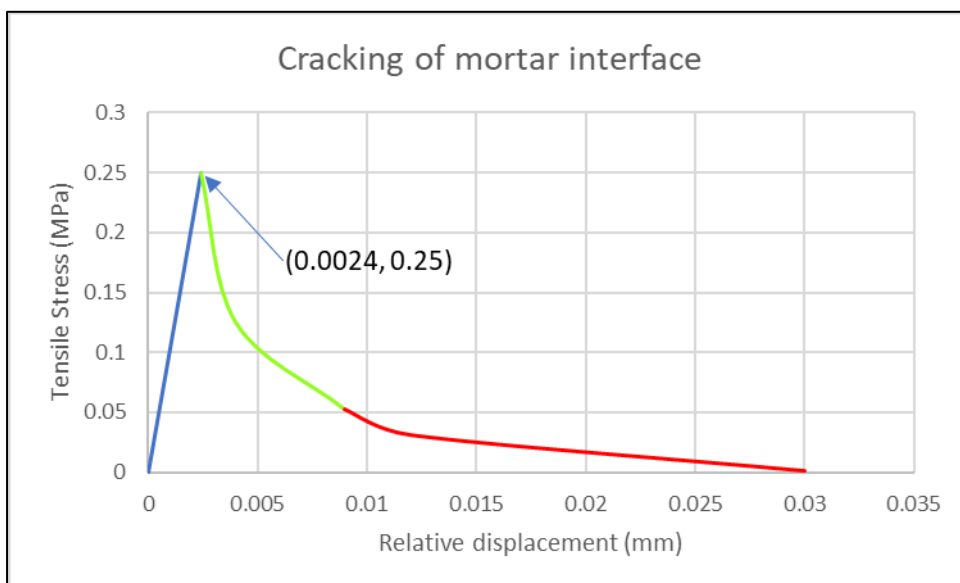
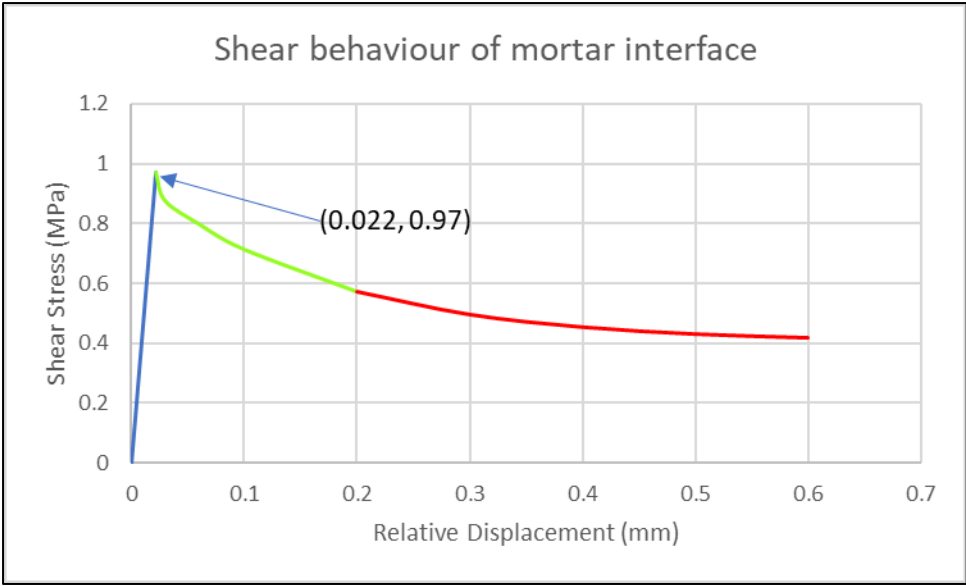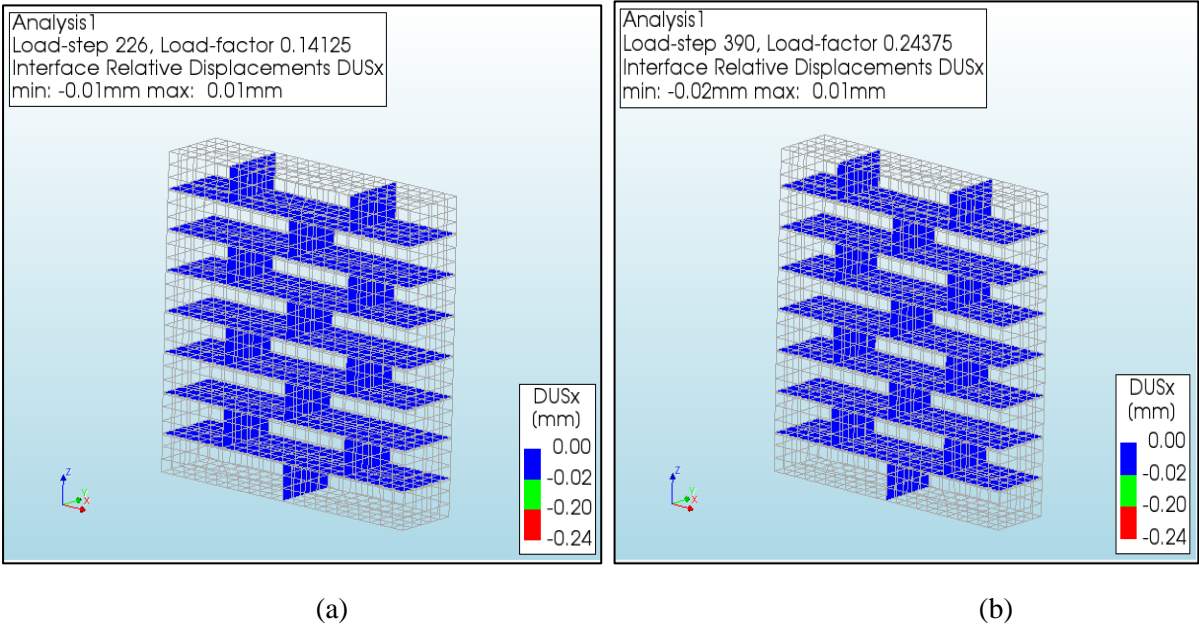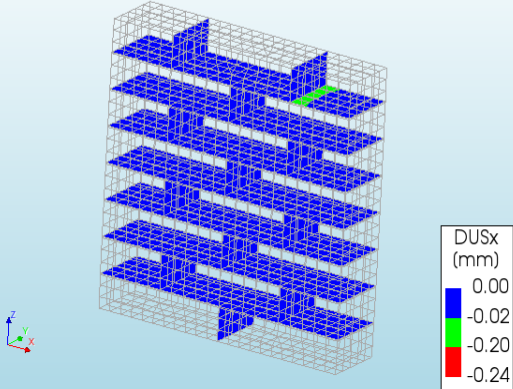**Figure F.2**. Behaviour of mortar element of Model 6 under tensile stress.

The point (0.0024, 0.25) indicates the value of relative displacement at peak mortar tensile strength. The value of relative displacement was calculated by dividing the tensile strength of the mortar by the normal stiffness modulus.

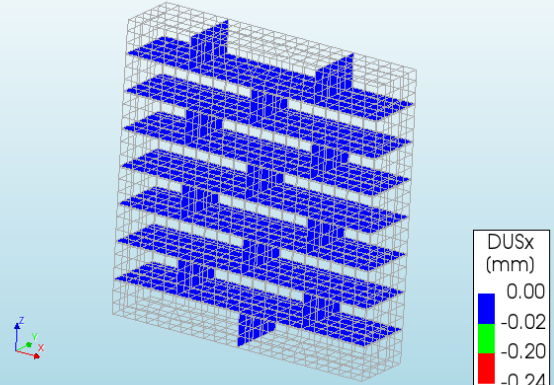(a)   (b)

(c)   (d)
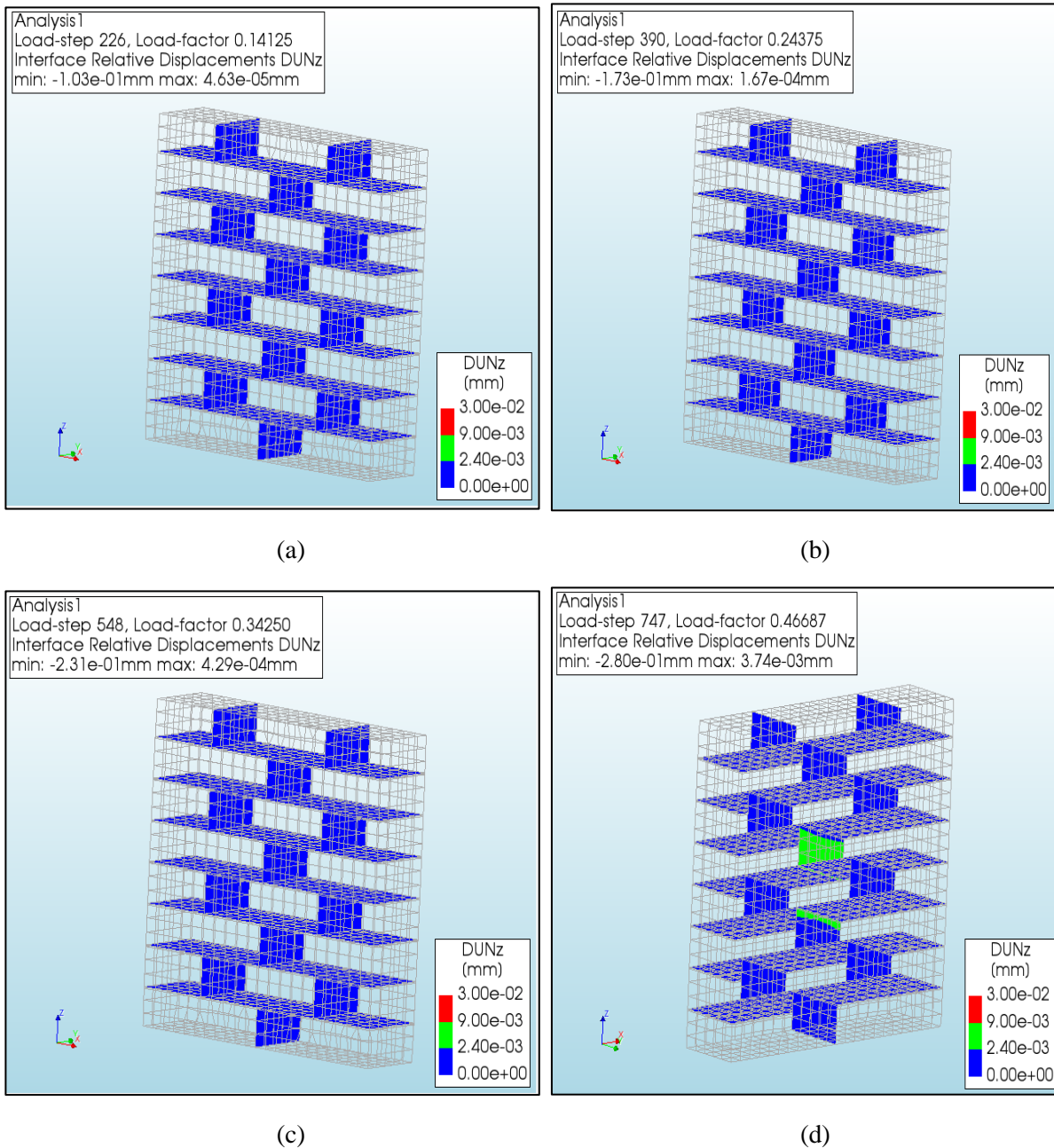
Figure F.3. Progression of DUNz (+ve) in the specimen.

The evolution of relative displacement DUNz (+ve) in the specimen during the analysis is shown in **Figs. F.3(a – d)**. From **Fig. F.2**, it can be said that there is an onset of cracking in the mortar interface if the relative displacement value exceeds 0.0024. This value was exceeded during the analysis as can be seen from **Figure F.3d**. It can also be observed that the cracking of mortar only occurred in head joints.

F.3 Analysis for cracking failure of brick

In this section, the cracking failure of brick is discussed. The constitutive law for the behaviour of a brick element under tensile stress is shown in **Fig. F.4**.
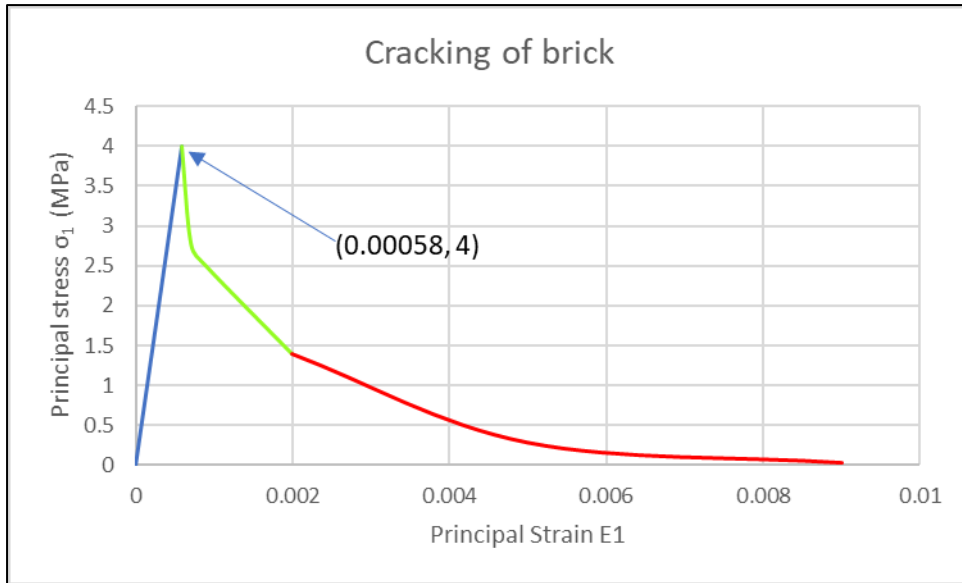
Figure F.4: Behaviour of a brick element under tensile stress.

The point (0.00058, 4) indicates the value of principal strain at the tensile strength of the brick. The value of principal strain was calculated by dividing the tensile strength of the brick by Young's Modulus.

(a)　　　　　　　　　　　　　　　　　　(b)

<div align="center">(c)   (d)</div>
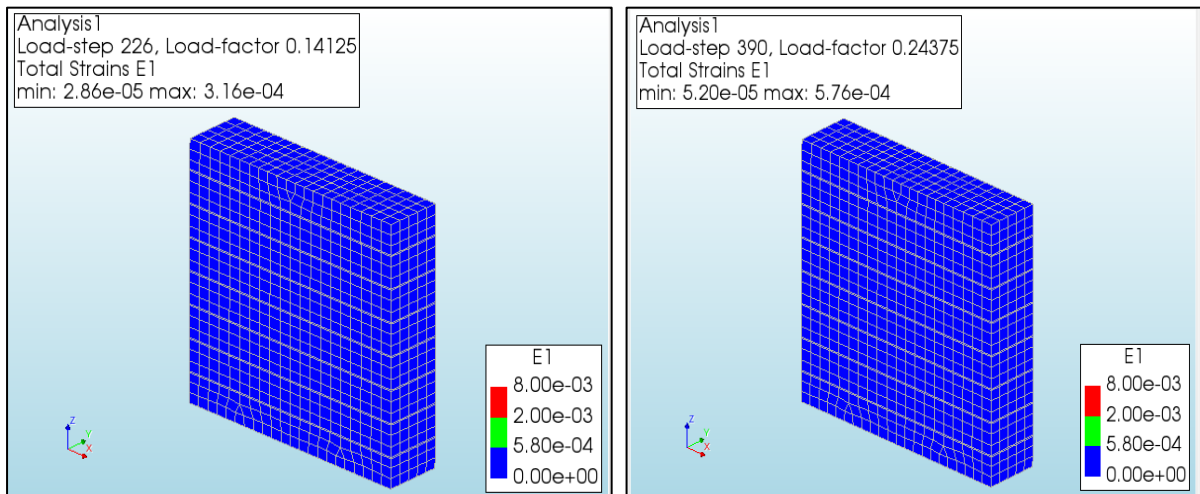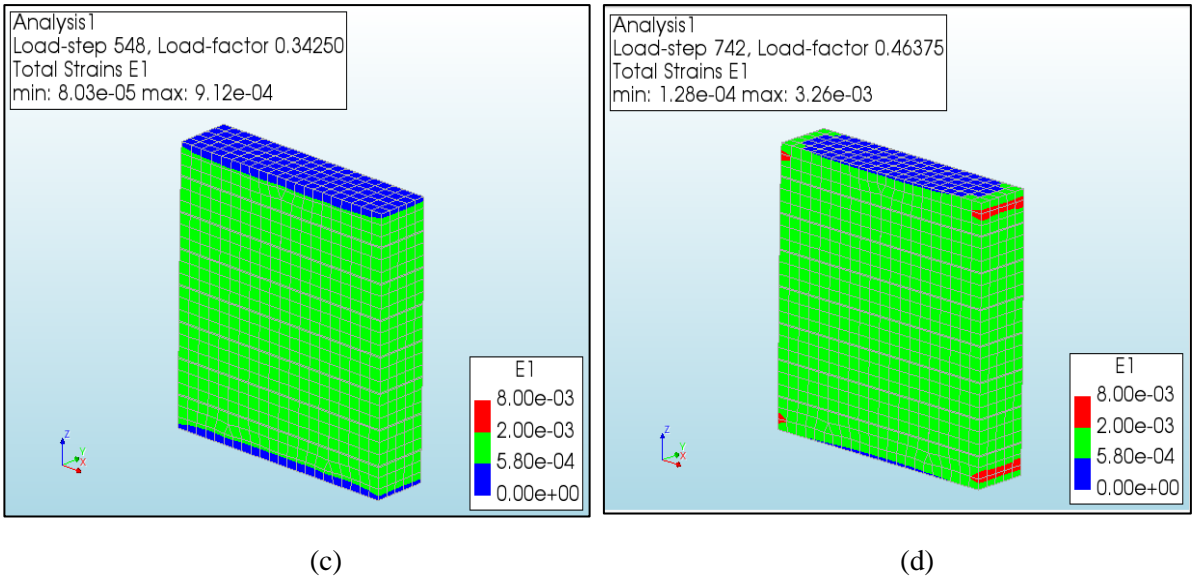
Fig. F.5: Progression of principal strain E1.

The evolution of principal strain E1 in the specimen during the analysis is shown in **Figs. F.5 (a – e)**.

F.4 Analysis of crushing of brick

In this section, the crushing failure of a brick is discussed. The figure shown below represents the behaviour of the brick under compression loading.
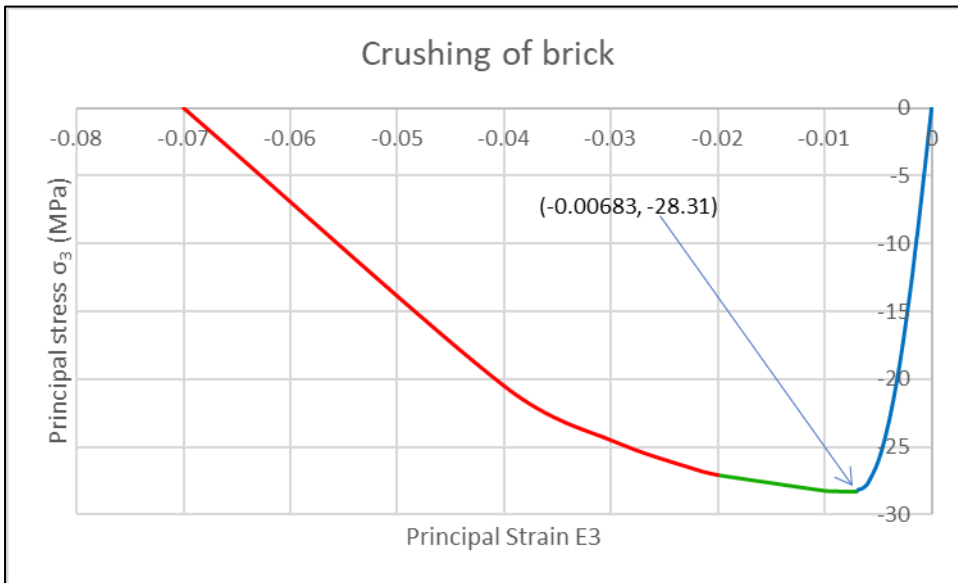
Figure F.6. Constitutive law for crushing of brick element.

(a)   (b)

(c)   (d)
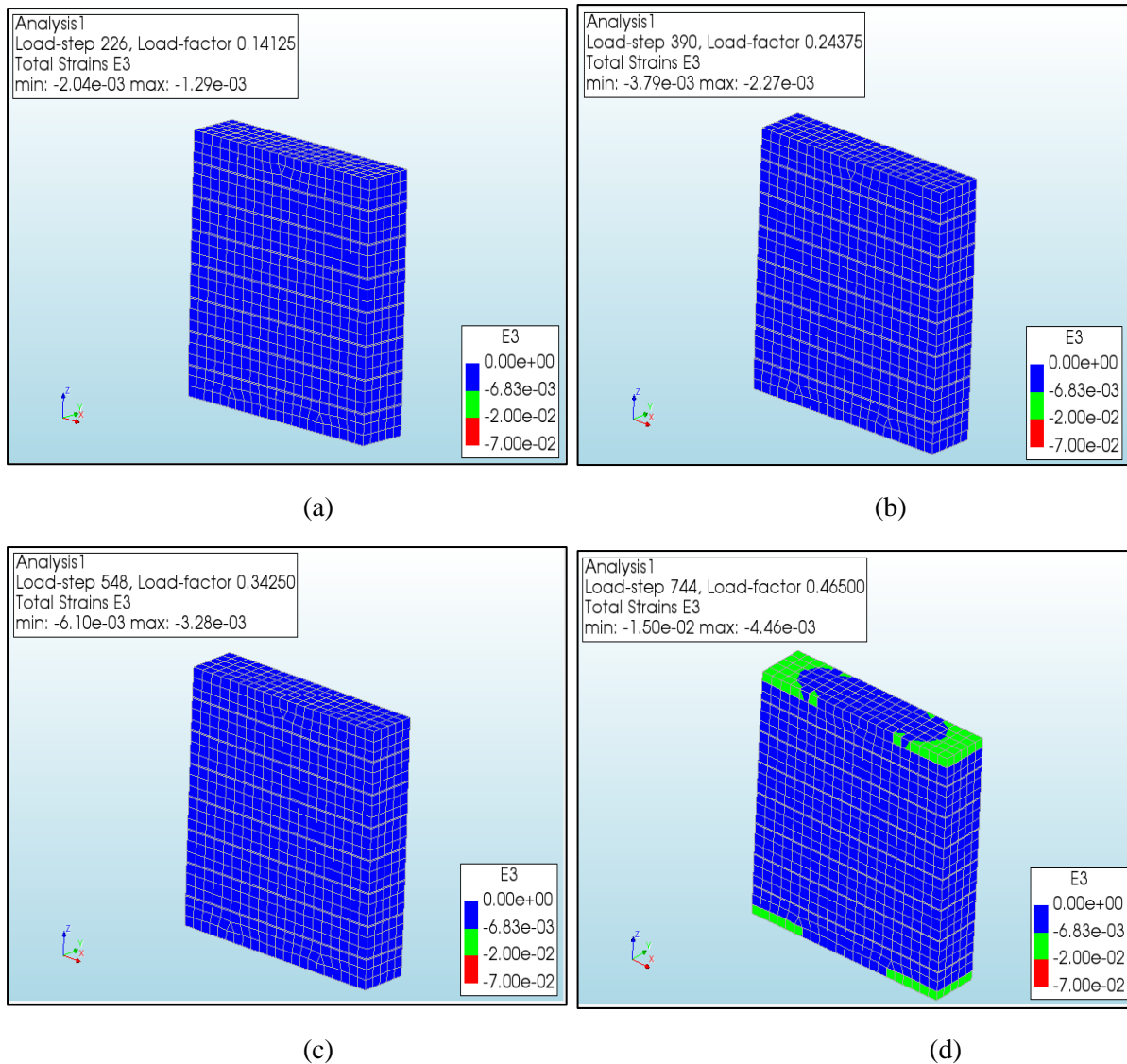
Figure F.7. Progression of principal strain E3

The evolution of principal strain E3 in the specimen during the analysis is shown in **Figs. F.7(a – d)**.

F.5 Analysis for crushing of mortar

In this section, the crushing of the mortar interface is discussed. The negative value of relative displacement was utilized to analyse the potential crushing of the mortar interface.

(a)

(b)

(c)

(d)
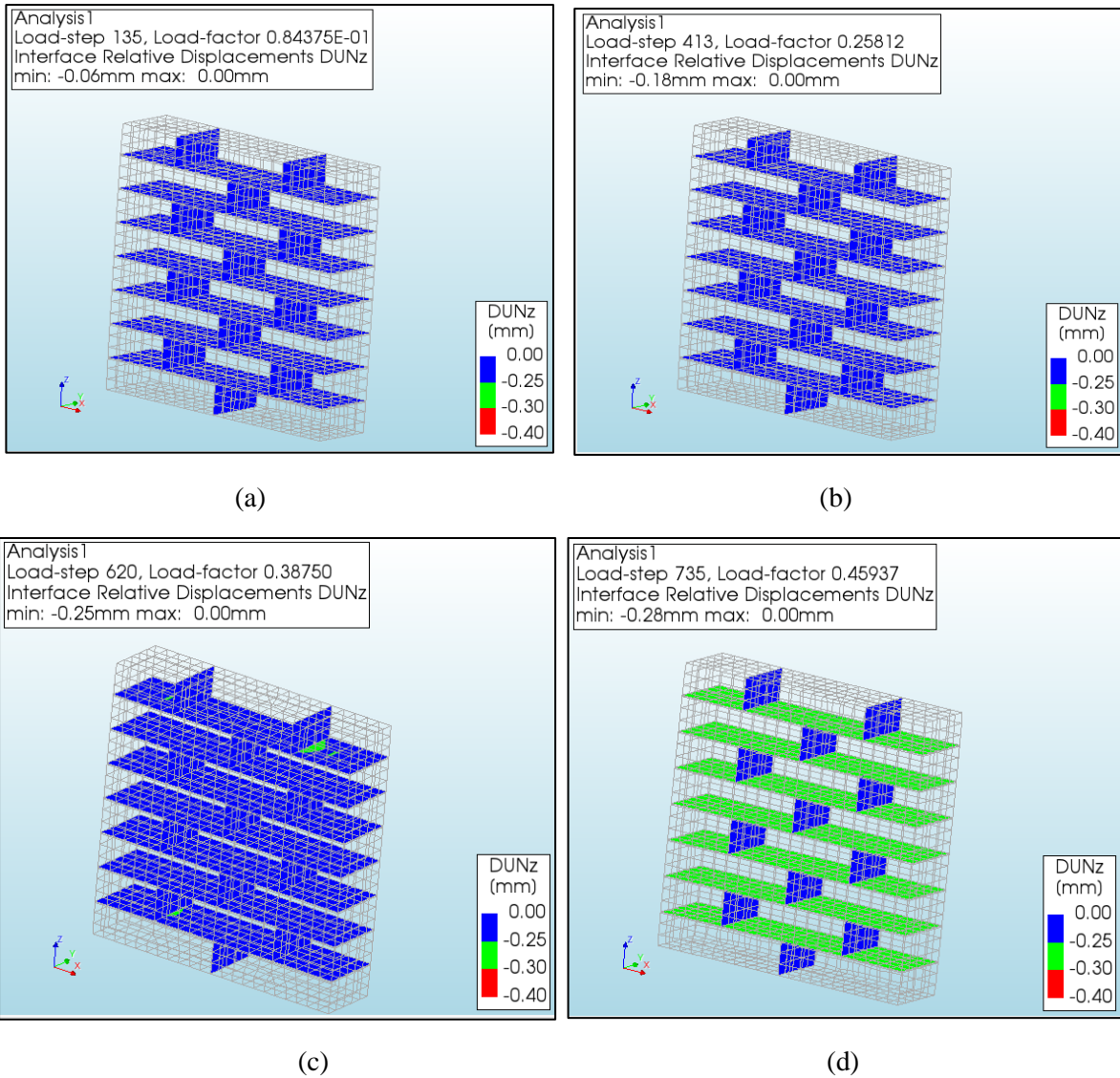
Figure F.8. Progression of relative displacement DUNz (-ve)

The evolution of relative displacement DUNz (-ve) in the specimen during the analysis is shown in **Figs. F.8 (a – d)**. From **Table F.1**, it can be observed that the value of equivalent plastic relative displacement is 0.025. This can be interpreted as the strain at peak compressive stress of mortar. To obtain the relative displacement, the strain is multiplied by the thickness of the mortar interface. In the 620th load step, the value of 0.25 is exceeded.

F.6 Analysis for shear failure of mortar interface

In this section, the shear failure of the mortar interface is discussed. The constitutive law for the behaviour of a mortar element under shear stress is shown in **Figure F.9**.

106

Figure F.9. Behaviour of mortar element under shear stress.

The point (0.021, 0.97) indicates the value of relative displacement at peak mortar shear strength. The value of relative displacement was calculated by dividing the shear strength of the mortar by the shear stiffness modulus.

(a)   (b)

(c)   (d)

Figure F.10. Progression of relative displacement DUSx

(a)   (b)
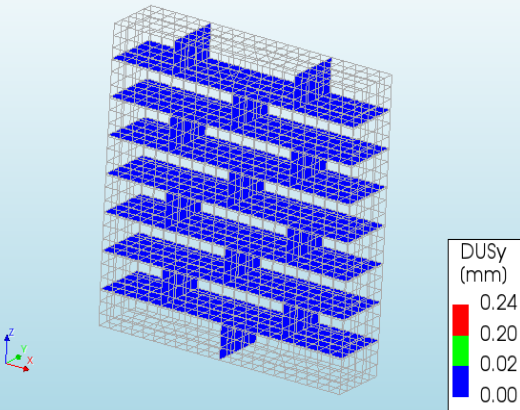
(c)   (d)

Figure F.11. Progression of relative displacement DUSy

The evolution of relative displacement DUSx in the specimen during the analysis is shown in **Figs. F.10 (a – d)** while the evolution of relative displacement DUSy is shown in **Figs. F.11 (a - d)**. From both **Figs. F.10 (a – d)** and **Figs. F.11 (a – d)**, it can be noted that the critical value 0.021, which indicates the onset of shear failure, was exceeded. Hence it can be concluded that the shear failure of the specimen did take place. Shear failure of mortar occurred in the topmost and the bottommost bed joints.

APPENDIX – G

In this section, the results of Model 7 have been discussed in a detailed manner.

Table G.1: List of input parameters in DIANA, corresponding values and references used for this model.

Parameter	Value	Reference
BRICK		
Young's Modulus	6902 N/mm^2	Jafari (2021)
Poisson's ratio	0.18	Zahra (2021)
Crack orientation	Rotating	
Tensile curve	Exponential	Chang (2021)
Tensile strength	4 N/mm^2	Jafari (2021); $f_{tb} = 0.67 \times$ Modulus of rupture
Mode 1 Tensile fracture energy	0.152 N/mm	Adjusted
Compression curve	Parabolic	Petracca et al. (2017)
Compressive strength	28.31 N/mm^2	Thamboo (2020), obtained from compression test of clay brick
Compressive fracture energy	12.16 N/mm	
MORTAR		
Young's Modulus	914.4 N/mm^2	Jafari (2021)
Poisson's ratio	0.18	Zahra (2021)
Crack orientation	Rotating	
Tensile curve	Exponential	Chang (2021)
Tensile strength	0.57 N/mm^2	Jafari (2021); $f_{tb} = 0.67 \times$ Modulus of rupture
Mode 1 Tensile fracture energy	0.012 N/mm	Adjusted
Compression curve	Parabolic	Petracca et al. (2017)
Compressive strength	3.81 N/mm^2	Jafari (2021)
Compressive fracture energy	2.5 N/mm	
CONVERGENCE METHOD		
Load steps	1600	
Step size	0.000625	
Maximum number of iterations	1000	
Method	Newton Raphson	
Type	Regular	
Energy Convergence tolerance	0.001	
Displacement Convergence tolerance	NA	
Force convergence tolerance	0.01	
Satisfied Simultaneously?	No	

G.1 Stress-Strain plot of Model
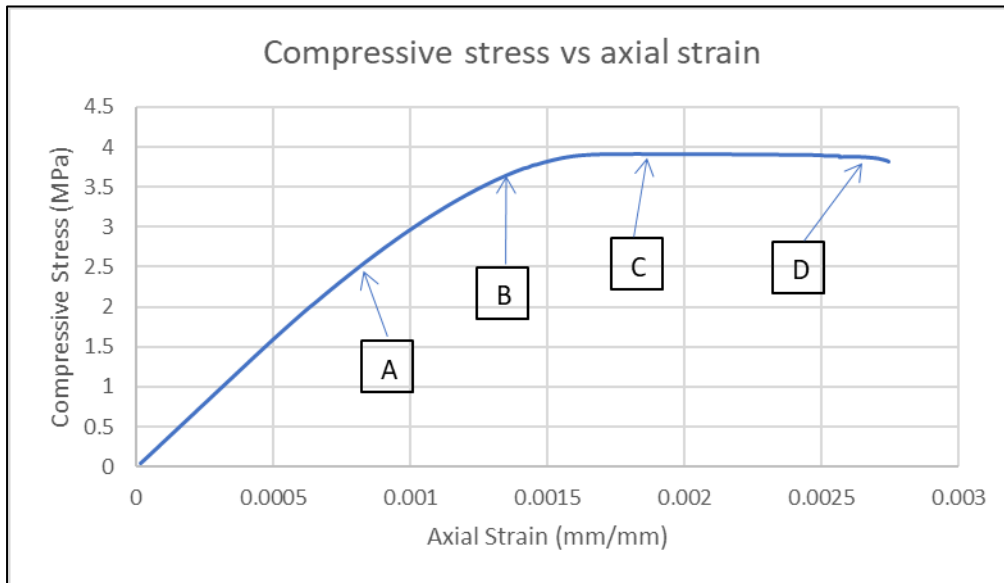
Figure G.1. Plot of compressive stress vs. axial strain along with the mentioned load levels.

Fig. G.1 shows the plot of compressive stress-axial strain for Model 7. The load levels shown in the figure have been used to study the progression of potential failure mechanisms.

G.2 Analysis for cracking of mortar

In this section, the cracking of mortar is discussed. The constitutive law for cracking of mortar is shown below in **Fig G.2**.
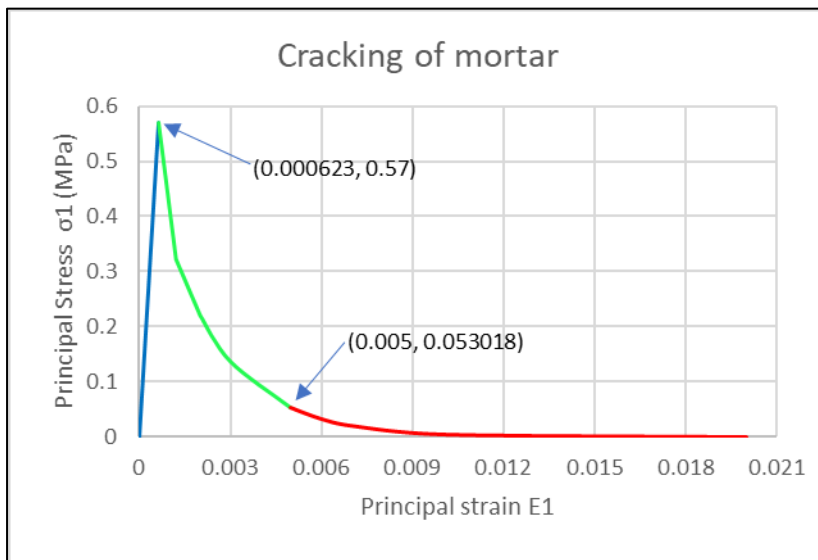
Figure G.2. Constitutive law of mortar element of Model 7.

(a)   (b)

(c)   (d)
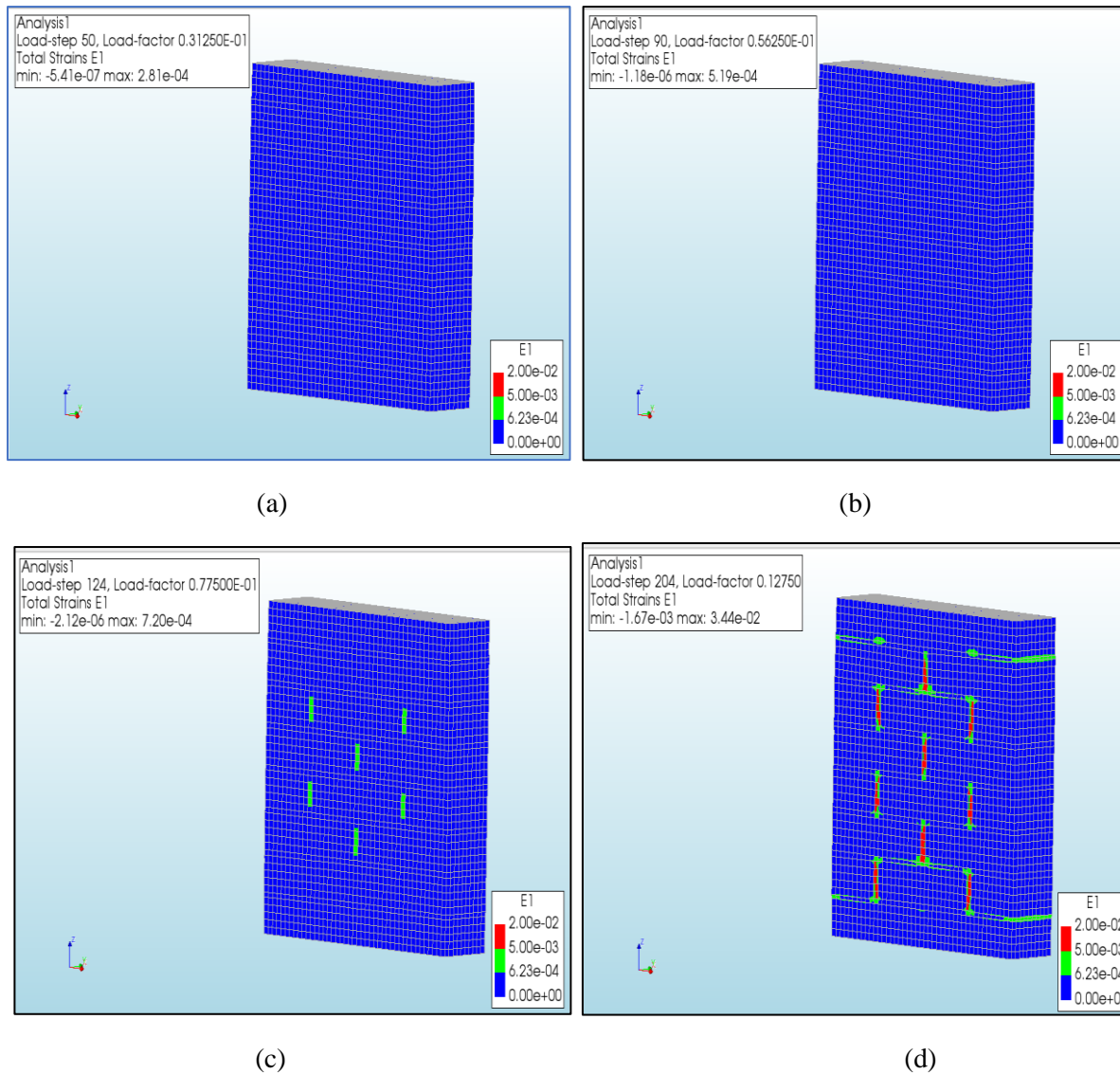
Figure G.3. Progression of Principal Strain E1

The evolution of relative displacement DUNz (+ve) in the specimen during the analysis is shown in **Figs. G.3(a – d)**. From **Fig. G.2**, it can be said that there is an onset of cracking in the mortar interface if the relative displacement value exceeds 0.000623. This value was exceeded during the analysis as can be seen from **Figure G.3c**. Cracking of mortar primarily occurred in the head joints. But towards the end of the analysis, mortar cracking could also be observed in the bed joints.

G.3 Analysis for crushing of mortar

In this section, the crushing failure of mortar is discussed. The constitutive law for crushing of mortar is shown in **Fig G.4**.
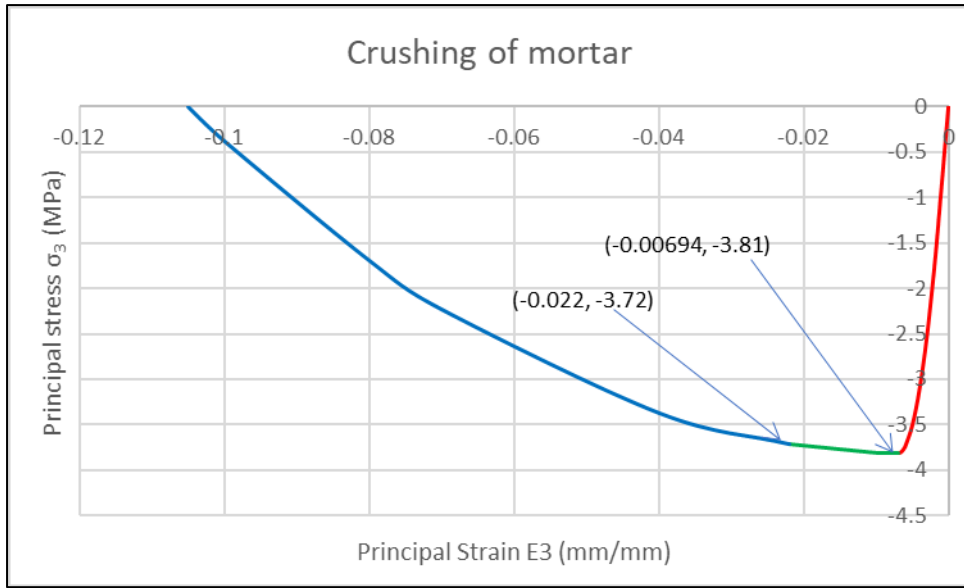
Figure G.4. Constitutive law for crushing failure of mortar for Model 7.

(a)

(b)

(c)

(d)
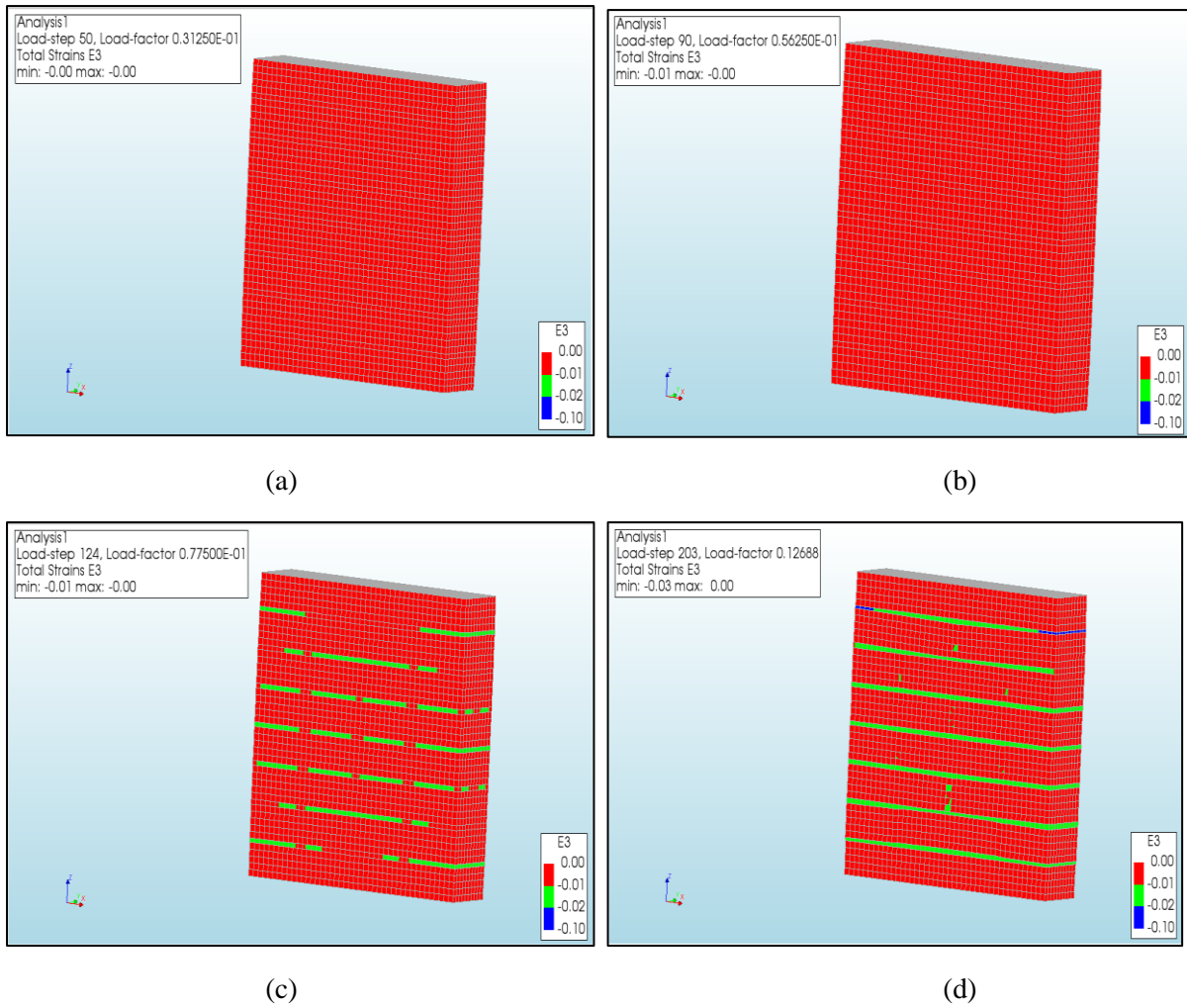
Figure G.5. Progression of principal strain E3.

The evolution of principal strain E3 in the specimen during the analysis is shown in **Figs. G.5 (a – d)**.

G.4 Analysis for cracking of brick

In this section, the cracking failure of brick is discussed.
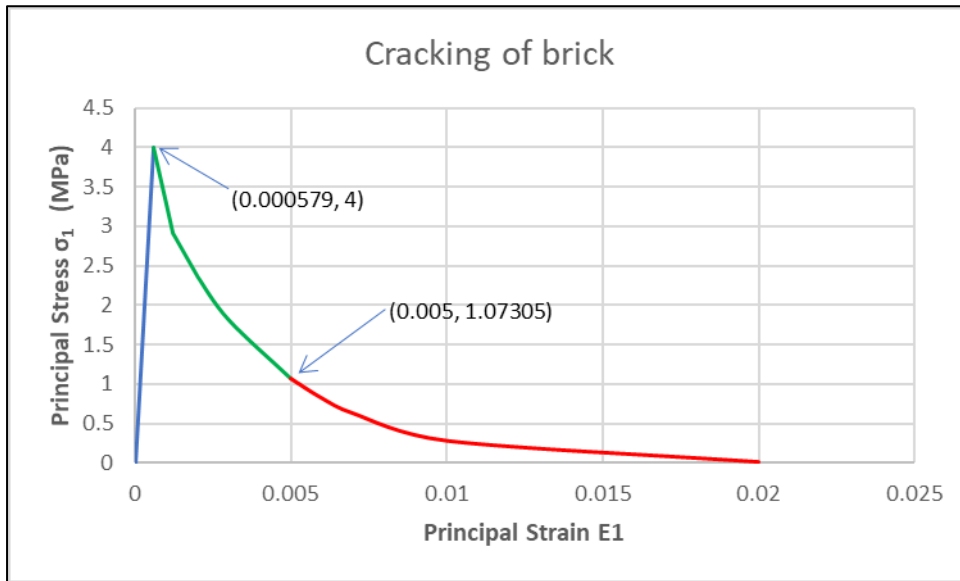
Figure G.6. Constitutive law for cracking of brick element of Model 7.

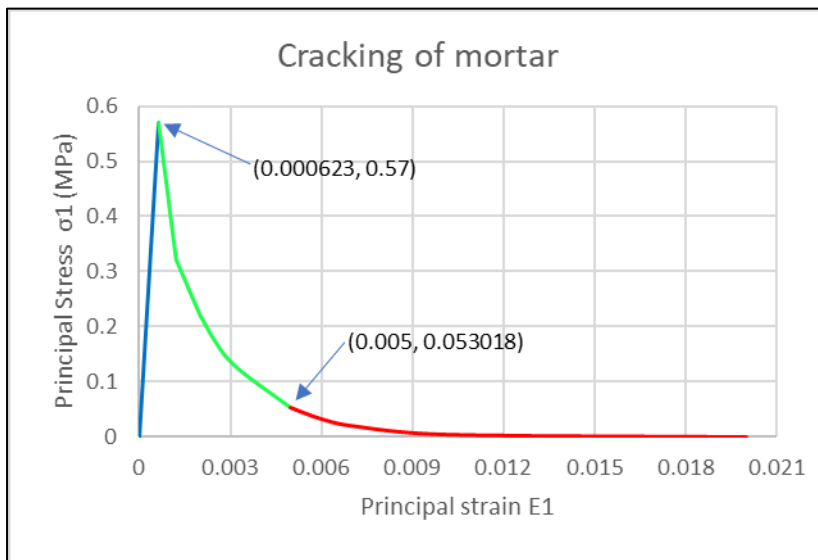<div style="display:flex">(a)   (b)</div>

(c)   (d)
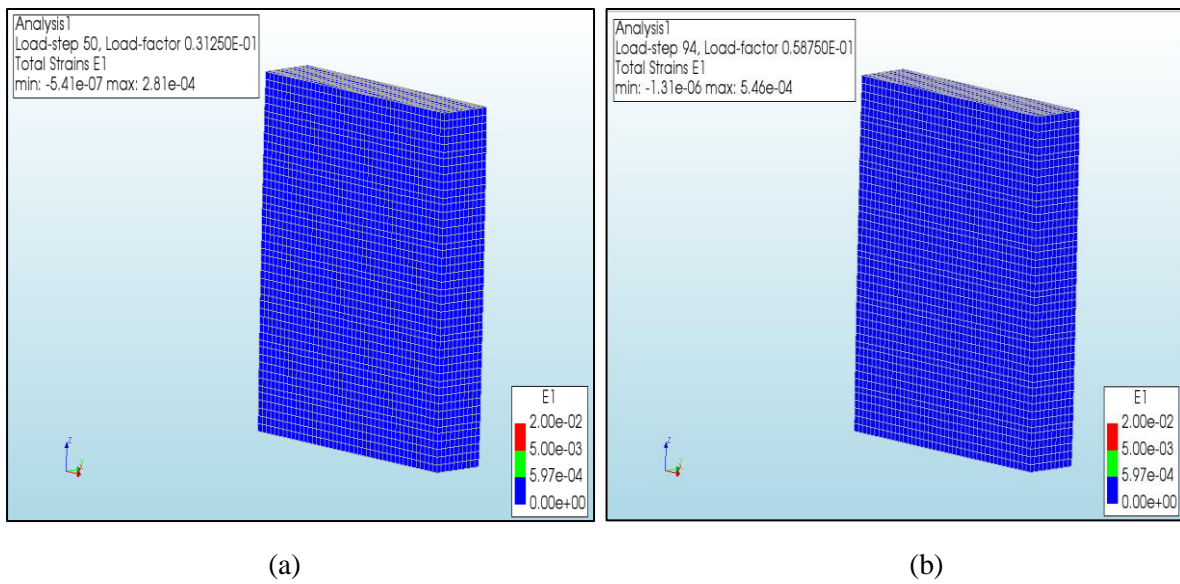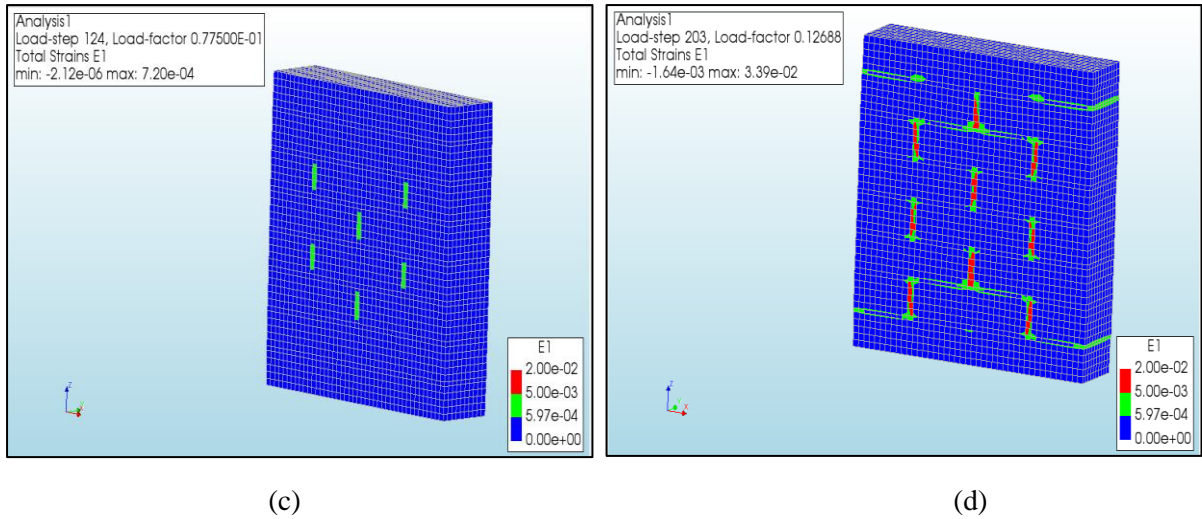
Figure G.7. Progression of principal strain E1.

The evolution of principal strain E1 in the specimen during the analysis is shown in **Figs. G.7 (a – d)**.

G.5 Analysis for crushing of brick

In this section, the crushing failure of brick is discussed.
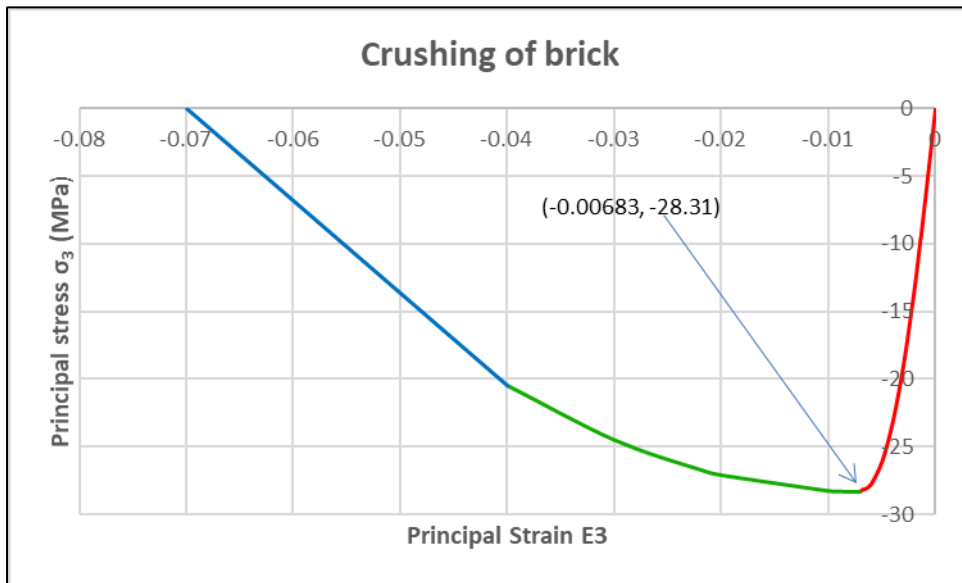
Figure G.8. Constitutive law for crushing failure of brick for Model 9.
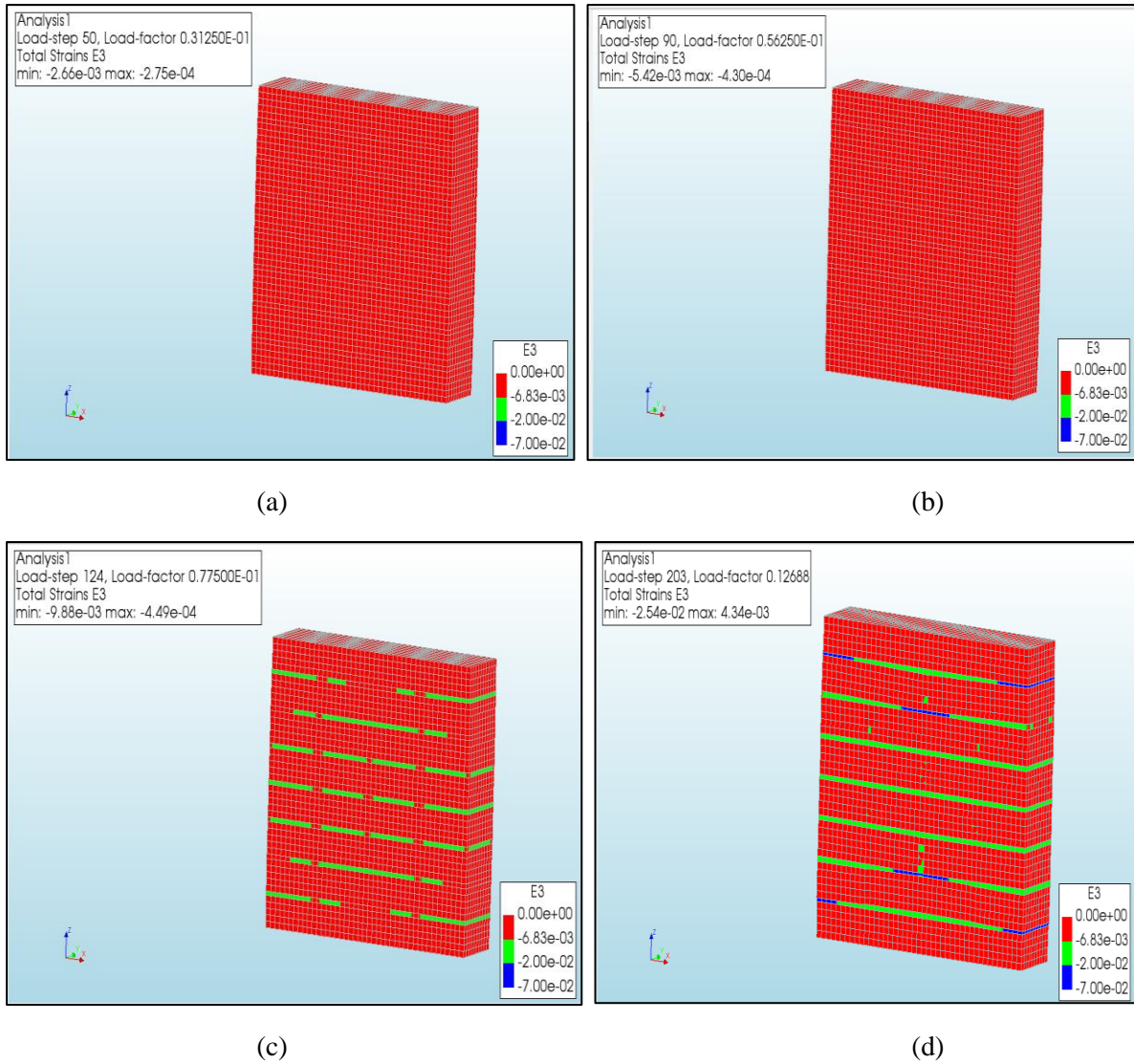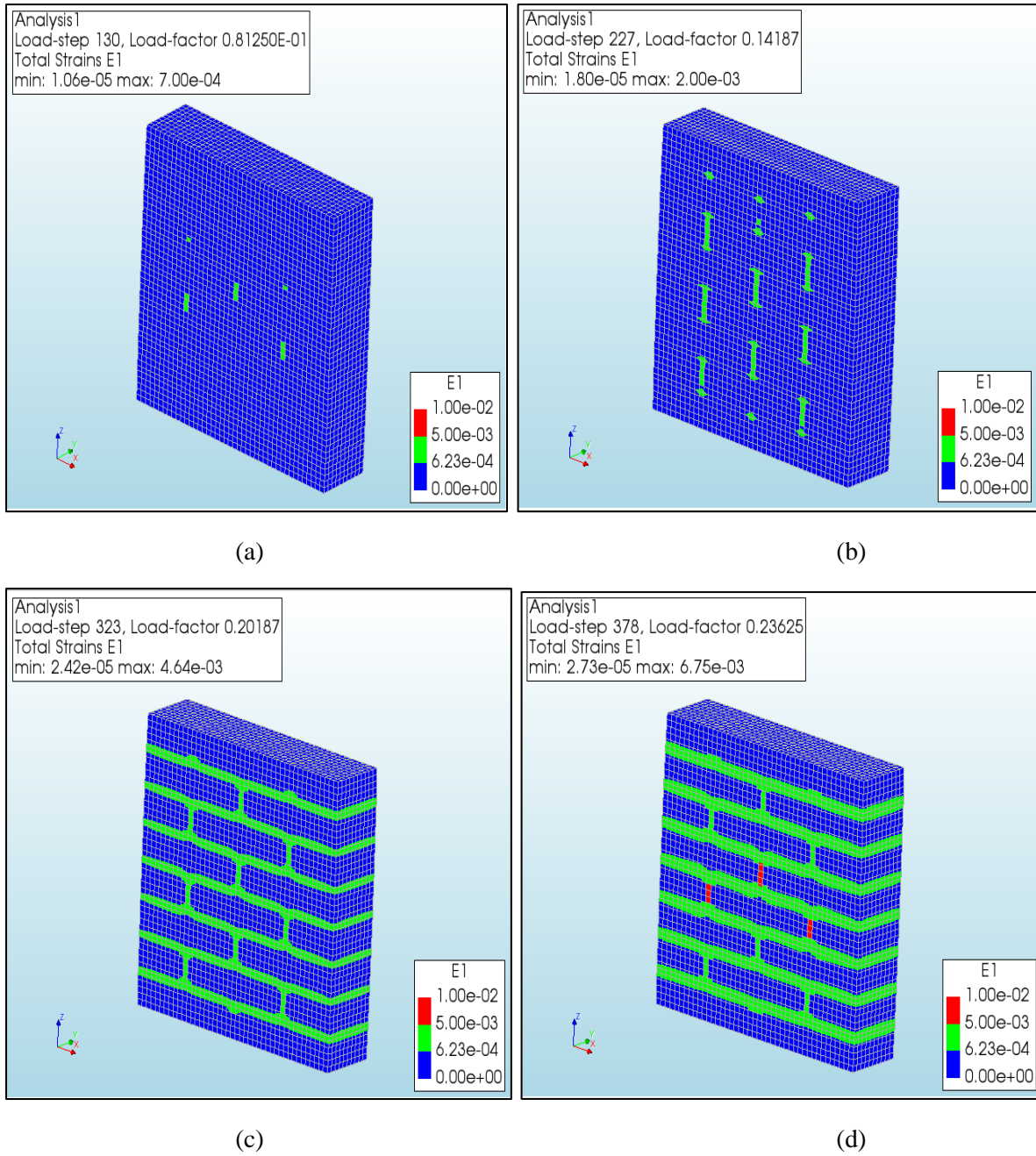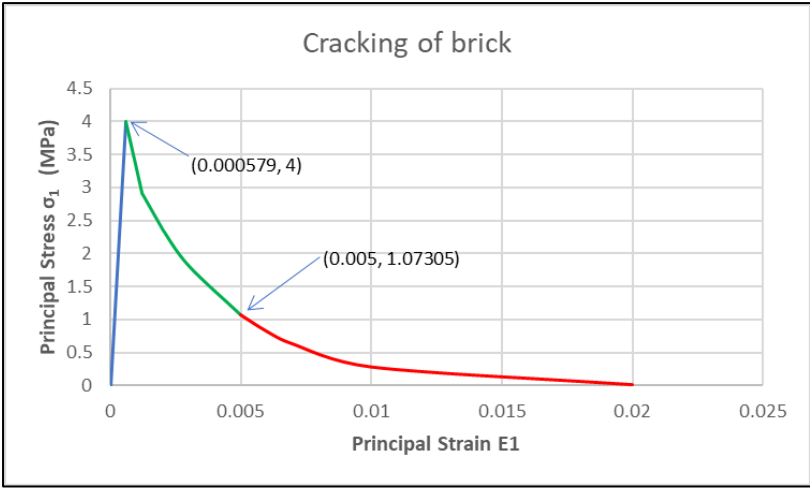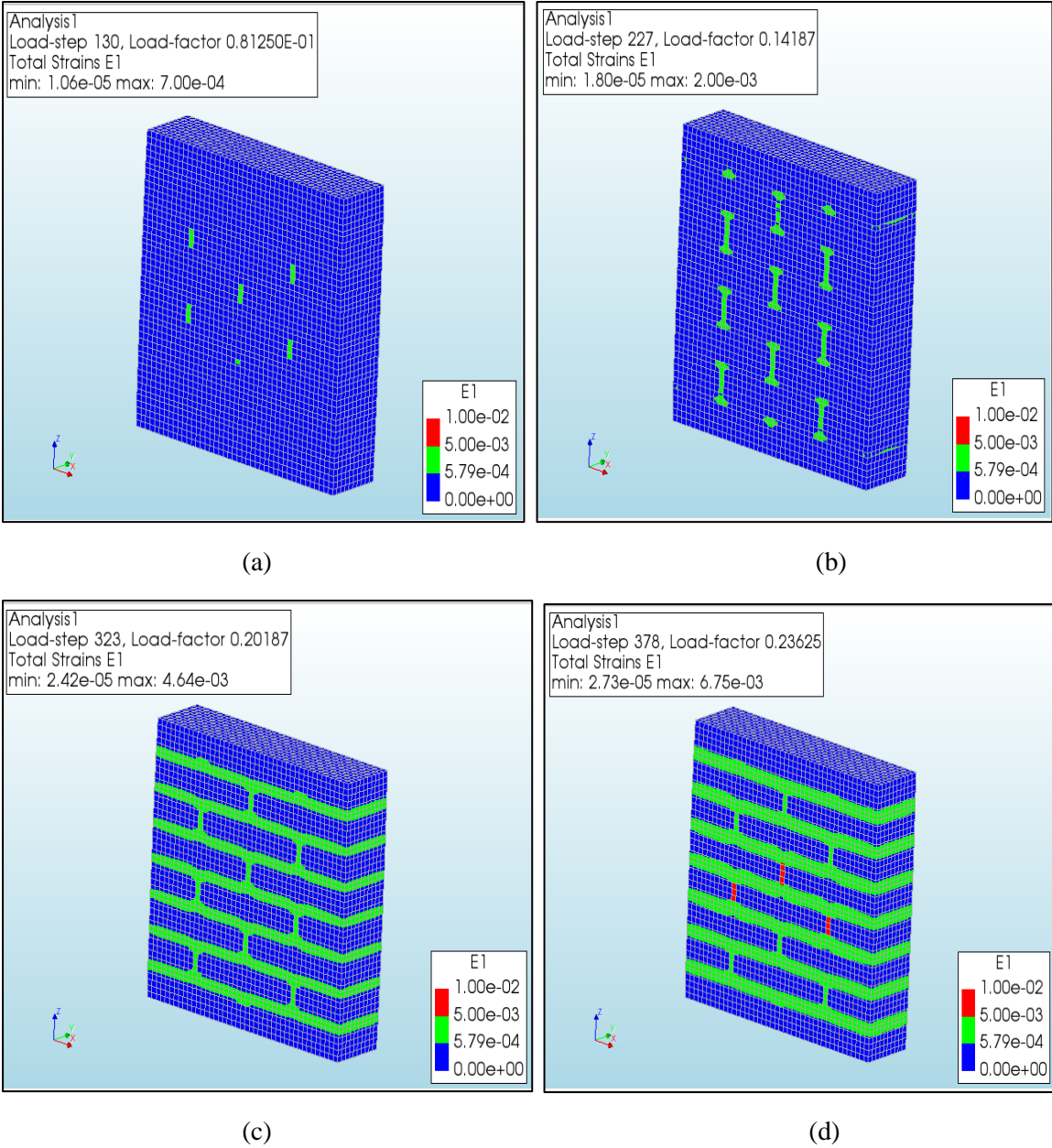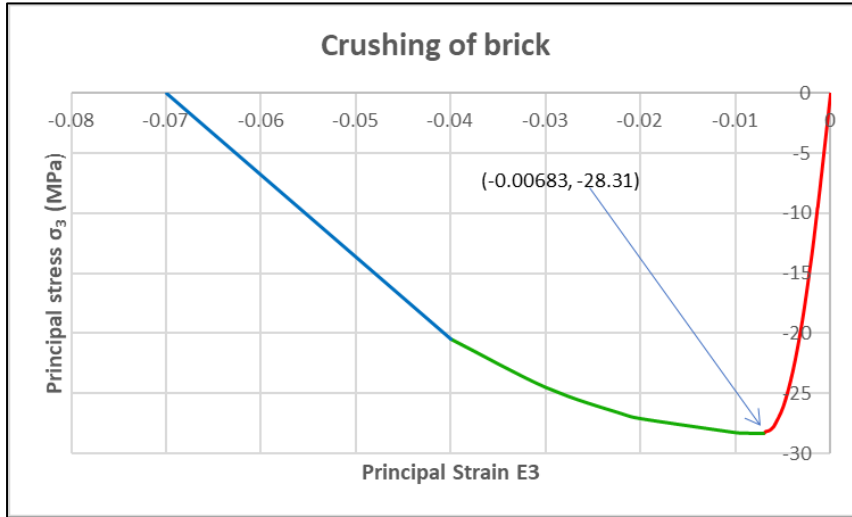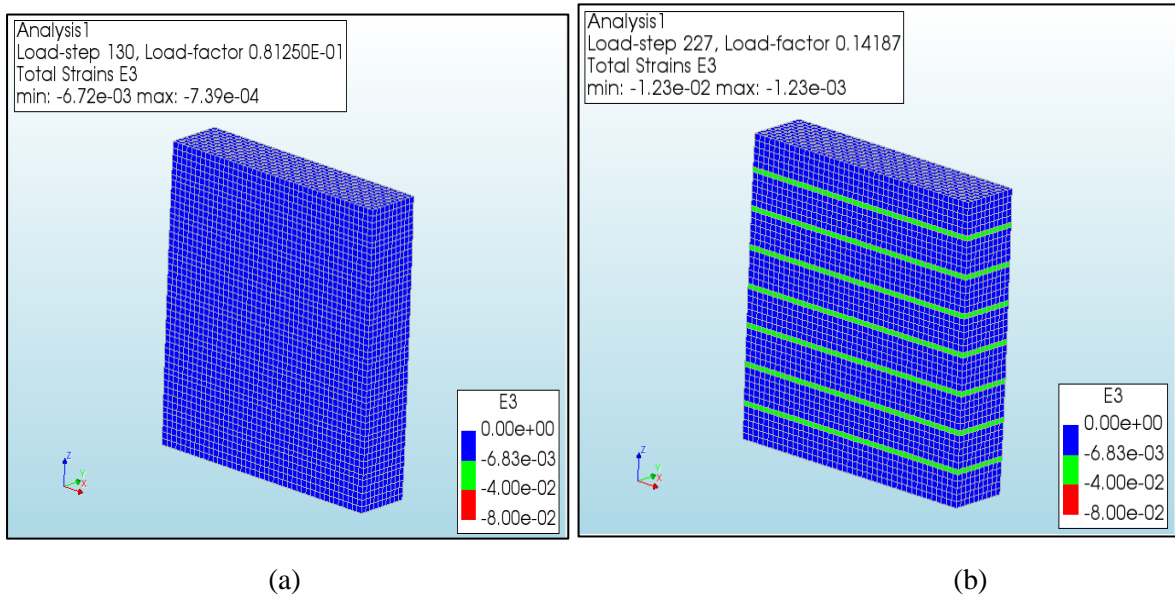
Figure G.9. Progression of Principal strain E3

The evolution of principal strain E3 in the specimen during the analysis is shown in **Figs.G.9(a – d)**.

APPENDIX – H

In this section, the results of Model 8 are discussed in detail.

H.1 Checking Convergence norms

(a)   (b)

(c)
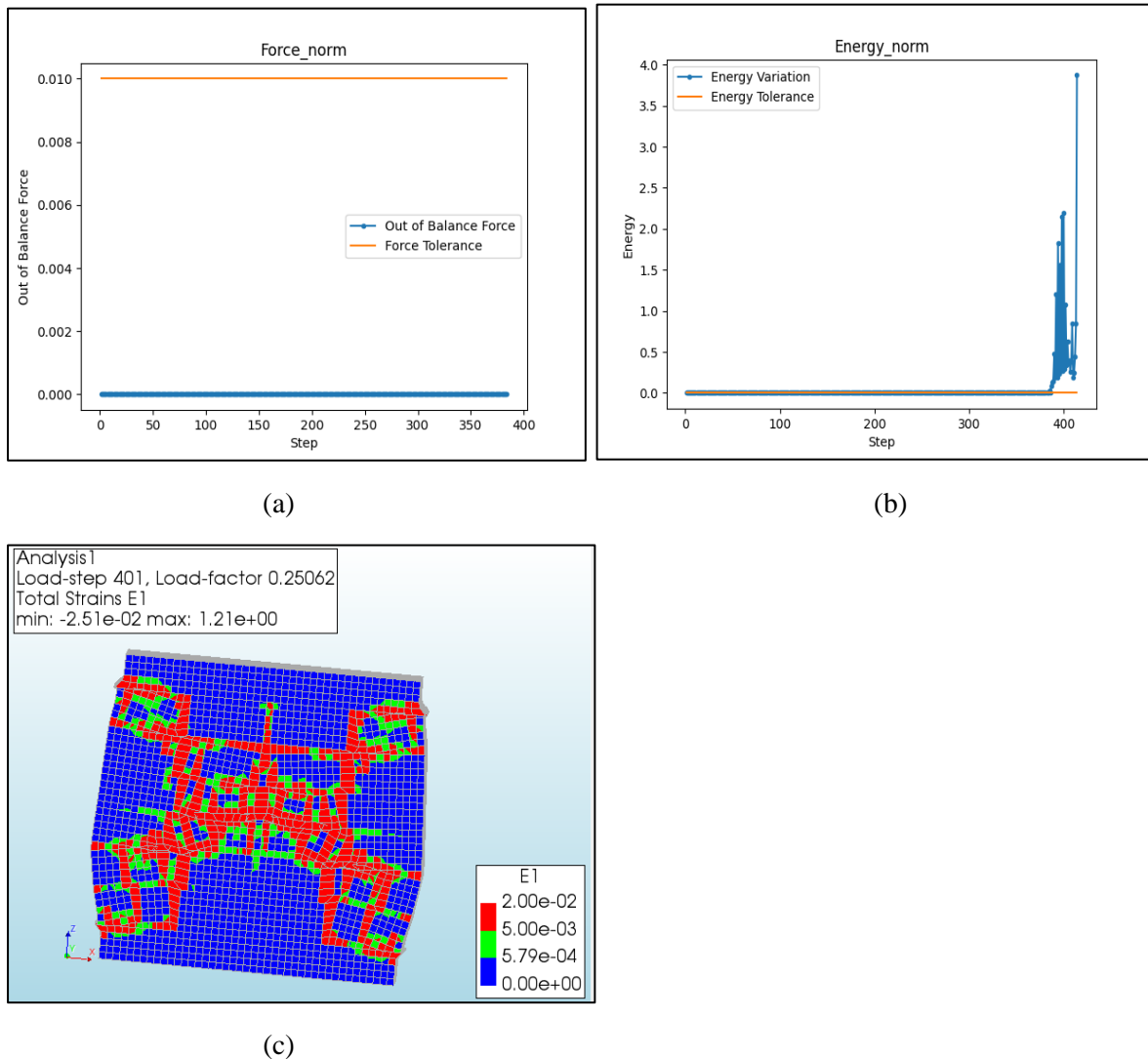
Figure H.1 Variation of (a) force; (b) energy during analysis; (c) Principal strain E1 at load step 401

Fig. H.1 shows the variation in force, and energy during analysis. By observing the variations in force and energy after the analysis, it can be said that the results of this analysis are trustworthy till load step 385. All the variations till load step 385 are well within the convergence norms. The analysis is performed only till load step 385. **Fig. H.1c** shows an unrealistic deformation at the edge and central part of specimen which accounts for the high variation of beyond load step 385.

H.2 Stress-Strain plot of the model
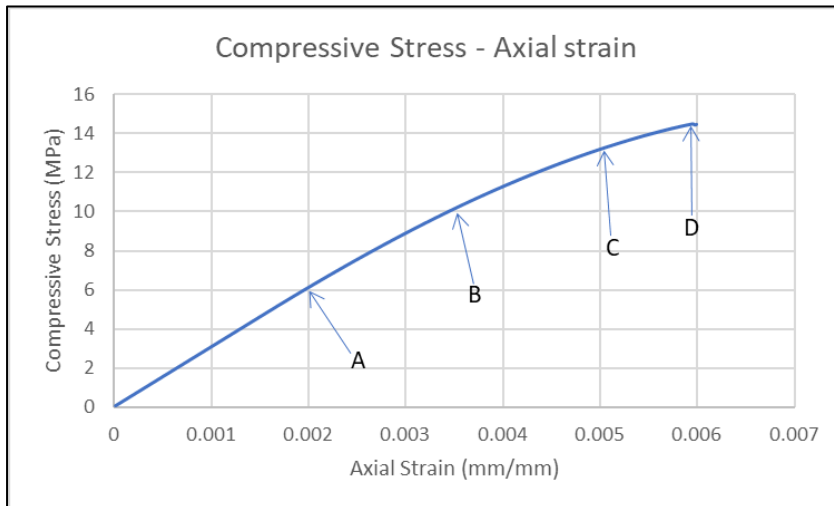
Figure H.2: Plot of compressive stress vs. axial strain along with specified load levels.

Fig. H.2 shows the plot of compressive stress-axial strain for Model 8. The load levels shown in the figure have been used to study the progression of potential failure mechanisms.

H.3 Analysis for cracking of mortar

In this section, the cracking of mortar is discussed. The constitutive law for cracking of mortar is shown below in **Fig. H.3.**

Figure H.3. Constitutive law of mortar element of Model 8.

(a)

(b)

(c)

(d)

Figure H.4. Progression of Principal Strain E1.

The evolution of principal strain E1 in the specimen during the analysis is shown in **Figs. H.4(a – d)**.

H.4 Analysis for cracking of brick

In this section, the cracking failure of brick has been discussed.

Figure H.5: Constitutive law for cracking of brick for Model 8.

(a)

(b)

(c)

(d)

Figure H.6: Progression of Principal Strain E1.

The evolution of principal strain E1 in the specimen during the analysis is shown in **Figs. H.6(a – d)**.

H.5 Analysis for crushing of brick

In this section, the crushing failure of brick is discussed.

Figure H.7 Constitutive law for crushing failure of brick for Model 10.

(a)   (b)
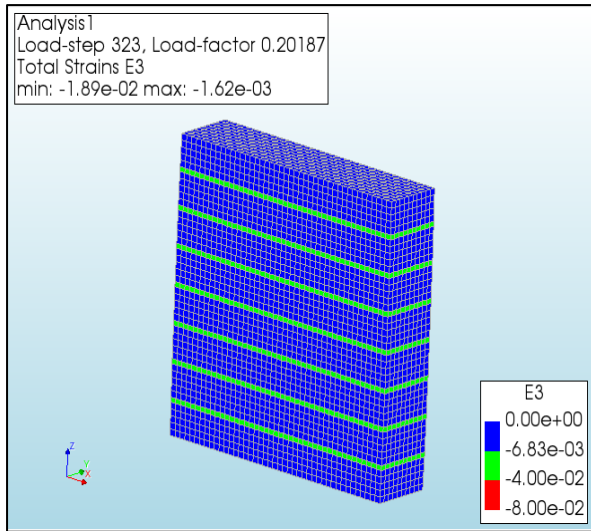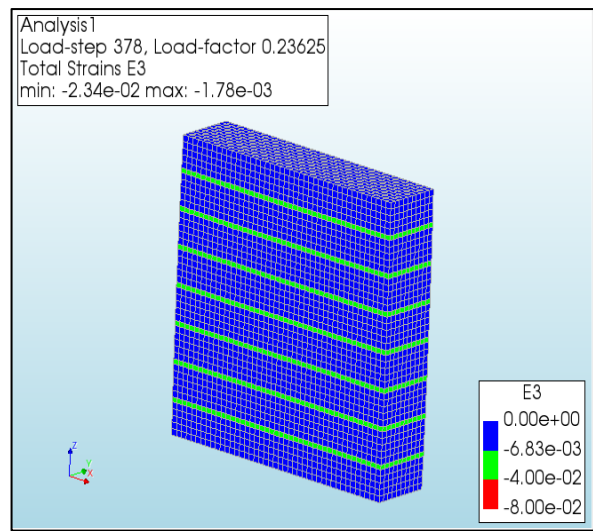
(c)   (d)

Figure H.8. Progression of Principal Strain E3.

The evolution of principal strain E3 in the specimen during the analysis is shown in **Figs.H.8(a – d)**.

APPENDIX – I

In this section, the results of Model 9 are discussed in detail.

I.1 Checking Convergence Norms
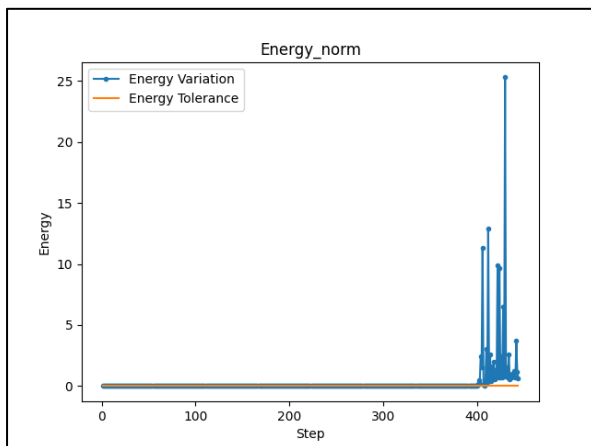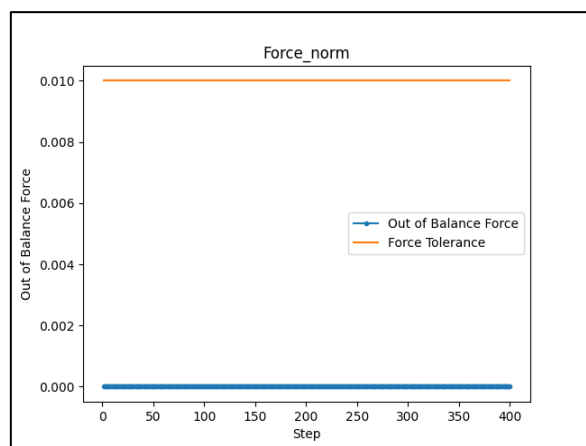
(a)   (b)

Fig. I.1 shows the variation in force, and energy during analysis. By observing the variations in force and energy after the analysis, it can be said that the results of this analysis are trustworthy till load step 400. All the variations till load step 400 are well within the convergence norms. The analysis is performed only till load step 400.

I.2 Stress-Strain plot of Model 9
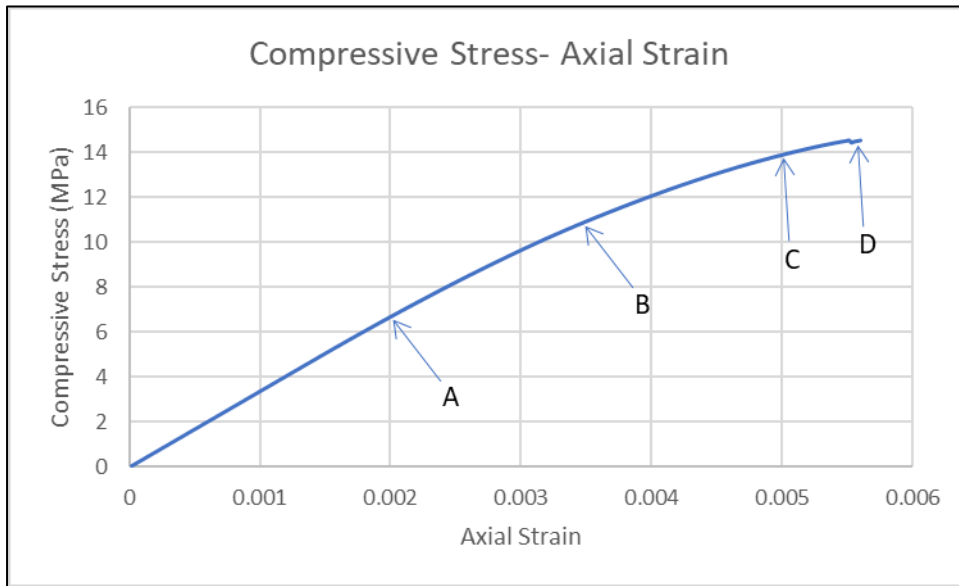
Fig. I.2: Plot of compressive stress vs. axial strain along with specified load levels.

Fig. H.2 shows the plot of compressive stress-axial strain for Model 9. The load levels shown in the figure have been used to study the progression of potential failure mechanisms.

I.3 Analysis for cracking of mortar

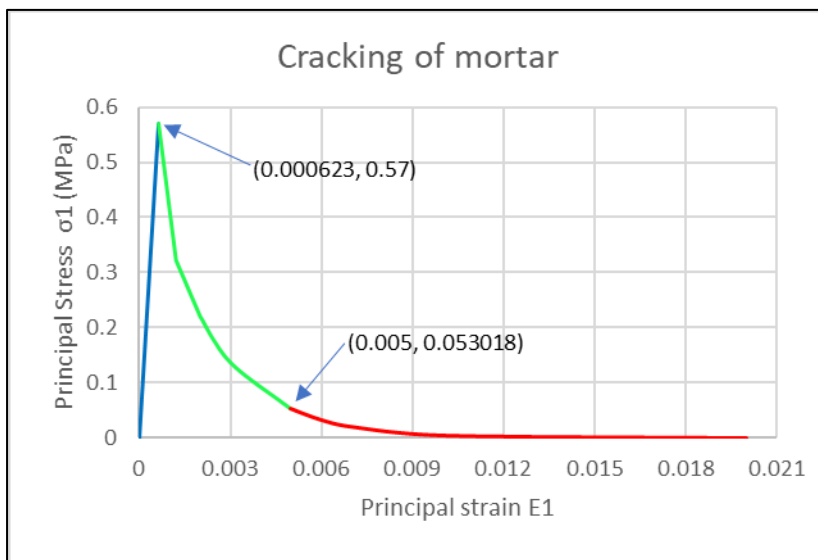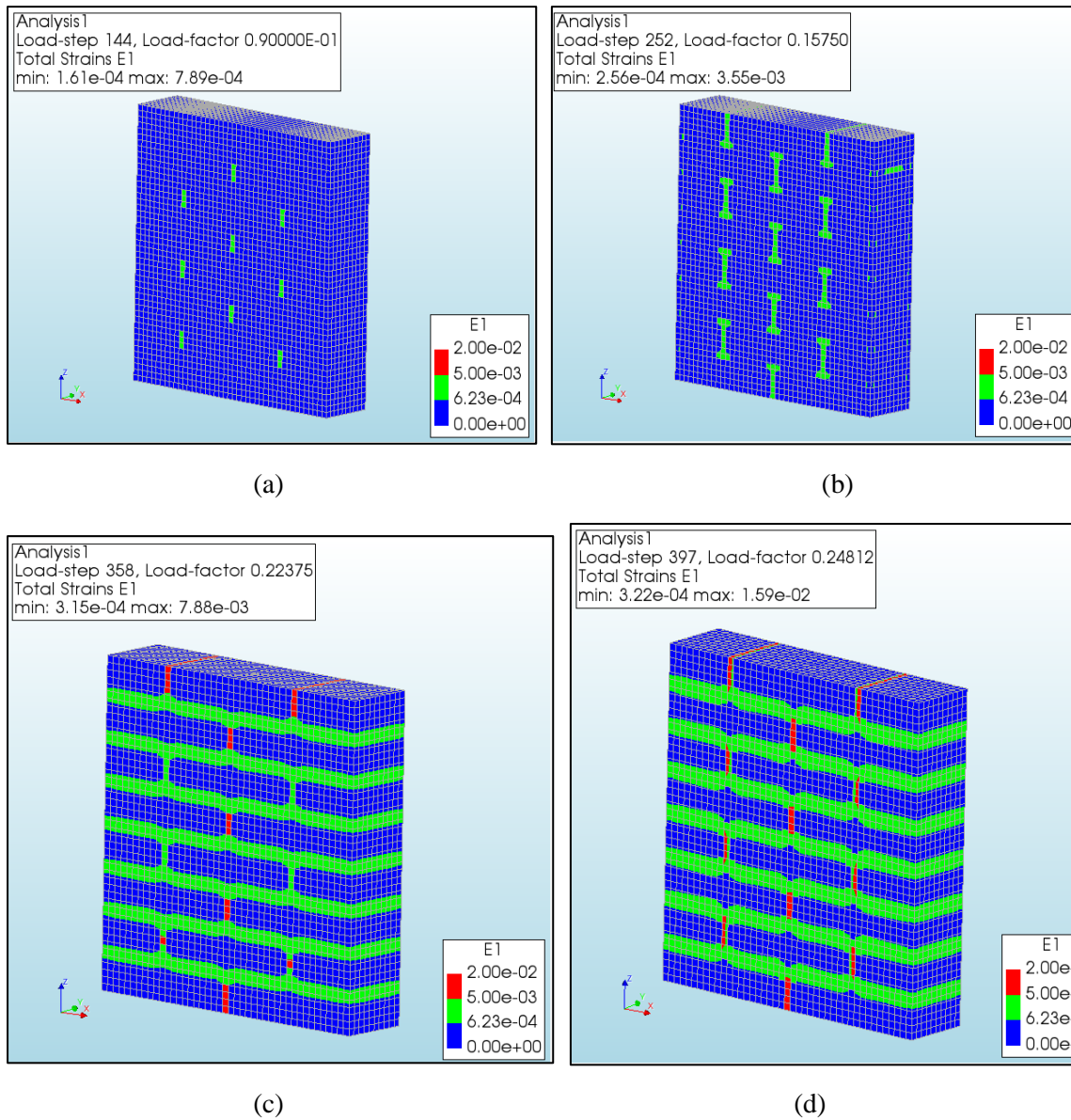In this section, the cracking of mortar is discussed. The constitutive law for cracking of mortar is shown below in **Fig. I.3.**

Figure I.3. Constitutive law of mortar element of Model 8.

(a)   (b)

(c)   (d)

Figure I.4: Progression of Principal Strain E1.

The evolution of principal strain E1 in the specimen during the analysis is shown in **Figs. I.4(a – d)**.

I.4 Analysis for cracking of brick

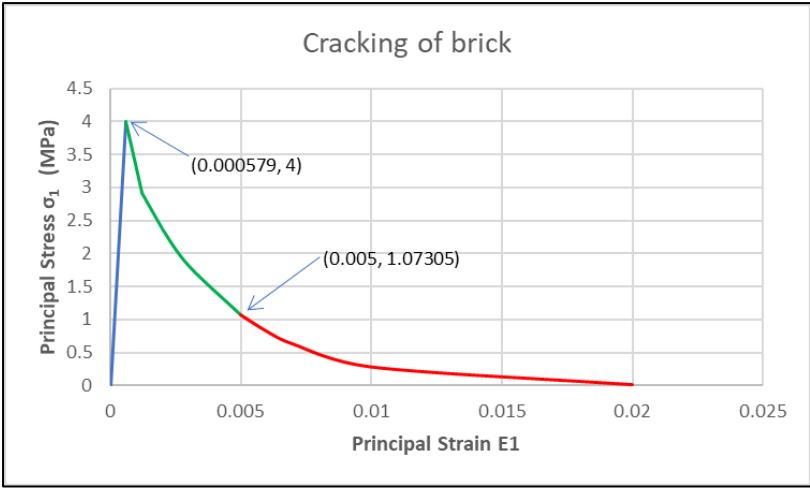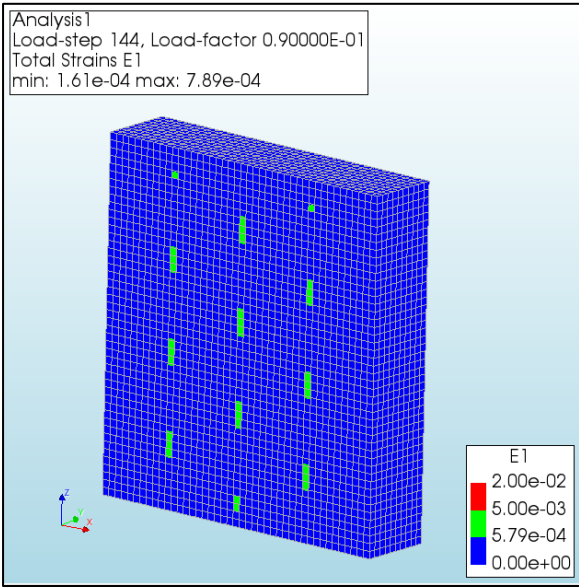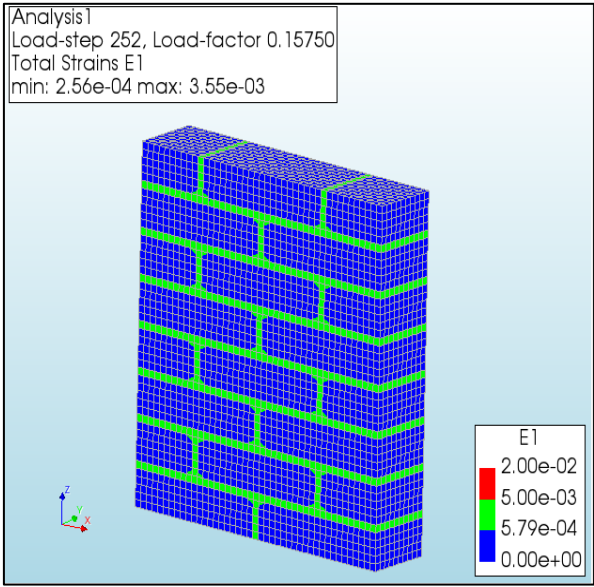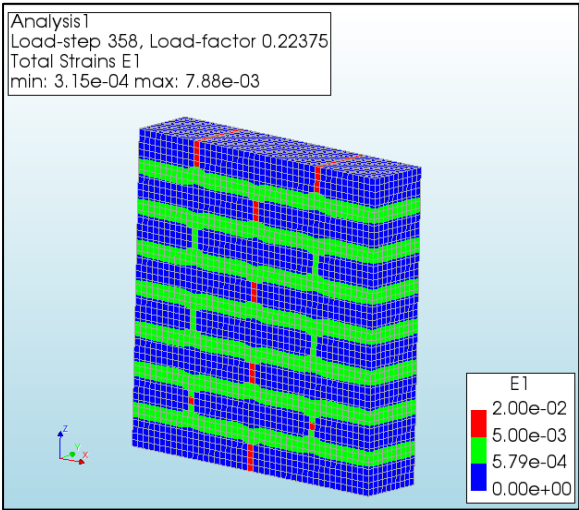In this section, the cracking failure of brick has been discussed.

Figure I.5: Constitutive law for cracking of brick for Model 8.
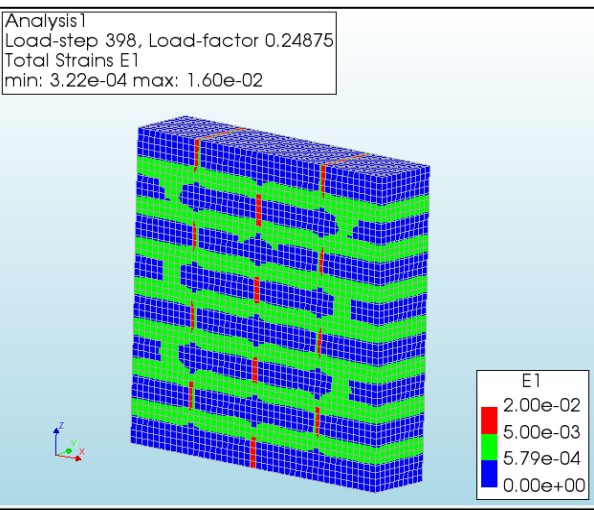

(a)

(b)

(c)

(d)

Figure I.6: Constitutive law for cracking of brick for Model 9.

I.5 Analysis for crushing of brick

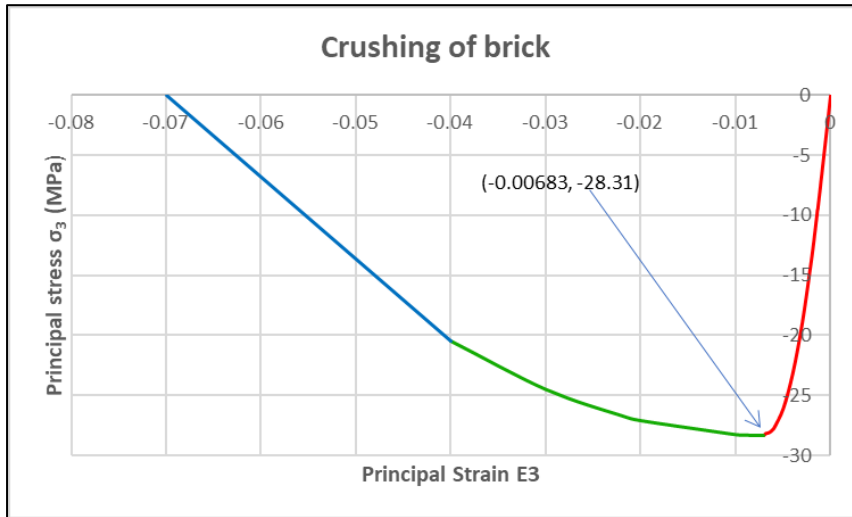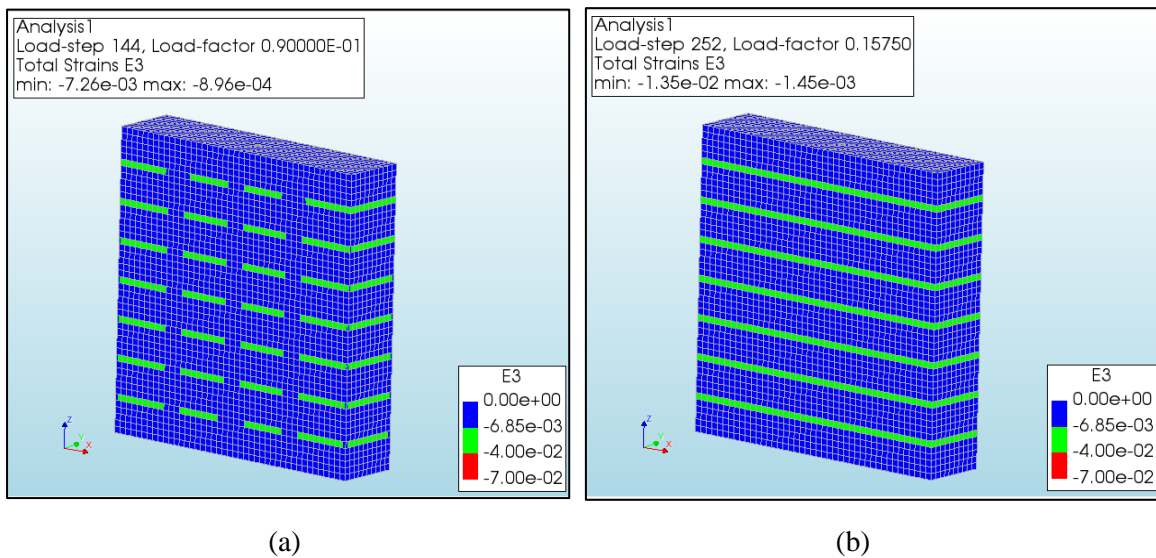In this section, the crushing failure of brick is discussed.

Figure I.7 Constitutive law for crushing failure of brick for Model 9.

(a)   (b)

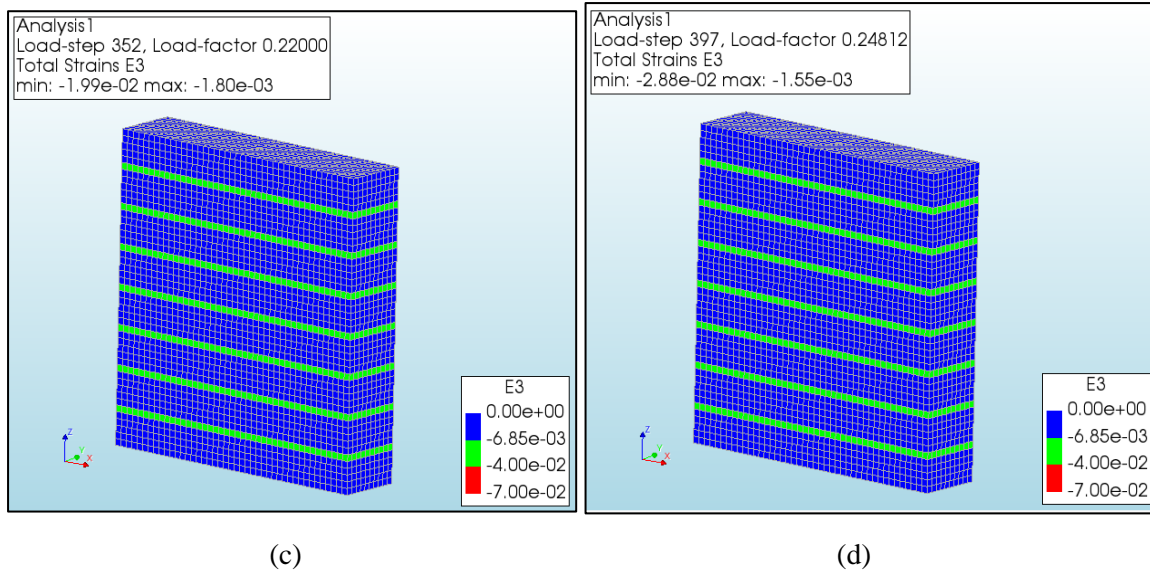(c)   (d)

Figure I.8. Progression of Principal Strain E3.

The evolution of principal strain E3 in the specimen during the analysis is shown in **I.8 (a-d).**